

Université du Québec
Institut National de la Recherche Scientifique
Énergie, Matériaux et Télécommunications

TIP-ENHANCED RAMAN SPECTROSCOPY FOR NANOELECTRONICS

Par
Mischa Nicklaus

Thèse présentée pour l'obtention du grade de
Philosophiae doctor (Ph.D.)
en sciences de l'énergie et des matériaux

Jury d'évaluation

Président du jury et
examineur interne

Professeur François Légaré
INRS – EMT, Canada

Examineur externe

Professeur Matthew Dawber
Dept. of Physics and Astronomy
Stony Brook University, USA

Examineur externe

Professeur Jean-Pierre Cloarec
École Centrale de Lyon, France

Directeur de recherche

Professeur Andreas Rüdiger
INRS – EMT, Canada

Abstract

The technological progress of electronics through miniaturization has reached the nanoscale while new materials with high performance and functional properties gain importance. Quality control and the scientific understanding of expected size effects in electronic nanostructures are required more than ever to consolidate existing technologies and to determine scaling limits of new materials. Conventional techniques, including scanning electron and scanning probe microscopy, provide topographic information but only very limited chemical information to analyze the physical properties of nanomaterials, especially without *a priori* knowledge about the sample. Chemical and structural sensitivity is accessible by Raman or infrared spectroscopy, but with a spatial resolution limited to the microscale by the diffraction limit of light. Tip-enhanced Raman spectroscopy (TERS) combines the virtues of scanning probe microscopy with those of optical spectroscopy to overcome the diffraction limit through the excitation of surface plasmons on a scanning probe tip to confine light to nanometers.

TERS has been applied primarily to molecules and organic samples. Nanoelectronic devices, which are typically composed of metallic or semiconducting substrates and nanostructures with considerable variations in permittivity, are yet to be investigated systematically. First and foremost, this requires a reliable TERS system for operation on non-transparent and non-conductive samples. In this work, a TERS system is installed to operate on opaque samples by employing optical side access. TERS probes are fabricated by electrochemical etching and operated in scanning tunneling microscopy and atomic force microscopy with quartz tuning forks to enable scanning on various surfaces. The chemical sensitivity and lateral resolution of the system is evaluated on carbon nanotubes as reference sample.

TERS is successfully applied to ferroelectric, lead titanate nano-crystals on a platinumized silicon substrate as a model system for nanostructured, charge-based memory devices at the onset of finite size effects. TERS allows for the chemical identification of the lead titanate (PbTiO_3) and the verification of the ferroelectric phase of the crystals with a lateral resolution as small as 4 nm under ambient conditions. Furthermore, the TERS spectra indicate the close proximity of the crystals to their paraelectric phase transition. A detailed analysis identifies the combination of local heat introduced by the laser and the finite size of the crystal to be at the origin of this transition.

Considerable variations in permittivity across the sample and between sample and substrate cause a modulation of the surface plasmon resonance frequency and thus variations in the enhancement factor of the tip. A quantitative analysis of the TERS spectra relates the plasmon frequency shift to the sample's composition, morphology, and atomic structure. Small variations of the sample's refractive index are imaged with nanoscale resolution and confirm the presence of grain boundaries in individual crystals. These results provide a deeper understanding of nucleation during the growth process of the sample. Our experimental findings and the interpretation of the plasmon frequency modulation are confirmed by a time-domain simulation.

Acknowledgements

During my work on this project and my last four years in Canada, I received support and motivation from many people who deserve a great thank you.

First of all, I feel greatly indebted to my advisor, Prof. Andreas Rüdiger, for giving me this opportunity and putting his trust in me to undertake this project with his startup fund. His enormous contribution of time and support inside and outside of the laboratory as well as our countless scientific discussions led to the success of this project.

I would like to thank the examiners, Prof. François Légaré, Prof. Matthew Dawber, and Prof. Jean-Pierre Cloarec, for their invested time and effort as part of the jury committee.

Furthermore, I would like to thank all our group members, past and present. A few members in particular deserve special thanks: Dr. Christian Nauenheim, a big thank you, for being a great conversational partner about the scientific details as well as goals in life, and for his support with the tip-etching setup; Mathieu Moretti for always asking the type of questions that help you to find the next logical step; Ivan Velasco, for his work to keep every item in the laboratory always operational; Andreas Büscher, for his programming support in Matlab that led to the discovery of the SPR shift; and Julien Plathier, for rapidly realizing a TERS analysis program and his great support with the French translation of this thesis.

Thanks are due to the engineers of AIST-NT who provided technical and know-how support far beyond their contractual duties, even past midnight, local time, in Moscow. Special thanks go to Andrey Krayev for his support with SPM and TERS and Vasili Gavriyuk for his tremendously important help with the optical setup and his useful little programs.

Dr. Sylvain Vedraïne and Prof. François Lagugné-Labarthet from the University of Western Ontario deserve thanks for an excellent job in calculating the finite-difference time-domain simulations for my TERS experiment.

I would like to thank Dr. Günter Hoffmann for introducing me to tuning fork TERS, Nina Rauhut for her vital hints about tip production and carbon nanotubes, and Dr. Ralf Vogelgesang for his critical notes and important advice concerning the choice of the right sample.

Last but not least, I would like to thank my friends and family whose simple existence often provides the motivation for my work.

A big thank you goes to my friend Tania, who helped me to settle into Montréal and made everything feel a lot easier during the first few months.

Thank you, Hawley, not only for your love and trust, but also for your forbearing support with the snares of the English language which often demanded your in-depth understanding of the science behind my language ingenuities.

I owe my greatest gratitude to my parents Edith and Jürgen for their immeasurable, comprehensive support, throughout my education and during my years in Canada, and who made it possible that I can write these lines today.

Contents

1	Introduction	1
1.1	History of microscopy	2
1.2	Tip-enhanced Raman spectroscopy.....	3
1.3	Motivation	4
1.4	Objectives	5
1.5	Outline.....	5
2	Methods and materials	7
2.1	Scanning probe microscopy.....	7
2.1.1	Scanning tunneling microscopy.....	7
2.1.2	Atomic force microscopy.....	8
2.1.3	Tuning Fork AFM.....	9
2.1.4	Piezoresponse Force Microscopy	10
2.2	Raman Scattering.....	12
2.2.1	Phonon modes.....	13
2.2.2	Raman effect.....	13
2.2.3	Raman spectroscopy setup.....	15
2.2.4	Raman spectrum of silicon.....	17
2.3	Fluorescence	18
2.4	Far-field optics.....	19
2.4.1	Rayleigh criterion	19
2.4.2	Numerical aperture and optical resolution of a lens.....	20
2.4.3	Focal volume.....	21
2.4.4	Optical penetration depth.....	22
2.5	The optical near-field.....	23
2.5.1	Transition between near-field and far-field	23
2.5.2	Surface plasmons	24
2.5.3	Field enhancement.....	26
2.5.4	Enhancement factor.....	28
2.5.5	Plasmon resonance frequency	29
2.6	Surface-enhanced Raman spectroscopy.....	31
2.6.1	SERS substrates	31
2.6.2	Gap-enhancement	32
2.6.3	Chemical enhancement	33
2.7	Tip-enhanced Raman spectroscopy.....	33
2.7.1	Optical excitation and detection.....	34
2.7.2	Scanning probe methods.....	35
2.7.3	Setup of our TERS system	36
2.8	Ferroelectrics	39

2.8.1	Electromechanical properties	39
2.8.2	Crystal structure of lead titanate	41
3	Fabrication of the TERS tips	43
3.1	Tip material	43
3.2	Electrochemical etching of TERS tips	45
3.2.1	Experimental setup	46
3.2.2	Electrochemical reaction	46
3.2.3	Experiments and results	47
3.2.4	Tip shape	53
3.2.5	Summary	54
3.3	Alternative fabrication methods	55
4	TERS on carbon nanotubes	57
4.1	Sample preparation and characterization	57
4.1.1	TERS substrates	57
4.1.2	Selection and characterization of CNTs	61
4.1.3	Carbon nanotube deposition	63
4.2	Alignment between objective and tip	64
4.3	TERS mapping	66
4.4	Objective scan	69
4.5	System stability and resolution	70
4.6	Chemical sensitivity	72
4.7	Summary	73
5	TERS on lead titanate nano-crystals	75
5.1	The superparaelectric limit	75
5.2	Sample preparation	77
5.3	Preliminary sample characterization	78
5.3.1	AFM topography scans	78
5.3.2	Piezoelectric measurements	79
5.3.3	Confocal Raman measurements	81
5.4	Tuning fork AFM measurements	83
5.4.1	Probe preparation	83
5.4.2	Quality factor	84
5.4.3	Oscillation amplitude	86
5.4.4	Tuning fork topography scans	87
5.4.5	Tip-sample distance	88
5.5	TERS experiments	89
5.5.1	Probe selection	90
5.5.2	TERS mappings	91
5.6	Data analysis and discussion	95
5.6.1	Tip-generated background	95
5.6.2	TERS spectrum of the PbTiO ₃ islands	99

5.6.3	TERS map of PbTiO ₃	103
5.6.4	Surface plasmon resonance mapping.....	104
5.6.5	Origin of the surface plasmon resonance shift.....	106
5.6.6	Finite-difference time-domain simulation.....	108
5.6.7	High resolution mapping.....	109
5.7	Summary	112
6	Conclusions	115
7	Outlook	119
8	Abbreviations	121
9	Bibliography	123
10	Publications and conference contributions	135

1 Introduction

The computer and chip industry, with its efforts to create ever higher performing electronic devices, has driven dimensions towards the nanoscale like no other field. Microscopy techniques, such as scanning electron microscopy (SEM) and tip-only scanning probe techniques (AFM or STM), are indispensable quality control tools even before devices are electrically characterized to check their functionality.

Nanoscience holds the promise of novel functionalities, but miniaturization also implies the possible loss of macroscopic properties, such as ferroelectricity, while classical models become increasingly incorrect with smaller numbers of atoms. Furthermore, the integration of novel materials leads to physical and chemical effects that require investigation. This development creates an unmatched demand for microscopy techniques that provide chemical and structural information on the nanoscale; a demand that is simultaneously evolving in the life sciences, which are making breath-taking progress in the understanding of biochemical and molecular processes.

Despite their ease of use, electron microscopy and conventional scanning probe microscopy are limited in their ability to provide chemical and structural information without *a priori* knowledge about the sample. Such information is, however, readily accessible by optical spectroscopy methods such as Raman and infrared (IR) spectroscopy. These widely complementary techniques are diffraction limited in their lateral resolution to several hundred nanometers. In order to combine the virtues of scanning probe and optical spectroscopy, Tip-Enhanced Raman Spectroscopy (TERS) was contrived to achieve chemical and structural surface characterization with nanometer resolution and molecular sensitivity. Figure 1.1.1 illustrates the connection of high spatial resolution with chemical information by taking the analogy of photography.



Figure 1.1.1: Photography as an analogy to TERS: (a) Blurry colors: Classic optical microscopy is limited to the micro-scale. (b) Black and white: High topography resolution with SEM or AFM but (almost) no chemical information. (c) Color photography: TERS combines high lateral resolution with chemical information. (Photo: Basilique Notre Dame de Montréal by Harold Stiver, idea: Yason Yeo)

1.1 History of microscopy

The first optical microscopes appeared around 400 years ago and have ever since been limited in their resolution by the diffraction limit of light. In other words, conventional optical microscopes are not able to resolve details below several hundred nanometers. Higher resolution became possible around 60 years ago with the introduction of electron microscopes, which extended the diffraction limit by using high energetic electrons with a Compton-wavelength shorter than the wavelength of light. Scanning electron microscopes (SEM) achieve a resolution of a few nanometers but require vacuum conditions. In the early 1980's, scanning probe microscopy (SPM) was developed to provide atomic resolution: In 1981, Binnig and Rohrer¹ invented the scanning tunneling microscope (STM) [1] which uses piezoelectric actuators [2, 3] to scan a sharp tip over the surface of a sample with Ångström precision. Monitoring the electric tunnel current between tip and sample, the orbitals² of silicon atoms were visualized for the first time [4]; shortly after, Binnig built the first atomic force microscope (AFM), opening the door for topography scans of *non*-conductive samples [5]. STM and AFM can be operated under ambient conditions and soon became routine laboratory techniques creating a billion dollar market for microscope and probe manufacturers [6]. However, despite their advantage of high resolution, SEM and SPM provide only limited chemical information about the sample when compared to the information provided by optical techniques including Raman spectroscopy.

The Raman effect is particularly useful for physics and material science as it provides by far the richest source of chemical and structural information through the vibrational spectrum of the sample. The effect was predicted by the Austrian physicist Adolf Smekal in 1923 [7] and experimentally confirmed by Landsberg et al. [8] in crystals, and by Raman³ et al. [9-11] in liquids in 1928. Due to the very low cross section of Raman scattering, it took until the development of the laser as a strong monochromatic light source in the 1960s [12] to establish Raman spectroscopy as a routine tool for chemical analysis [13, 14]. Currently, micro-Raman spectroscopy is used to create a chemical image (map) by scanning the laser over the surface of the sample while recording a Raman spectrum at every position. The maximum lateral resolution of scanning laser microscopy is, however, still diffraction-limited to several hundred nanometers.

Breaking the diffraction limit

In 1928, Edward Synge published one of the earliest theories regarding breaking the optical diffraction limit. He proposed a subwavelength aperture be moved

¹ Gerd Binnig and Heinrich Rohrer were awarded the Nobel Prize in physics in 1986 for inventing the scanning tunneling microscope

² More precisely the electronic *density of states* at the surface of a silicon crystal.

³ The Indian physicist Sir Venkata Raman was awarded the Nobel Prize in physics in 1930 for his work on the Raman scattering effect that was named after him.

across a sample while shining light through it to investigate the sample's surface [15]. In a later publication [16], Synge suggested the use of a piezoelectric scanner to move the sample with the required precision. It took another four decades before Ash et al. imaged a sample with a sub-wavelength aperture [17], based on microwaves, to achieve millimeter resolution⁴. The invention of scanning probe microscopy gained the attention of the near-field optics community still seeking a way to accomplish sub-wavelength imaging in the visible range. In 1984, Lewis et al. fabricated a mask with a sub-wavelength aperture to scan a sample in the visible spectral range [19], and Pohl et al. presented the first scans using a metalized quartz tip with an aperture of 20 nm at its apex to guide and constrain the light close to the sample [20]. This technique was named near-field scanning optical microscopy (NSOM or SNOM) and is now typically based on tapered and metal-coated fiber probes [21-27] operated by an SPM. The lateral resolution is about 30-50 nm [28], defined by the aperture of the fiber, and even single-molecule sensitivity on dye molecules can be achieved [29]. However, the bottleneck of SNOM is the tremendous loss of light intensity, by about a factor of 10^5 , when passing through the sub-wavelength aperture [30]. Therefore, SNOM is limited to signal-rich phenomena like fluorescence or Rayleigh scattering and does not qualify for Raman spectroscopy [30], which has a scattering cross section of $\sim 10^{-30}$ cm² that is significantly smaller than the cross section of fluorescence ($\sim 10^{-16}$ cm²) [31].

1.2 Tip-enhanced Raman spectroscopy

In 1974, Fleischmann discovered an enhancement of the Raman signal by several orders of magnitude in an experiment where pyridine molecules adsorbed on a rough silver electrode were excited with a green laser [32]. This effect became known as surface-enhanced Raman scattering (SERS) and became a method for the detection of Raman intensities from small amounts of molecules, down to single molecules. Despite his groundbreaking finding, Fleischmann prematurely assumed that the enhancement was attributed to an increased surface area due to the rough electrode, which would lead to an increased density of scattering molecules adsorbed on the surface [33]. A short time after, two different origins of the signal enhancement were identified: An electromagnetic effect, which is today known to be based on surface plasmons that are generated on the substrate [34, 35]; and a charge transfer effect between the molecule and the silver electrode, often referred to as chemical enhancement [36, 37].

In 1985, John Wessel [38] proposed the idea of transferring the enhancement effect of SERS onto scanning probe microscopy by replacing the metallic substrate with a tip to be scanned over the sample to achieve imaging capabilities. This method was experimentally realized by Renato Zenobi et al. [39], Mark Anderson [40], and Satoshi Kawata et al. [41] in 2000 and became known as tip-enhanced Raman spectroscopy (TERS). Instead of funneling the photons through a small

⁴ Although Ash had reportedly no knowledge about the earlier idea of Synge [18], the experiment served as proof-of-concept.

aperture as in SNOM, TERS creates an optical near-field by externally focusing a laser on the tip to excite a surface plasmon at the apex of a metallic tip. Under specific resonance conditions, determined by the tip material, its radius, the laser wavelength, and the permittivity and geometry of the surrounding environment, the oscillating electric field of the laser excites a surface plasmon resonance (SPR). The resulting electromagnetic near-field reaches very high field intensities that allow for a detectable amount of Raman-scattered photons when the sample is brought into proximity of the tip. Furthermore, the light intensity I decreases rapidly with increasing tip-sample distance d following approximately an $I \propto (r + d)^{-10}$ dependence where r is the radius of the tip [42]. When the tip is scanned at a distance of 1-2 nm over the surface of the sample, the distance dependence of the near-field thus allows for an optical resolution of a few nanometers. Single-molecule sensitivity was achieved on resonant Raman scattering molecules in 2005 [43] with an inverted microscope setup, and sub-molecular spatial resolution in 2013 in vacuum [44]. But despite the demand from the industrial and scientific community and the impressive progress over the last decade, TERS is not yet a routine measurement technique. While the experimental tools now allow for dedicated TERS configurations, the remaining challenges are mainly due to the lack of a consistent production process of TERS tips and the experimental complexity of combined laser spectroscopy and scanning probe microscopy.

1.3 Motivation

For a long time, the success of the chip industry has been firmly linked to market growth and technological advancement through miniaturization by better production processes. Although immersion and deep UV lithography succeeded in reaching feature sizes of 22 nm (mass production 2013), and electron beam lithography less than 10 nm, downsizing led to significant challenges, e.g. increased leakage currents in RAMs and transistors, electromigration in interconnects, and fatigue in memory cells. These effects are increasingly countered by the implementation of new materials, e.g. low-permittivity dielectrics as insulators in CMOS circuits, high-permittivity dielectrics in DRAMs, or phase change materials for nonvolatile memories. Furthermore, the development pipeline contains carbon nanotubes for field effect transistors, graphene as transparent electrodes, ferroelectric tunnel junctions as well as ferroelectric and multiferroic crystals for memory devices, functional organic molecules for bottom up processes, and many more [45, 46].

Recent years have seen a demand for a deeper understanding of the chemical and structural effects that take place in nanoelectronic devices during operation, raising questions that cannot be answered by macroscopic models or indirect electronic characterization alone. A fundamental understanding of these physical effects is necessary to develop device models that would allow for the systematic development of novel materials and tailored devices.

An example of an effect that requires deeper understanding is the superparaelectric limit of ferroelectric crystals. These crystals have been a highly ranked

candidate for nonvolatile memories, which raises questions about their scalability: Since the intrinsic polarization of ferroelectrics is based on their crystalline structure, and since this structure undergoes a size-driven phase transition as the surface-to-volume ratio increases in small crystals, ferroelectrics can become paraelectric and lose their polarization on the nanoscale at the so-called superparaelectric limit. Theoretical models predict different size limits for various ferroelectrics, all of which are of the order of several nanometers [47]. To test these models, a characterization tool needs to be both sensitive enough to measure the polarization or atomic structure on such small volumes and be able to provide the lateral resolution to probe on the nanoscale. With its ability to provide Raman spectra of nanoscale features, TERS closes this gap in surface characterization, paving the way to a deeper understanding of chemical, structural, and electronic properties.

The development of advanced materials and their implementation in nanoelectronics has already built up a multitude of scientific questions that are increasingly difficult to answer by electronic characterization or high resolution microscopes without chemical sensitivity. TERS, however, still remains a method that is mainly found in universities and scientific groups that focus their research on the development of TERS rather than on the investigation of new materials and related questions. This is due to several reasons, primarily the inconsistency in achieved field enhancement with TERS tips that are produced under nominally identical conditions. Secondly, the optical interaction between tip and sample leads to differences in the TERS spectra as compared to confocally measured Raman spectra [48]. Differences occur because of strong electric field gradients close to the tip that influence the polarizability of the sample and thus the Raman spectrum. Furthermore, frequency variations of the surface plasmon resonance of the tip, caused by the permittivity of the sample [49, 50] as well as by distance variations between tip and sample [51-53], have a large impact on the obtained TERS signal.

1.4 Objectives

The goals of this project are twofold:

1. Definition and realization of a TERS system suitable for the analysis of nano-electronic devices. This implies, in particular, non-transparent and partially non-conductive samples and requires quantitative verification of the functionality in terms of stability, resolution and chemical sensitivity on carbon nanotubes as a known reference sample.
2. Investigation of finite size effects on individual ferroelectric lead titanate nano-islands by TERS

1.5 Outline

Chapter 2 starts with an overview of the methods and physical concepts that are required for TERS. The design and functionality of the TERS system is discussed in section 2.7. The chapter closes with a discussion on ferroelectricity in section 2.8.

The crucial component of scanning near-field microscopy is the tip. Regardless of several announcements, TERS probes are still not commercially available. The development of a tip production process, based on electrochemical etching, and the morphological analysis of the produced TERS tips is addressed in chapter 3.

In chapter 4, we use TERS on carbon nanotubes as a reference sample. The nanotubes are selected to investigate the enhancement capabilities of the electrochemically etched tips and to evaluate the stability and precision of the TERS system.

Chapter 5 starts with a description of the sample for the investigation of the superparaelectric limit. We refer to a previously well-characterized lead titanate sample [54]. In order to investigate insulating lead titanate, we upgrade the TERS system to operate with quartz tuning forks as AFM probe with our gold tips attached to them (section 5.4). The TERS mapping on lead titanate is presented in section 5.5 and followed by a comprehensive data analysis in section 5.6. This involves ultra-high resolution TERS images of the chemical composition and crystal structure of the lead titanate islands through the analysis of their Raman spectrum, quantitative investigations of the tip-sample interaction that leads to a shift of the surface plasmon resonance frequency, and last but not least, a comparison of our results with a finite-difference simulation that independently confirms our findings.

2 Methods and materials

TERS combines Raman spectroscopy with a scanning probe microscopy technique, either AFM or STM, in order to image the Raman signature of a sample with nanometer resolution and molecular sensitivity. This chapter explains the microscopy and spectroscopy methods required for TERS and their underlying physical effects, discusses the design requirements of the TERS system with respect to nanoelectronic samples, and provides a concise description of the physical properties of ferroelectrics.

2.1 Scanning probe microscopy

Both scanning probe microscopy techniques, AFM and STM, rely on a piezoelectric scanner⁵ to move a tip line by line over the surface of a sample with nanometer precision. During scanning, the tip-sample distance is kept constant based on the tunnel current (in STM), or the Van der Waals force or Pauli repulsion (in AFM). Therefore, STM can only be applied to conductive samples while AFM can also be applied to insulating surfaces.

2.1.1 Scanning tunneling microscopy

STM is based on the quantum mechanical tunneling effect that describes the ability of electrons in a quantum well to surmount (*tunnel* through) small energy-potential barriers with a finite probability. The tunneling probability is based on the location probability density $|\psi|^2$ of the electron wave function ψ , and exponentially decreases with increasing width of the energy barrier.

In STM, the tunneling effect leads to a tunnel current through the gap between the STM tip and a conductive sample when a potential difference is applied⁶. The current allows for a distance control with picometer precision. STM utilizes this effect to measure the topography of a conductive sample with atomic resolution [1, 4, 55]. Two scanning modes can be used: In *constant height mode*, the tip scans the sample laterally without vertical movement and the tunnel current is plotted as an image of the surface. For larger areas and rough topographies, it is necessary to control the vertical position of the tip during scanning in order to follow the surface and avoid tip crashes. This is achieved in *constant current mode*: The tunnel current is fixed by the controller to follow the topography of the sample. Resolutions of about 0.01 nm vertically and 0.1 nm laterally are achieved with atomically sharp tips. Because the tunneling effect relies on the distance between the orbitals of the sample atoms and the orbitals of the outermost tip atom, it is even possible to visualize the electron wave function of molecules [55].

⁵ By applying a voltage to a piezoelectric crystal, it can be deformed by pm/V (inverse piezoelectric effect). This allows for precise motion control, which is essential for scanning probe microscopy.

⁶ Typical current values are in the range of nA under a bias between 0.01 and 1 V.

For TERS, the main advantage of STM over AFM is that STM can be operated in combination with any type of sharp and metallic tip while AFM typically requires beam deflection cantilevers (see next section). STM tips can be fabricated relatively easily from solid metallic wires by electrochemical etching (see section 3.2). Furthermore, the STM feedback is controlled electronically (and not optically as in AFM) and is therefore not interfering with the TERS laser.

2.1.2 Atomic force microscopy

In contrast to STM, atomic force microscopy (AFM) can also be used to investigate *non*-conductive samples. An AFM probe consists of a tip with a radius of a few nanometers that is located at the end of a flexible cantilever. The cantilever is small⁷ enough to bend under atomic forces resulting from van der Waals interaction or Pauli repulsion when the tip interacts with the sample. The cantilever reflects a laser beam onto a four-sector photodiode to measure the deflection of the beam and thereby the deformation of the cantilever in contact with the surface at a precision of typically 0.1 nm. The deflection is then used as feedback signal for the controller to image the topography of the sample (see Fig. 2.1.1).

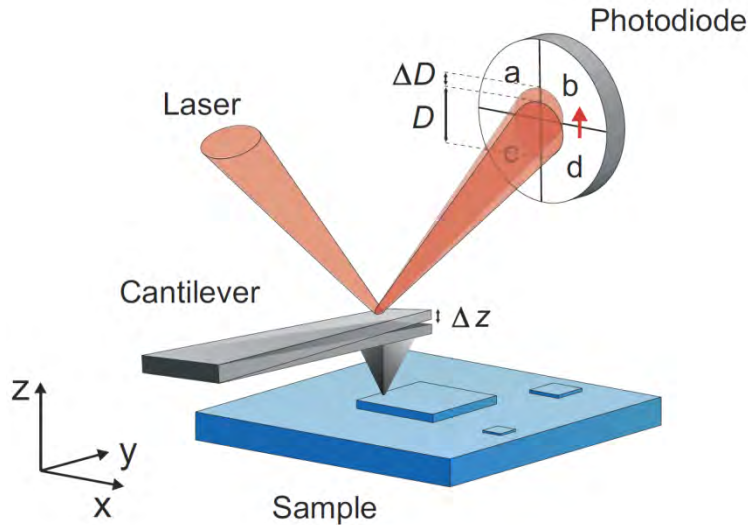


Figure 2.1.1: Sketch of the beam deflection geometry of an AFM. Topographic features of the sample bend the cantilever by Δz which leads to a deflection of the spot on the four-sector photo diode by ΔD . The controller compensates for the movement of the tip by varying the vertical position of the sample relative to the tip to follow the topography. (Figure taken from reference [47].)

Basic feedback modes

AFM is primarily associated with three feedback modes, *contact mode*, *non-contact mode*, and *intermittent mode* (also known as *tapping mode*):

⁷ A standard cantilever has a thickness of 3 μm , a width of 30 μm , and a length varying between 100 μm and 400 μm . Common spring constants are between 0.01 and 80 N/m.

- In *contact mode*, the tip is brought into mechanical contact⁸ with the sample, which causes the cantilever to bend upwards. During scanning, the AFM keeps the deflection of the cantilever constant to follow the topography. The physical connection between tip and sample can be used to apply a voltage in order to measure the conductivity (conductive AFM) or the piezoresponse (PFM) of the sample.
- In *non-contact mode*, the cantilever is vertically oscillated above the sample. A piezoelectric dither excites the cantilever at its mechanical resonance frequency while the amplitude and phase are measured by a lock-in amplifier that is synchronized to the dither piezo [56, 57]. The interaction is based on the attractive van der Waals forces that dominate a few nanometers above the surface. When the tip oscillates in this region, the oscillation amplitude and the mechanic resonance frequency of the cantilever are reduced. The AFM controller can either use the amplitude or, less commonly, the frequency shift as feedback parameter to follow the surface of the sample during scanning. Typical oscillation amplitudes are between 1 and 10 nm with a minimum tip-sample distance of about 1-2 nm at the closest point of the oscillation cycle. Non-contact mode allows for higher resolution than contact mode and tapping mode and circumvents the problem of tip wear.
- *Tapping mode*, also known as *intermittent mode*, uses larger oscillation amplitudes (10-80 nm). The tip “touches” the sample for a short moment during the oscillation cycle leading to a reduction of the oscillation amplitude which is used as feedback parameter by the AFM. Tapping mode is typically more stable than non-contact mode and provides better results on soft samples.

2.1.3 Tuning Fork AFM

Apart from the above listed main operation modes of AFM, near-field optical microscopy is often operated with *tuning fork* AFM [58]. Instead of using a cantilever as optical lever arm for the deflection laser, quartz tuning forks (TF) are used as AFM probes for non-contact mode scanning [22, 26]. The tuning fork is equipped with a sharp tip, similar to an STM tip, and mechanically excited at its resonance frequency of typically 32 kHz by a dither piezo in the AFM head. When the TF oscillates, the piezoelectric effect of the quartz crystal generates an electric potential between the electrodes on the fork that is proportional to the bending of the prongs. The AFM measures the oscillating voltage and thus the oscillation of the fork with a lock-in amplifier and a precision of μV , corresponding to a sub-nanometer oscillation.

The tip can be oscillated either vertically like an AFM cantilever, or parallel to the surface in *shear-force* mode, where the fork is oriented orthogonally to the

⁸ The mechanic interaction between tip and sample is based on to the Pauli repulsion.

sample (see Fig. 2.1.2). The parallel oscillation in shear force mode ensures a constant tip-sample distance throughout the oscillation cycle, which is advantageous for TERS. With decreasing tip-sample distance, the resonance frequency of the fork decreases and can be used as a feedback parameter for the AFM [58]. The measurement of the frequency shift is achieved by a phase-locked loop (PLL) controller which ensures that the fork is always oscillated at its resonance frequency during the scan. Due to the high Q-factor of the tuning fork (~ 7000 under ambient conditions), the resonance shift can be measured with a precision of below 1 Hz and therefore provides a very precise measure of the tip-sample distance with an accuracy of 50 pm. The change of the resonance frequency with respect to the tip-sample distance is shown in a calibration measurement in Figure 5.4.4 on page 89. The high stiffness of the quartz tuning fork allows for oscillation amplitudes of only a few hundred picometers and therefore enables lateral resolutions in the range of nanometers. The preparation of the tuning forks as well as the calibration measurements and topography scans in shear-force mode are described in section 5.4.

Further discussion on the electric and mechanical properties of tuning forks and their application in AFM can be found in the literature [56, 58-62].

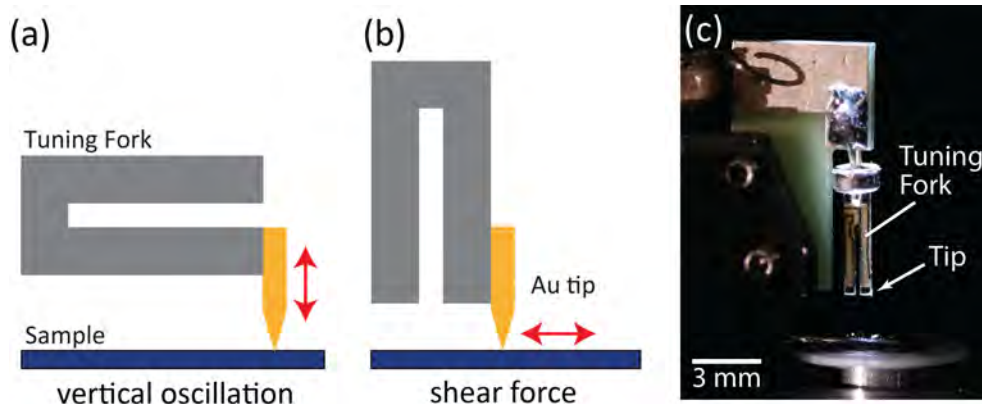


Figure 2.1.2: Sketches of the vertical oscillation mode (a) and shear-force mode (b) of a tuning fork AFM. The red arrow indicates the oscillation direction. (c) Photo of a tuning fork with a gold tip (barely visible) glued to one prong installed in the shear force mode AFM head of our system. The fork is soldered on an epoxy plate that provides the electrical connections to the microscope.

2.1.4 Piezoresponse Force Microscopy

Piezoresponse force microscopy (PFM) is based on contact mode AFM and used to manipulate and visualize ferroelectric domains by the inverse piezoelectric effect.

PFM scans the surface of a sample with an electrically conducting tip. A lock-in amplifier applies an oscillating voltage to the tip at a frequency (f_{PFM}) that is higher than the reaction speed of the feedback circuit of the AFM. The electric field under the tip locally excites the ferroelectric crystal and induces a deformation of the order of picometers, which couples mechanically to the cantilever. The deformation

is measured by two lock-in amplifiers. The first lock-in amplifier analyzes the vertical movement, and the second amplifier analyzes the horizontal movement of the laser spot on the AFM photodiode to measure the oscillation amplitude of the crystal and the phase shift between excitation and piezoelectric reaction (see Fig. 2.1.3). Ideally, the vertical signal is associated with ferroelectric out-of-plane domains while the horizontal signal, caused by a lateral movement of the tip that induces torsion of the cantilever, is associated with in-plane domains⁹. The sample is scanned line by line to generate an amplitude image that reveals the magnitude of the piezoelectric coefficient and a phase image that shows the orientation of the domains. A lateral PFM scan of the ferroelectric titanate thin film that we use as reference sample for confocal Raman spectroscopy is presented in Figure 2.1.4.

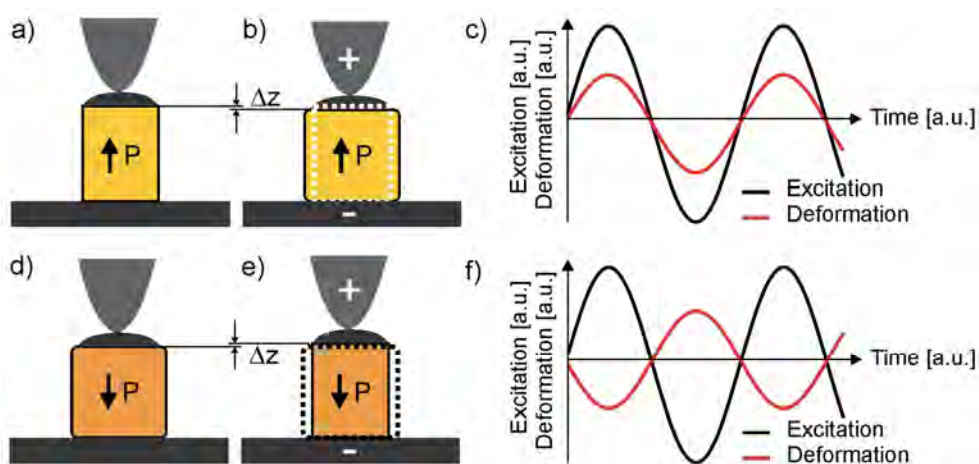


Figure 2.1.3: Principle of the phase shift between two antiparallel sample polarizations in PFM. In the figures a-c, the polarization of the piezoelectric domain (orange) is pointing upwards. The piezoelectric contraction under a positive voltage applied by the tip (grey) to the top electrode on the crystal is given as Δz and the resulting mechanical deformation is in phase with the excitation voltage. Figures d-f show the same situation with a downwards pointing polarization. The mechanical response is phase-shifted by 180 degrees. (Figures taken from reference [63].)

⁹ A detailed description of the interpretation of the vertical and horizontal signals in PFM is provided by Frank Peter in reference [63].

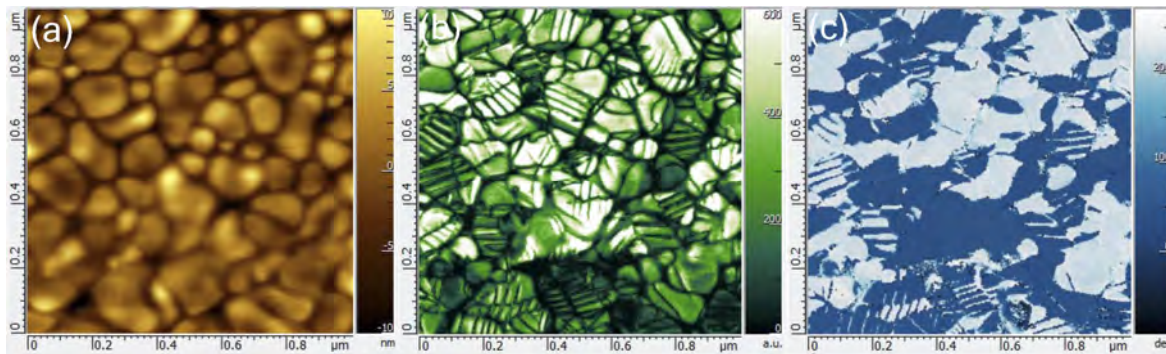


Figure 2.1.4: Topography image (a), lateral amplitude image (b), and phase image (c) generated by a PFM scan of a lead titanate thin film. The film has a thickness of 100 nm and was grown on a platinum substrate by chemical solution deposition. These scans were acquired on our PFM system (*SmartSPM 1000, AIST-NT Inc.*) and published in an application note [64].

Can PFM be used to investigate the superparaelectric limit?

The size-induced transition from the ferroelectric phase to the paraelectric phase typically takes place at grain sizes of a few nanometers. Since ferroelectricity implies the presence of piezoelectricity, the absence of the latter as measured by PFM has been interpreted as the absence of ferroelectricity [65]. Such negative evidence is problematic as the absence of a detectable piezoelectric signal might also be due to a bad electric contact between tip and sample [63].

We published a novel and alternative AFM method for measuring the size of ferroelectric domains in non-contact mode using the electrostatic field of a dipole molecule deliberately placed at the end of the AFM tip. This method circumvents the contact problem because it only senses the electric field above the ferroelectric domains. Our simulations showed that this method can be used to visualize domains with nanometer resolution [66]. However, a suitable technique has to provide information about the actual structural phase of the sample.

2.2 Raman Scattering

The Raman effect describes an inelastic interaction of photons with matter, which either leads to a vibrational and rotational excitation of molecules, or to the excitation of phonons in crystals. The principle is applied in Raman spectroscopy to measure the spectrum of phonon energies to derive chemical and structural information about the sample.

The following sections provide a concise overview of the Raman effect and its implementation as a spectroscopy tool. The complexity and wealth of information about the sample that can be drawn from a Raman spectrum is discussed in several books (see e.g. refs. [67, 68]). A discussion of the effects related to confocal Raman spectroscopy on nanoscale materials is found in reference [14].

2.2.1 Phonon modes

Raman scattering leads to the excitation of vibrational modes in matter. In crystals, such lattice vibrations can be described as *phonons*. Phonons are delocalized quasi-particles with the energy E and the propagation vector \vec{k} . Similar to electrons in the electronic energy-band model, phonons have discrete energies that depend on the structural properties of the material. The phonons are assigned to $3p$ dispersion branches (phonon modes), where p is the number of atoms per unit cell. These modes are either acoustic (A) or optical (O): Acoustic if the atoms oscillate in phase with their nearest neighbor and optical if the oscillation between oppositely charged atoms is 180-degree phase shifted (see Fig. 2.2.1).

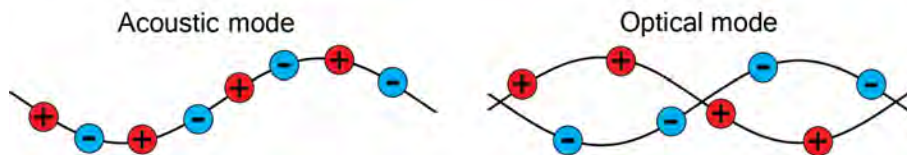


Figure 2.2.1: Sketch of an acoustic and optical transversal phonon. While in the acoustic mode ions with opposite charge oscillate in phase, the optical mode shows an inverse oscillation which leads to an alternating dipole moment that couples optically.

These modes are further subdivided into *polarization* modes that can be either longitudinal (L) or transversal (T). In the longitudinal mode, the atoms oscillate parallel to \vec{k} , and in transversal mode, the oscillation is directed perpendicularly to \vec{k} . For a 3-dimensional primitive unit cell with p atoms, this leads to 3 acoustic branches (LA, TA₁, TA₂) and $3p - 3$ optical branches (LO, TO₁, TO₂). For our confocal Raman reference sample, silicon, we discuss the phonon dispersion and Raman spectrum in section 2.2.4.

2.2.2 Raman effect

A photon can interact with matter by promoting an electron into a higher virtual energy state equal to the energy E_i of the incoming photon. The electron instantaneously undergoes a radiative transition back into a lower energy state. This can either be its original state, as in the case of Rayleigh scattering, or it excites a vibrational or rotational mode of the energy E_k above the original state. The latter case describes the event of Raman scattering and the emitted photon has an energy $E_R = E_i - E_k$. Due to the low cross-section of the Raman effect, only about one Raman photon is scattered along with 10^6 Rayleigh-scattered photons. The optical spectrum of the Raman light represents the energies of the vibrational modes (phonons) of the sample. The effect is shown in the Jablonski diagram in Figure 2.2.2.

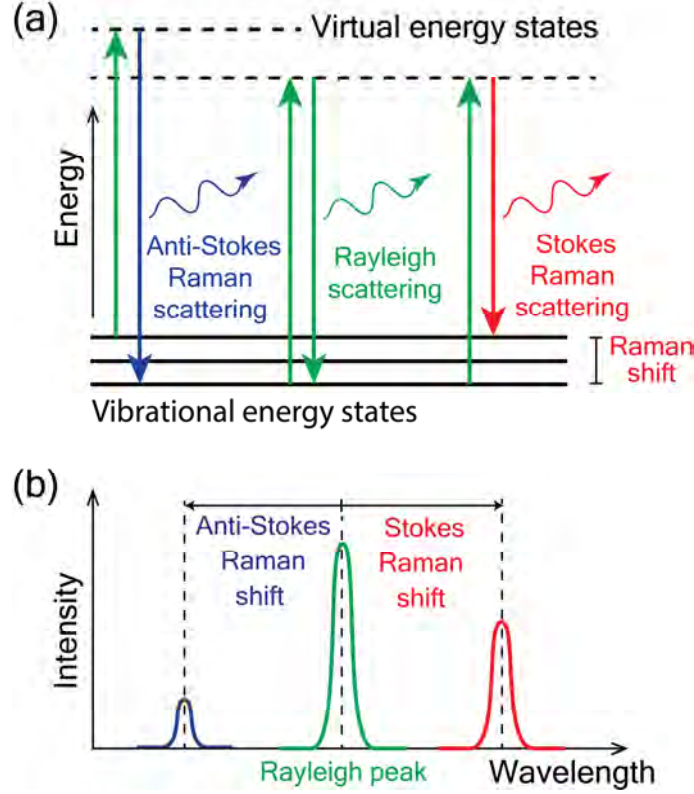


Figure 2.2.2: (a) Jablonski diagram of the radiative Rayleigh and Raman transitions in matter. The Raman shift is given by the energy difference between the initial and final state and can be either negative (Stokes shift) if a phonon was generated, or positive (anti-Stokes shift) if a phonon was absorbed. (b) Energy spectrum including the Stokes and anti-Stokes regime. Note the lower intensity of the anti-Stokes peak compared to the Stokes peak. The ratio is given by the density of excited vibrational modes in the sample and is therefore temperature dependent. It can be used to determine the local temperature.

This description is based on the quantum mechanical model, but the Raman effect can also be explained using the wave model: A change of polarizability α of the dipoles in a vibrationally excited molecule or lattice leads to three different oscillation bands of the dipole. The dipole moment p given by

$$p = \alpha \cdot E_{\text{ext}} \quad (2.2.1)$$

where E_{ext} is the external electric field and α is the polarizability given by

$$\alpha = \alpha_0 + \alpha_1 \cdot \cos(\omega_s \cdot t) \quad (2.2.2)$$

where ω_s is the frequency of the vibration, t is the time, α_0 is the polarizability of the chemical bond, and α_1 is the change of polarizability caused by the vibrational excitation. Under the influence of light, the oscillating electric field with amplitude E_0 and frequency ω_0 is described by

$$E_{\text{ext}}(t) = E_0 \cdot \cos(\omega_0 \cdot t) \quad (2.2.3)$$

and leads to an oscillating dipole moment:

$$p(t) = \underbrace{\alpha_0 E_0 \cos(\omega_0 t)}_{\text{I}} + \underbrace{\frac{\alpha_1 E_0}{2} \cos((\omega_0 - \omega_s)t)}_{\text{II}} + \underbrace{\frac{\alpha_1 E_0}{2} \cos((\omega_0 + \omega_s)t)}_{\text{III}} \quad (2.2.4)$$

The three oscillation bands (I, II and III) have the frequencies ω_0 , $\omega_0 - \omega_s$, and $\omega_0 + \omega_s$. The three resulting optical emissions are known as Rayleigh scattering, Stokes- and anti-Stokes shift of the Raman scattering, respectively.

2.2.3 Raman spectroscopy setup

A Raman spectroscopy setup generally consists of a narrow-band monochromatic light source, a sample holder, and the spectrometer with a photon detector. The light is scattered at the sample and the photons are collected and spectrally resolved to obtain the Raman spectrum. The first Raman setups used monochromatized white light sources which were replaced during the 1960s by lasers due to their narrower spectral linewidth and significantly higher power. Nowadays, most Raman systems are designed as confocal Raman scanning microscopes: A single objective with a high numerical aperture is used to focus the excitation light on the sample and simultaneously collects the backscattered Raman light. This setup has several advantages:

- The focusing of the excitation beam leads to high light intensities on the sample.
- The objective can be very close to the sample and therefore covers a large solid angle to ensure a wide collection angle of the scattered photons.
- The focal volume can be of the order of μm^3 , which enables the analysis of small sample volumes and Raman imaging¹⁰ (“mapping”) at micrometer resolution.

Since a confocal setup uses the same objective for excitation and detection, the excitation beam has to be separated from the detection beam by a beam splitter. Furthermore, the collected light not only contains the Raman signal, but also several orders of magnitude more intense Rayleigh-scattered light that must be filtered out. This can be achieved by a dichroic mirror, which reflects the Rayleigh light but is transparent for the Raman light. In this configuration, the beam-splitting and suppression of the Rayleigh light is achieved by a single component and the lowest detectable wavenumbers are around 50 cm^{-1} in the visible range.

Another option, which allows for tuning of the excitation wavelength, uses a multi-stage spectrometer in connection with a double-prism or a semi-transparent mirror as beam-splitter. In this case, the Rayleigh light is filtered out by the

¹⁰ The sample is scanned line by line and a spectrum is recorded in every point. The data can be visualized by plotting the intensity or shift of a peak to create a 2- or 3-dimensional image of the sample.

spectrometer. Such setups can access very small wavenumbers, down to 5 cm^{-1} , but suffer from a low light throughput that can be as much as 10 times smaller when comparing a triple-stage spectrometer to setups with a dichroic mirror¹¹. Since the Raman signals in TERS are generally low and Raman imaging is very time sensitive, the use of dichroic mirrors is favorable for TERS.

Our setup has two edge filters installed in series, which provides a suppression of the Rayleigh line by a factor of 10^{12} below 70 cm^{-1} wavenumbers at 632.8 nm but still provides a transparency of 90 % for higher wavenumbers. Raman spectrometers require a high spectral resolution because most Raman lines occur between 0 cm^{-1} and 2000 cm^{-1} and are typically very narrow due to the well-defined oscillation energy of the atomic bonds. The required dispersion can be achieved by spectrometers that have a large focal length and diffraction gratings with a high line density (e.g. 50 cm focal length, 1800 lines/mm grating).

A common configuration for a spectrometer that is also used in our setup is the Czerny-Turner design (see Fig. 2.2.3): The incoming beam is focused on an entrance pinhole that blocks all non-parallel components of the detection beam in order to reduce the optical broadening of the Raman peaks and to limit the detection volume to the first diffraction maximum (k-vector filter). Two parabolic mirrors and a diffraction grating project the focal plane of the spectrally resolved light on the photon detector.

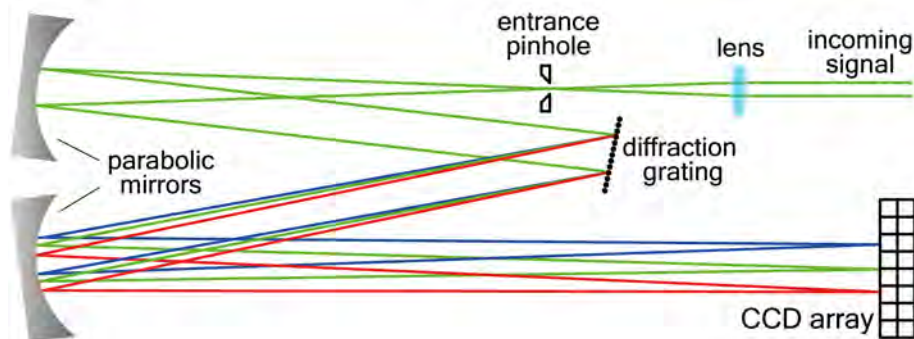


Figure 2.2.3: Sketch of a Raman spectrometer in Czerny-Turner configuration. A diffraction grating is used as a dispersive element. By rotating the grating, the spectral range on the CCD can be moved so that the investigation of fluorescence spectra at higher wavenumbers is also possible.

The detection of the weak Raman signals requires a sensitive photon detector which is either a photomultiplier tube (PMT) or a cooled CCD¹² array. PMTs have a quantum yield¹³ of 10-40 % and have been the standard photon detectors for

¹¹ Based on the specifications of the Raman spectrometer T64000 from Horiba and the book *Raman Scattering in Materials Science* [69].

¹² A charge coupled device (CCD) consists of a 2-dimensional array of individual p-n junctions (pixel). An incoming photon creates an electron hole-pair at the junction which leads to an electron accumulation over time that is measured during the readout period as a function of the detected photons.

¹³ Quantum yield: Ratio between incoming and detected photons. Based on *Hamamatsu* specifications.

several decades. Due to the advances of the semiconductor industry, CCDs caught up and nowadays feature a quantum yield of 95 % in the visible range and 80 % in the infrared region¹⁴. Another advantage of CCDs lies in their small pixel size which allows for simultaneous detection in many channels so that an entire spectrum can be recorded at once. CCDs, however, suffer from high thermal noise and are therefore cooled down to -70 °C or below when detecting Raman light. The cooling is achieved by Peltier elements or liquid nitrogen. As a rule of thumb, the signal-to-noise ratio doubles every 6-7 K. Today, CCD arrays are the standard detector for Raman spectroscopy and PMTs are only used in time-critical applications with sufficient light intensities (e.g. in flow cytometers) due to their faster read-out times.

2.2.4 Raman spectrum of silicon

In this project, crystal silicon is routinely used as a reference sample for the alignment and calibration of the Raman spectrometer because it has a strong and narrow Raman peak at 522 cm⁻¹.

The wavenumbers $\tilde{\nu}$ of the Raman modes can be calculated based on the wavelengths of the excitation and scattered light. We measured the first order Raman mode of silicon at $\lambda_1 = 654.4$ nm under excitation with a red laser at $\lambda_0 = 632.8$ nm (see Fig. 2.2.4):

$$\tilde{\nu} = \left(\frac{1}{\lambda_0} - \frac{1}{\lambda_1} \right) = \left(\frac{1}{632.8 \text{ nm}} - \frac{1}{654.4 \text{ nm}} \right) = 522 \text{ cm}^{-1} \quad (2.2.5)$$

Wavenumbers are measured in reciprocal centimeters and are proportional to energy. Given $\tilde{\nu} = 1/\lambda$ and $c = \nu \cdot \lambda$, where c is the speed of light, ν is the frequency of an electro-magnetic wave and h is the Planck constant, the energy equals

$$E = h \cdot \nu = h \cdot c \cdot \tilde{\nu} \quad (2.2.6)$$

1 eV equals 8065.5 cm⁻¹. This leads to a phonon energy of 65 meV for the 522 cm⁻¹ Raman mode in silicon (and is in accordance with the literature [13, 70-72]). The primitive unit cell of silicon has $p = 2$ atoms, which leads to $3p = 6$ branches with 3 acoustic and 3 optical phonons (LA, TA₁, TA₂, LO, TO₁, TO₂) while typically only the optical phonons appear in the Raman spectrum. Due to the small momentum of a photon¹⁵, only phonons in the center Γ of the Brillouin Zone can be excited. In the case of silicon, the optical phonons are degenerated at Γ , which leads to a single and very strong first-order peak at 522 cm⁻¹. The phonon dispersion along selected axes in the Brillouin Zone is shown in Figure 2.2.5.

¹⁴ Specifications of *Andor iDus 420* and *Andor iDus InGaAs*.

¹⁵ The momentum of a photon is given by $k = 2\pi/\lambda_0$, which is small compared to k-vectors of phonons in the reciprocal space, and which are of the order of $2\pi/a$, where a is the lattice parameter of the crystal.

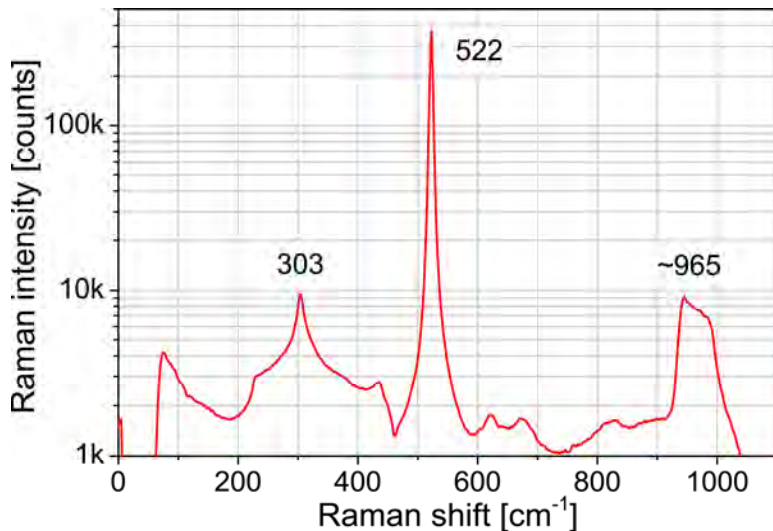


Figure 2.2.4: Semi-logarithmic plot of the measured Raman spectrum of silicon. The strongest mode at 522 cm^{-1} is 50 times more intense than the second order mode at 965 cm^{-1} . The mode at 303 cm^{-1} originates from a peak in the inverse lifetime of the 522 cm^{-1} phonon, based on the decay into two acoustic phonons, and only exists in the presence of light [70].

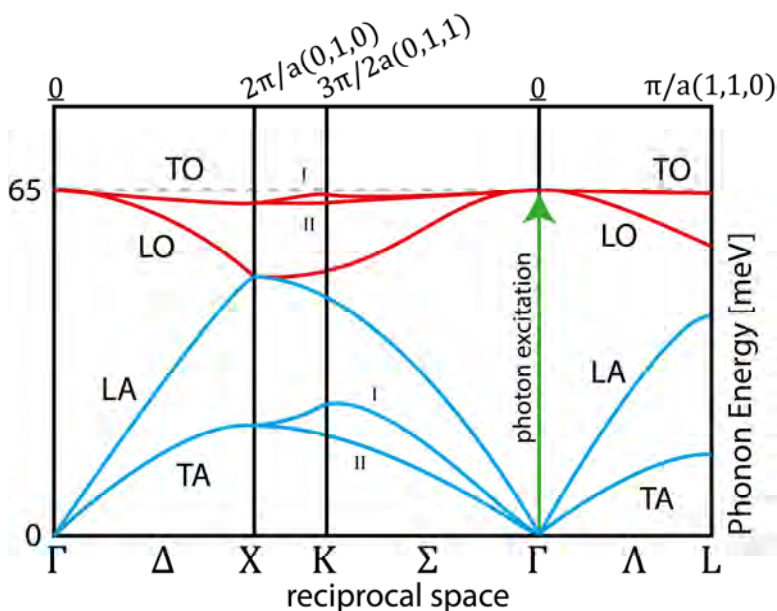


Figure 2.2.5: Phonon dispersion in silicon. The chosen points in the reciprocal space depict axes with high symmetry in the Brillouin zone. The phonon modes at the Γ point are degenerated at 65 meV and 0 meV . (figure based on ref. [71])

2.3 Fluorescence

Fluorescent light emission occurs when an electron relaxes radiatively from an energetically excited quantum state to its ground state. The relaxation process can follow various competing pathways that typically involve non-radiative transitions between vibrational modes in the excited state, and which reduce the energy of the

emitted fluorescence photon. A fluorescence spectrum is generally much broader than a Raman spectrum and typically occurs at higher wavenumbers. Superposition of fluorescent- and Raman-scattered light can, however, impede the detection of the weaker Raman peaks. On biological samples, fluorescence often already occurs in the spectral region of the phonon modes and therefore IR lasers are typically used for Raman spectroscopy in life sciences.

In this project, fluorescence comes into play with the observed shift of the plasmon resonance on the TERS tip.

2.4 Far-field optics

This section discusses the effect of optical diffraction on the size of the focal volume of an objective and thus the optical resolution of a microscope. In TERS, the size of the focal volume has to be kept small in order to reduce the background signal from the far-field with respect to the Raman signal from the tip.

2.4.1 Rayleigh criterion

Light can be described as a transversal electromagnetic (EM) wave of the wavelength λ that consists of an oscillating electric field \vec{E} and a magnetic field \vec{B} propagating in the direction of the wave vector \vec{k} with $|\vec{k}| = 2\pi/\lambda$. Since \vec{E} and \vec{B} are coupled, the properties of a free propagating plane wave can be described by one of its components: $\vec{E} = \vec{E}_0 \cdot \cos(\omega t + kx + \phi)$ with the angular frequency $\omega = 2\pi\nu = c \cdot 2\pi/\lambda$, time t , location x , and the phase ϕ . The superposition of waves from a monochromatic and coherent light source causes constructive and destructive interference depending on the difference between their phases. When light is scattered by an object, every point of this object can be treated as a new light source and the superposition of all emitted waves becomes the interference image of the object in the far-field. If the size of the scatterer is similar or smaller than the wavelength of the light, the phase shift generates a *diffraction* pattern with interference minima and maxima visible in the far-field. Figure 2.4.1(a) shows the circular diffraction pattern of light created by a point source. The disc around the maximum in the center to the first minimum is called *Airy disk*.

The optical resolution of a microscope or objective is limited by the size of the focal volume, which has a finite size due to the *optical diffraction limit*. The resolution is given by the minimum distance at which two point-objects remain optically separated. Ernst Abbe defined this minimum distance as the separation between the principal maximum and the first minimum of the Bessel function that describes the diffraction pattern of a point object [73]. This distance is equivalent to the radius of the Airy disk. This classification became known as the *Rayleigh criterion* [74] (see Fig. 2.4.1(b)).

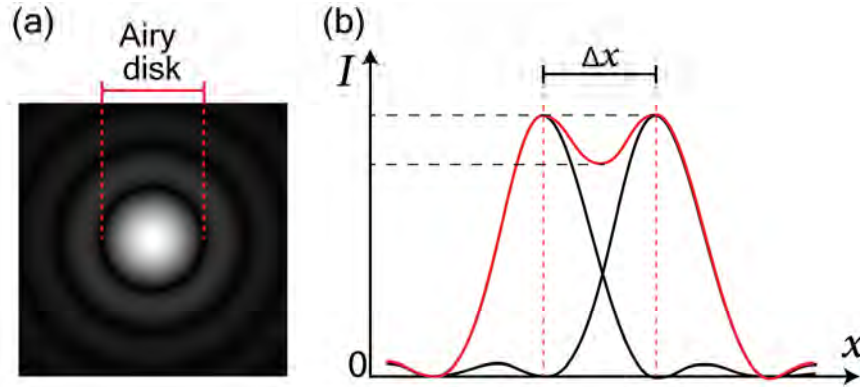


Figure 2.4.1: (a) Simulation of the diffraction pattern of a point source of light. (b) Sketch of the Rayleigh criterion. The red curve shows the superposition of the diffraction pattern of two adjacent point objects. Δx is the radius of the Airy disk and describes the distance between both point objects when the interference maximum of one object falls on the first minimum of the other object.

2.4.2 Numerical aperture and optical resolution of a lens

The size of the Airy disk and consequently the maximum possible resolution of a conventional optical microscope, are governed by the wavelength λ and the numerical aperture (NA) of the objective. The NA describes the ability of a lens to focus light and is defined by

$$\text{NA} = n \cdot \sin \theta \quad (2.4.1)$$

where n is the refractive index of the surrounding medium and θ is the half opening-angle of the objective (Fig. 2.4.2).

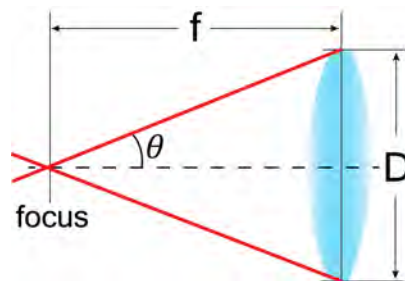


Figure 2.4.2: Sketch of the geometry of a lens with the focal length f , the lens diameter D , and the half opening-angle θ .

The diameter d_{AD} of the Airy disk is directly related to the NA of the objective and the wavelength of the light as follows:

$$d_{\text{AD}} = 1.22 \frac{\lambda}{\text{NA}} \quad (2.4.2)$$

The factor 1.22 derives from the first zero of the Bessel function (divided by π) that describes the diffraction pattern of a point source. Based on the Rayleigh criterion and the size of the Airy disc, the optical resolution Δx of an objective is:

$$\boxed{\Delta x = 0.61 \frac{\lambda}{\text{NA}}} \quad (2.4.3)$$

In general, the working distance (WD) of an objective scales in inverse proportion to its NA and hence the sample is placed very close to the objective in high resolution microscopes which leaves little to no space for the scanning probe in the case of TERS. The most powerful optical microscopes reach NAs of about 1.5 with oil immersion objectives and achieve resolutions of approximately 200 nm in the visible range.

The TERS system used in this project is based on a 0.42 NA-objective, which leads to an optical resolution of 1 μm at a wavelength of 632.8 nm. The working distance of 15 mm provides enough space for the TERS tip between objective and sample.

There are several ways to increase the NA of a microscope in order to decrease the size of the focus:

- A **short focal length f** and **large lens diameter D** increase the opening angle θ and thereby the NA. This requires large objectives with small WDs. Common optical microscopes that view the sample in top-access have NAs of ~ 0.7 and WDs of several millimeters. Higher NAs are technically possible but then the WD becomes impractical for most applications.
- **Inverted microscopes** solve this problem by positioning the objective under the sample in *bottom access*. The transparent sample is therefore placed on a thin glass slide with a thickness of 130 μm to 170 μm . At this distance, a numerical aperture of close to 1 becomes possible. Inverted setups also allow for a higher refractive index n by using water or oil as optical medium between the objective and the cover-slide. Such *immersion objectives* reach NAs of 1.3 for water and 1.5 for oil.
- A **parabolic mirror** that surrounds the sample on one side, and thus covers a solid angle of half a sphere, has been used in TERS to reach an NA of 1 in connection with a large WD [75]. This setup, however, requires a small sample in order to avoid shadowing the center of the beam.

2.4.3 Focal volume

The focal volume of an objective lens is defined by the spot diameter $d_{\text{AD}} = 1.22 \cdot \lambda / \text{NA}$ (see equation 2.4.2) and the focal depth Δz . The focal depth is half of the width of the optical intensity profile along the optical axis and based on the wavelength and the NA of the objective [14]:

$$\Delta z = \frac{\lambda}{n \sin^2 \theta} \quad (2.4.4)$$

This equation can be simplified in air ($n = 1$):

$$\Delta z = \frac{\lambda}{\text{NA}^2} \quad (2.4.5)$$

With d_{AD} and Δz , the focal volume can be described geometrically as a rotational ellipsoid (Fig. 2.4.3). In confocal Raman spectroscopy, the focal volume defines the scattering sample volume from where the Raman light is collected. This has a direct implication in TERS because the confocal volume thereby generates an unwanted background signal additional to the TERS signal from the tip. It is therefore beneficial to use a high NA objective to decrease the focal volume, and to choose a sample that only fills a fraction of the focal volume, such as 2-dimensional (thin films), 1-dimensional (nano-rods or nano-tubes), or even 0-dimensional (molecules, quantum dots) objects in connection with a Raman inactive substrate.

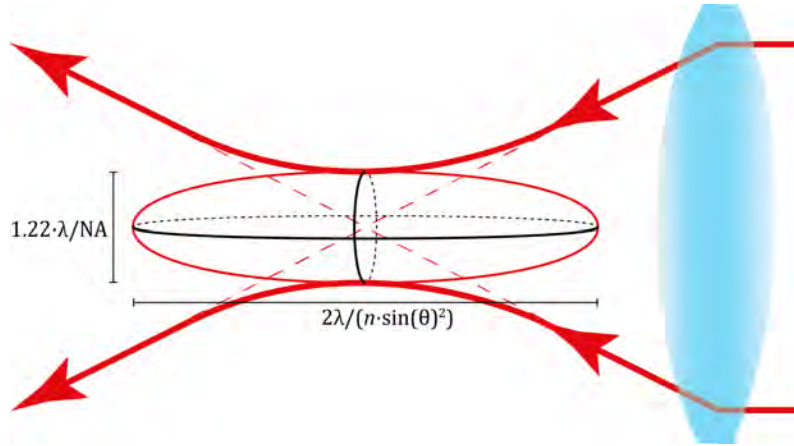


Figure 2.4.3: Sketch of the light-intensity profile in the focus of an objective: The bold red lines indicate the focal cone of the objective and the ellipsoid represents the focal volume. The 3-dimensional focus forms a rotational ellipsoid. (The sizes of focus and lens are not true to scale.)

2.4.4 Optical penetration depth

For opaque samples, in which the bandgap is smaller than the energy of the excitation light, the fundamental absorption dominates and the penetration depth of light becomes considerably smaller than Δz . The ratio between the incoming intensity I_0 and the intensity I_f at a given depth l can be described based on the Lambert-Beer law and the optical absorption κ [76]:

$$\frac{I_f}{I_0} = \exp\left(-\frac{4\pi\kappa}{\lambda}l\right) \quad (2.4.6)$$

where λ is the wavelength and the absorption κ is wavelength-dependent and defined as the imaginary part of the refractive index $\tilde{n} = n + i\kappa$. n and κ are linked to the permittivity $\varepsilon = \varepsilon' + i\varepsilon''$ of the material by

$$\varepsilon' = n^2 - \kappa^2 \quad (2.4.7)$$

$$\varepsilon'' = 2n\kappa \quad (2.4.8)$$

The penetration depth δ is defined as the depth l when $I_f/I_0 = 1/e$ and can be derived from equation 2.4.6 leading to:

$$\delta = \frac{\lambda}{4\pi\kappa} \quad (2.4.9)$$

In light-absorbing matter, δ is typically of the order of nanometers.

2.5 The optical near-field

The far-field approximation is not valid if the optical field needs to be described close to its source at distances d that are equal or smaller than the wavelength. The *angular spectrum representation* formulates the field distribution as a superposition of the plane waves with the evanescent waves as solutions of the Maxwell equations. Evanescent waves decay exponentially and are therefore dominant at small distances.

A detailed mathematical description of the near-field and the transition region to the far-field can be found in the literature [77-79] and goes beyond the scope of this section. However, this chapter discusses the phenomenological implications of the optical near-field with respect to the field enhancement effect in TERS.

2.5.1 Transition between near-field and far-field

While the propagation vector \vec{k} of the far-field is perpendicular to the wavefront and points away from the source, the propagation vector of the evanescent wave is complex and does not define a propagation direction in real space [77]. This has direct implications for the energy which is not propagating through free space and can only be transmitted by capacitive or inductive coupling. Within the so-called *reactive* region ($d \lesssim \lambda/2\pi$), an external disturbance of the field can affect the source in return.

The extension of the near-field and the transition region depends on the size L and the shape of the emitter (antenna) with respect to the optical wavelength λ . The near-field enhancement effect in TERS is based on antennas that are about 10-times smaller than λ ($10L \lesssim \lambda$). For small antennas, the regions of the EM field can be classified [80] into:

- | | | |
|-----|--------------------------|----------------------------|
| (a) | $d < \lambda$ | Near-field |
| (b) | $\lambda < d < 2\lambda$ | Transition or Fresnel zone |
| (c) | $d > 2\lambda$ | Far-field |

The near-field can be further divided into a *reactive* region where $d < \lambda/2\pi$ and a *radiative* region at larger distances (see Fig. 2.5.1). The reactive region is the area in the proximity of the antenna, where the antenna gains energy from the electromagnetic field¹⁶. Due to the complex interaction of emission and absorption between antenna and field, this region is very difficult to describe mathematically and one reason why not all experimental observations in SERS and TERS have been fully understood yet [18, 77].

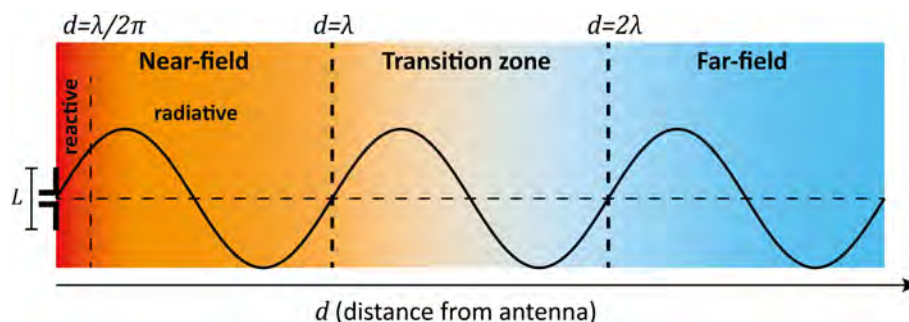


Figure 2.5.1: Spatial separation of the different field regions in distance d to a small antenna of the size $L < \lambda/10$. The reactive region depicts the volume from which the antenna can draw energy from the electric field. In the case of external excitation with a red laser, this region has a size of about 100 nm.

2.5.2 Surface plasmons

A plasmon is a quasiparticle that represents a quantized oscillation of the charge-carrier density. Surface plasmons can exist at the interface between a metal (negative permittivity) and a dielectric (positive permittivity). If the interface is exposed to light, the electric component of the EM field excites the free electron gas in the metal and the electrons follow the external field. Depending on the frequency, the light is either reflected or transmitted. If the excitation frequency is lower than the frequency of the plasmon, the light is reflected. If the frequency is higher, the electrons can no longer screen the electric field, which can result in a propagating longitudinal wave of oscillating electrons along the surface, a so called *surface plasmon polariton* (see Fig. 2.5.2).

¹⁶ In TERS, the radius of the tip-apex, which creates the near-field, has a size of about 30 nm. Under an excitation in the visible spectrum, the reactive region has a size of 50-100 nm.

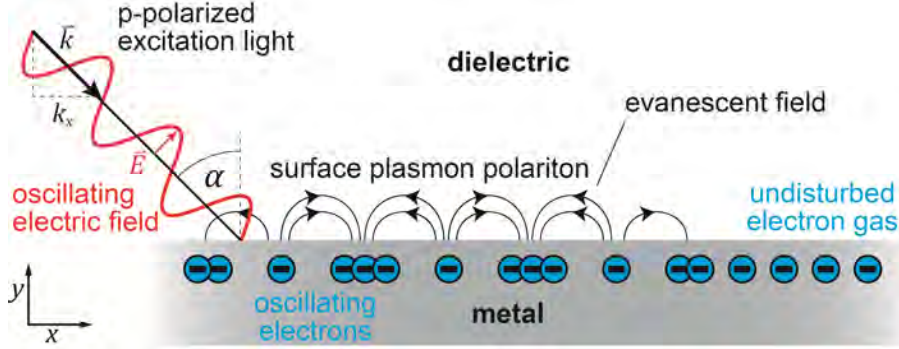


Figure 2.5.2: Excitation of a surface plasmon by p-polarized light at the interface between a metal and a dielectric. The oscillating electrons in the metal create a non-radiative evanescent field within the reactive region of the near-field, leading to an excitation of the adjacent electrons and thereby a propagating plasmon.

The plasmon frequency of metals typically lies in the UV range, which is why most metals reflect the entire visible spectrum and appear silvery. Some noble metals like gold and silver have a lower plasmon frequency in the visible range and are therefore of high interest for optical applications [81]. Although the plasmon frequencies of alkali metals are also located in the visible spectrum, they turn out to be unsuitable for most applications due to their chemical reactivity and softness [82, 83]. Plasmon frequencies in the infrared range can be achieved by heavily doped semiconductors [84].

The excitation of a surface plasmon needs to fulfill energy and momentum conservation. The momentum k_{sp} of the surface plasmon is directed along the interface:

$$k_{\text{sp}} = \frac{\omega}{c} \cdot \sqrt{\frac{\epsilon_{\text{met}}}{\epsilon_{\text{met}} + 1}} \quad (2.5.1)$$

where ϵ_{met} is the permittivity of the metal at the frequency ω [85, 86]. This momentum needs to be matched by the x -component of the momentum k_{EM} of the incoming electromagnetic wave:

$$k_x = k_{\text{EM}} \cdot \sin \alpha = \omega/c \cdot n \cdot \sin \alpha \quad (2.5.2)$$

When $k_{\text{sp}} = k_x$, this leads to

$$n \cdot \sin \alpha = \sqrt{\frac{\epsilon_{\text{met}}}{\epsilon_{\text{met}} + 1}} \quad (2.5.3)$$

Equation 2.5.3 has two implications: First, the negative permittivity of metals requires the left side of the equation to be greater than one. This is only fulfilled when the refractive index n of the dielectric medium is larger than 1 and thus the direct excitation of plasmons at a planar air-metal interface is not possible and an optic medium like glass with $n \approx 1.4$ is required [87, 88]; second, k-vector matching is only achieved under the right excitation angle α , which complicates the coupling.

Once the plasmon is coupled into a waveguide, it can be directed, divided and also coupled out again as an EM wave. Under ideal conditions, surface plasmons can travel distances of several hundred micrometers and optical waveguides are therefore a candidate for interconnects in optical computers.

2.5.3 Field enhancement

Surface plasmons generate an evanescent field that reaches several nanometers into the dielectric medium. As long as the permittivity of the dielectric is the same along the interface, the evanescent field is only of theoretical importance. If, however, an external perturbation leads to a change of permittivity, the plasmon can be scattered or its excitation by light inhibited or altered¹⁷. The surface plasmon polariton can then decouple from the interface and emit an EM wave that propagates with the same wavelength as the excitation light. The optical fields can be amplified by bringing the surface plasmon into resonance: If the size of the propagation medium is a multiple of half of the wavelength of the plasmon, a standing wave is formed and referred to as localized surface plasmon resonance (SPR). The evanescent field at the antinodes of the SPR can become several orders of magnitude stronger than the EM field of the optical excitation. The metal/dielectric interface acts as a nano-antenna that creates a strong field in its direct vicinity and retrieves its energy from the reactive region. This effect takes place at the nanoscale and is used in nano-optics to focus light at dimensions that are classically prohibited by the diffraction limit and therefore not accessible with conventional optics. This localized field-enhancement effect is the basis of surface- and tip-enhanced Raman spectroscopy.

Even though the direct excitation of surface plasmons by photons at a planar metal-air interface is physically not allowed in accordance with equation 2.5.3 due to k-vector matching, surface plasmons can be excited on metallic nanostructures, such as colloidal particles, because the propagation vector k of the localized plasmon is close to zero and thus matches the momentum of the photon. In SERS, the nanostructure is provided by a roughened metal substrate, while in TERS, the SPR is excited at the apex of a metallic tip that is considered to be spherical to simplify the following model.

¹⁷ This effect is used in *surface plasmon resonance spectroscopy* (SPRS) to detect the accumulation of molecules at the surface of a metal and belongs to the most sensitive commercially available methods for molecule detection.

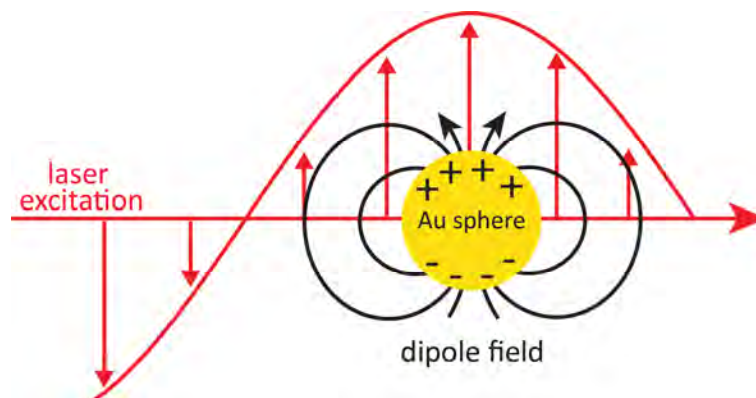


Figure 2.5.3: Sketch of the excitation of a surface plasmon resonance on a gold nanoparticle. The red arrows depict the electric field of the excitation laser and the black lines describe the electric dipole field of the displaced electrons in the gold sphere.

The excitation of plasmons on non-planar structures can be described in a model based on the polarizability α of a nanometric, metallic sphere. As shown in Figure 2.5.3, an external electric field \vec{E} displaces the free electrons in the sphere and induces a dipole moment \vec{p} :

$$\vec{p} = \vec{E} \cdot \alpha(\lambda) \quad (2.5.4)$$

The polarizability depends on several parameters: the size of the sphere, type of metal, external permittivity, and the excitation wavelength. For a given sphere, the polarizability α can be derived from the Clausius-Mossotti relation, which leads to:

$$\alpha = 4\pi\epsilon_0 r^3 \underbrace{\frac{\epsilon_{\text{met}}(\lambda, r) - \epsilon_{\text{env}}}{\epsilon_{\text{met}}(\lambda, r) + 2\epsilon_{\text{env}}}}_{:=g} \quad (2.5.5)$$

where r is the radius of the sphere, ϵ_{env} is the permittivity of the environment (e.g. 1 for air), and ϵ_{met} is the permittivity of the metallic sphere at the excitation frequency. This fraction represents the enhancement of the electric field and is often referred to as the g -factor. It is maximized when the denominator is zero:

$$\epsilon_{\text{met}} = -2 \cdot \epsilon_{\text{env}} \quad (2.5.6)$$

This leads to an increase of the polarizability and enhancement of the electric near-field E_{NF} at the surface of the metal particle by the factor g :

$$E_{NF} \propto g \cdot E_0 \quad (2.5.7)$$

In SERS and TERS, the sample is brought into the near-field which results in an enhancement of the Raman scattering by the factor g :

$$E_{\text{Raman}} \propto \sigma \cdot E_{\text{NF}} \propto g \cdot E_0 \quad (2.5.8)$$

where σ is the Raman cross section of the sample. Because the backscattered Raman light has almost the same wavelength as the excitation laser, the Raman light fulfills the resonance condition of the surface plasmon on the tip as well, leading to a second signal enhancement. The enhancement in the detection path is described by the factor g' which leads to an overall enhancement by the factor gg' :

$$E_{\text{TERS}} \propto g' \cdot E_{\text{Raman}} \propto \sigma \cdot g' \cdot g \cdot E_0 \quad (2.5.9)$$

And the TERS intensity can be described by:

$$I_{\text{TERS}} \propto |E_{\text{TERS}}|^2 \propto \sigma^2 \cdot |g'g|^2 \cdot I_0 \quad (2.5.10)$$

Based on the assumption that the frequency shift of the Raman signal is small compared to the width of the plasmon resonance, the two enhancement factors g and g' are commonly considered to be equal, which leads to the so-called Raman 4th power rule¹⁸:

$$I_{\text{TERS}} \propto g^4 \quad (2.5.11)$$

In the visible range, g -factors up to 1000 are theoretically predicted and values between 10 to 100 have been verified experimentally [89]. Due to the 4th power rule, this leads to an enhancement of the Raman signal at the tip of up to seven orders of magnitude [43]. Such high enhancement factors are only reached directly at the surface of the nanoparticle and the electric field falls off rapidly following the distance dependence

$$E \propto (r + d)^{-10} \quad (2.5.12)$$

where r is the radius of the tip and d is the distance to the sample [42, 43]. The rapid loss in field intensity over a few nanometers enables the high lateral resolutions of nanometers that are achieved in TERS when the probe tip that is generating the surface plasmon is scanned across the sample.

2.5.4 Enhancement factor

The definition of tip enhancement varies throughout the literature [89]. First of all, one needs to distinguish between E-field enhancement (g -factor) and phenomenological Raman enhancement. The Raman enhancement can be determined by a tip-in/tip-out experiment in which the TERS signal I_{near} (i.e. signal measured with tip) is compared to the confocal Raman signal I_{far} (i.e. signal measured without tip).

¹⁸ Our TERS measurements show later, however, that the width of the plasmon resonance affects the measured spectrum and hence the factors g and g' can deviate from each other.

This factor, however, also scales with the volume ratio between the confocal volume of the objective and the size of the near-field of the tip. To compensate for this volume effect, a correction factor λ^2/L^2 was introduced where λ is the wavelength and L the diameter of the near-field [90]. The size of the near-field at the tip can be approximated by $L = \sqrt{2 \cdot r \cdot d}$ where r is the tip radius and d the distance to the sample [90]. This leads to a “area-corrected” enhancement factor $\text{EF}_{2\text{D}}$:

$$\text{EF}_{2\text{D}} = \frac{I_{\text{near}}}{I_{\text{far}}} \frac{\lambda^2}{L^2} \quad (2.5.13)$$

This term was specifically developed for a 2-dimensional scenario in which a thin film or opaque sample covers the entire area of the focus of the objective. For the excitation of 1-dimensional objects, such as single carbon nanotubes whose diameter can be approximated to be zero, we suggest to define the enhancement factor EF as follows:

$$\text{EF}_{1\text{D}} = \frac{I_{\text{near}}}{I_{\text{far}}} \cdot \frac{d_{\text{AD}}}{L} \quad (2.5.14)$$

where d_{AD} is the diameter of the confocal volume (eq. 2.4.2). This leads to

$$\text{EF}_{1\text{D}} = \frac{I_{\text{near}}}{I_{\text{far}}} \cdot \underbrace{1.22 \cdot \frac{\lambda}{\text{NA}} / \sqrt{2 \cdot r \cdot d}}_{\text{correction factor}} \quad (2.5.15)$$

The nominator of the correction factor cancels out with the measurement geometry of the far-field. By simply determining $I_{\text{near}}/I_{\text{far}}$ on carbon nanotubes, the tip-enhancement factor EF can thus be measured as a tip parameter that is independent from the sample geometry, wavelength, and objective of the TERS system. Furthermore, EF is now directly linked to the g -factor by the fourth power rule leading to $\text{EF} \approx g^4$.

2.5.5 Plasmon resonance frequency

The resonance frequency of the plasmon at the tip is met by the excitation light when the polarizability α of the tip is maximized according to the equations 2.5.5 and 2.5.6. The resonance frequency depends on the type of material (commonly gold or silver), the size and shape of the structure because it affects its optical permittivity, and the permittivity of the surrounding materials within the reactive region. Furthermore, other metallic objects such as the substrate or an agglomeration of dimers can increase the enhancement as will be discussed in section 2.6.2. The plasmon resonance of silver takes place at slightly higher frequencies than gold, and a red-shift is found at increasing particle sizes. A compilation of the resonance frequencies of different spherical nanoparticles is shown in Figure 2.5.4.

Since the plasmon resonance frequency changes with differing particle size, ellipsoidal particles that have a short and a long axis exhibit a splitting of the resonance frequency. Depending on the excitation mode given by the polarization

axis of the incoming light, the particles can be excited along either their long axis or their short axis. By keeping the short axis constant, increasing the long axis leads to a red-shift as it can be found in nanoparticles with different aspect ratios (see Fig. 2.5.5). The plasmon excitation at the end of a tapered wire that is used as a TERS tip can be approximated by an ellipsoidal particle. The observed resonance frequencies for silver are therefore in the green spectral region and for gold in the red spectral region when the polarization of the excitation laser is oriented parallel to the tip axis.

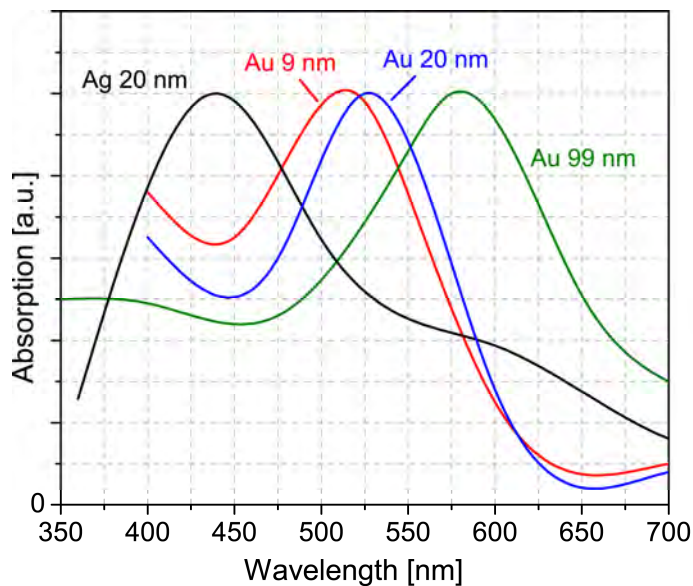


Figure 2.5.4: Absorption spectra of spherical silver and gold nanoparticles with different sizes in aqueous solution (normalized to the maximum absorption). Silver has a lower plasmon frequency than gold. The comparison of the gold particles shows that a larger diameter leads to a red-shift of the resonance. The values are taken from reference [91] for Ag, reference [92] for Au 9 nm and Au 99 nm, and reference [93] for Au 20 nm.

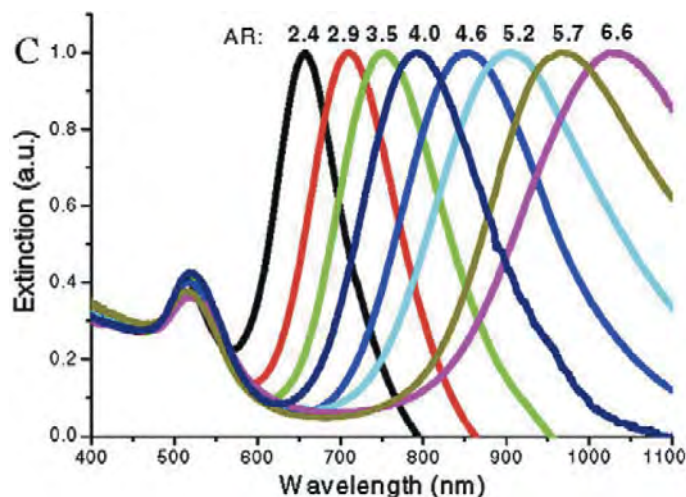


Figure 2.5.5: Ellipsoidal gold nanoparticles with different aspect ratios (AR) between 2.4 and 6.6. The short axis is constant at 20 nm while the long axis varies. Higher aspect ratios lead to a red-shift of the longitudinal mode. Note that all particles have an absorption maximum at around 520 nm originating from the short axis (transversal mode). (Figure taken from reference [94].)

2.6 Surface-enhanced Raman spectroscopy

Surface-enhanced Raman spectroscopy (SERS) can detect low concentrations of molecules by utilizing the near-field enhancement of localized surface plasmons on a rough metallic substrate, typically silver, to increase the Raman signal of the sample molecules. Since TERS is based on the same field-enhancement effect it can be seen as a further development of SERS. The following provides an overview of the related physical effects and their relevance to TERS tips. A description of SERS can be found e.g. in the works of Moskovits et al. [95] and Kneipp et al. [96].

The sample, typically a highly diluted solution or aerosol of molecules, is adsorbed on the surface of a SERS substrate that features a high density of hot-spots that generate SPRs under laser excitation. If a Raman-active molecule is adsorbed in such a hot-spot, the intensity of the emitted Raman signal of the molecule can be 10^{10} times higher than of a free molecule in the optical focus [97, 98]. This leads to a very high chemical sensitivity at low molecule concentrations [99, 100]. It is difficult to give a precise estimation of the detection limit because it is essentially limited by the probability and the time that it takes for a single molecule to appear in a hot-spot. However, detection limits of 0.1 pg/ml can be found in the literature [101].

2.6.1 SERS substrates

A SERS substrate consists of a nano-structured surface with a high density of SPRs in order to increase the probability that a sample molecule is adsorbed at a position with a strong electro-magnetic field enhancement. SPRs can occur at spherical, triangular, or sharp nanostructures and edges, as well as between nano-gaps on the surface [102]. The basic production methods aim at increasing the statistical chance of obtaining hot-spots by creating a rough surface. Commonly,

silver or gold is deposited by evaporation or sputter-deposition on a glass surface. The roughness can be further increased by an oxidation-reduction cycle [103, 104]. The high density of differently shaped surface irregularities in the focus of the laser will lead to a high probability of exciting a surface plasmon. More control can be gained by structuring the surface by electron-beam lithography: Triangular, spherical or rectangular islands can then be deliberately shaped to generate SPRs [105, 106]. Furthermore, lithography can also be used to pattern a layer of seeds that initiate island growth in a subsequent epitaxial deposition step [107]. If the access to lithography techniques is not available or too expensive, a *bottom up* approach with colloidal nanoparticles can be used. Nanoparticles are nowadays available with different shapes, sizes, and claddings to precisely match the plasmon resonance frequency. They can be deposited randomly or as self-assembling monolayers on a glass substrate [94, 108-110]. The particle size and shape, the type of metal, and the deposition density is chosen according to the laser wavelength.

2.6.2 Gap-enhancement

The strong electromagnetic fields near the interface of a metallic nanostructure that carries a localized surface plasmon can be further amplified in the gap between two metallic structures [105, 111-113]. The plasmons on both sides can interact with each other if the gap is smaller than the reactive region of the near-field and both particles are in resonance (same frequency and phase). This enhancement effect is known to create very strong signals in surface-enhanced Raman spectroscopy when a sample molecule gets into the gap [95]. The effect can be simulated for dimers of spherical metallic nanoparticles and shows a strong increase of the field in the gap between the particles (see Fig. 2.6.1) [112]. Investigations of plasmon coupling were extended to elongated particles and wires for application of optical antennas [111].

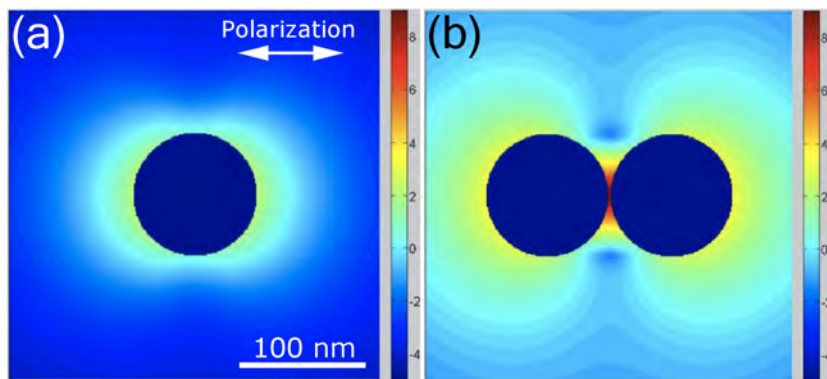


Figure 2.6.1: (a) Calculated E-field intensity (logarithmic scale) in the vicinity of 100 nm gold spheres under optical excitation (633 nm). The field intensity is amplified along the horizontally oriented polarization axis and is highest close to the surface of the sphere. (b) When bringing two spheres together, the field intensity rises by another 6 orders of magnitude in the 2 nm gap between the particles due to the gap-enhancement effect. (Figure taken from ref. [112].).

A similar effect is observed in TERS when the tip is brought into nanometric distance of a metallic surface. The evanescent field of the surface plasmon at the tip can create an image charge in the metallic substrate and the field becomes strongly confined in the gap between tip and substrate [49, 114, 115]. Therefore, thin samples such as single molecules [116], CNTs [117], or DNA strands [118] can be placed on a flat gold substrate to achieve stronger TERS signals. We were able to show the influence of the gap-TERS effect in our TERS experiment on carbon nanotubes discussed in section 4.3.

2.6.3 Chemical enhancement

Deeper analysis of SERS Raman spectra showed that the enhancement of the Raman signal is attributable to at least two independent effects. Despite the great success of the electromagnetic model (surface plasmons), the comparison of different SERS experiments showed a *sample dependence* of the enhancement factor which can be explained by a charge-transfer effect between the Raman-active molecules and the metallic substrate. This effect is referred to as chemical enhancement [119].

While surface plasmons still account for the majority of the electro-magnetic enhancement, by about 10^4 - 10^7 , the chemical enhancement can add an additional factor of 10-100 [36, 120]. In a few words, chemical enhancement occurs when the Raman-active molecules are in contact with a metal surface. The bands close to the Fermi level become occupied by the metal electrons of the conduction band and allow for *resonant Raman* excitation of the molecule [36]. Resonant Raman scattering describes the optical excitation across the bandgap and has much higher cross sections than non-resonant Raman scattering. It has to be noted that not all Raman modes of the molecules are resonantly excited and therefore a resonant Raman spectrum can differ from the spectrum of the bulk material [121]. An early quantitative analysis of the chemical enhancement can be found in reference [122] as well as further discussions in references [123-125].

Chemical enhancement is mainly present in SERS but can also contribute to the Raman signal in TERS if the tip is in close contact with the sample, e.g. in contact mode or tapping mode AFM.

2.7 Tip-enhanced Raman spectroscopy

Tip-enhanced Raman spectroscopy (TERS) combines the nanometer resolution of a scanning probe microscope (SPM) with the chemical sensitivity of a Raman spectrometer. The interaction of both systems takes place at the apex of a metallic SPM tip at which the Raman laser excites a surface plasmon resonance. The SPR creates an optical near-field that enhances the electromagnetic field of the laser by several orders of magnitude [43]. The field-enhancement is strongly confined to a region of a few nanometers around the apex of the TERS tip following an d^{-10} distance dependence (see equation 2.5.12). While the SPM scans the tip over the sample, a Raman spectrum is recorded at every position to generate a 2-dimensional map of the surface. The field enhancement and the optical confinement allow for the

detection of Raman signals from very small sample volumes and even single molecules with a lateral resolution of nanometers.

2.7.1 Optical excitation and detection

TERS systems are operated with a confocal setup in which the optical excitation and Raman detection are achieved through the same objective. In order to generate SPRs in the visible spectral region that create a vertical field at the apex of the TERS tip, the longitudinal mode of the tip is excited by the Raman laser. Therefore, the electric component of the EM-wave, and thus the polarization axis of the laser, must be parallel to the tip axis. This can be achieved by linearly polarized light in side-access [117, 126, 127] or with a large numerical aperture in bottom or top-access to obtain a large field component parallel to the tip. Under excitation in bottom or top-access, the parallel component of the E-field cancels out in the center of the focus because the tip is excited in radial symmetry through the objective. This problem can be avoided by blocking half of the excitation beam [128] or by using radially polarized light [129-132] (also known as *doughnut mode*).

The direction of the optical access of the Raman system must be chosen according to the properties of the sample and the substrate. For *transparent samples*, (typically single molecules or thin films on a glass substrate) the substrate can be placed on an inverted optical microscope with the confocal objective located below the sample (bottom access). This leaves the upper side of the sample free for the SPM head and allows for the use of high-NA objectives from beneath. Nanoelectronic devices and most functional materials, on the other hand, are fabricated on *non-transparent substrates* like silicon wafers or metallic electrodes and therefore require optical access from top or side with an objective that leaves enough space for the scanning probe. Objectives with working distances of several millimeters typically have an NA between 0.4 and 0.7 and hence collect less light than high NA objectives used in inverted setups.

Importance of the numerical aperture in TERS

The numerical aperture plays an important role in the *excitation* as well as in the *detection* path in TERS. For the excitation, it is beneficial if the confocal volume is kept as small as possible in order to reduce the background far-field signal from the sample.

In the detection path, the numerical aperture defines the solid angle Ω , under which the objective collects the backscattered Raman light. Ω scales quadratically with the half-opening angle θ of the objective:

$$\Omega = 4\pi \cdot \sin^2(\theta/2) \quad (2.7.1)$$

By inserting the function of the numerical aperture from equation 2.4.1, the solid angle can be given as a function of the NA:

$$\Omega = 4\pi \cdot \sin^2(\arcsin(\text{NA})/2) \quad (2.7.2)$$

The solid angle of a half sphere is given by 2π and the ratio of the detectable Raman signal that is backscattered into the direction of the objective is given by:

$$\frac{I_{\text{detected}}}{I_{\text{backscattered}}} = 2 \cdot \sin^2(\arcsin(\text{NA})/2) \quad (2.7.3)$$

While an objective with an NA of 1 theoretically collects 100 % of the backscattered Raman signal, an NA of 0.9 collects only 56 %, and an NA of 0.42 only collects 9 % (see graph in Figure 2.7.1). The use of a high NA objective can therefore drastically decrease the integration time.

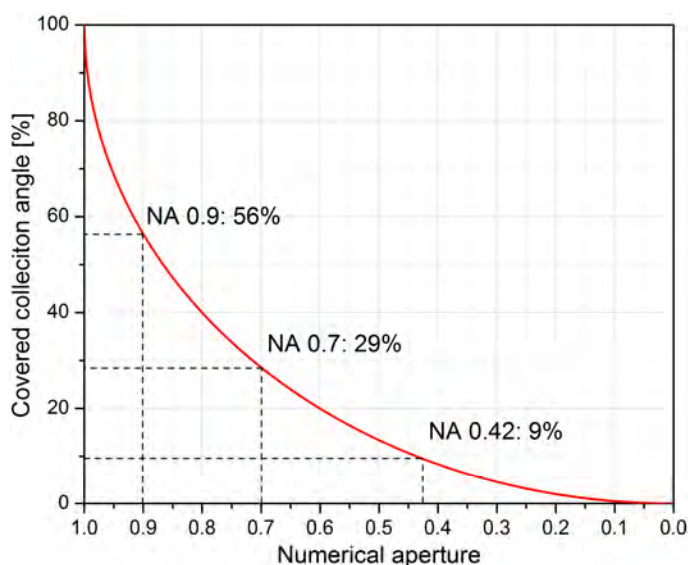


Figure 2.7.1: Fraction of detected intensity compared to backscattered intensity as a function of the numerical aperture of the collecting objective in air.

2.7.2 Scanning probe methods

TERS is operated either with a scanning tunneling microscope (STM) or an atomic force microscope (AFM), depending on the electric conductivity of the sample. *Conductive samples*, including small molecules or nano-particles on a metallic substrate, are investigated with STM-TERS. The substrate is electrically grounded and scanned with an electrochemically etched metallic tip in constant current mode providing a stable tip-sample distance. *Non-conductive samples*, on the other hand, require the use of atomic force microscopy. The different AFM scanning modes have different advantages and disadvantages for TERS:

- **Contact mode:** Pro: The direct contact between tip and sample leads to a high tip enhancement due to the r^{-10} distance dependence. Chemical enhancement can occur additionally. Con: Tip wear can change the shape of

the tip apex during scanning and thus the ability of the tip to generate a surface plasmon resonance.

- **Non-contact mode:** Pro: Almost no tip wear occurs due to weak tip-sample interaction forces. This enables the usage of very sharp tips. Con: Very small oscillation amplitudes are required to keep the tip close to the sample which requires a very sensitive AFM control loop.
- **Tapping mode:** Pro: The tip “touches” the sample during every cycle for a short time and leads to a high TERS signal during this moment, possibly including chemical enhancement. Cons: Low TERS signal during the rest of the oscillation cycle (depending on the oscillation amplitude). Tip wear can occur.

All three modes require AFM cantilevers that are coated with an additional metallization layer in order to be used for TERS. Metallization is typically achieved by thermal evaporation of gold or silver. Since the electrochemical etching of STM tips is more cost-efficient than the coating of AFM cantilevers, quartz tuning fork mode AFM was identified as a way to extend the area of application of etched tips to non-conductive samples. The etched tip is glued by hand to a tuning fork and used as an AFM probe:

- **Tuning Fork AFM:** Pro: Constant tip sample-distance due to horizontal oscillation (shear force mode) or due to very small oscillation amplitude below 1 nm (vertical oscillation mode). Electrochemically etched tips can be used. An electronic feedback circuit obviates the need for an AFM laser so that no interfere with the TERS laser can occur. Con: The relatively big probe only allows for optical access by objectives of NA 0.5 or lower when used in top or side access for non-transparent samples.

2.7.3 Setup of our TERS system

We planned our TERS system based on the requirements of *non-transparent* and *non-conductive* samples and substrates in order to meet the demands of nanoelectronics and to provide analysis capabilities for the widest possible range of samples. The TERS microscope is based on an upright sample scanner with a range of 100 μm x 100 μm x 15 μm (*SmartSPM, AIST-NT Inc.*) and allows for optical top and side-access (see Fig. 2.7.2). In order to control the tip production entirely in our laboratory, we use STM and tuning fork AFM with tapered gold tips that we etch electrochemically on-site prior to the TERS experiments.

The STM is operated in constant current mode and the tuning fork is operated with a PLL controller in shear-force mode. The size of the tuning fork head and the sample scanner requires a working distance of 20 mm, which is met by a 0.42 NA objective¹⁹ (*M Plan APO NUV BF, Mitutoyo Inc.*) under an inclination of 65° to the

¹⁹ A higher NA would require a different design of the sample holder and would then limit the maximum sample size to a few millimeters.

tip axis. The excitation wavelength of 632.8 nm was chosen to match the plasmon resonance frequency of the gold tips and is provided by a linear-polarized, helium-neon laser (*25-LHP-928-249, CVI Melles Griot*) with a line width of 12 MHz ($16 \cdot 10^{-6}$ nm). This leads to a focal ellipse on the sample of $1.8 \mu\text{m} \times 6 \mu\text{m}$ due to the inclination of the objective. A piezoelectric objective scanner can move the focus position in three directions by $30 \mu\text{m} \times 30 \mu\text{m} \times 12 \mu\text{m}$ with nanometer precision. The objective scanner facilitates the optical alignment between tip and laser because the laser position can be adjusted to optimize the TERS signal while tip and sample are in contact (our publication about this concept can be found in ref. [117]). Last but not least, the microscope can be positioned independently from the optical setup in three directions with micrometer precision which adds up to 9 degrees of freedom in total.

The excitation beam is controlled by an optical preparation unit (*Nanofinder 30* from *Tokyo Instruments Inc.*). A neutral density filter regulates the laser power over three orders of magnitude from 10 mW to 10 μW and a beam expander is used to adjust the laser diameter according to the entrance pupil of the objective. The polarization can be turned by a rotatable half wave plate between vertical and horizontal polarization before the light is reflected towards the objective by a dichroic mirror that acts as beam splitter. In the detection path, the backscattered light is divided according to its wavelength by the dichroic mirror. While the Rayleigh light is reflected onto a PMT, the Raman and fluorescence signal passes through a second dichroic mirror (to ensure a sufficient rejection of the Rayleigh light) and is focused by a motorized objective onto the entrance pinhole of the spectrometer²⁰.

The Raman spectrometer is built in a Czerny-Turner configuration (see section 2.2.3) with a focal length of 520 mm. The light is spectrally dispersed by one of the following grating options that are placed on a rotatable turret: 150, 600, and 1800 lines/mm. The light is detected by a CCD array (*iDus 420 BU* from *Andor Technology*) that is cooled to $-80 \text{ }^\circ\text{C}$ by Peltier elements to reduce the thermal noise. The CCD has a resolution of 255×1024 pixels, which leads to a spectral resolution of $\sim 2 \text{ cm}^{-1}/\text{pixel}$ over a spectral range of 1800 cm^{-1} in the configuration that is used for TERS (600 lines/mm-grating at 632.8 nm wavelength). In vertical direction, the spectrum covers about 12 lines out of 255 and the residual area of the CCD is discarded by software to limit the influence of cosmic events: When cosmic particles hit the CCD sensor, they induce an electron-hole separation which leads to sharp peaks in the Raman spectrum. We determined the number of cosmic events to be $\sim 10^{-6}$ per second and pixel which leads to about 1 event/min in the recorded Raman spectrum.

Since only the red-shifted Raman and fluorescence signal pass through the dichroic mirror, the backscattered Rayleigh light is reflected and passes a semitransparent mirror and is detected by a PMT. A motorized objective and an

²⁰ In TERS, the entrance pinhole of the spectrometer has to be kept at the size of the first Airy disk in order to limit the Raman signal of the confocal background. This requires a precise alignment of the objective as part of the initiation routine.

entrance pinhole in front of the PMT provide the k-vector filtering. In connection with the objective scanner, the PMT is used to generate an image of the backscattered Rayleigh light from the TERS tip to control the alignment procedure between the tip and the objective (see section 4.2). The beam path of the entire setup is shown in Figure 2.7.3.

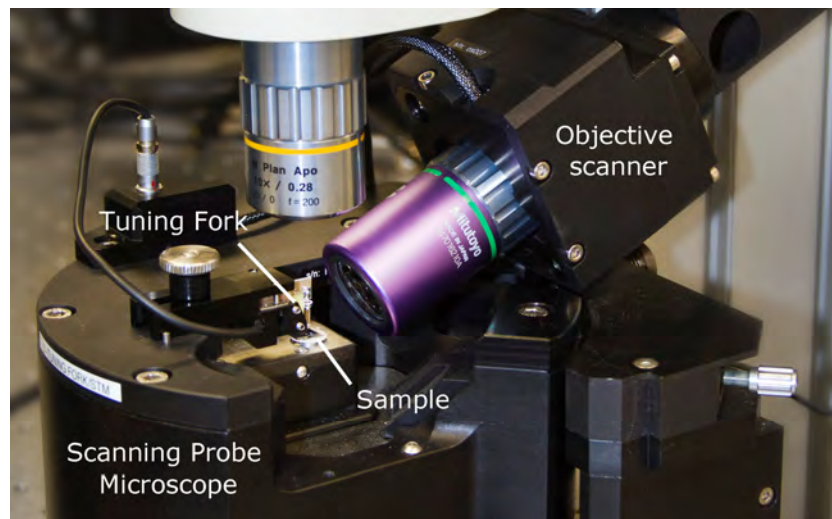


Figure 2.7.2: Photo of the scanning probe microscope with installed tuning fork and sample. The confocal side objective (purple) and the camera objective (silver) are clearly visible.

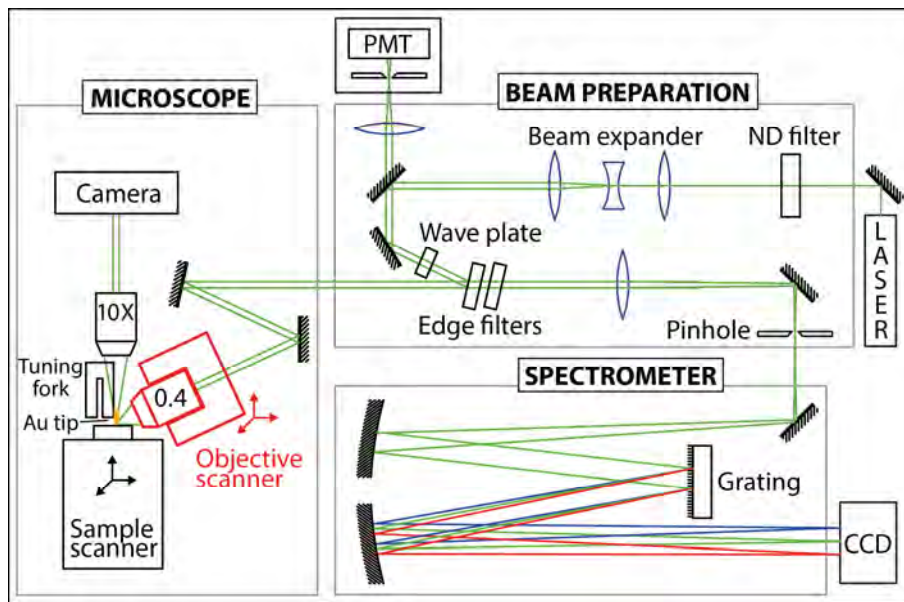


Figure 2.7.3: Sketch of the optical setup of our system. The laser light is guided through the beam preparation to adjust the laser power, beam diameter and polarization orientation. The edge filter reflects the excitation light into the confocal objective. The backscattered light is either reflected (Rayleigh light) into a PMT or passes the edge filter (Stokes light) and is focused on the entrance slit of the spectrometer.

2.8 Ferroelectrics

Ferroelectrics are often referred to as advanced or functional materials due to their electronic and structural properties. They exhibit a dipole moment that can be switched by an external electric field. This property made ferroelectrics a candidate for memory devices. This section classifies ferroelectrics in the group of crystalline materials and describes the dielectric properties of ferroelectrics and the perovskite crystal structure on the example of lead titanate due to its relevance for the TERS measurements in chapter 5.

2.8.1 Electromechanical properties

All crystals can be classified into one of 32 crystal classes (point groups) and their electric displacement D_i is given by:

$$D_i = \varepsilon_0 \varepsilon_{ij} E_j \quad (2.8.1)$$

where ε_0 is the vacuum permittivity, E_j is the electric field in direction j and ε_{ij} is the permittivity tensor, a material parameter.

Among these 32 crystal classes, 21 are non-centrosymmetric, and 20 of these show an electric displacement when exposed to mechanical stress. This so-called piezoelectric effect is given by the second term of eq. 2.8.2:

$$D_i = \varepsilon_0 \varepsilon_{ij} E_j + d_{ijk} T_{jk} \quad (2.8.2)$$

where d_{ijk} denotes the piezoelectric tensor and T_{jk} denotes the mechanical stress. Note that there is also an *inverse piezoelectric effect* that leads to a mechanical strain η_{ij} under an external electric field E :

$$\eta_{ij} = d_{ijk}^T E_k \quad (2.8.3)$$

where d_{ijk}^T is the transpose of d_{ijk} . The inverse piezoelectric effect is used, for example, by piezoelectric scanners in SPMs because it allows for movements by picometers per volt. Since d_{ijk} and T_{jk} are symmetric in jk , the Voigt notation is conventionally used:

Tensor notation	11	22	33	23,32	31,13	12,21
Voigt notation	1	2	3	4	5	6

Given this notation, equation 2.8.2 becomes

$$D_i = \varepsilon_0 \varepsilon_{ij} E_j + d_{ik} T_k \quad (2.8.4)$$

Among the piezoelectric point groups, ten have a unique polar axis causing the *pyroelectric effect*. The effect generates a spontaneous, temperature-dependent polarization expressed by a third term:

$$D_i = \varepsilon_0 \varepsilon_{ij} E_j + d_{ik} T_k + \gamma_i \Delta T \quad (2.8.5)$$

where γ_i is the pyroelectric coefficient and ΔT is the change of temperature. In some of the pyroelectric crystals, the polarization axis has two stable states and can be switched by an electric field. These crystals are referred to as *ferroelectrics*. The inherent spontaneous polarization P_i^S affects the electrical displacement:

$$D_i = \varepsilon_0 \varepsilon_{ij} E_j + d_{ik} T_k + \gamma_i \Delta T + P_i^S \quad (2.8.6)$$

The spontaneous polarization is the dominating contribution to the electric displacement in most ferroelectrics. While piezoelectricity and pyroelectricity are based on structural properties, ferroelectricity is an electric property of polarization reversibility. An overview of the crystal classifications is given in Figure 2.8.1.

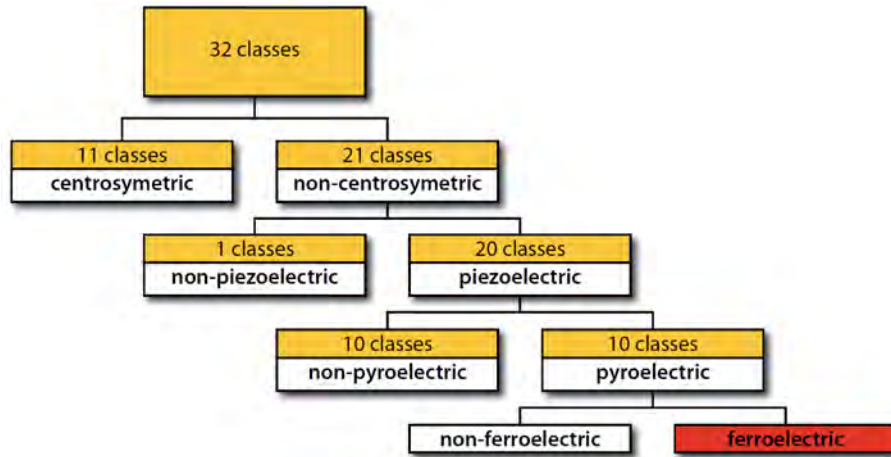


Figure 2.8.1: Electromechanical classification of the different crystal classes. (Figure from ref. [47].)

The polarization of a ferroelectric crystal as a function of the external electric field follows a hysteresis loop as shown in Figure 2.8.2. Starting from an unpolarized state, a positive external electric field aligns the dipoles, giving rise to an overall polarization P (dashed line). When the electric field is decreased to zero, the polarization remains at the spontaneous polarization P_S^+ . By applying a negative electric field, the polarization switches when the field drops below the coercive field E_c^- and remains at P_S^- when no field is applied. To switch the polarization back to positive values, the electric field has to be increased again above E_c^+ . This describes a complete cycle of the hysteresis loop. The switching between both states of spontaneous polarization (P_S^+ and P_S^-) can, for example, be used in FeRAMs [133], FerroFETs [134, 135], and resistively switching tunnel junctions [136].

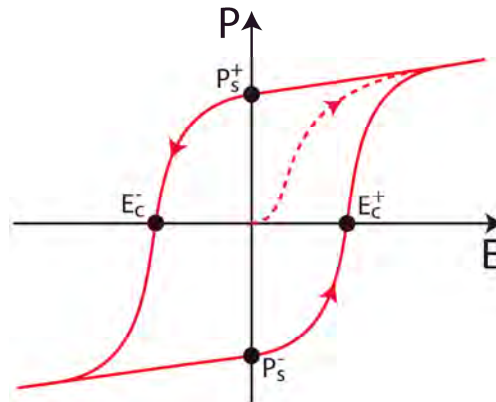


Figure 2.8.2: Sketch of a ferroelectric hysteresis: The polarization P is plotted over the electric field E to obtain a hysteresis loop of a ferroelectric crystal. E_c is the coercive field and P_s is the spontaneous polarization.

2.8.2 Crystal structure of lead titanate

Lead titanate (PbTiO_3) is part of a large group of ferroelectrics that appear in the *perovskite structure* that is defined by an $\text{A}^{2+}\text{B}^{4+}\text{X}_3^{2-}$ unit cell where X is typically oxygen (Fig. 2.8.3). In lead titanate, **Pb** occupies the corners of the cubic cell and **Ti** is located in the center of the oxygen octahedron.

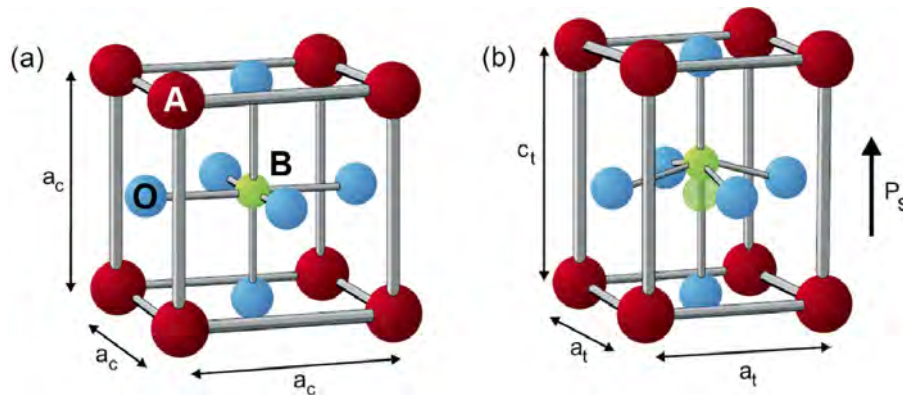


Figure 2.8.3: (a) Perovskite structure of an ABO_3 unit cell in the cubic state. (b) Tetragonal state in which the central ion is shifted relative to the oxygen atoms, giving rise to a spontaneous polarization. (Figure taken from ref. [47].)

Lead titanate exhibits a phase-transition temperature of $T_0 \approx 490 \text{ }^\circ\text{C}$ [137]. Above T_0 , lead titanate is in its *paraelectric* phase, which implies a cubic lattice structure without spontaneous polarization. Below T_0 , lead titanate energetically prefers to displace the positively charged central ion (**Ti**) by several picometers in respect to the negatively charged oxygen octahedron. This leads to a tetragonal distortion of the unit cell with a polarization P_s and is referred to as *ferroelectric phase* (see Fig. 2.8.3 b). At surfaces and interfaces, lead titanate can also exhibit a polarization by a rotation of the oxygen octahedron, referred to as *antiferrodistortive ordering* [138].

The phase transition can be modeled by the Ginzberg-Landau theory in which the free energy F of the system is described as a function of the temperature, the polarization P of the crystal, and an external electric field [139]. F is plotted in an energy landscape diagram as a function of the polarization P in Figure 2.8.4. The graph describes a double well potential for the ferroelectric phase, with the two possible polarization states $+P_s$ and $-P_s$.

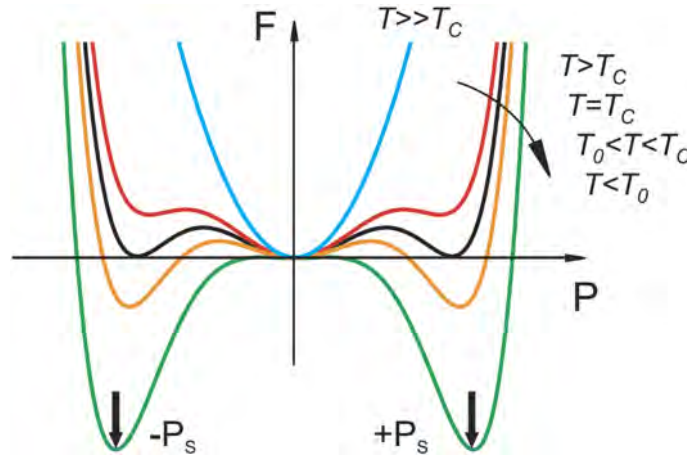


Figure 2.8.4: Free energy F as a function of the polarization P for a ferroelectric with a first-order phase transition plotted at various temperatures T . Far above the Curie temperature $T \gg T_C$, only one energetic minimum is found at $P = 0$ (paraelectric phase). At the Curie temperature $T = T_C$, the energy for the paraelectric and ferroelectric states are equal. At lower temperatures $T < T_C$, the ferroelectric phase is energetically more favorable, and below the phase-transition temperature T_0 the paraelectric phase is unstable. The abrupt (non-continuous) switching of the polarization between $P = 0$ and $P = \pm P_s$ defines a first-order phase transition. (Figure taken from ref. [140].)

For very small crystals, the phase-transition temperature becomes size dependent and decreases with smaller particle diameters. Ishikawa et al. measured the transition temperature as a function of the particle size for lead titanate and showed a steep decrease of the transition temperature below a size of 30 nm [141]. The minimum size, at which the ferroelectric phase becomes unstable, is referred to as the *superparaelectric limit*. Chapter 5 starts with a discussion about measuring the superparaelectric limit by Raman spectroscopy.

3 Fabrication of the TERS tips

The crucial component of a TERS system is the scanning probe. The probe measures the topography of the sample and generates the enhancement of the electromagnetic field in the focus of the Raman laser. As described in section 2.5, the properties of the metallic apex of the tip determine whether or not a surface plasmon resonance (SPR) can be excited at the end of the tip. The surface plasmon excitation depends on the permittivity of the metal (typically gold or silver), the shape, the surface roughness, and the position of grain boundaries. An ideal TERS tip should have the following properties:

- Curvature of less than 50 nm at the tip apex to allow for the optical excitation of localized surface plasmons [142]
- Surface roughness below 1 nm (RMS) to avoid plasmon scattering and adsorption of carbon [142, 143]
- No crystal defects or grain boundaries at the apex to avoid scattering and damping of the localized surface plasmons [144]
- Chemical inertness to avoid oxidation and loss of enhancement [145]
- Mechanical resistance to avoid tip wear during scanning
- Raman inactivity to avoid interference with the Raman signal from the sample

There are primarily two methods for producing TERS tips and the chosen production method depends on the scanning probe method that is to be used for TERS: 1) TERS tips for STM and tuning fork AFM are typically electrochemically etched from a solid metal wire to achieve a sharp tip that allows for the excitation of localized surface plasmons. The difficulty of this method is the reproducibility of uniform tips with a constant radius. 2) TERS in tapping mode and non-contact mode AFM relies on silicon AFM cantilevers that are coated with a thin metallic film. The goal of this production method is to achieve a rough metallic layer at the apex of the AFM tip which, similar to a SERS substrate, provides hot-spots for SPRs. The disadvantage of coated AFM tips is that the position of the hot-spot defies control and consequently the production yield of functioning tips is limited. Furthermore, the coating process and the inevitably high consumption of AFM cantilevers are cost-intensive.

In order to establish a reliable and cost-efficient production process of TERS tips, we build an electrochemical etching setup for gold tips (described in section 3.2).

3.1 Tip material

TERS tips are typically made of gold, silver, or aluminum: Gold tips can be optically excited in the red spectral region, silver tips in the green spectral region, and aluminum tips in the near-UV spectral region [146]. These metals can fulfill the

plasmon resonance condition $\epsilon_{\text{tip}} = -2\epsilon_{\text{env}}$ (eq. 2.5.6) for spherical nano-particles under excitation in the visible spectrum. The real and imaginary parts of the permittivity of selected metals are shown in Figure 3.1.1.

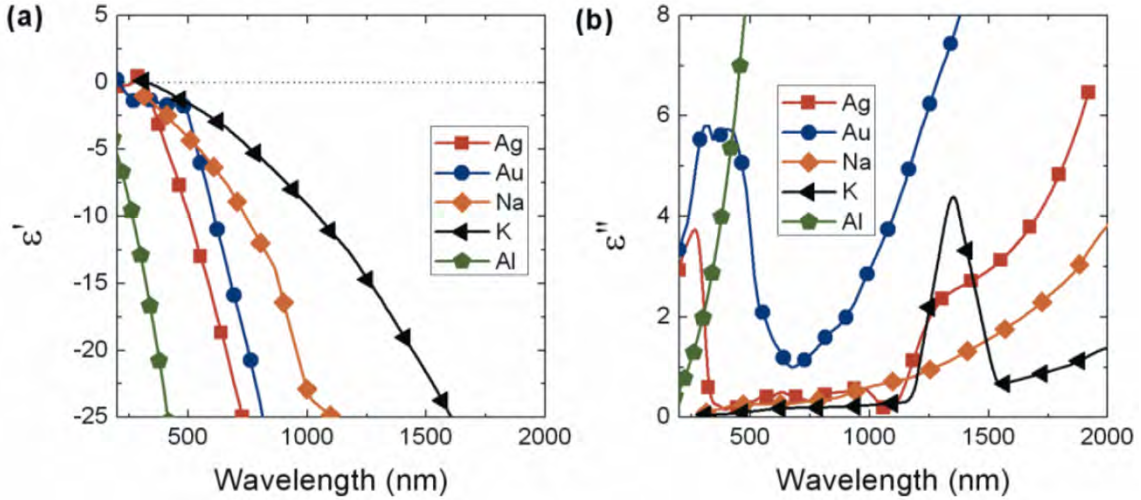


Figure 3.1.1: Permittivity at optical frequencies of various metals. (a) Real component ϵ' and (b) imaginary component ϵ'' . (Figures taken from ref. [82].)

Silver exhibits lower electronic damping (ϵ'') than gold and thus generates a stronger field enhancement. However, the surface of silver quickly oxidizes and sulphurizes under ambient conditions leading to a loss of the tip enhancement within a few hours [147, 148]. Figure 3.1.2 shows the decrease of the Raman signal from a silver SERS substrate as it oxidized. Silver tips are therefore mainly used under vacuum conditions where oxidation can be limited, or in experiments that require very high enhancement factors (e.g. to achieve molecular sensitivity [149]).

Gold tips, on the other hand, are chemically inert and therefore maintain their enhancement effect under ambient conditions over time. Therefore, gold tips are advantageous when being used for long scans and can be stored over periods of several months. The disadvantages of gold are its higher optical damping compared to silver and its ductility which makes gold tips prone to tip wear. Nevertheless, continuous scanning periods of 62 hours were already reported for gold TERS tips in tuning fork shear-force mode AFM [150].

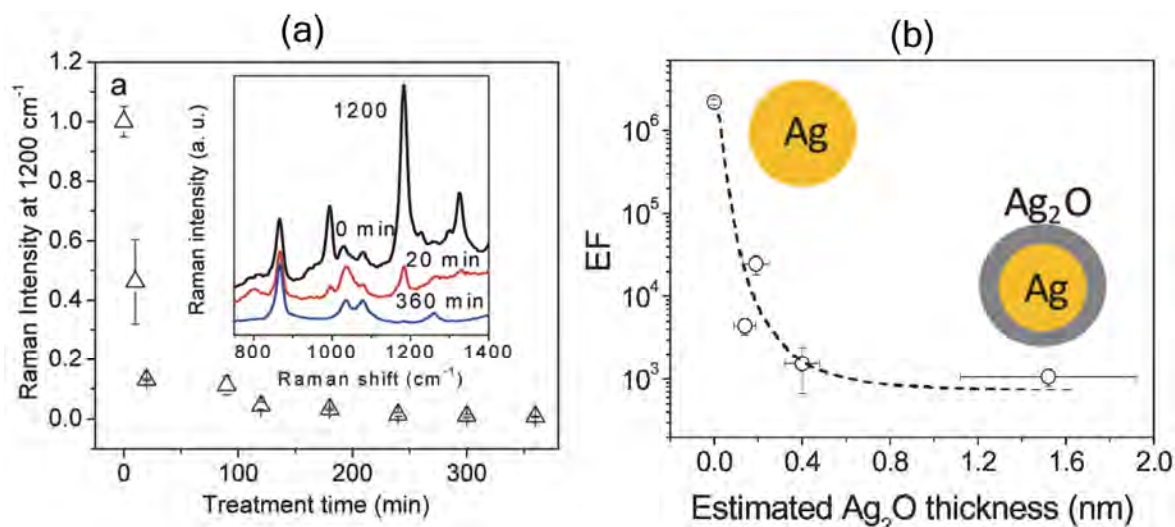


Figure 3.1.2: Study by Han et al. [145] that shows the decrease of the SERS signal from an oxidizing silver substrate: (a) Oxidation of a SERS substrate under ozone atmosphere over time. The Raman intensity of trans-1,2-bis(4-pyridyl)ethylene molecules on a SERS substrate is reduced due to oxidation of the substrate. (b) Estimated silver-oxide thickness in relation to the observed enhancement factor (EF) of the SERS substrate. The first Ag₂O monolayer reduces the enhancement by more than one order of magnitude. (Figures taken from ref. [145].)

3.2 Electrochemical etching of TERS tips

Conical TERS-tips can be produced by electrochemical etching of solid metallic wires. The end of the wire is immersed in an electrolyte solution in the center of an electrode ring and a voltage is applied. The surface tension of the electrolyte leads to a meniscus at the interface between the electrolyte and the wire. While the etching progresses at the surface of the electrolyte and the diameter of the wire decreases, the meniscus becomes smaller resulting in a wire with a hyperbolic shape and a sharp tip. This method can lead to tip radii of approximately 30 nm²¹. Electrochemical etching is widely used for the production of sharp tungsten tips for STM, with KOH [151] or NaOH [152, 153] as electrolyte and an etching voltage of 2-3 V DC. Since tungsten cannot be used for TERS tips, several methods were developed for the etching of noble metals. Silver can be etched with ammonia [154-156], perchloric acid and ethanol [154], or hydrochloric acid and methanol [157] as electrolytes. Gold is typically etched with hydrochloric acid that is often diluted with ethanol [143, 144, 158-160]. Most methods require an electric cut-off circuit [143, 161] that quickly interrupts the voltage and stops the etching process at the desired tip radius to prevent *overetching*. For gold, however, rectangular voltage pulses can be used as an alternative to DC etching and lead to tip radii in the range of nanometers even without a cutoff circuit [144, 158]. Our first etching experiments confirm that DC etching leads, in most cases, to blunt gold tips with a tip radius of about 1 μm if no

²¹ If the etching is stopped too early, the wire is still blunt at the end. If the etching is stopped too late, the tip will become blunt again after reaching its smallest radius.

cut-off circuit is used. We therefore develop an etching setup that allows us to investigate the influence of the etching voltage profile on the tip shape and the tip radius. The goal is to develop a recipe that results in hyperbolic gold tips with a radius of 30 nm and a low surface roughness. The etched part of the tip should be no longer than 300 μm to avoid vibrations and deformation during scanning while the apex should have a small opening angle (high aspect ratio) to support the creation of surface plasmons.

3.2.1 Experimental setup

The etching setup consists of a vertical positioning stage that controls the immersion depth of the wire in the acid (37% HCl in H₂O, 38 ml). A glass tube with 25 mm diameter separates the tip from the electrode ring (gold wire, 250 μm diameter). Most components of the setup are made from high density polyethylene (HDPE) to chemically withstand the corrosive effect of the hydrochloric acid used as electrolyte. The setup is shown in Figure 3.2.1.

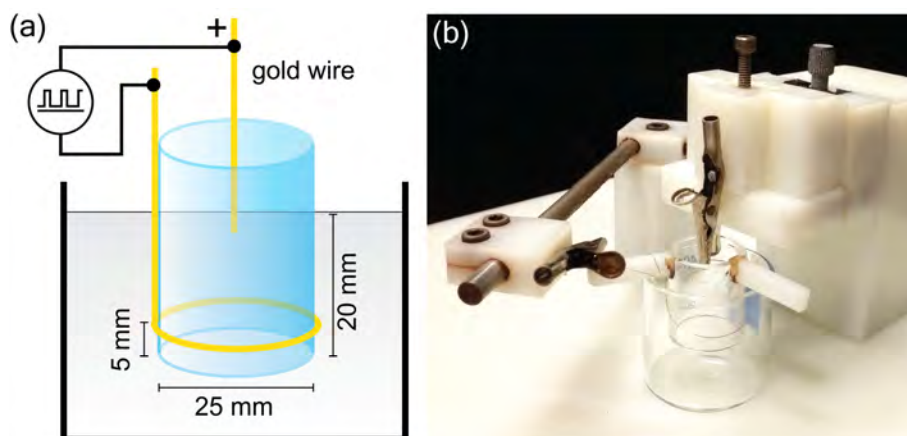


Figure 3.2.1: (a) Sketch of the etching setup. The gold wire is immersed into the solution by 1 mm. (b) Photo of the developed etching setup. The crocodile clamp holds the gold wire.

The etching voltage is provided by either a signal monitor unit (SMU, *Keithley 2400 SourceMeter*) for DC and AC pulses below 10 Hz, or a signal generator (*Keithley 3390 Arbitrary Waveform Generator*) for higher frequencies. The applied voltages are monitored with an oscilloscope (*Tektronix TDS 2024C*).

3.2.2 Electrochemical reaction

The electrolyte solution consists of HCl in water that dissociates to



thus releasing Cl^- chloride anions. By applying a positive voltage to the gold tip (anode), the electric potential initiates a reaction at about 1.5 V between the gold and the chloride ions to produce chloroaurate complexes:



The Au-Cl reaction decreases the diameter of the wire and eventually leads to a hyperbolic tip while the reaction products dissolve in the etching solution. Apart from the reactive Cl^- ions, the positive electric potential at the tip also attracts the chloroaurate reaction products (AuCl_4^-) and other anions in the solution. Those create an electrical double layer on the tip and slow down the reaction by blocking the access of Cl^- [90]. Furthermore, the generation of H_2 gas bubbles at the tip leads to a rough tip surface [144, 158]. Both effects have to be controlled by the choice of electrolyte, etching voltage, and geometry of the setup. An overview of the chemical reactions can be found in reference [162] and a discussion about the influence of the etching voltage on the tip shape is provided in references [90, 142, 159].

3.2.3 Experiments and results

The following experiments are based on published etching procedures (see refs. [90, 143, 144, 158]). The methods are adapted with the goal of establishing a simple and reliable method in our laboratory for the production of gold tips that can be used for STM and tuning fork TERS.

DC etching

In a set of preliminary etching experiments, a DC voltage is applied to the gold wire and the electrode ring is grounded. The wire has a diameter of 250 μm and was annealed by the provider to increase its crystallinity (Au wire, 99.999% purity, *Goodfellow Inc.*). Tip and ring are immersed 1 mm into the electrolyte (37% HCl in aqueous solution, diluted 1:1 with ethanol²²) in the center of the electrode ring.

In order to identify the optimal etching voltage, the current is measured as a function of the applied voltage. Figure 3.2.2 (a) shows a voltammogram of the etching process demonstrating the change of resistivity of the electrochemical cell at different voltages. The oxidation process of the gold in the electrolyte starts between 1.0 V and 1.5 V and slows down above 1.8 V due to the saturation of the electrolyte with the reaction products. At higher voltages, the electric field promotes the attraction of Cl^- ions and thus current and etching rate increase again.

Based on the voltammogram, 1.7 V is chosen as the etching voltage to measure the current as a function of time during the etching process (Fig. 3.2.2 (b)). At the beginning, the current drops quickly due to the shielding effect of the reaction products, and then decreases slowly over time due to increasing resistance of the

²² Ethanol supposedly acts as “chemical intermediate [...] to diminish depolarization effects occurring on the electrodes” [144], which should result in less bubbling and hence in a lower surface roughness [143]. Discussions with other research groups revealed, however, differing opinions on its relevance. Ethanol certainly increases the complexity of the chemical reaction, making it more difficult to understand the etching process (see ref. [162]). As we see later, our best results were achieved without ethanol.

electrochemical cell. Close to the end of the etching, the graph shows a second drop from 0.8 mA to 0.2 mA, where it remains for 20 seconds before the electric connection between tip and electrolyte breaks down entirely.

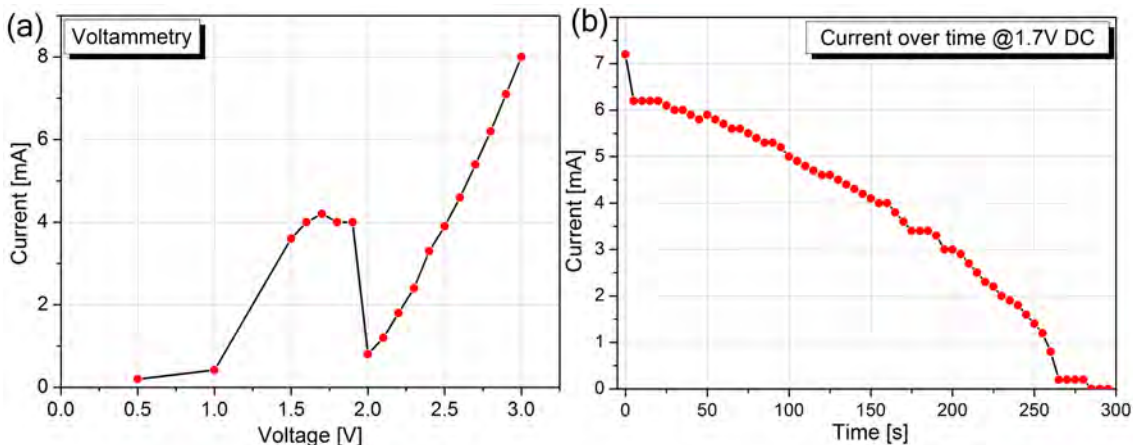


Figure 3.2.2: (a) Voltammogram of a gold tip etched in a 1:1 HCl:Ethanol solution. (b) Current development over time during an etching cycle with 1.7 V DC. The etching current decreases as a function of time.

The current drop at 260 s is probably related to the pinching off of the immersed portion of the wire (etching mainly occurs around the meniscus [90, 142]): When the lower part falls off because the wire becomes too thin to withstand the pulling gravitational force of the lower part, the diameter is typically of the order of nanometers²³. Due to capillary forces, the meniscus remains attached to the upper part and the etching progresses for a short time with a low current.

Several tips are fabricated and the etching is terminated manually by pulling the tip out of the solution after the lower part of the wire drops off. Immediately after etching, the tips are carefully cleaned with ethanol to remove the residues of the acid and reaction products. Optical investigation of the tips shows a conical shape with a length of several hundred micrometers. In order to also evaluate radius and surface roughness, the tips are analyzed by SEM²⁴ (see Fig. 3.2.3). All tips have a tip radius of 200 nm or more and show variations in shape in connection with a high surface roughness of up to several hundred nanometers (RMS).

²³ We calculated the minimum diameter for a gold wire based on the critical tensile stress at which gold starts to plastically deform (~ 200 MPa [163]) and the gravitational force of the immersed wire. For a 250 μm thin gold wire that is immersed 1 mm, the critical radius is approximately 10 nm.

²⁴ SEM typically leads to the deposition of a thin carbon layer on the tip. It is therefore not recommended to verify the radius of a tip that is afterwards used for TERS.

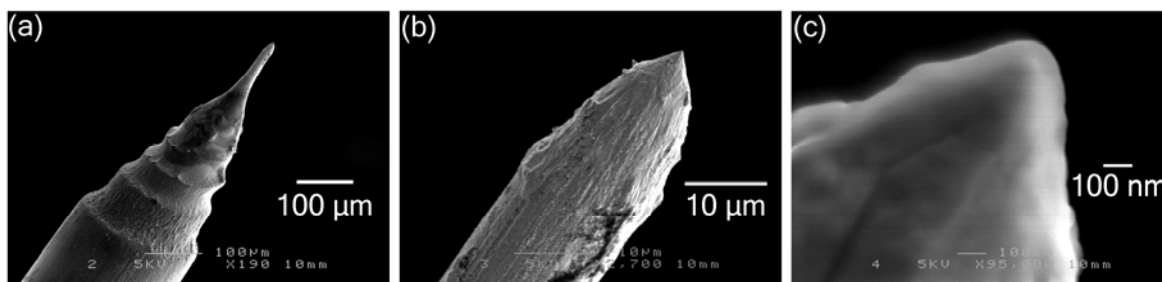


Figure 3.2.3: SEM images of an electrochemically etched gold tip with 1.7 V DC at different magnifications. (a) 500 μm long conical shape. The uneven profile along the tip axis is probably caused by variations of the ion concentration at the tip during etching. (b) High surface roughness close to the apex. (c) Tip radius of about 150 nm with a low aspect ratio ($\sim 80^\circ$ opening angle).

Our DC etching results show a high surface roughness on the last 10 μm to the apex of the tip. All obtained tip radii are above 100 nm and thus not small enough to fulfill the requirements to excite a surface plasmon resonance.

The voltammetry curve in Figure 3.2.2 (b) shows that the etching continues to progress after the lower part of the wire drops off. This effect is known as overetching. In order to maintain a tip with a radius of nanometers, the current must be stopped and the tip has to be pulled out of the electrolyte at the right moment. Based on the wire thickness and the observed etching time, the radius decreases by approximately 500 nm/s. At this rate, the process has to be terminated within 20 ms to obtain a tip radius of the order of 30 nm. This cut-off speed cannot be achieved by hand but requires an electronic cut-off circuit that monitors the current and terminates the etching as a current drop is detected.

Pulse etching

As an alternative to DC etching, repetitive voltage pulses with a rectangular shape can be applied to the tip and lead to reportedly sharp tips even without the use of an electronic cut-off circuit [158]. A variation of the electric field affects the etching process in, at least, three ways: 1) Electrowetting causes a height modulation of the meniscus which promotes the distribution of Cl^- ions [90, 144]. 2) During the off-time, the AuCl_4^- ions descend and thus reduce the electric double layer at the tip [90]. 3) At high pulse frequencies, potentially generated gas bubbles at the tip surface detach at an early stage of growth, thus reducing the roughness of the tip [158]. Williams et al. [158] and Kharintsev et al. [144] observed tip radii of 30 nm with different pulse durations. While Kharintsev used a relatively long cycle time of 0.5 s with a rectangular profile that alternates between 1.5 and 1.9 V (1.5 V offset, pulse voltage 0.4 V, pulse time 250 ms), Williams suggested the use of 8 V pulses with a length of 30 μs and a cycle time of 330 μs with a 0.5 V offset (see Fig. 3.2.4 for a sketch of the applied signal).

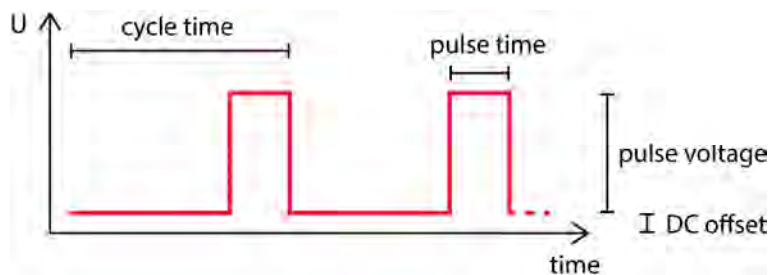


Figure 3.2.4: Sketch of the voltage profile that is applied to the tip.

We therefore conduct several etching series with different electrolyte mixtures and pulse-voltage profiles. Every series is carried out with 10 gold tips made of gold wire with a $100\ \mu\text{m}$ diameter. The tips are manually retracted after the meniscus collapses and immediately rinsed with ethanol to remove residues of the electrolyte. The tips are then analyzed with an optical microscope to verify the tip shape, and by SEM to evaluate the tip radius and surface roughness.

The first three series are etched with a rectangular voltage profile that alternates between $1.5\ \text{V}$ and $1.9\ \text{V}$ with a cycle time of $440\ \text{ms}$. We employ this profile with three different HCl mixtures as electrolytes:

- 1) 37 % $\text{HCl}:\text{H}_2\text{O}$ mixed 1:1 with ethanol
- 2) 37 % $\text{HCl}:\text{H}_2\text{O}$ mixed 1:1 with methanol
- 3) 37 % $\text{HCl}:\text{H}_2\text{O}$ (undiluted)

Optical microscopy shows that the macroscopic shape of the tips is highly reproducible within each series. Investigation by SEM, however, reveals variations of the tip radii and the tip roughness. While the ethanol and methanol solutions lead to radii between $200\ \text{nm}$ and $3\ \mu\text{m}$, etching with hydrochloric acid alone leads to significantly sharper tips with radii between $30\ \text{nm}$ and $100\ \text{nm}$. Selected SEM images are shown in Figure 3.2.5.

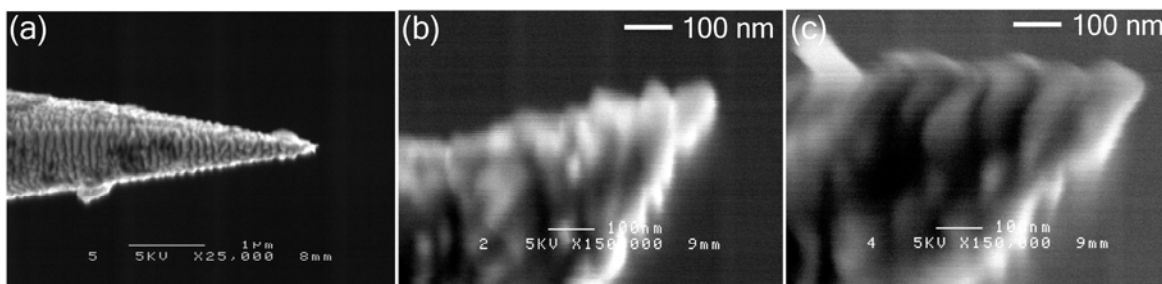


Figure 3.2.5: SEM images at various magnifications of tips etched in hydrochloric acid with a rectangular voltage profile between 1.5 and $1.9\ \text{V}$ (series 3). The tips show a very rough surface but sharp tip radii of the order of $30\ \text{nm}$.

Since all tips exhibit a very rough surface, this etching method appears not to qualify for TERS. However, the results show that sharp tips can be achieved even without a cut-off circuit when using voltage pulses. Williams et al. [158] assumed that short and high voltage pulses of $8\ \text{V}$ prevent bubbles from sticking to the tip

and hence allow for the creation of a smooth tip surface. Consequently, we use a signal generator to apply 30 μs short pulses of 8 V to the tip and the output voltage is monitored by an oscilloscope. Since the signal generator is not a constant voltage source and the output voltage depends on the ohmic load²⁵ of the electrochemical cell as well as on the internal capacitance of the signal generator, the actual voltage is found to be only 5 V which is lower than the nominally applied 8 V. Series 4 is etched with unmixed hydrochloric acid and these settings:

- 4) 5 V pulse for 30 μs every 330 μs in addition to a DC offset of 0.5 V

The voltage, however, increases during the process due to increasing resistivity. The maximum output power supplied by the signal generator thus turns out to be insufficient for the application of 8 V pulses over the entire etching process²⁶. We therefore conduct a second experiment with a lower etching voltage of 3.5 V to decrease the current in order to achieve a more stable voltage throughout the process:

- 5) 3.5 V pulse for 30 μs every 330 μs in addition to a DC offset of 0.5 V

Investigation by SEM shows that all tips have a very smooth surface. While the 3.5 V tips are smooth over the whole tip length, the 5 V tips become rough at approximately 10 μm from the apex (see Figs. 3.2.6 and 3.2.7). This supports the theory that the voltage pulses free the surface from gas bubbles at an early stage, leading to a smooth surface at the origin of the bubbles but higher surface roughness above this point due to ascending gas. More important, however, are the tip radii, which vary between 30 nm and 300 nm when tips are etched with 5 V pulses and are around 30 nm when tips are etched with 3.5 V pulses. Since the 3.5 V pulses lead to consistently good radii, we employ this etching method to the production of TERS tips used on tuning forks in chapter 5.

The statistical distribution of the tip radii achieved in etching series 1 to 5 is shown in Figure 3.2.8. The optical images of all tips are presented in Figure 3.2.9.

²⁵ The resistivity of the etching setup is voltage dependent and changes during the etching process of the tip between 300 Ω and several $\text{k}\Omega$ (see Fig. 3.2.2). The impedance of the signal generator is therefore set to the initially measured resistivity of 300 Ω .

²⁶ In the literature, the applied voltages during pulse etching with a signal generator might be lower than reported. Monitoring the pulse voltage by an oscilloscope appears to be necessary.

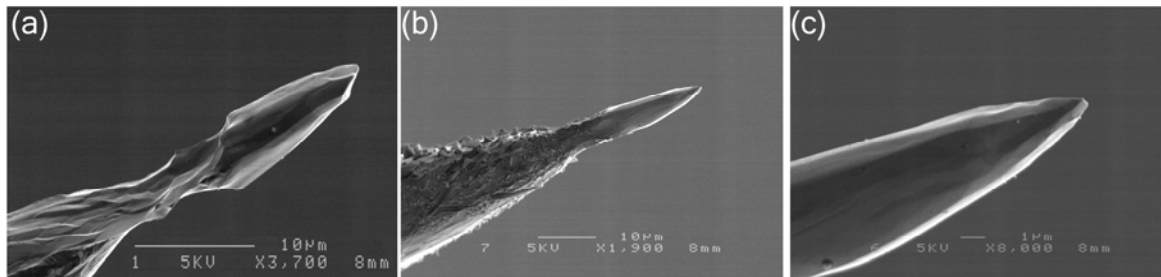


Figure 3.2.6: SEM images of tips etched with 5 V pulses (series 4). (a-b) The tips are smooth close to the apex but otherwise rough due to ascending gas bubbles during etching. (c) Magnification of the apex of tip in scan (b). The tip radius is of the order of several hundred nanometers.

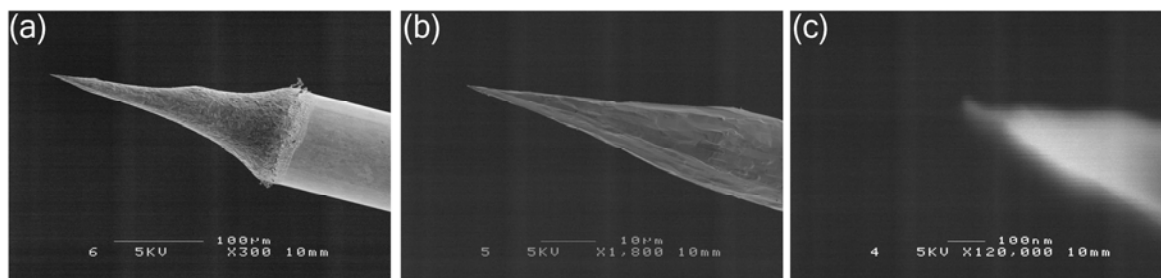


Figure 3.2.7: SEM images at different magnifications of a tip etched with 3.5 V pulses (series 5). The surface of the tip is very smooth and the radius of the apex is about 20 nm with a high aspect ratio.

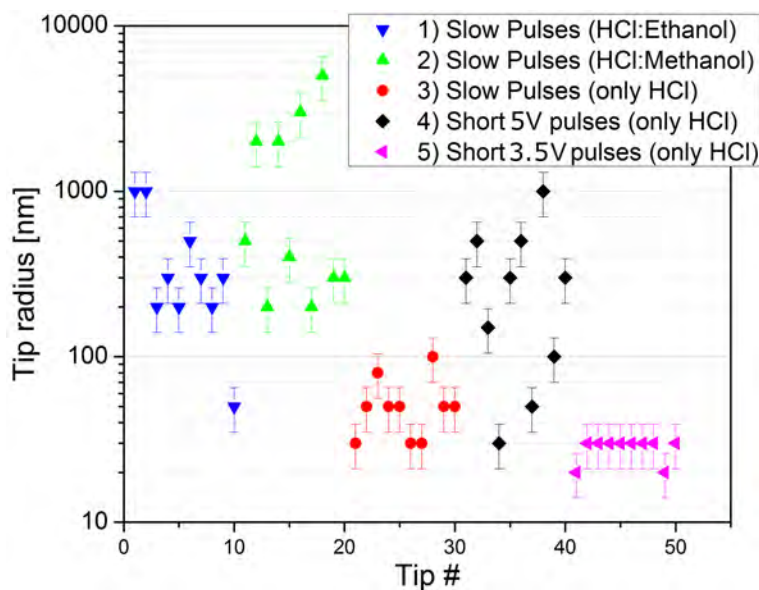
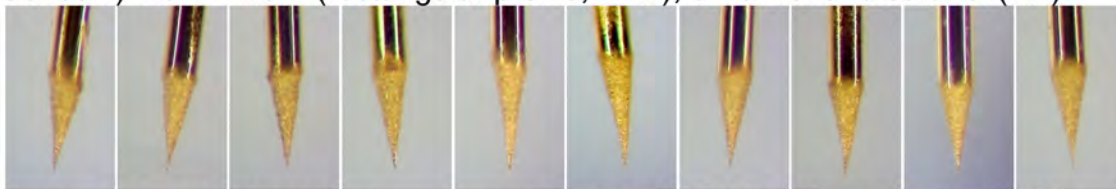
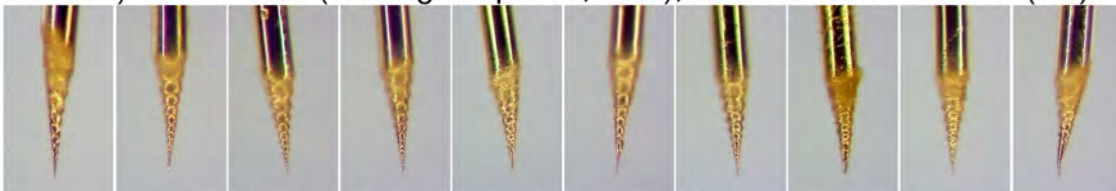


Figure 3.2.8: Tip radii achieved in the various etching series as measured by SEM. Series 1) and 4) are the processes that were closely based on literature and show the possibility of achieving sharp tips but with a relatively low yield. Our modifications, that include the change of the electrolyte to only hydrochloric acid and the reduction of the pulse voltage to 3.5 V, have a clear impact on the sharpness and reproducibility of the tips (series 5). (The error bars are estimates based on the SEM resolution for the given magnification.)

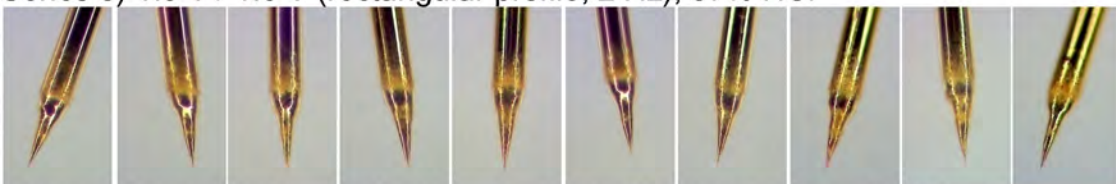
Series 1) 1.9 V / 1.5 V (rectangular profile, 2 Hz), 37% HCl and ethanol (1:1)



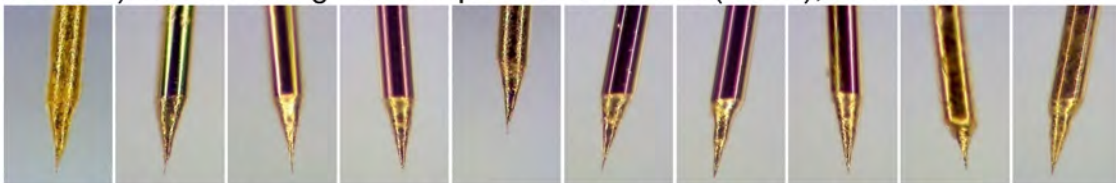
Series 2) 1.9 V / 1.5 V (rectangular profile, 2 Hz), 37% HCl and methanol (1:1)



Series 3) 1.9 V / 1.5 V (rectangular profile, 2 Hz), 37% HCl



Series 4) Pulse-etching with 5 V pulses +0.5 V DC (3 kHz), 37% HCl



Series 5) Pulse-etching with 3.5 V pulses +0.5 V DC (3 kHz), 37% HCl



Figure 3.2.9: Optical images of the etched tips from series 1 to 5. The gold wire has a diameter of 100 μm and can be used as scale bar.

3.2.4 Tip shape

The shape of the tip can vary significantly as seen in Figure 3.2.9. These differences are mainly related to variations during the etching process that is governed by the concentration of Cl^- ions and reaction-hampering products such as gold complexes or ascending gas bubbles. Since these effects depend on the chemical solution, applied voltage, elapsed etching time, and the direction of the electric field, various tip shapes can be observed. The interplay of these effects makes it difficult to investigate their origins individually.

The basic, hyperbolic tip shape, however, is caused by a descending meniscus at the surface of the electrolyte as the radius of the wire decreases. The meniscus

height h of a liquid around an immersed wire with the radius R was derived by Extrand et al. [164] and is given by:

$$h = \left[2 \left(\frac{\gamma}{\rho g} \right) (1 - \sin \vartheta_a) \right]^{1/2} \left[1 + \frac{1}{R} \left(\frac{\gamma}{\rho g} \right)^{1/2} \right]^{-1/2} \quad (3.2.3)$$

where γ is the surface tension, ρ is the density of the liquid, g is the gravitational constant and ϑ_a is the contact angle. This equation can be used to simulate the profile of an etched tip when we assume that the etching takes place equally over the height of the meniscus. We plot equation 3.2.3 with the values $\gamma_{\text{HCl}} = 70 \text{ mN/m}$ [165] and $\rho_{\text{HCl}} = 1.19 \text{ kg/l}$ [166], and compare it to the hyperbolic profile of a tip with a diameter of $250 \text{ }\mu\text{m}$ that was etched with 5 V pulses in hydrochloric acid. Figure 3.2.10 shows the simulated tip shape in comparison with the tip profile measured by SEM. The contact angle was kept as variable and shows the best fit for $\vartheta_a = 56^\circ$, which equals the contact angle of water on gold [167].

The simulation shows a good quantitative agreement with the etched profile of the tip. We therefore assume that this particular tip was not much affected by the reaction hampering products. All other observed tip shapes are likely to be alterations of this hyperbolic profile and can be explained by local concentration fluctuations of the Cl^- ions and reaction products affecting the local etching speed, surface tension, and the contact angle of the meniscus.

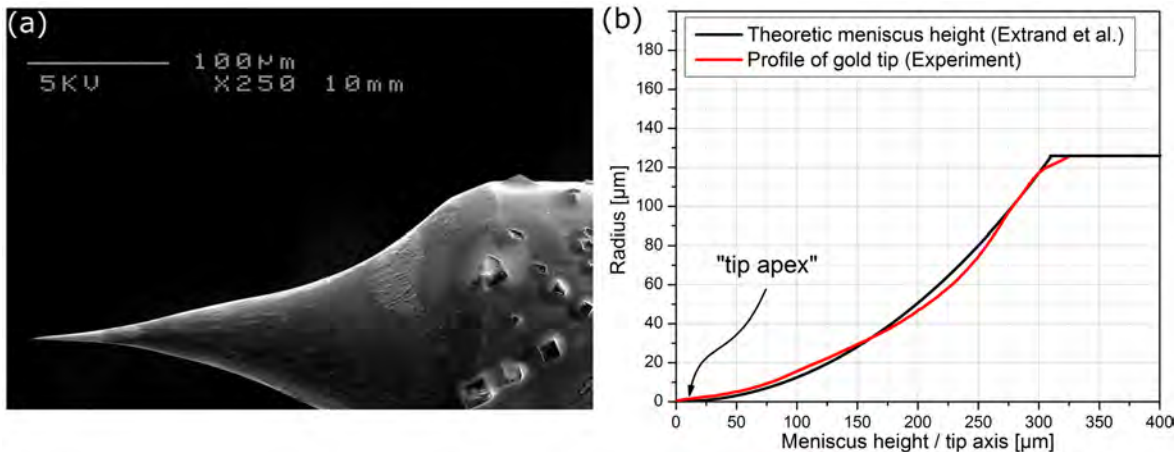


Figure 3.2.10: (a) SEM image of electrochemically etched gold tip. (b) Comparison between the profile of the tip (as measured by SEM) and the theoretic meniscus height at a given radius.

3.2.5 Summary

Our etching experiments confirm that the use of constant voltage etching of gold tips without a cut-off circuit leads to a delayed collapse of the meniscus (overetching) at the apex of the tip and therefore falls short of generating sharp tip radii that are suitable for the generation of a surface plasmon resonance.

We combined the etching setup described by Kharintsev [144] with the high frequency pulse etching process described by Williams [158]. The modified setup in combination with a pulse voltage of 3.5 V leads to highly reproducible and sharp tips with a radius of 30 nm and a very low surface roughness. The developed etching method can now be used to fabricate gold TERS tips for STM and tuning fork shear-force mode AFM.

3.3 Alternative fabrication methods

We would like to finish this chapter with a brief overview of alternative tip production methods. The main alternative to electrochemical etching of TERS tips is the deposition of a rough film of gold or silver on a silicon AFM cantilever by evaporation [39, 41, 168-173] or sputtering [40], similar to the production of SERS substrates [100, 174, 175]. The AFM tip is therefore placed in an evaporation chamber and coated at a low rate between 0.1 nm/s and 0.01 nm/s in order to allow for the crystalline growth of nano-islands. Materials with different permittivities can be used as a sublayer under the metal film to tune the plasmon resonance [176].

Apart from electrochemical etching and thermal deposition methods, several other concepts were reported in recent years. These are, without any claim to completeness, deposition of nanoparticles on AFM tips [177], chemical growth of metallic nanostructures on AFM tips [178, 179], mask-assisted growth of gold cones on AFM tips [180], deliberate shaping of the tip apex by a focused ion beam [181, 182], growth of nanowires with gold seeds to be used as probes [183, 184], and the use of electrochemically etched tips in AFM by bending the etched tip to form an AFM cantilever [185].

4 TERS on carbon nanotubes

After we developed the tip-etching process solely based on geometric parameters (tip-radius and surface roughness), we will now investigate the near-field enhancement capabilities of the TERS tips by Raman mapping of carbon nanotubes (CNTs).

CNTs are an ideal reference sample for TERS for various reasons. First of all, metallic CNTs with a diameter of around 1.3 nm are resonant Raman scatterers with a strong Raman signal under red light excitation. Their small volume only covers a small fraction of the confocal laser focus, reducing the confocal background signal and facilitating the determination of the enhancement factor. Secondly, the small diameter allows for measurement of the extension of the optical near-field and thus the lateral resolution of the tip when scanning across the CNTs.

This chapter starts with the preparation of suitable substrates for TERS and the deposition of CNTs to obtain a reference sample that can be used to verify the enhancement of the TERS tips. The CNT sample is then used for TERS mappings that feature an optical resolution of 14 nm and the spectral sensitivity to determine the electronic properties of the CNTs.

4.1 Sample preparation and characterization

For these test purposes, we decided to deposit the CNTs on a gold substrate to benefit from the gap-enhancement effect that leads to an increased amplification of the electric field at the tip over a metallic substrate. Furthermore, an electrically conductive substrate enables the use of scanning tunneling microscopy, which facilitates the probe production.

4.1.1 TERS substrates

In order to analyze nanometric samples such as molecules, nanotubes, or even small crystals, these samples must be fixed to a substrate with negligible Raman background. Metallic sample holders, as are used for confocal Raman spectroscopy, are generally Raman inactive but often too rough to be scanned by STM or AFM with nanometer resolution. A good alternative are fluorescence-free microscope cover glasses that are very flat and feature (almost) no Raman scattering. Furthermore, they can be easily used in inverted microscopes, which require transparent and very thin substrates ($< 200 \mu\text{m}$ thickness).

In some cases, a metallic surface can be beneficial for use with TERS, e.g. to take advantage of the gap-enhancement effect or to scan the sample in STM mode. Therefore, the substrates are commonly coated with a thin film of gold. The gold films can be deposited by sputter deposition or thermal evaporation onto glass or mica. Mica even enables the growth of atomically flat films which, however, require thermal treatment after a few weeks of storage in order to re-crystallize the surface.

Because of the high chemical sensitivity of TERS, it is important to use clean substrates to avoid Raman signals from contaminants on the surface. The signals from contaminants are often found to be broad in the region between 1200 cm^{-1} and 1600 cm^{-1} , which is characteristic of amorphous carbon and organic residues. As long as the gold layer is connected to the glass by an adhesion layer, such as titanium, it is mechanically stable and can be cleaned with acetone in an ultrasonic bath or with Piranha²⁷.

Another source of contamination is sulfur (e.g. as contained in breath) that preferably bonds to gold and generates a Raman signature at about 300 cm^{-1} [186]. Sulfur-gold bonds are chemically stable due to the high binding energy ($\sim 2\text{ eV}$ [187]) and therefore a contamination with sulfur typically requires replacement of the substrate.

Glass substrates

Silicate glass is often used as a substrate for AFM because of its low roughness (0.2 nm RMS) and its chemically inert surface that enables cleaning with corrosive solutions. Glass slides are typically not made of pure fused silica because of its high melting point. Instead, additives are employed to decrease the melting point, often resulting in undesired fluorescence and Raman scattering. Fluorescence-free glass, however, can be made of borosilicate and is typically used in TERS. Figure 4.1.1 shows an AFM measurement of the surface of a fluorescence-free glass cover slip.

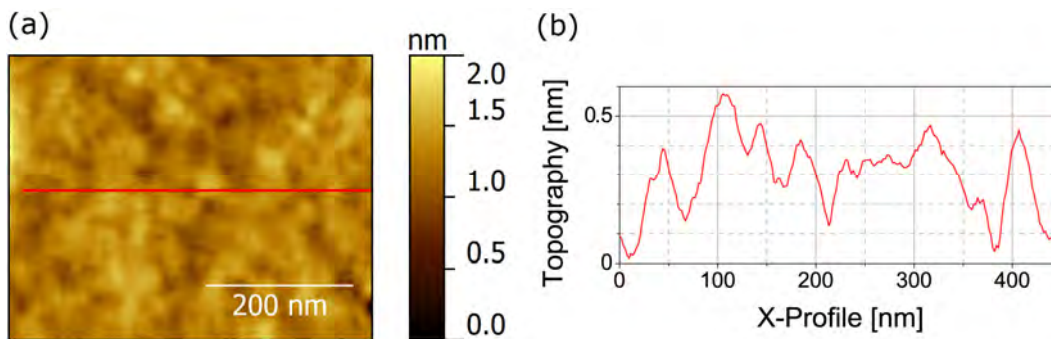


Figure 4.1.1: (a) AFM topography image of the surface of a cover glass. The red line indicates the path of the cross section shown in (b) and corresponds to a roughness of 0.2 nm RMS .

The Raman spectrum of a nominally fluorescence-free glass measured with a high laser intensity (10 mW focused by a 0.9 NA objective) is shown in Figure 4.1.2. The spectrum shows a relatively weak Raman signal in addition to a broad fluorescence background. With the experimental settings typical of a TERS experiment on our system ($200\text{ }\mu\text{W}$ laser power, 0.4 NA objective), the substrate signal would be 300 times smaller, leading to only 0.1 counts/s , which is below the systems detection limit.

²⁷ “Piranha” is a 3:1 mixture of sulfuric acid and hydrogen peroxide. It is highly efficient in dissolving organic substances, hence the name.

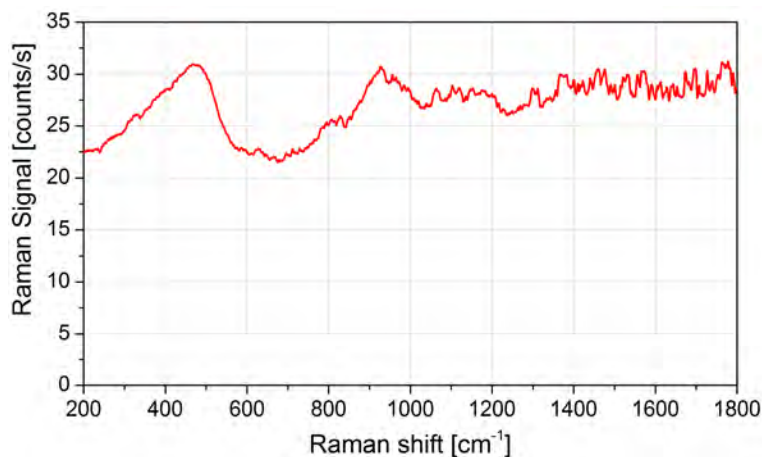


Figure 4.1.2: Raman spectrum of a nominally fluorescence-free borosilicate glass slide. The spectrum was recorded with a 0.9 NA objective, 10 mW laser power at 632.8 nm wavelength, and 6 minutes integration time. Peaks are visible at 450 cm^{-1} and 950 cm^{-1} on top of a flat background.

Substrate metallization

Gold thin films with a thickness of a few nanometers are still transparent and therefore suitable for TERS in optical bottom-access on inverted microscopes. The optical transparency is wavelength dependent and can be calculated from the refractive index of the metal. We calculated the thickness of a gold film with a transparency of 50 % in the visible spectrum (see Fig. 4.1.3). The values of the optical dielectric function of gold were taken from the supplemental material of reference [188], and the penetration depth was calculated by equation 2.4.6.

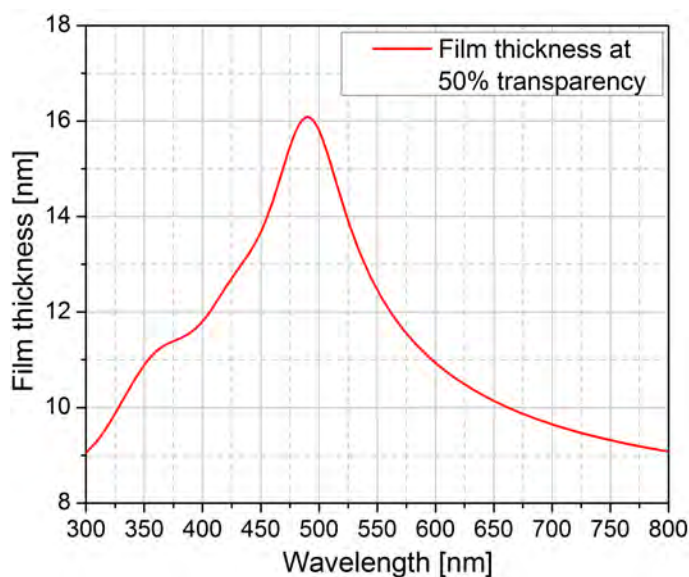


Figure 4.1.3: Film thickness of crystalline gold at 50% transparency at a given wavelength. The highest transparency lies in the optical blue-green region and decreases for longer wavelengths.

We do not require a transparent reference sample for our experiments in side-access TERS and can therefore use thicker gold films to ensure a dense gold coverage of the substrate. To test the deposition on glass, a non-crystalline gold layer of 50 nm thickness is deposited by plasma sputtering onto a glass coverslip with a 5 nm thick adhesion layer of titanium. The plasma ions are accelerated onto a gold target and dislodge the gold atoms which form agglomerations on their way to the substrate. This process led to a relatively rough surface as shown in Figure 4.1.4.

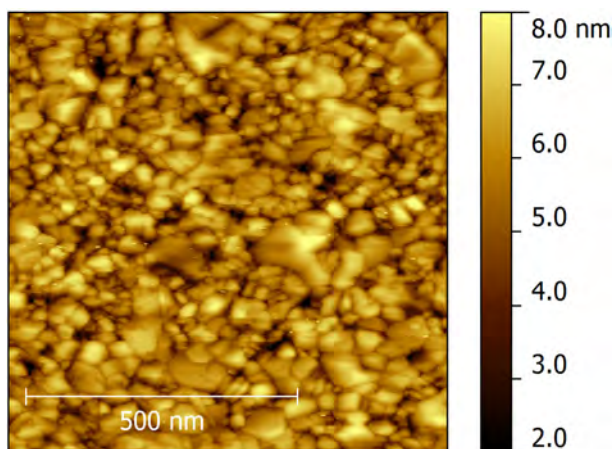


Figure 4.1.4: STM topography scan of the surface of a 50 nm thick sputtered gold layer. The high surface roughness complicates the analysis of molecules. The surface morphology, however, was stable over longer periods of time according to measurements that were acquired two years apart.

Crystalline gold substrates

Substrates with a lower roughness can be achieved by thermal evaporation of gold on glass, or, if atomically flat surfaces are required, by epitaxial growth on freshly cleaved mica [189-192]. Because crystalline gold surfaces stay atomically flat for only a few days, an annealing process is required to “refresh” the surface [193].

We now investigate the recrystallization of a 150 nm thick gold film by annealing. The film was purchased as epitaxially grown gold on mica one year prior to the experiments. A gas burner is placed under a glass test-tube which is constantly purged with nitrogen to ensure a dry and clean atmosphere. The empty test tube is heated to evaporate the surface water and the substrate is placed in the bottom of the tube with the gold layer facing upwards. Due to the curvature of the tube, the mica sample touches the tube only at its edges and the surface has no contact to the glass tube. The annealing process is carried out in two steps: First, the test tube is positioned 2 cm above a blue gas flame for 1 minute to heat the gold layer to a temperature just below its melting point. Second, the distance between tube and flame is increased to 5 cm to allow the surface to recrystallize at a constant temperature for about 2 minutes. The burner is then removed and the sample is cooled in the tube under a nitrogen flow for 3 min. Figure 4.1.5 shows an AFM scan of the topography of the recrystallized surface. The gold layer formed islands with diame-

ters of several hundred nanometers that have a roughness of 0.1 nm to 0.2 nm (RMS). Larger islands can be achieved by repeating the above-described annealing procedure [193].

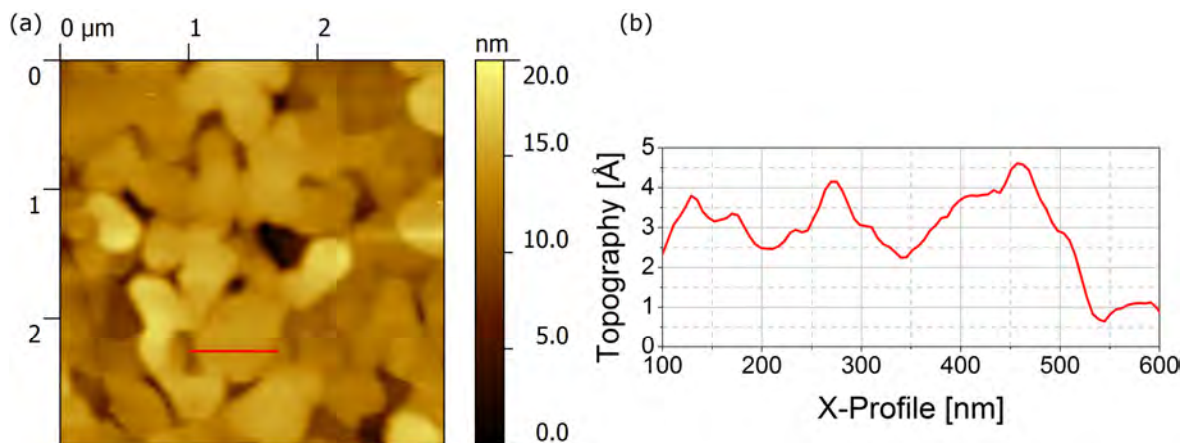


Figure 4.1.5: (a) Non-contact AFM scan of the topography of a freshly annealed gold film on mica. The terraces have sizes of several hundred nanometers and can serve as substrate for molecules or nano-objects in TERS. The cross section of the surface of an island is indicated by a red line and shown in part (b). The cross section reveals a surface roughness of only a few Ångström. (Mechanical vibrations of the AFM were averaged out over 5 adjacent scan lines, approximately the radius of the tip.)

If the atomically flat gold film does not need to be dense, the substrate can also be coated with crystalline nano-plates [194]. The specimen can then be dispersed on the gold-plated substrate and the TERS scans are only performed on the surface of the plates.

For the following TERS experiments on CNTs, we decided to use the sputtered gold film on glass as a substrate. The sputtered films are easy to prepare and the surface remains stable over time, which is important when using the substrate for a reference sample.

4.1.2 Selection and characterization of CNTs

CNTs consist of sp^2 -hybridized carbon atoms that form a hollow tube of typically a few nanometers in diameter and up to several millimeters in length [195]. Depending on their chirality, CNTs can be either metallic or semiconducting and their 1-dimensional electronic density of states leads to discrete and very sharp (~ 10 meV [196]) interband transitions (Van Hove singularities). Unlike in 3-dimensional structures, optical excitation or absorption in 1-dimensional structures is therefore only possible if the wavelength of the excitation light matches the transition energy of the electrons. The transition energies depend on the diameter and structure of the CNT and are depicted in the *Kataura plot* (see Fig. 4.1.6) [196-198].

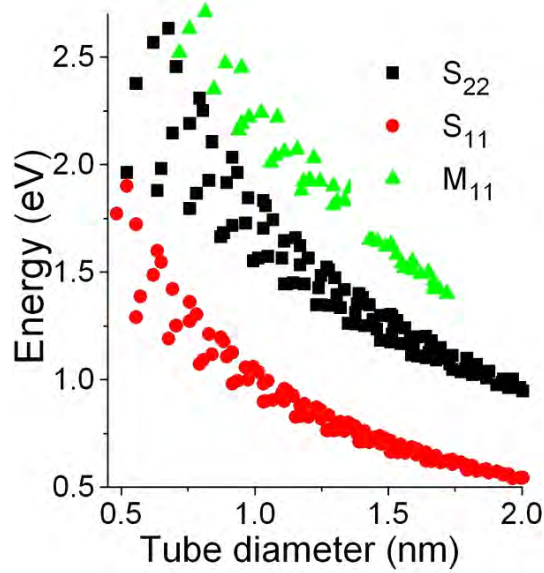


Figure 4.1.6: The Kataura plot shows the transition energies of metallic (M_{11}) and semiconducting (S_{11} , S_{22}) carbon nanotubes for various tube diameters. Metallic CNTs with a diameter of 1.3 nm and semiconducting CNTs with a diameter of 0.9 nm have an absorption maximum at a wavelength of 633 nm (1.96 eV). (Figure taken from ref. [199].)

Our TERS laser has a photon-energy of 1.96 eV (632.8 nm) and resonant Raman scattering is therefore expected from metallic single-wall CNTs with a 1.3 nm diameter. We purchased predominantly metallic CNTs in aqueous solution (1 mg CNTs in 100 ml, 90% metallic, *NanoIntegrus Inc.*) for deposition on sputter-coated gold substrates. To determine the Raman spectrum of the CNTs, a drop of the CNT solution is cast onto a glass cover slip. The Raman spectrum of the CNTs is recorded confocally on an inverted Raman setup with a 0.9 NA objective. The CNT spectrum that is shown in Figure 4.1.7 is dominated by the G-band at 1580 cm^{-1} . This band represents the in-plane oscillations of the carbon atoms. The peak at 1325 cm^{-1} is called the D-band (“D” for *defect*) and only appears in the presence of point defects in the carbon-lattice. The ratio between the G-band and the D-band can be used to determine the concentration of defects in the CNTs. Our Raman spectrum shows a low D-band and thus confirms the high quality of the CNTs.

The Raman mode at around 200 cm^{-1} is referred to as radial breathing mode (RBM) as present in CNTs with diameters of 1-2 nm. This phonon mode originates from a radial oscillation that is vertical to the CNT axis, and its energy is related to the CNT’s diameter d :

$$\tilde{\nu} = (234 \text{ nm} \cdot \text{cm}^{-1})/d - 10 \text{ cm}^{-1} \quad (4.1.1)$$

where $\tilde{\nu}$ is the spectral position of the RBM mode [200]. The Raman spectrum shows two RBMs at positions 173 cm^{-1} and 196 cm^{-1} which correspond to a tube diameter of 1.26 nm and 1.44 nm, respectively. These values are in good agreement with the diameters predicted by the Kataura plot for resonant scattering. Note that equation 4.1.1 describes the phonon energy of free SW-CNTs and our experimentally observed

energies can be affected by the environment, namely the solvent, the substrate, or the interaction with other CNTs. The Raman spectrum in Figure 4.1.7 does not reveal information about the presence of CNTs with other diameters because non-resonant Raman excitation is too weak to become visible.

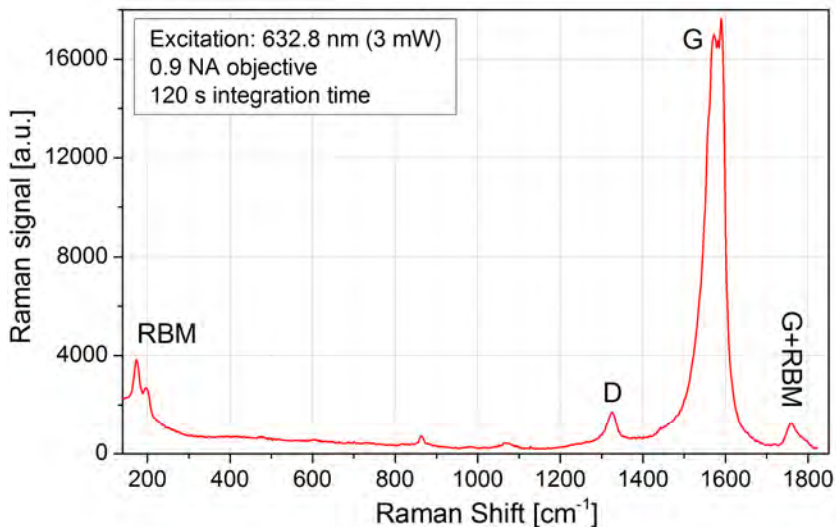


Figure 4.1.7: Confocal Raman spectrum of our CNTs in aqueous solution on a cover glass. The G-band and the radial breathing modes (RBM) are clearly visible. The D-band is relatively small compared to the G-band which indicates a low density of defects. The background Raman signal of the cover glass was measured independently and subtracted from the recorded CNT spectrum.

4.1.3 Carbon nanotube deposition

We decided to use the sputtered gold film on glass as a substrate for the production of the CNT reference sample. In contrast to the crystalline gold film on mica, the glass substrate is Raman inactive and the surface roughness of the sputter-coated film remains constant over time.

The aqueous CNT solution (10 μg CNTs per ml water) is sonicated for five minutes to evenly distribute the CNTs. 30 μl of the solution are drop-cast on a 12 mm x 12 mm glass substrate that was previously sputter-coated with a 50 nm thick gold film. After drying the solution for 30 min in air to allow the CNTs to attach to the surface, the substrate is purged with clean water and dried in nitrogen flow. The sample is then scanned by AFM to measure the length and distribution of the CNTs on the surface.

The AFM topography scans in Figure 4.1.8 show that the CNTs vary in length from 100 nm to 2 μm and are evenly distributed over the surface, with a density of approximately 1 CNT/ μm^2 . This is a good density for our TERS experiments because it is low enough to ensure the presence of a single CNT within the focus of the objective (to reduce the far-field signal), but high enough to locate a CNT within a small scan range.

While the apparent width of the CNTs in the AFM scan mainly depends on the tip radius²⁸, the height provides a realistic measure of the diameter of the CNTs. Figure 4.1.8 (b) shows CNTs with thicknesses between 1 nm and 10 nm. The variation in diameters is likely caused by the formation of CNT bundles and was previously observed elsewhere [201]. In order to use the deposited CNTs as a reference sample for TERS, bundles of CNTs with different chiralities are useful because they provide a broader spectrum of excitable transition energies, increasing the chances to obtain resonant Raman scattering.

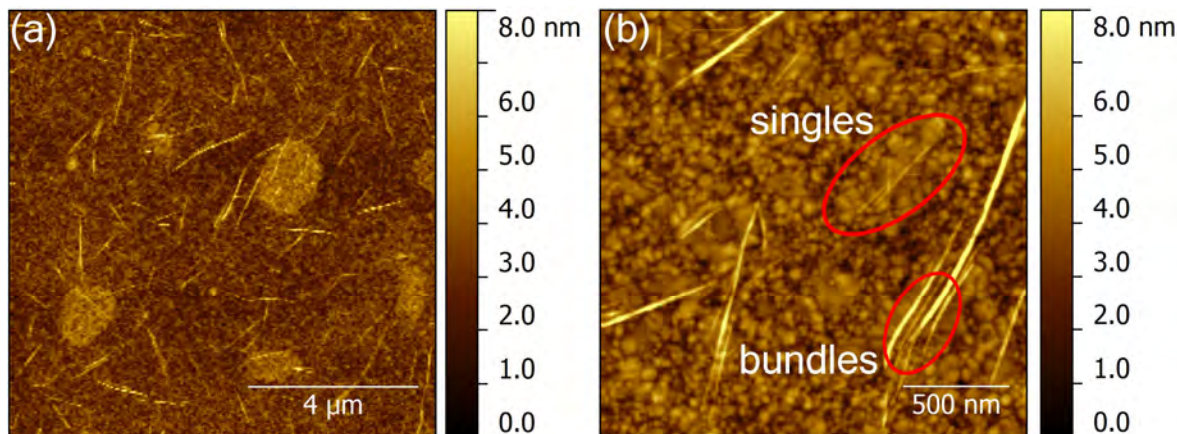


Figure 4.1.8: AFM topography scans of CNTs on a sputtered gold substrate. (a) The $10\ \mu\text{m} \times 10\ \mu\text{m}$ scan shows dispersed CNTs of lengths varying between 100 nm and 2 μm as linear objects on the substrate. The round “spots” may be residues from the solvent. (b) AFM image with increased resolution ($2\ \mu\text{m} \times 2\ \mu\text{m}$). The CNTs vary in thickness from 1 nm to 10 nm, which is likely related to their presence as single CNTs or bundles. The CNTs are more frequently located on larger gold islands, probably due to an increased surface contact in these areas.

4.2 Alignment between objective and tip

Before aligning the tip, the calibration of the spectrometer and the alignment of the optical axis are checked with the silicon reference sample. In order to optimally collect the TERS signal from the near-field of the tip and to keep the influence of the far-field as small as possible, the apex of the tip has to be precisely positioned in the focus of the objective. The TERS system was designed to allow for control of the objective position relative to the tip by employing a piezoelectric objective scanner. This scanner allows for movements in all three dimensions with nanometer precision, and can control the position of the laser focus even when the tip is in contact with the sample. Furthermore, the sample can be moved relative to the tip while the alignment between laser and tip is not compromised. The alignment between tip and objective is carried out in three steps:

1. *Rough alignment:* The confocal objective accesses the tip from the side under a 65° angle to the tip axis. The focus of the objective has to be brought close

²⁸ The radius of a standard silicon AFM tip for tapping mode is about 5-20 nm.

to the end of the tip in all three dimensions. This is carried out by hand with three positioning screws that move the entire SPM in front of the objective with micrometer precision. The sample is retracted from the tip by 5 mm and the reflection of the de-focused laser spot, including the shadow of the tip, becomes visible on the sample holder. When the tip is moved into the focus, the orientation of the tip shadow indicates if the tip is in front or behind the focal plane. The rough alignment is completed when the laser beam can be entirely blocked by a small movement of the tip.

2. *Objective scan:* The objective scanner is used to create a far-field image of the apex of the tip by scanning the tip in side view ($30\ \mu\text{m} \times 30\ \mu\text{m}$ scan range). The intensity of the backscattered light is recorded by the PMT and the signal is plotted as a function of the objective position to create an image of the tip. If the rough alignment was successful, the tip apex should have an apparent radius of about $1\ \mu\text{m}$ in accordance with the optical diffraction limit (see Fig. 4.2.1). The laser position can now be placed on the end of the tip by moving the objective scanner. If the tip apex is not visible, or the outline of the tip appears blurry, step 1 needs repeating. The resulting far-field image also serves as a map of the tip to control the focus position during the TERS experiment to optimize the tip enhancement.

Note: In order to use the PMT image for alignment, it is important that the focus of the PMT coincides with the focus of the Raman spectrometer. This can be achieved by aligning the pinholes of the PMT and the spectrometer when the laser is focused on a flat and Raman-active sample such as a polished silicon crystal.

3. *TERS signal optimization:* For the last alignment step, the tip is brought into contact with a CNT to verify the tip enhancement based on the TERS spectrum (an STM scan of the CNT sample is shown in Figure 4.2.2). The STM feedback keeps the tip at a constant distance of approximately 1-2 nm above the CNT. At the same time, the Raman spectrum is measured with an integration time of 5 s while the laser illuminates the tip in p-polarization (parallel to the tip-axis) with a power of $200\ \mu\text{W}$. At this power and integration time, the G-band of the CNT is too weak to be seen in the confocal background signal, becoming visible only if the tip provides enhancement. The focus position of the tip can now be fine-tuned by small movements with the objective scanner until the peak of the G-band is maximized. If no TERS signal is visible, the tip is either not positioned on a Raman active CNT or does not provide enhancement.

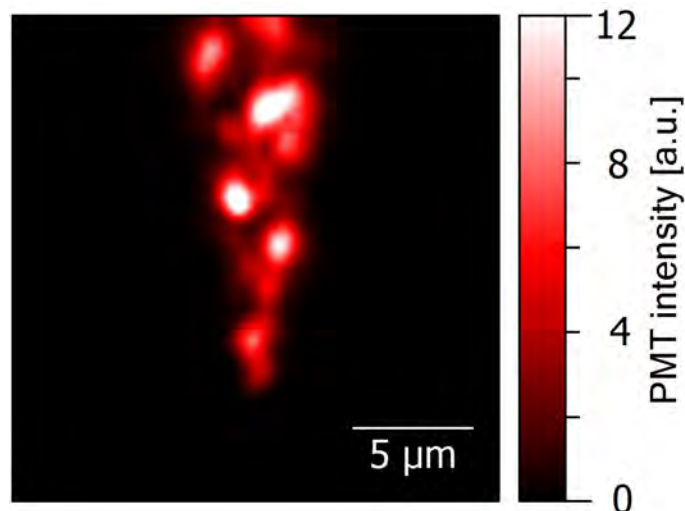


Figure 4.2.1: Objective scan of the Rayleigh scattered light from a tip in side view measured by the PMT (500 μ W laser power, polarization parallel to the tip axis). The scan reveals an interference pattern of plasmons on the surface of the tip.

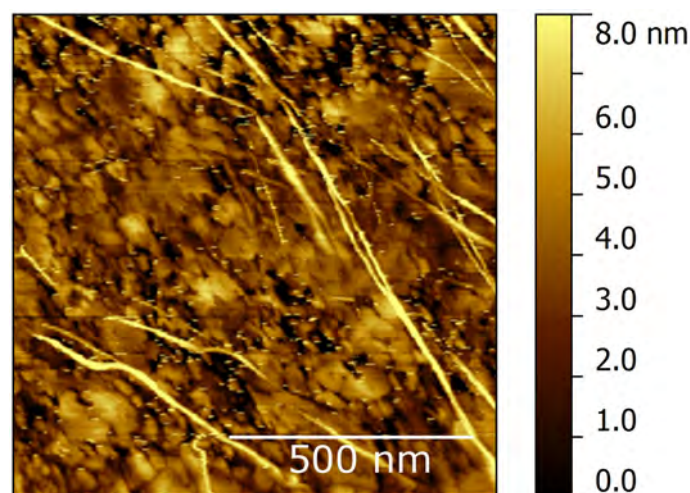


Figure 4.2.2: STM scan of the CNT reference sample. The scan was conducted at a 0.1 V tip voltage and a 500 pA tunnel current in constant current mode. At several positions, the CNTs appear split, which is an indication of bundling. We assume that the STM tip occasionally touched the CNT bundles during the scan and separated them. Bundling might also explain the observation of large CNT diameters.

4.3 TERS mapping

TERS mapping describes the 2-dimensional Raman imaging in which the TERS tip scans the sample along a predefined grid while a Raman spectrum is recorded at every grid point. The spectral map is typically visualized (“rendered”) by plotting the intensity of a selected Raman mode as a false color image to show the location of a specific Raman scatterer or chemical constituent with an optical

resolution of nanometers. The mapping of an area can take several hours, depending on the integration time and resolution.

The TERS mapping on CNTs is carried out in STM mode with a 0.5 V tip voltage and a 0.1 nA constant tunnel current, leading to a tip-sample distance of 1-2 nm. We scan an area of 400 nm x 400 nm with a resolution of 32x32 points corresponding to a point-to-point distance of 12.5 nm. The 632.8 nm laser excites the tip with a power of 200 μ W through a 0.42 NA objective in side access (p-polarization). The Raman spectrum is recorded with an integration time of 10 s per point, leading to a total acquisition time of 3 hours. The Raman map is rendered by plotting the intensity of the G-band of the CNTs between 1550 cm^{-1} and 1650 cm^{-1} . The TERS map shows the position of the CNTs (see Fig. 4.3.1 (a)). The topography data of the same area was recorded prior to TERS mapping and is shown for comparison in Figure 4.3.1 (b).

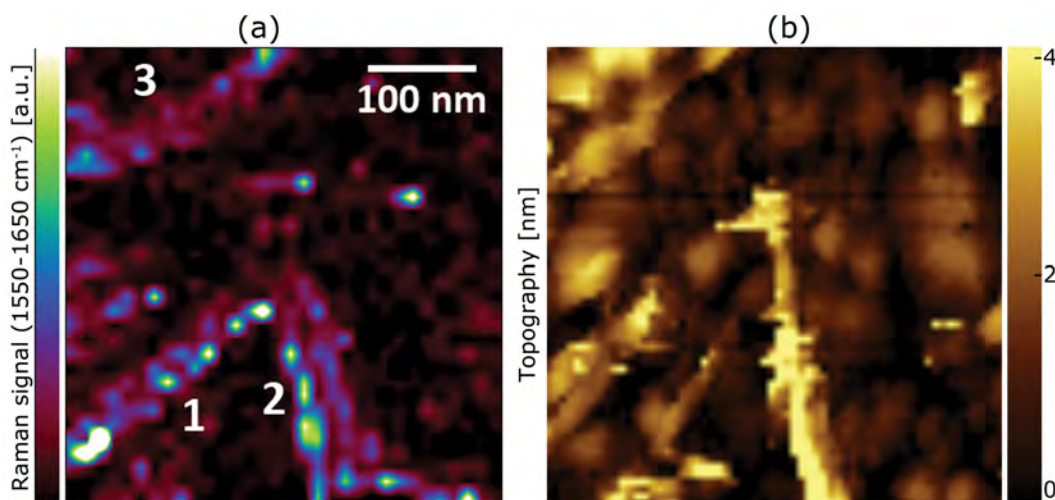


Figure 4.3.1: (a) TERS map of three CNTs on a gold substrate over an area of 400 nm x 400 nm with 32 x 32 points (interpolated). The image shows the sum of the Raman signal between 1550 cm^{-1} and 1650 cm^{-1} (spectral region of the G-band) and the CNTs are indicated by numbers. (b) Section of the same area from a topography scan that was recorded prior to TERS mapping. The CNTs appear as linear objects over the gold substrate.

The TERS map shows three CNTs, numbered 1 to 3, whose positions can be confirmed by comparison with the topography image. The CNTs do not show a constant Raman signal but instead appear as a connection of “hot-spots” where the G-band increases. This variation can be explained by the roughness of the substrate which causes varying resonance conditions for the surface plasmons at the tip and therefore a change of the enhancement factor depending on the tip position. Local topography features of the sputtered gold substrate, such as curvature, crystallinity and grain size, affect the distribution of the near-field at the apex of the tip and alter the tip enhancement leading to the appearance of hot-spots in the TERS map. The distances between these hot-spots vary between 20 nm to 50 nm, which approximately corresponds to the feature size of the sputtered gold substrate (cf.

Fig. 4.1.4). Another reason for the variations could be that the distance between the grid points is larger than the extension of the near-field at the tip and that the CNT is sometimes positioned between two TERS points without becoming visible.

We also considered the possibility that the hot-spots are the antinodes of localized surface plasmon resonances on the CNT itself. The propagation speed of surface plasmons on CNTs lies between $v_{\text{pl}} = 4 \cdot 10^6$ m/s and $v'_{\text{pl}} = 1 \cdot 10^6$ m/s [202]. This can be used to calculate the distance between two antinodes, which is half of the wavelength λ_{pl} of the plasmon. With the given excitation wavelength $\lambda_0 = 633$ nm and the speed of light $c = 3 \cdot 10^8$ m/s, the distance between two antinodes is:

$$\lambda_{\text{pl}} = \frac{1}{2} \cdot \frac{v_{\text{pl}} \cdot \lambda_0}{c} \lesssim 4.2 \text{ nm} \quad (4.3.1)$$

A size of 4 nm is, however, too small to match our findings.

Figure 4.3.2 shows three Raman spectra at different tip positions *on* and *close to* a CNT, revealing large variations in G-band intensity. On the CNT, the Raman signal of the G-band is about 5 counts above the background and increases up to 50 counts at a hot-spot. The signal from the G-band vanishes completely when the tip is displaced laterally by only 20 nm from the CNT. This distance can be considered as an approximation of the lateral resolution of the scan. The G-band signal is enhanced approximately 55 times when the tip is placed on the CNT as compared to the noise level of the background (no G-band visible). The ratio $I_{\text{near}}/I_{\text{far}} = 50$ can be used to obtain a lower estimate of the tip-enhancement factor EF according to equation 2.5.15: Given a tip radius of $r = 30$ nm, a tip-sample distance of $h = 1$ nm, and an optical excitation at $\lambda = 633$ nm through an objective with an NA of 0.42, the tip enhancement can be estimated to be at least $\text{EF} = 13,000$. This corresponds to an enhancement of the E-field by $g \approx \sqrt[4]{\text{EF}}$, giving approximately a factor of $g = 10.7$.

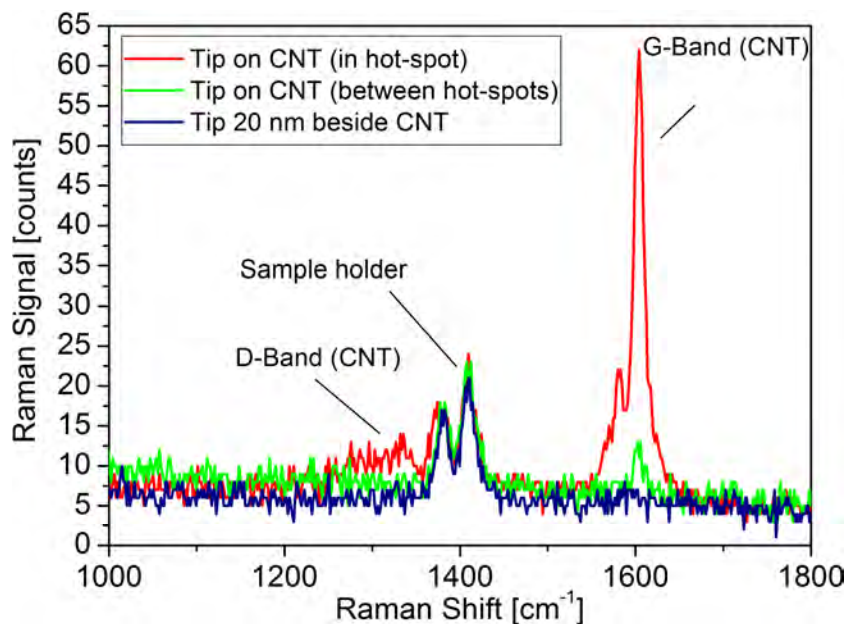


Figure 4.3.2: The graph shows the Raman spectra between 1000 cm^{-1} and 1800 cm^{-1} as a comparison of three different tip positions extracted from the TERS map. While the intensity of the G-band is strongly correlated with the position of the tip, the far-field signal, clearly visible by the peaks around 1400 cm^{-1} that stem from the alumina sample holder, is constant. Note that the Raman spectrum recorded in a hot-spot also shows an increase of the D-band.

4.4 Objective scan

In order to evaluate the required precision of the objective alignment, we acquire a side-view objective scan of the tip to measure the TERS signal while the tip is in contact with a CNT. The image is recorded by moving the focus of the objective stepwise over an area of $15\text{ }\mu\text{m} \times 15\text{ }\mu\text{m}$ with 32×32 points while a Raman spectrum is recorded for every point (1 s integration time, $200\text{ }\mu\text{W}$ laser power).

The data is visualized in Figure 4.4.1 (a) by plotting the intensity of the CNT's G-band in false color. The Raman map shows an enhancement of the Raman signal at the location where the tip touches the sample. The enhancement appears as a hot-spot with a diameter of $3\text{ }\mu\text{m}$ at the end of the tip. The cross section of the hot-spot demonstrates that the alignment between tip and objective requires sub-wavelength precision: A misalignment of only 400 nm leads to a signal loss of 50 % (see Fig. 4.4.1 (b)). This value is obtained with a 0.42 NA objective that generates a laser spot with a diameter of approximately $2\text{ }\mu\text{m}$. Objectives with higher NA require an accordingly higher alignment precision, presenting a trade-off between stability and collected signal.

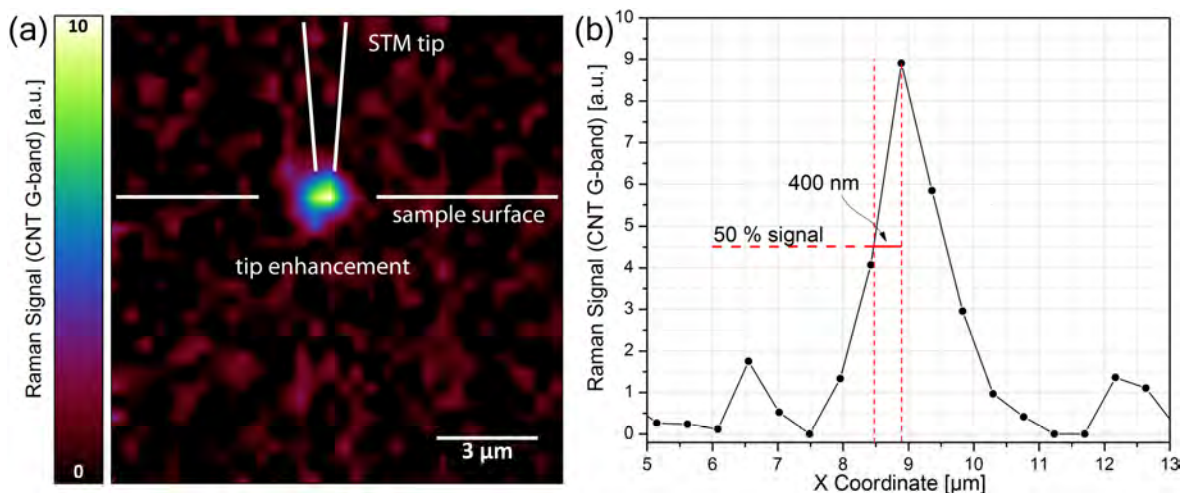


Figure 4.4.1: (a) Confocal Raman map in side view of the apex of a TERS tip in contact with a CNT. A full Raman spectrum was recorded at every point and the map was generated from the G-band signal of the CNT at 1600 cm^{-1} . (b) Vertical cross section of the TERS hot-spot at the end of the tip. The red lines indicate the distance corresponding to a 50 % signal loss.

4.5 System stability and resolution

In order to assess the lateral resolution and the system stability for long scan times, a second mapping is carried out with 64×64 points (8 nm point distance) resulting in an acquisition time of 12 h. Figure 4.5.1 (a) shows a map of the CNT's G-band amplitude after background subtraction. The map reveals several objects with a Raman signal in the respective spectral region around 1600 cm^{-1} of which at least one is an individual CNTs (marked by a green circle).

After approximately 6 hours, we observe a decrease of the Raman signal and the simultaneously recorded PMT signal (Fig. 4.5.1 (b)). The signal loss is likely due to a drift of the tip relative to the position of the objective during the acquisition time. A drift of about one micrometer can already lead to the observed signal loss of 80%, as we showed previously in Figure 4.4.1 (b).

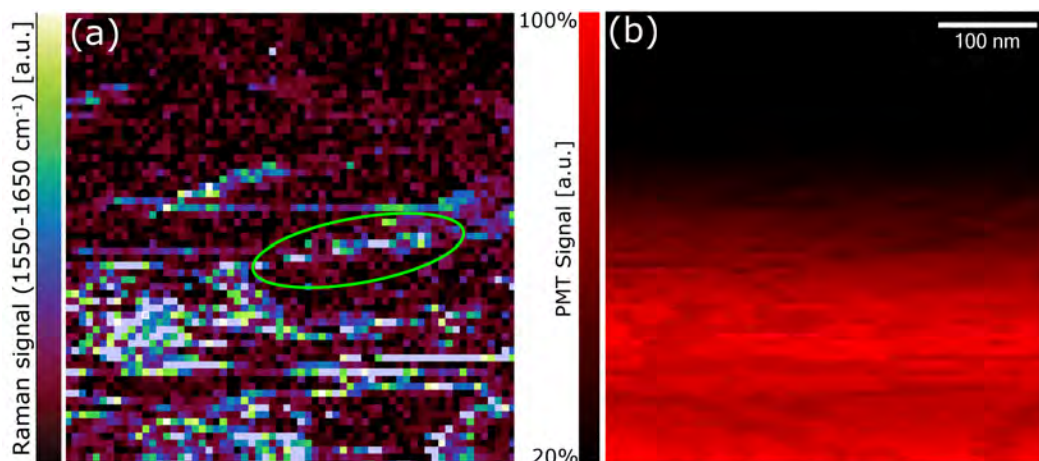


Figure 4.5.1: TERS map of CNTs on gold over an area of 500 nm x 500 nm with 64x64 points. Scan direction: Horizontal line scans from bottom to top. (a) Raman signal of the CNT G-band. (b) The simultaneously recorded PMT signal shows a signal loss of 80% over the whole scan.

The lateral resolution of the TERS map can be calculated based on the width of the optical signal of a CNT. We therefore determine the cross section of the CNT's TERS signal marked by the green circle in Figure 4.5.1 (a) over a length of 80 nm and a width of 150 nm. An average value of the G-band intensity in the TERS map is calculated for 10 lines parallel to the CNT at a distance of 8 nm. The values are plotted on the graph in Figure 4.5.2 (a) and a Gauss model is used to provide a curve fit of the cross-section. The FWHM of the fit has a size of 14 nm (± 2 nm) and can be interpreted as the lateral resolution of this scan.

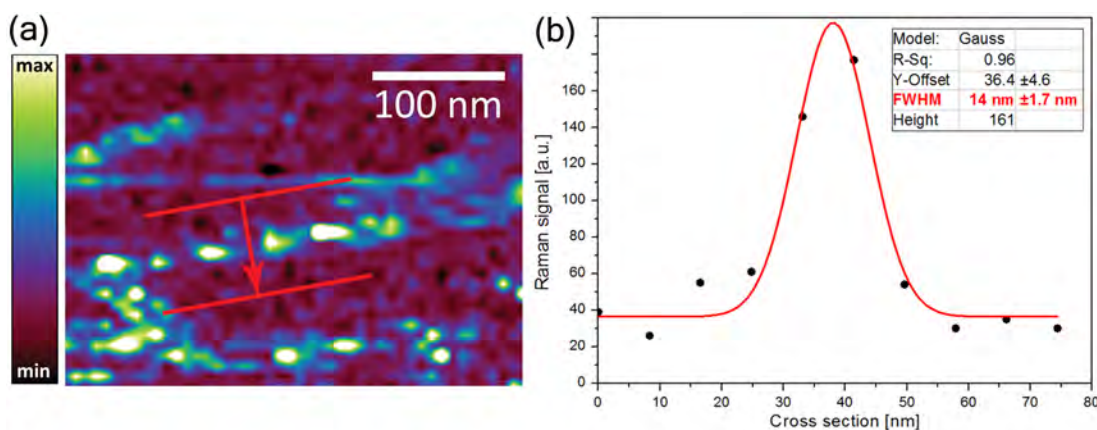


Figure 4.5.2: (a) Section of the previously acquired TERS map showing the marked CNT from Figure 4.5.1 (a). The red lines indicate the direction of the cross section plotted in (b): Intensity profile of the Raman signal of a CNT. The black dots show the average Raman intensity of the G-band at various positions along a path perpendicular to the axis of the CNT. The fit (red) has a width of 14 nm (FWHM).

4.6 Chemical sensitivity

The TERS spectrum of the CNTs contains the electronic properties of the CNT based on the shape of the G-band:

The G-band splits into a G^+ ($\sim 1600\text{ cm}^{-1}$) and G^- ($\sim 1580\text{ cm}^{-1}$) mode as shown in Figure 4.6.1. Both modes originate from the stretching oscillation of the carbon bonds, but their energies depend on the chirality and oscillation direction with respect to the CNT axis and therefore split into TO and LO modes with different energies. The ratio between the G^+ and G^- mode reveals whether the CNT is semiconducting or metallic.

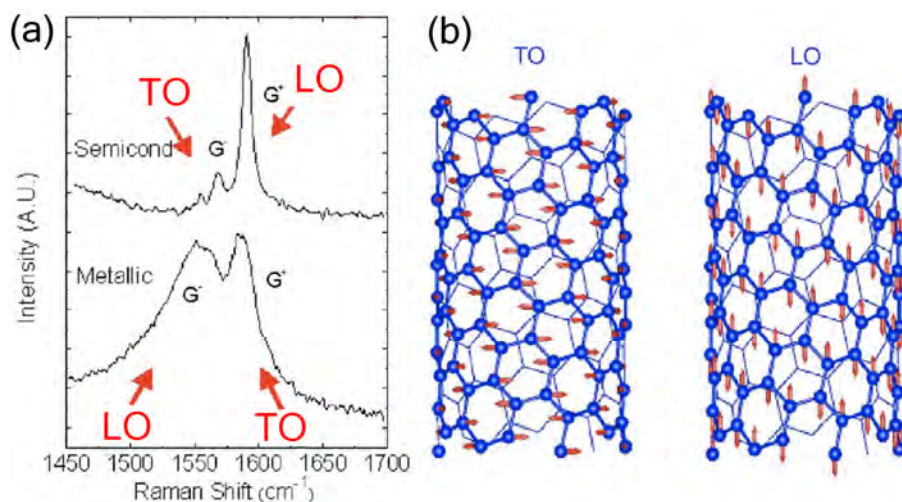


Figure 4.6.1: (a) Raman spectra of the G^+ and G^- band of a semiconducting SW-CNT and a metallic SW-CNT. Both bands appear broader in the metallic CNT. (b) Illustration of the transversal optical and longitudinal optical phonons in a SW-CNT. (Images from ref. [203] and ref. [204], respectively).

Based on the shape of the G-band, we can conclude that the TERS spectrum in Figure 4.3.2 shows the scattering of a semiconducting CNT. According to the Kataura plot (Fig. 4.1.6), the diameter of semiconducting CNTs that can be excited at the wavelength of 633 nm (1.96 eV) lies between 0.5 nm and 0.9 nm. Because the topography image shows a larger diameter, the CNT must be part of a bundle of CNTs, confirming our initial assumption.

Figure 4.6.2 shows the TERS spectra of a metallic (red graph) and a semiconducting (black graph) CNT. Both spectra were extracted from the TERS map in Figure 4.5.1 (a). The metallic CNT has a diameter of approximately 1.3 nm according to the Kataura plot. The spectrum of the metallic CNT also reveals a radial breathing mode at about 190 cm^{-1} which confirms the diameter of 1.3 nm (see eq. 4.1.1). The semiconducting CNT is too thin to exhibit an RBM.

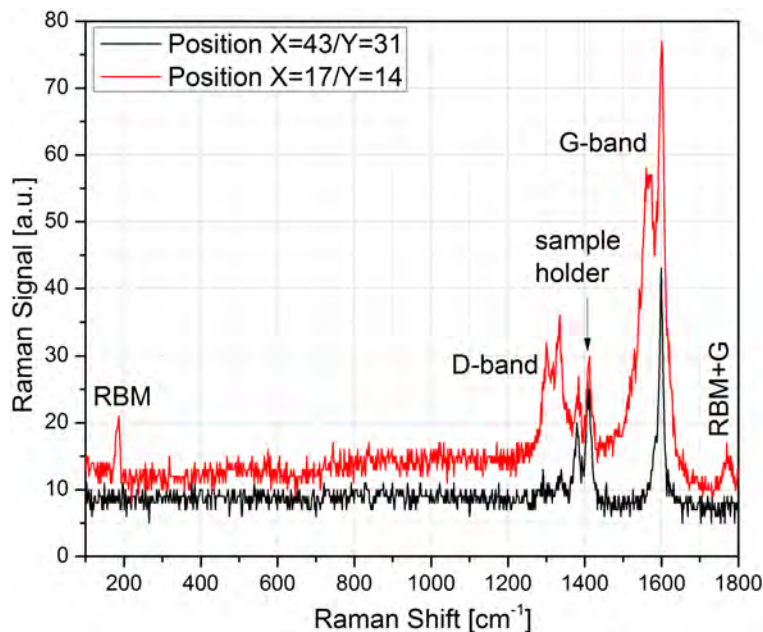


Figure 4.6.2: TERS Raman spectrum at two different positions of the Raman map from Fig. 4.5.1 (a). The red graph shows the RBM, the D-band and the G-band with a higher intensity than the CNT presented in the black graph. The given coordinates correspond to the pixels of the TERS map with the origin (0/0) located in the bottom left corner.

4.7 Summary

We identified a suitable method to deposit CNTs on a sputtered gold substrate in order to prepare a reference sample for TERS. This sample can be used for the alignment between tip and objective to maximize the TERS signal when the tip is in contact with a CNT.

We conducted a side view objective scan of the Raman signal from the tip, which showed the requirement of subwavelength precision for the alignment process. A misalignment over time, most likely caused by thermal drift, was observed during a 12 hour TERS mapping and led to an 80 % decrease in the TERS signal. This underlines the importance of a precise objective alignment and of a very stable microscope for long-lasting scans.

Based on the TERS signal across the diameter of a CNT, we determined the lateral resolution of the TERS scan to be around 14 nm, which is about 60 times below the diffraction limit of our confocal setup. The TERS maps, however, show a variation in the TERS signal intensity along the CNTs where a constant signal was expected. These variations are presumably related to the roughness of the gold substrate that leads to varying geometric conditions between tip and substrate during mapping. This shows that the investigation of nano-objects by TERS requires very smooth substrates because the plasmon resonance on the tip is very sensitive to perturbations in the distribution of the electric field at the tip apex.

We also successfully determined the diameter and electronic properties of the CNTs based on the position of the RBM and the shape of the G-band in the TERS spectra. These observations were in excellent agreement with the Kataura plot.

5 TERS on lead titanate nano-crystals

The following TERS experiments are conducted on a platinized silicon substrate that was patterned with ferroelectric lead titanate (PbTiO_3) nano-islands. The individual islands were epitaxially grown with a diameter of about 100 nm, a thickness of 30 nm, and at distances of 250 nm. This sample geometry is well suited to investigations with TERS because the grains are too small to provide a Raman signal with conventional confocal spectroscopy but are still large enough to be ferroelectric. Their nanometric size allows for testing of the chemical sensitivity and the lateral resolution of TERS on ferroelectrics, while the low density of 10 islands per μm^2 (20 % area coverage) generates effectively no far-field background that would otherwise interfere with the tip signal.

The first three sections of this chapter contain the description, preparation and characterization of the ferroelectric lead titanate nano-islands. The PbTiO_3 islands are analyzed by AFM and PFM to measure the size and thickness of the islands and to confirm that the islands are in the ferroelectric state. Confocal Raman spectroscopy on a dense PbTiO_3 film is carried out to obtain a reference Raman spectrum of the material. The fourth section covers the development of quartz tuning fork AFM probes with TERS tips. Tuning fork AFM allows for scanning the non-conductive lead titanate crystals with electrochemically etched tips. The fifth section describes the TERS mappings on the lead titanate crystals. It is followed by the interpretation and discussion of the results in section 5.6, including a comparison with finite-difference time-domain (FDTD) simulations that support our findings.

5.1 The superparaelectric limit

Lead titanate exhibits a phase transition between the ferroelectric (polar) and paraelectric (non-polar) phase at about 490 °C for bulk crystals (see section 2.8). The phase-transition temperature is accessible by Raman spectroscopy through the energy shift of the phonon modes when the crystal structure changes between the ferroelectric phase (tetragonal) and paraelectric phase (cubic). Burns et al. investigated the behavior of the phonon modes in the ferroelectric phase of PbTiO_3 at temperatures between 20 °C and 500 °C [137, 205]. Their findings showed a shift of the phonon modes towards lower wavenumbers with increasing temperature and an increased damping which eventually leads to the disappearance of the Raman peaks upon the transition to the paraelectric phase [206].

For small crystals (diameter < 50 nm), the transition temperature becomes size dependent and decreases with smaller grain size [141]. Below a specific size, referred to as the *superparaelectric limit* in analogy to the superparamagnetic limit, the ferroelectric phase becomes unstable primarily due to strong depolarization fields generated by surface charges. This leads to a size-driven phase transition from the ferroelectric to the paraelectric phase [207, 208]. The size of the superparaelectric limit and its dependence on the environment, such as surface charges, or the lattice

structure and orientation of the substrate, are still subject of investigation. A deeper understanding of the size effects is not only of interest for fundamental research, but also important for the scaling of ferroelectric materials in nanoelectronics, e.g. for the development of ferroelectric memories.

Ishikawa et al. used Raman spectroscopy to determine the transition temperature of PbTiO_3 powders with grain sizes as small as 22 nm [141]. Figure 5.1.1 shows the temperature at which the Raman mode $E(1\text{TO})$ disappears²⁹ as a function of the diameter D of the particles. The values were fitted by Ishikawa based on the assumption that the change of the transition temperature $\Delta T_0(D)$ scales with $1/D$ [209]. His findings suggest that at room temperature, the PbTiO_3 crystals lose their ferroelectric properties below a size of 13 nm³⁰.

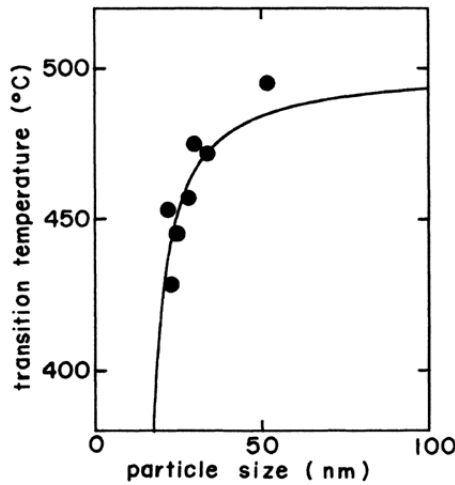


Figure 5.1.1: Transition temperature vs. particle size in lead titanate: The experimental values (black points) were determined by the disappearance of the $E(1\text{TO})$ Raman mode and fitted by the expression $T_0 = 500 \text{ }^\circ\text{C} - 588.5 \text{ }^\circ\text{C nm}/(D - 12.6 \text{ nm})$ (solid line). (Figure taken from ref. [141].)

When ferroelectrics are epitaxially grown on metallic substrates, such as thin films on a platinum bottom electrode for applications in nanoelectronics, the electrode compensates the surface charges of the ferroelectric, stabilizing the ferroelectric phase even below sizes of 13 nm. Aside from the challenges of the controlled fabrication of ferroelectric nanostructures, it is difficult to characterize the functional properties of the nano-crystals. The use of confocal Raman spectroscopy on individual ferroelectric nano-crystals grown on a substrate is hindered by the small volume of the crystals and the limited resolution of the confocal objective. For small ferroelectric samples, the method of choice has been piezoelectric response force microscopy (PFM) because it allows for the determination of the piezoelectric

²⁹ The transversal optical mode $E(1\text{TO})$ is associated with the oscillation of the central ion relative to the oxygen octahedron. Its damping can be explained by a reduction of the restoring forces when the perovskite structure undergoes a phase transition from the ferroelectric to the paraelectric phase [137].

³⁰ This value refers to the diameter of monodisperse nanograins. It does not take into consideration the strong anisotropy effects in c -axis oriented thin films which stabilizes the polar axis.

properties of crystals on the nanoscale (see section 2.1.4). The superparaelectric limit, however, takes place at film thicknesses that are difficult to access by PFM either because the piezoresponse is below the detection limit or because the applied fields exceed the breakdown voltage of such ultrathin films. Furthermore, PFM can only provide negative evidence for the superparaelectric limit since the *absence* of piezoresponse must be used as measure for the phase change.

For this matter, TERS can provide an alternative to PFM because it locally increases the light intensity, generating enough Raman scattering in nanometric volumes to produce Raman spectra that reveal the structural state of the crystal. In lead titanate, some Raman modes undergo a blue-shift when the crystal structure approaches its phase transition. This shift could be used to extrapolate the superparaelectric limit. Furthermore, the high lateral resolution of TERS allows for the analysis of structural variations within an individual ferroelectric nano-crystal³¹.

5.2 Sample preparation

The following experiments are carried out on two lead titanate samples. For the confocal Raman reference measurements, a 100 nm thin film was prepared by chemical solution deposition (CSD) [211-213]. A precursor solution was spin-coated on the surface of a platinized silicon substrate (Si/SiO₂/TiO₂/Pt) and subsequently tempered for crystallization by rapid thermal annealing. The columnar growth led to a film of single-crystalline islands with different crystallographic orientations and diameters in the range of several hundred nanometers. This sample was produced by Ann-Christin Dippel and will be referred to as PbTiO₃ thin film.

The fabrication of lead titanate nanostructures suited for the TERS measurements and with sizes close to the superparaelectric limit is more complicated. Roelofs et al. used a chemical solution deposition (CSD) process (see Sec. 5.2) with a highly diluted precursor solution to generate small lead titanate islands of diameters between 20 nm and 200 nm [65]. These islands showed an undirected growth with a preferential nucleation at the grain boundaries of the platinum substrate. Furthermore, Bühlmann et al. and Clemens et al. discovered that lead titanate also exhibits a preferential nucleation on TiO₂ [54, 214, 215]. They used this effect for a more controlled approach by patterning a platinum substrate by nano-lithography with TiO₂ grains that acted as seeds for the nucleation of PbTiO₃ islands during a subsequent CSD process. By this method, the resulting island size can be controlled by the seed size and concentration of the precursor solution:

TiO₂ islands were deposited on the platinum surface of a Si/SiO₂/TiO₂/Pt(111) substrate. During the subsequent CSD process, the substrate was spin-coated with the precursor and growth of the lead titanate occurred only at the positions of the previously deposited TiO₂ nucleation seeds. It is assumed that the TiO₂ seeds

³¹ TERS was conducted on ferroelectric BaTiO₃ crystals with a size of several hundred nanometers by Berweger et al. but only for phonon energies above 400 cm⁻¹ [210], while size effects would occur mainly below this energy [206].

completely dissolved during the growth of the lead titanate islands. The result is a rectangular pattern of triangular, 30 nm thick lead titanate islands. This sample, referred to as lead titanate islands, was prepared by Sven Clemens and the production process is illustrated in Figure 5.2.1.

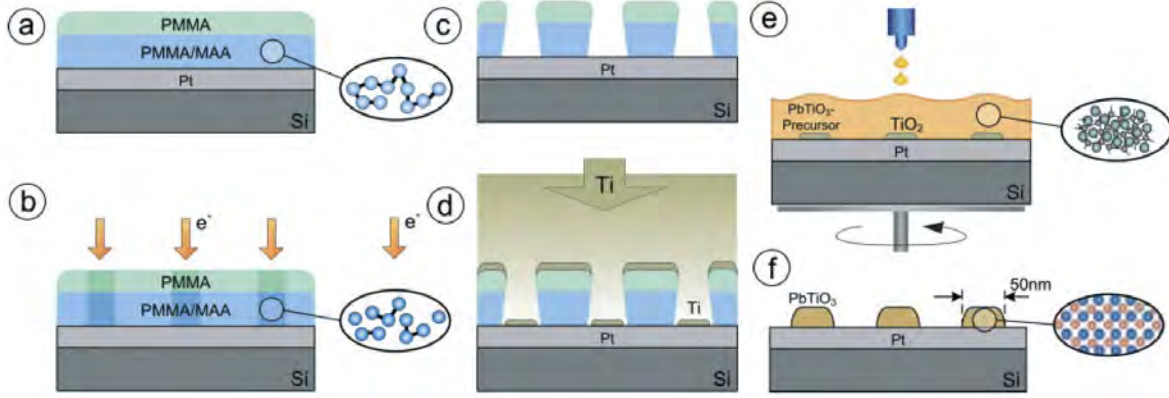


Figure 5.2.1: Illustration of the PbTiO_3 nano-island growth by TiO_2 seeding with photolithography. a) The photo resist was spin-coated on a silicon substrate with a 100 nm thick (111)-platinum layer. b) Electron beam lithography was used to pattern the resist. c) After development, an undercut resist profile was obtained as the lower resist had a higher electron sensitivity. d) A 2 nm thin titanium layer was evaporated on the mask before the resist was removed by a solvent (lift-off). e) The highly diluted PbTiO_3 precursor solution was spin-coated on the seeded substrate and dried on a hot plate which resulted in an amorphous layer of PbTiO_3 . f) The layer was crystallized at 700 °C and small PbTiO_3 islands were obtained on the nucleation sites. (Taken from ref. [54].)

5.3 Preliminary sample characterization

In this section, AFM and PFM are used to verify the size and crystallinity as well as the ferroelectric state of the PbTiO_3 nano-islands. A reference Raman spectrum of a thin film prepared by CSD is acquired by confocal Raman spectroscopy and the Raman modes are assigned to the lattice vibrations of the crystal.

5.3.1 AFM topography scans

Two topography scans of the PbTiO_3 islands on the platinum sample are measured in tapping-mode AFM. The larger scan covers an area of $5 \mu\text{m} \times 5 \mu\text{m}$ and shows the pattern of the seeded PbTiO_3 islands (see Fig. 5.3.1 (a)). The islands grew in various shapes due to imperfect crystallization. A second scan on an area of $1 \mu\text{m} \times 1 \mu\text{m}$ shows the triangular shape of the islands that indicates their epitaxial growth mode (see Fig. 5.3.1 (b)). The islands have a side length of about 100 nm and a defined distance of 250 nm. Their thickness is about 30 nm, with steep side walls and a flat surface. Some islands, however, are round or thin due to imperfect crystallization and might be partially or completely amorphous.

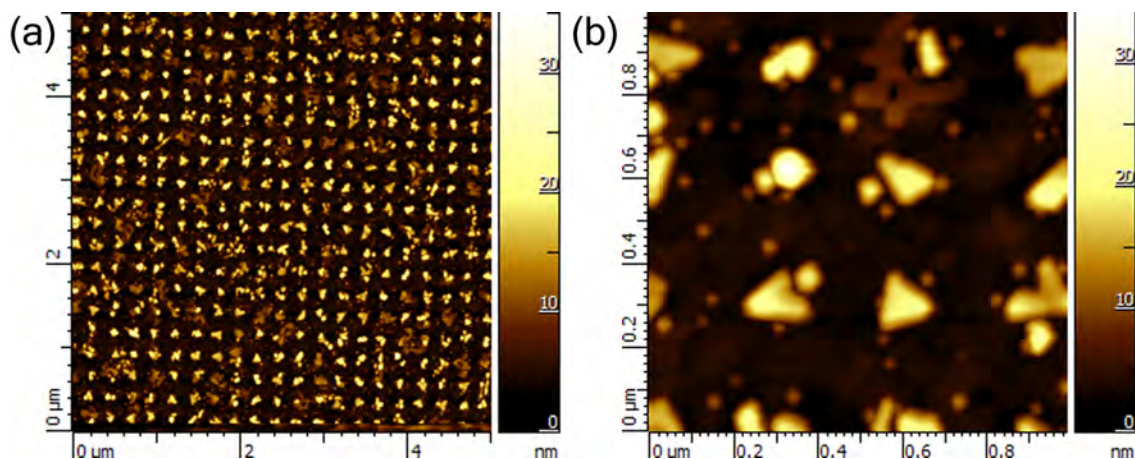


Figure 5.3.1: Tapping mode AFM topography scans on the seeded PbTiO_3 islands. (a) $5 \mu\text{m} \times 5 \mu\text{m}$ scan that shows the geometric arrangement of the islands. (b) $1 \mu\text{m} \times 1 \mu\text{m}$ scan that reveals the details and orientation of the grains.

5.3.2 Piezoelectric measurements

In order to get a better understanding of the piezoelectric response of the islands, and to confirm their ferroelectric switching, the sample is characterized by piezoresponse force microscopy (PFM).

PFM relies on an electrical point contact through a metalized atomic force microscopy tip to excite and to sense the local piezoelectric response (see section 2.1.4). Therefore, the lead titanate nano-islands are scanned in contact mode AFM with a conductive cantilever³² that applies an alternating voltage with an amplitude of 1.5 V while the platinum substrate is electrically grounded. The frequency is chosen to equal the contact resonance of the cantilever at 360 kHz. Figure 5.3.2 shows an image of the PFM amplitude of several islands in comparison to the simultaneously acquired topography.

Piezoresponse is only detected on the nucleation sites of the islands and additional topography features are inactive. The piezoresponse appears unequally distributed over the islands with a pronounced response on the perimeter while the centers are less active. Clemens et al. observed a similar behavior on islands that were produced in the same way but were subsequently embedded in a low-k dielectric and polished down to achieve electrical contact to the islands [214]. Although their explanation focuses on a residual insulating layer on the top of the islands, our experiment shows a similar piezoelectric response on the non-embedded islands. A possible explanation is that the columnar growth started simultaneously at the corners of the TiO_2 seeds and led to less tetragonal and thus less piezoelectric grain boundaries in the middle of the lead titanate islands. The PFM image also shows that the island on the bottom right corner is not piezoelectric. In topography, the island has a triangular shape that appears to consist of three grains, one at each

³² ANSCM-PT from *AppNano Inc.*, 25 nm PtIr coating, spring constant of 3 N/m, $f_0 = 60$ kHz frequency

corner, and the grain boundaries are slightly lower. The lateral response of this island (not shown) was silent as well.

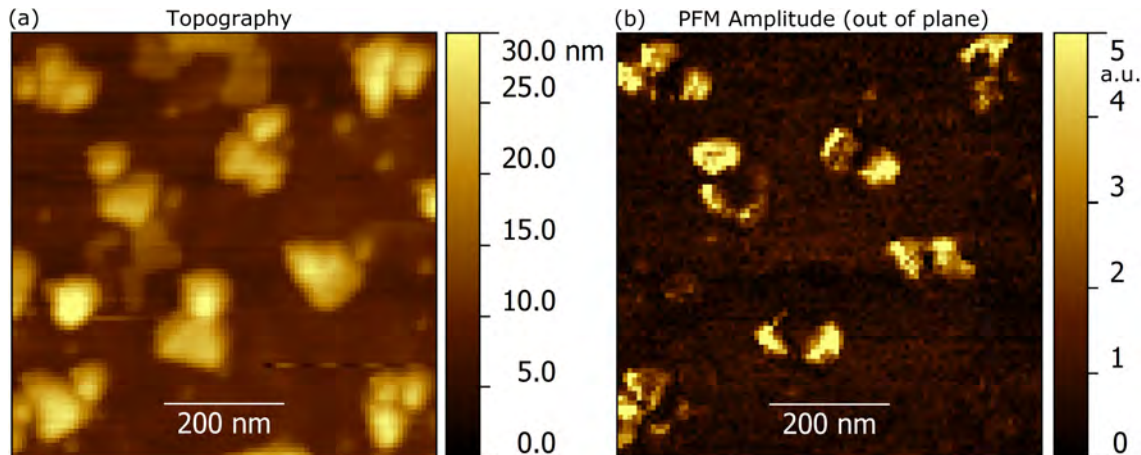


Figure 5.3.2: PFM scan of lead titanate nano-islands. The AFM topography image (a) was recorded simultaneously with the vertical piezoresponse shown in (b). The amplitude of the piezoelectric response is strongest on the side of the islands and decreases towards their center. Not all topography features and islands appear to be piezoelectric in the PFM image.

In a second experiment, PFM is used to confirm the ferroelectric switching of the islands by recording a hysteresis curve. Therefore, the cantilever is placed on an island and pulses of different voltages between -7 V and 7 V are applied to switch the polarization. After every pulse, the vertical phase of the piezoresponse is measured to check whether the polarization under the tip was switched. The plot of the phase as a function of the switching voltage creates a hysteresis curve that shows the positive and negative switching voltages (coercive fields) (see Fig. 5.3.3). The hysteresis curve confirms that the PbTiO_3 nano-islands are ferroelectric and that the polarization switched at -4 V and $+3$ V. The asymmetry between the switching voltages is referred to as imprint and is caused by an asymmetry between the bottom electrode (platinum film) and top electrode (AFM tip).

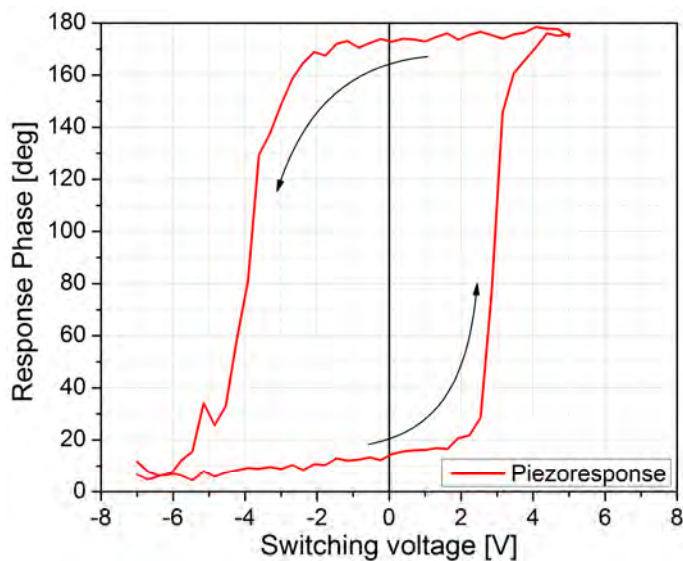


Figure 5.3.3: Ferroelectric hysteresis curve measured on a single island by PFM. The switching appears around +3 V and -4 V and approaches 180° and 0°, respectively.

5.3.3 Confocal Raman measurements

Bulk lead titanate crystals were extensively analyzed by Raman spectroscopy in the past [137, 205, 206, 216, 217]. The structural change from tetragonal to cubic, which is associated with the phase-change from the ferroelectric to the paraelectric phase, leads to strong damping of the Raman modes which are thus no longer visible in the paraelectric phase. The energy of the phonon modes in the ferroelectric phase of lead titanate is known to be temperature- [137, 206], pressure- [216], and size-dependent [141, 207]. In particular, the Raman signature of lead titanate is reported to be undetectable

Generally, phonon modes are more strongly damped and shift to lower energies when the lead titanate in its ferroelectric phase approaches the phase-change temperature. Before using TERS to analyze the Raman spectrum of the lead titanate nano-islands, the confocal Raman spectrum of a 100 nm thick and dense lead titanate thin film, which was produced by CSD, is measured to obtain a reference spectrum. Therefore, the thin film sample is placed in the focus of a 0.7 NA objective and excited at a wavelength of 632.8 nm in confocal top access with a power of 0.4 mW. Two spectra between 70 cm^{-1} and 1800 cm^{-1} (600 lines/mm grating) are recorded, each with a 10 minute integration time and summed up after the removal of cosmic events. The long integration time is necessary because of the small film thickness in order to achieve a sufficient signal-to-noise ratio. Figure 5.3.4 shows the recorded spectrum.

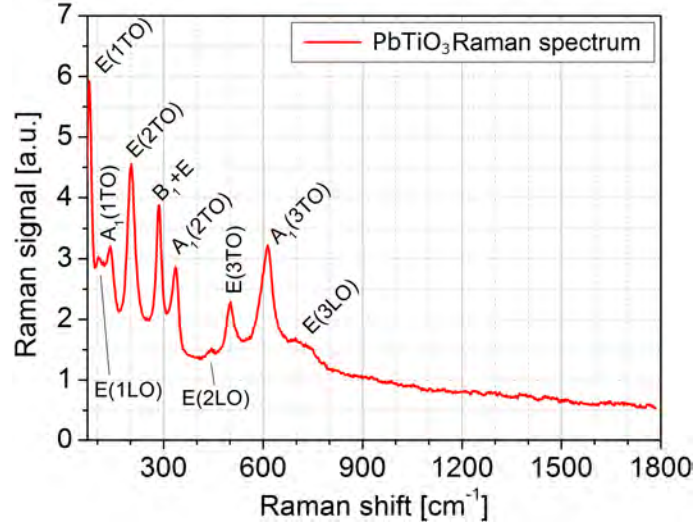


Figure 5.3.4: Confocal Raman spectrum of a 100 nm PbTiO_3 thin film (632.8 nm excitation). The phonon modes were identified by comparison to published results in refs. [205, 217].

The peaks were identified by comparison to the spectra of lead titanate crystals published by Burns et al. [205] and Chingprado et al. [217]. The phonon modes in our thin film show a shift towards low wavenumbers in comparison to the literature. This shift is probably caused by the smaller grain size in our thin film. By AFM, we determined the size of the majority of the grains to be between 100 and 300 nm. A comparison of the identified Raman peaks is presented in table 1.

Phonon mode	Chingprado [217] 0.6 – 1.2 μm thin film	Burns [205] bulk crystal	Our thin film 100 nm thickness
E(1TO)	88	89	74
E(1LO)	128	128	106
$A_1(1\text{TO})$	149	127	138
$A_1(1\text{LO})$		215	<i>too weak</i>
E(2TO)	220	221	201
B_1+E	289	290	285
$A_1(2\text{TO})$	359	364	335
E(2LO)+ $A_1(2\text{LO})$	440	445	442
E(3TO)	506	508	500
$A_1(3\text{TO})$	644	651	613
E(3LO)	687	717	~ 700
$A_1(3\text{LO})$	794	797	<i>too weak</i>

Table 1: Phonon modes in ferroelectric PbTiO_3 measured by Raman spectroscopy in cm^{-1} . The table shows the comparison between the phonon modes reported in literature with the findings in our thin film. A crystallographic description of the modes is given in references [138, 206].

5.4 Tuning fork AFM measurements

Lead titanate has a bandgap of 3.2 eV and is therefore electrically insulating which limits the use of STM as a scanning probe technique for TERS experiments. Insulating samples, however, can be scanned by AFM with silicon cantilevers or with etched metal tips on quartz tuning forks. In order to take advantage of the previously developed etching process of gold tips, we decided to use tuning fork AFM in shear-force mode for the TERS experiments on lead titanate. In this section, we describe the preparation of tuning fork probes that provide stable scanning conditions over long measurement periods as required for TERS mapping.

5.4.1 Probe preparation

Quartz tuning forks are primarily used as frequency generators in electronic circuits. They are typically contained by a sealed metallic cylinder under vacuum to decrease friction losses during oscillation in order to maintain high quality factors. For AFM, the metallic cylinder has to be removed³³ and a tip has to be fixed to one of the prongs.

The industrial parameters of tuning forks are: the resonance frequency, the capacitance, the quality factor (Q-factor), and the outer dimensions of the cylinder. Typically not specified, but of equal importance for usage in microscopy, are the size of the fork, the shape of the prongs, and the relative orientation between the prongs and the electric contacts. The shape of the prongs varies because the forks are usually shortened to tune the resonance frequency during the production process. For tuning, most manufacturers polish the prongs under a 45°-angle, making it difficult to attach the TERS tips. The orientation of the electric contacts determines the orientation of the fork in the AFM and must be in line with the oscillation direction of the excitation piezo. Therefore the forks should be chosen according to the design of the AFM head.

In our setup, the electric contacts of the tuning fork are soldered to electrodes on a fiberglass plate that is mounted to the AFM head which contains the excitation piezo. The solder connection is typically strong enough to provide sufficient mechanical coupling to the fork. To fulfill the above-mentioned criteria, all experiments in this thesis are performed with an *AB38T-32.768KHZ* fork from *Abrakon Corporation*. This fork has 4 mm long prongs with a free resonance frequency of about 32 kHz and a Q-factor of 7000 under ambient conditions³⁴.

The crucial step of the probe preparation is to attach the tip to the tuning fork. After etching (see section 3.2), the tips are shortened to a length of about 300 μm with a razor blade under observation through a 20X stereo loupe (placing the tip on a soft base, such as insulation tape, facilitates the handling during cutting). A small tip mass is important in order to avoid affecting the Q-factor of

³³ The cylinder can be removed by lightly squeezing the perimeter around the base-plate with a pair of pliers, loosening the seam so that the fork can be pulled out.

³⁴ Resonance frequency in vacuum: 32,768 Hz (2^{15} Hz).

the fork by inducing an imbalance between the two prongs³⁵. Attaching the tip to the fork can be done with either UV-curable glue, when short curing times are required (e.g. for silver tips), or acrylic glue, which requires a 24-hour curing period. For gold tips, we use acrylic glue because it can be dissolved quickly by acetone when the tip needs replacing.

The tips are glued under observation with a stereo loupe. Cyanoacrylate glue is applied to one prong of the tuning fork that is then used to pick up the tip. At a viscosity of 1000 cP or higher, the glue provides enough surface tension to pick up the tip and to keep it in place during the curing period. Figure 5.4.1 shows a photo of a tuning fork (with attached gold tip) that is soldered to the holder plate.

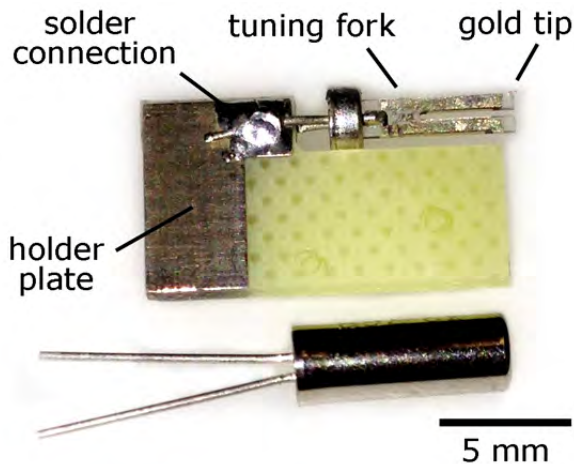


Figure 5.4.1: (top) Tuning fork soldered on the carrier plate of the AFM. A small gold tip is attached to the fork. (bottom) Original tuning fork encapsulated in its metal cylinder.

5.4.2 Quality factor

The stability and image quality of tuning fork AFM depends on the quality factor (Q -factor or Q) of the tuning fork. The Q -factor describes the ratio between the energy stored in the oscillator and the energy dissipated per oscillation cycle, and is defined as the full width at half maximum (FWHM) of the resonance peak in the power spectrum divided by the resonance frequency f_0 . The power spectrum describes the square of the oscillation amplitude as a function of the frequency and thus the Q -factor is given by:

$$Q = \frac{\text{FWHM of Amplitude}^2}{f_0} \quad (5.4.1)$$

A high Q -factor allows for the detection of small tip-sample interaction forces, while a low Q -factor implicates a broad resonance peak and compromises the AFM

³⁵ The high Q -factor of a tuning fork is related to its symmetric construction which assures that the center of mass remains still during the oscillation of the prongs. Adding a mass on one side of the fork induces an imbalance and hence leads to a lower Q -factor.

feedback. The feedback is controlled by a PLL-controller that measures the frequency shift of the tuning fork to determine the tip-sample distance and thus requires a narrow resonance peak. As we will see later, a frequency shift of -2 Hz with respect to the free resonance frequency indicates a tip-sample distance of about 1-2 nm. Our experiments show that the PLL-controller can measure the resonance frequency with sufficient accuracy for a resonance width of 30 Hz (FWHM). Consequently, 30 Hz is the upper limit for the resonance width of the tuning fork to obtain stable scanning conditions, corresponding to a Q-factor of about 1500.

When the tip is glued to the fork, the additional mass induces an imbalance between the prongs, leading to a reduced Q-factor in comparison to the oscillation of an unmodified tuning fork. In order to determine the upper limit of the tip mass that can be glued to the tuning fork before the Q-factor drops below 1500, a series of measurements with three different tip sizes is carried out. Every experiment is repeated with five tuning forks and the Q-factors are determined by equation 5.4.1 by measuring the oscillation amplitude as a function of the excitation frequency.

Tips with a diameter of 200 μm and a length of 1 mm result in a Q-factor of about 150 which is too low for stable scanning conditions. Series 2 is carried out with bonding-wire that has a diameter of only 30 μm and results in Q-factors of about 5100. The handling of such thin wires, however, is very difficult because the tips are barely visible by eye, making the etching and gluing procedure challenging. We decided to use a wire with a diameter of 100 μm but reduced the tip length to 0.3 mm. This allows for Q-factors of about 6500. The experimental results are shown in Table 2.

	Tip Diameter	Tip-Length	Tip mass	Q-factor
Free tuning fork				7000 ± 500
Series #1	200 μm	~ 2.0 mm	~ 1200 μg	150 ± 50
Series #2	30 μm	~ 2.0 mm	~ 30 μg	5100 ± 1000
Series #3	100 μm	~ 0.3 mm	~ 50 μg	6500 ± 900

Table 2: Average Q-factors (including variance) depending on the size of the tip that is attached to one prong of the tuning fork. A large tip mass leads to a reduction of the Q-factor.

Frequency drift over time

During the above described experiments, an increase in resonance frequency of several Hertz per minute was observed for tuning forks with low Q-factors. Since a change of the resonance frequency during scanning is interpreted by the microscope as a change in the tip-sample distance, such a frequency drift can affect the scanning stability. When the resonance frequency shifts to higher values, the feedback loop compensates for the shift by bringing the tip closer to the sample. This leads to an increase in shear-forces and causes damage to the tip. The dependence between the

frequency shift and the Q-factor of tuning forks with different tip sizes is therefore investigated systematically.

The shift of the resonance frequency is measured over 5 minutes during the mechanical excitation of the tuning forks with different tip masses attached to them. The plot in Figure 5.4.2 shows a strong correlation between the Q-factor of the tuning fork and the rate at which the resonance frequency increases. Q-factors below 1500 show a drift of the resonance frequency of 1 Hz/min. This could result in tip-crashes within a few minutes after landing the probe on the sample.

It might be that the imbalance due to the tip mass affects the structure of the quartz crystal or the glue in such a way as to lead to a stiffening of the oscillator and consequently to an increase of the resonance frequency. The effect of an increasing stiffness under deformation is, for example, known from metallic crystals as *work-hardening* and used to introduce perpendicular slide-planes that lead to a higher elastic modulus of the metal.

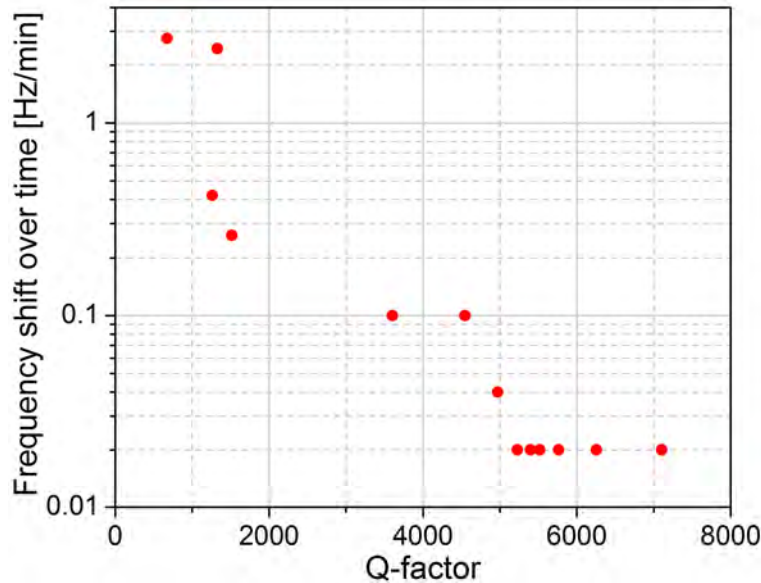


Figure 5.4.2: Semi-logarithmic plot of the drift rate of the resonance frequency for tuning forks with different Q-factors (various tip masses). The forks were excited with an oscillation amplitude of 1 nm for a period of 5 min and the frequency was measured before and after this period with a precision of 0.1 Hz. The plot shows that the drift rate increases with small Q-factors. Forks with Q-factors of 5000 or higher show a drift of less than 20 mHz/min (upper limit).

Our experiments show that 300 μm long tips made from 100 μm thick gold wire lead to Q-factors of about 6500. The resonance frequency of these probes is confirmed to be stable with a drift of less than 1 Hz/h, which qualifies them for long TERS mappings of well over several hours.

5.4.3 Oscillation amplitude

The oscillation amplitude of the tuning fork must be kept small during scanning because it has direct influence on the lateral resolution in shear-force mode

where the tip oscillates parallel to the surface. In order to measure the amplitude, the tuning fork is placed in front of an optical microscope and the objective is focused on the end of the tip. The tip position can be resolved with a resolution of about $0.5\ \mu\text{m}$ (NA 0.7 objective). The tuning fork is mechanically excited at its resonance frequency while the excitation amplitude is increased. With an excitation amplitude of 500 a.u., the tip apex blurs to a size of about $1\ \mu\text{m}$ ($\pm 50\%$). This size can be interpreted as the peak-to-peak oscillation amplitude. Stable scanning, however, is already possible with an excitation of 0.2 a.u. allowing for an amplitude of only $400\ \text{pm} \pm 200\ \text{pm}$ ³⁶. Such low oscillation amplitudes have no negative impact on the lateral resolution during scanning.

5.4.4 Tuning fork topography scans

The AFM is operated in tuning fork shear-force mode in order to oscillate the tip parallel to the sample's surface. This is advantageous for TERS because the tip-sample distance remains constant throughout the oscillation cycle.

The sample is scanned by a PLL-controller that keeps the shift of the resonance frequency of the tuning fork constant at -2 Hz (relative to the resonance frequency before landing) by varying the vertical position of the tip relative to the sample. The oscillation amplitude of the tuning fork is kept constant by an independent feedback-loop. Because the TERS scan does not require high scanning rates but a cautious treatment of the tip, the feedback parameters are optimized for a stable operation at slow scanning speeds, typically of 0.2 lines/second. These settings successfully avoid vertical overshooting of the tip at topography edges and reduce feedback oscillations.

Figure 5.4.3 shows a tuning fork topography scan on incompletely crystallized PbTiO_3 islands. The islands provide very small surface features the scanning of which underlines the high lateral resolution of the shear-force mode.

³⁶ We used the electronic response of the tuning fork to verify the linearity between the mechanical excitation and the oscillation amplitude. Non-linearity was found to be below 7 % over an excitation range from 0.4 nm to 1000 nm.

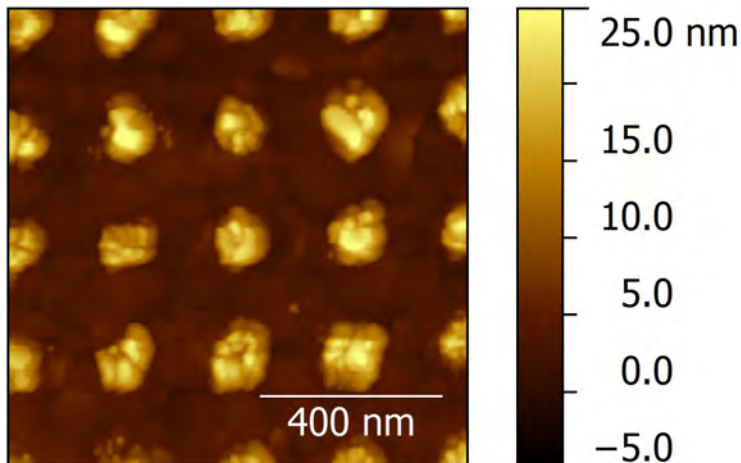


Figure 5.4.3: Shear-force mode AFM topography image with a tuning fork probe equipped with an electrochemically etched gold tip made from 100 μm thick wire. The scan was carried out at a line speed of 0.2 lines/sec and at a frequency setpoint of -2 Hz. The image shows imperfectly crystallized PbTiO_3 islands on a platinum substrate. The sample stems from the experiment series of the TiO_2 -seeded growth of lead titanate islands (see section 5.2).

5.4.5 Tip-sample distance

In order to evaluate the tip-sample distance, a landing curve is recorded using a gold tip on a platinum surface. The oscillation amplitude of the tuning fork is plotted as a function of the vertical position of the tip in Figure 5.4.4 (a). We assume that the tip touches the sample when the amplitude reaches zero and thus the vertical tip-sample distance is calibrated accordingly. This is a common assumption also used to measure the oscillation amplitude in vertical non-contact AFM.

In a second landing curve, the frequency shift of the tuning fork is measured as a function of the tip-sample distance (see Figure 5.4.4 (b)) while the distance is calibrated based on the previous amplitude measurement. At a resonance-frequency shift of -2 Hz, the tip has a distance of approximately 1.5 nm to the sample. The following TERS experiments are carried out with frequency setpoints between -2 Hz and -6 Hz, corresponding to tip-sample distances between 1.5 nm and 1 nm, respectively.

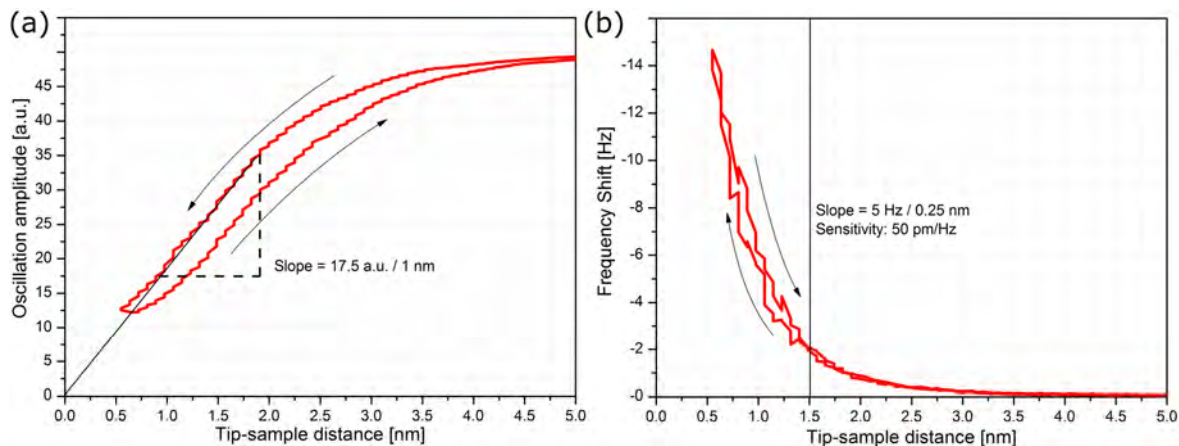


Figure 5.4.4: Tuning fork landing curve in AFM shear-force mode recorded with a gold tip over a platinum surface. (a) Oscillation amplitude vs. tip-sample distance. By extrapolating the oscillation amplitude to zero, the distance between tip and sample is approximated. (b) Resonance-frequency shift vs. tip-sample distance. The black vertical line indicates the tip-sample distance for the scanning setpoint of -2 Hz. The distance was calibrated based on the amplitude measurement shown in (a).

5.5 TERS experiments

The goal of the following TERS experiments is to record a Raman map that verifies the existence of ferroelectric ordering in the lead titanate islands. In this respect, TERS has two advantages over confocal Raman spectroscopy: First, the high light intensity within the near-field of the tip allows for Raman signal measurements of the nano-islands which are otherwise not accessible by confocal Raman spectroscopy due to their small volume; second, if we reproduce the high spatial resolution from the CNT experiments, it should be possible to optically identify structural variations within single islands.

The experiments are conducted with electrochemically etched gold tips, made from a 100 μm thick wire, that are attached to tuning forks to be operated in shear force mode AFM. The tip etching with 3.5 V pulses and the tuning fork preparation are described in sections 3.2 and 5.4, respectively. The TERS tip is optically excited by p-polarized light at a wavelength of 632.8 nm in side-access with a 0.42 NA objective. The experiment is carried out in four steps:

1. Testing of the tuning fork probes and TERS tips on CNTs to verify the scanning stability of the probe and the field enhancement of the tip.
2. Measurement of a single TERS spectrum on a PbTiO_3 island to determine the required laser power and integration time for subsequent TERS mapping.
3. Scan of the topography to identify an area of interest for the TERS mapping.
4. Scan of a high resolution TERS map.

5.5.1 Probe selection

After etching, the tips are attached to the tuning forks with acrylamide glue and cured for 24 hours at room temperature. In order to select only those tips with surface plasmon resonances for the TERS experiments on lead titanate, every probe is tested on carbon nanotubes that were deposited previously on a gold substrate (sect. 4.1.3). Therefore, the tip is aligned with the laser and the topography of the sample is scanned to locate a CNT. The topography scan is stopped immediately after finding a CNT in order to limit the effect of lateral drift, and the tip is placed above the CNT at a distance of approximately 1.5 nm. A TERS spectrum is recorded and compared to the measurement of a second spectrum with the tip laterally displaced by 50 nm from the CNT. A change of the CNT's G-band between both spectra indicates a near-field enhancement effect. The ratio can be used to determine the tip-enhancement factor. Figure 5.5.1 shows the TERS spectra acquired with two tips that provide tip enhancement on a CNT.

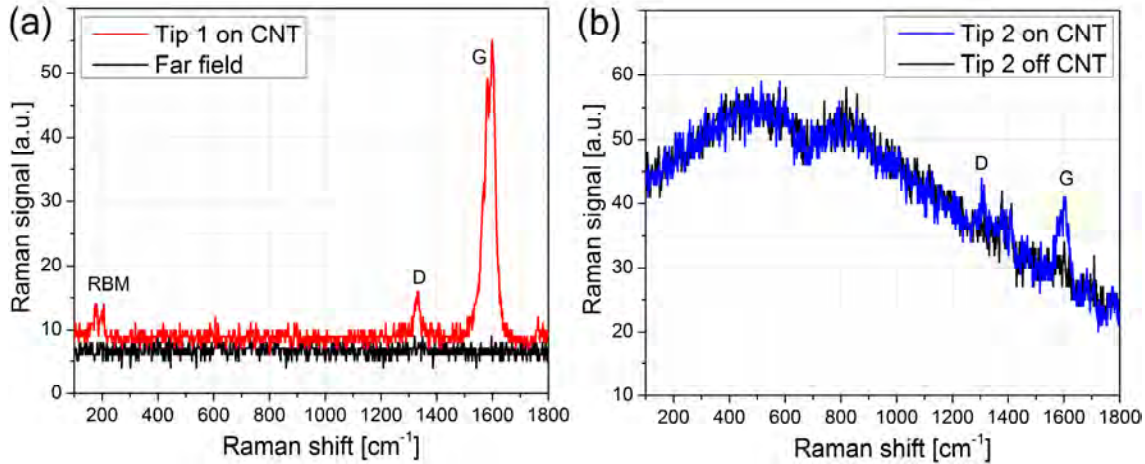


Figure 5.5.1: TERS spectra of two tips positioned on a CNT. The laser power is set to 700 μW and the integration time to 3 s for tip 1 and 20 s for tip 2. Both tips show an amplification of the G-band (1580 cm^{-1}). While tip 1 leads to a significantly enhanced Raman signal of the CNT (also revealing the radial breathing mode and the D-band), tip 2 shows a less pronounced enhancement of the G-band and suffers from a broad background.

When placed on a CNT, tip 1 provides a strong enhancement of the local electric field, leading to an amplification of the G-band at 1580 cm^{-1} , of the D-band at 1330 cm^{-1} , and also of the radial breathing mode (RBM) at 175 cm^{-1} . The confocal far-field signal (without tip enhancement) does not show any CNT Raman signal. By comparison of both spectra, the tip-enhancement factor EF can be estimated (see sect. 2.5.4 for definition). The ratio between the enhanced G-band signal and the noise of the far-field (0.87 counts RMS) is $I_{\text{near}}/I_{\text{far}} = 47$. Considering the correction factor for the sample and setup geometry according to equation 2.5.15, the enhancement factor of this tip is at least 9000, leading to an E-field enhancement of 9.7 ($r = 30\text{ nm}$, $h = 1.5\text{ nm}$, $\lambda = 633\text{ nm}$, $\text{NA} = 0.42$).

Tip 2 also shows an amplification of the G-band by a factor of 6 ($I_{\text{near}}/I_{\text{far}}$) when the tip is placed above a CNT. By considering the correction factor, the resulting enhancement factor of tip 2 is at least 1100 (E-field enhancement: ~ 5.8). This is a lower enhancement than observed with tip 1 and could be caused by some of the following reasons: (i) The SPR frequency of the tip does not exactly match the excitation frequency, (ii) the plasmon resonance is not located directly at the apex of the tip, (iii) the damping is higher due to adsorbates on the tip, (iv) the enhancement of tip 1 was boosted by gap-enhancement due to a beneficial local morphology of the gold substrate under the CNT.

It is worth noting that the spectrum of tip 2 suffers from a broad background signal that is centered at about 600 cm^{-1} . The broadness of the spectrum is an indication of fluorescence rather than Raman scattering and might originate from a fluorescence-like emission of adsorbates on the tip. This effect was already observed by other researchers during TERS experiments [53]. The optical scattering of molecules that are physisorbed directly to the surface of the tip can exceed the near-field spectrum of the sample due to the distance dependence of the near-field (see equation 2.5.12).

5.5.2 TERS mappings

The tips that showed enhancement of the Raman signal on CNTs are now used for the Raman mappings. The probe is placed over a lead titanate island to verify the tip enhancement on the new sample and to detect the Raman signature of lead titanate. In contradiction to the results on CNTs, tip 1 does not show a distinct Raman spectrum and no variation of the spectrum can be found at different tip positions *on* and *off* the islands even after increasing the laser power and integration time to 8.5 mW and 60 s, respectively.

The experiment is repeated with tip 2, starting with a laser power of 700 μW and 20 s integration time. The tip spectrum shows a broad peak around 600 cm^{-1} as it was observed previously when testing the tip on the CNTs. By laterally moving the tip from the platinum surface to a lead titanate island, a three-fold increase of the signal intensity is observed over a distance of 50 nm. The TERS spectra are later shown together with the TERS maps of the islands in Figure 5.5.4.

Topography scan and PMT image

Before starting the TERS mapping with tip 2, the sample's topography is scanned on $500\text{ nm} \times 500\text{ nm}$ to obtain a high resolution image of the islands under laser excitation (see Fig. 5.5.2 (a)). An image of the Rayleigh scattering is recorded simultaneously by the photo-multiplier tube (PMT) (see Fig. 5.5.2 (b)). The PMT detects the light intensity at wavenumbers below $\sim 60\text{ cm}^{-1}$ which is the spectral range that is *reflected* by the dichroic mirror in the direction of the PMT and thus not transmitted to the Raman spectrometer (see sketch of the optical setup in

Figure 2.7.3 on page 38). The majority of the PMT signal stems from the Rayleigh scattering of the tip and in the focus of the objective.

The topography scan shows four individual, differently shaped nano-islands which also become visible in the PMT image and which will be referred to as 1, 2, 3, and 4 (from left to right and top to bottom).

While island 1 and 4 appear round, island 3 shows a characteristic triangular shape that indicates epitaxial growth of the lead titanate. Island 2, with only 10 nm in height, is both flatter and broader than the other three islands. Most interestingly, however, is the PMT signal which provides a contrast of 20% over distances of a few nanometers. This is a clear indication of sub-wavelength resolution. The PMT signal increases at the perimeter of the islands and decreases towards their center (clearly visible for islands 1, 3 and 4). Island 2 shows an increase across almost the entire surface. A comparison with the topography reveals that the PMT contrast is not related to crosstalk with the vertical position of the tip but must have its origin in the interaction between tip and sample. As we will see later, the variation in the PMT signal is caused by a change of the resonance frequency of the SPR at the apex of the TERS tip during scanning.

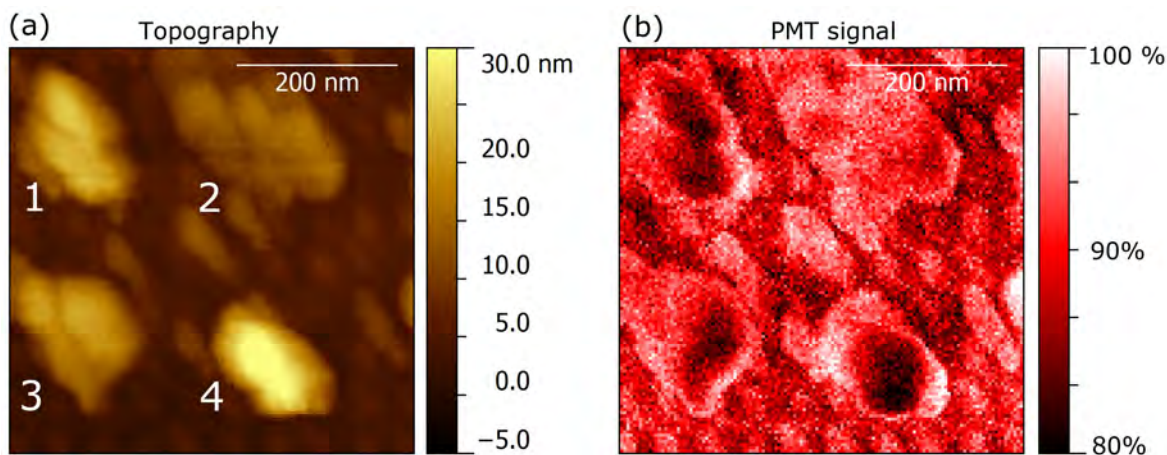


Figure 5.5.2: Images obtained by a 500 nm x 500 nm tuning fork AFM scan in shear-force mode during laser excitation of the tip on the PbTiO_3 islands. The vertical feedback was PLL-controlled at a resonance shift of -4 Hz and the oscillation amplitude was kept constant at about 0.4 nm. (a) Topography image of the islands numbered from 1 to 4. (b) Optical image recorded by the PMT showing a sharp contrast at the perimeter of the islands. The 100 % value of the PMT signal represents the highest recorded signal while 0 % is set to the dark current of the PMT.

TERS mapping

The TERS map is recorded on the same area as the topography scan with a resolution of 64x64 points. With 1 s integration time, a laser power of 8.5 mW is required to achieve a sufficient signal-to-noise ratio. These settings lead to a total acquisition time of 70 min for the entire image. The tip is scanned stepwise over the sample and remains steady for the recording of each spectrum. The recorded TERS image is shown in Figure 5.5.3 as false-color rendering of the signal intensity,

calculated by integrating the recorded intensity over the full spectral range from 70 cm^{-1} to 1800 cm^{-1} .

The islands are sharply separated from the platinum background by a threefold signal increase over a distance of only 15 nm (2 pixels). This confirms the strong optical confinement of light by the near-field enhancement of the tip. The resolution is about 100 times better than the confocal resolution of the 0.42 NA objective. A comparison of the TERS image with the topography scan shows a strong correlation with the height of the islands, but also some differences such as the increased scattering in the bottom right corner of island 4 which cannot be explained only by the topography of the sample.

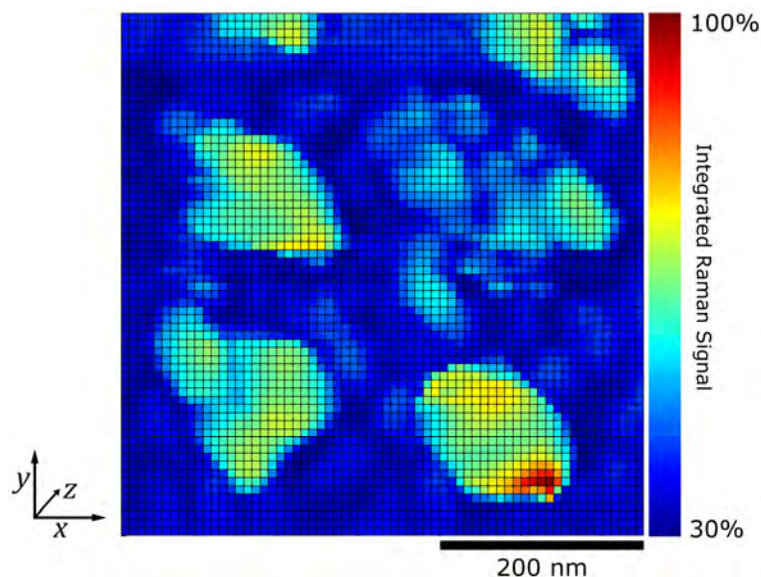


Figure 5.5.3: 64x64 points TERS map of PbTiO_3 islands on platinum. The signal intensity is integrated over the full spectral range from 70 cm^{-1} to 1800 cm^{-1} . The color bar is limited to the lowest and highest intensities, while 0% represents the dark-count of the CCD. An increase of the optical signal is seen at the position of the islands. Comparison to the topography in Figure 5.5.2 reveals a lateral drift of 50 nm to the bottom-right during the scan which corresponds to less than 1 nm/min.

Individual TERS spectra

We will now analyze the TERS spectra from different positions of the TERS map. Spectra from selected positions are presented in Figure 5.5.4. They all show a broad peak on the lead titanate islands and a lower peak, but with a similar spectral distribution, on the platinum substrate. We already observed such a spectrum during the TERS experiment on CNTs with the same tip (cf. Fig. 5.5.1 (b)). All these spectra, i.e. the TERS spectrum on CNTs, the TERS spectrum on the islands, and the TERS spectrum on the platinum substrate, consist of a broad “peak” with a width of 1000 cm^{-1} or more, centered somewhere between 500 cm^{-1} and 1000 cm^{-1} . We therefore assume that the broad spectrum does not originate from the sample but is generated by a fluorescent emission from the TERS tip due to a contaminant within the near-field. A fluorescent emission caused by adsorbed molecules was already

observed by Domke [42] and Pettinger et al. [53]. Pettinger suggested that the fluorescence peak of the molecule is further broadened because of a reduced lifetime of the excited state due to the adsorption of the fluorescent molecule to a metallic surface. This fluorescence background emission will be referred to as “tip fluorescence” from now on.

The TERS spectra on the islands also contain an additional Raman peak at 100 cm^{-1} that is not visible on the platinum substrate, which is likely to be caused by the Raman scattering from PbTiO_3 .

A close comparison of the Raman spectra shows:

- The tip fluorescence is higher when the tip is placed on the islands than when the tip is located over the platinum substrate.
- The spectra decrease towards large wavenumbers and the signals are almost identical at 1800 cm^{-1} .
- Differences between the islands can be found for small wavenumbers. For example, between islands 1 and 2 as well as at different positions on island 4.
- Island 4 shows a variation of the center of the broad fluorescence peak for different tip positions close to the bottom right corner.
- All spectra show a small feature at 650 cm^{-1} which is probably caused by the optical absorption of a mirror in the spectrometer.
- A small peak at 100 cm^{-1} can be found on the islands.

As we will show later, the variation of the tip fluorescence is caused by a position-dependent shift of the surface plasmon resonance frequency of the tip. In order to extract the much weaker Raman signal from the PbTiO_3 crystals, the tip fluorescence must first be filtered out. This is subject of the next section.

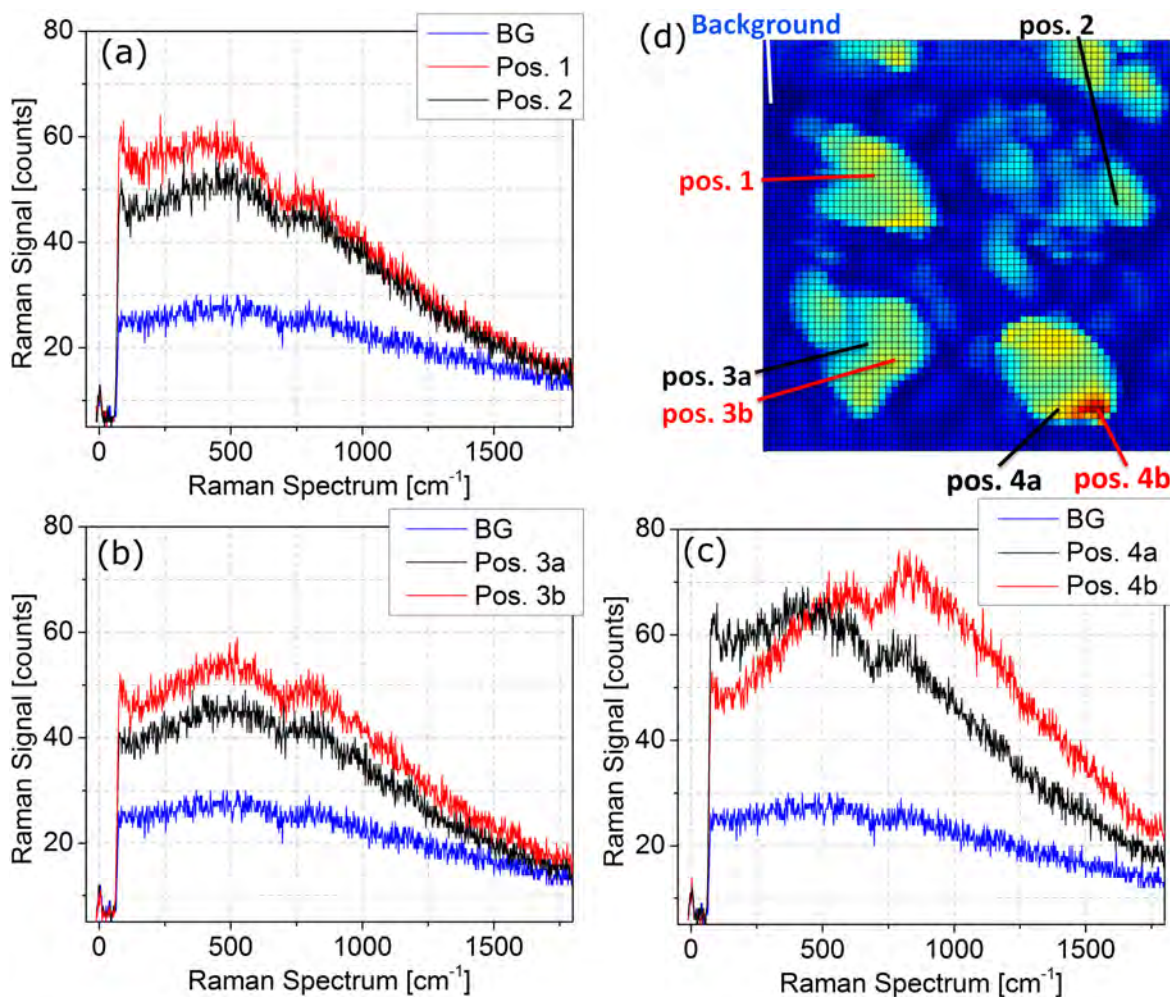


Figure 5.5.4: Selected spectra from different positions of the TERS map as indicated in (d). A background spectrum (BG) obtained on the platinum substrate is shown in every plot for comparison (blue).

5.6 Data analysis and discussion

The TERS Raman data contains a strong fluorescence background from the tip that appears to change its intensity and peak position depending on the tip position on the sample. This section discusses the physical background of the variation of the tip fluorescence and explains the algorithm applied to remove the fluorescence signal from every spectrum in order to extract the underlying Raman contribution that stems from the PbTiO₃ islands.

5.6.1 Tip-generated background

In order to subtract the varying background correctly from every spectrum, it is necessary to describe the tip fluorescence with a model that can be fitted to the data. We start with two assumptions which, as we will later see, are independently justified:

- Because platinum is intrinsically Raman inactive and not fluorescent, the TERS signal from the platinum substrate is caused solely by the tip fluorescence.
- The tip fluorescence is enhanced by the surface plasmon resonance of the TERS tip. The resonance frequency and amplitude of the surface plasmon varies as the tip moves across the sample, leading to an increase of the tip fluorescence over the islands.

Before we analyze the data based on this hypothesis, we increase the signal-to-noise ratio (SNR) of the TERS spectra by adding the spectra from similar regions for a preliminary analysis. The short integration time of 1 s per point led to high noise, but by adding n spectra, the integration time is virtually increased to n seconds and improves the SNR by \sqrt{n} .

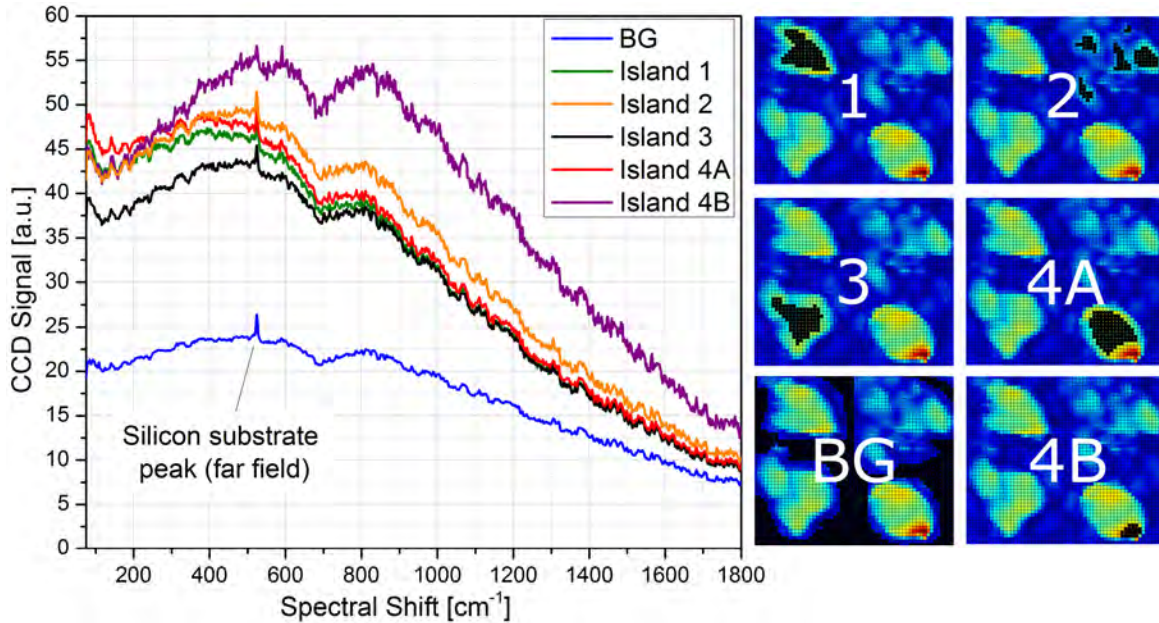


Figure 5.6.1: The graphs show the sum of the optical spectra of selected regions as indicated by the black colored areas in the respective pictograms on the right side. All graphs are normalized by area to allow for a quantitative comparison.

Figure 5.6.1 shows the sum spectra of six different areas for comparison. The spectra obtained on the islands appear as an amplified version of the spectrum that was measured over the platinum substrate. This again shows that the tip fluorescence depends on the position of the tip on the sample.

All spectra show a decrease in signal towards high wavenumbers. Furthermore, a Raman peak between 70 cm^{-1} and 120 cm^{-1} can be observed on the islands and is likely to be caused by Raman scattering from the PbTiO_3 . Due to the reduced noise, even the Raman peak of the silicon substrate buried 100 nm under the platinum film becomes visible at 520 cm^{-1} as part of the far-field signal and is equally found in every spectrum.

Division by background

In the next step, the TERS spectra that were integrated over the area of the islands are mathematically divided by the spectrum of the tip fluorescence as obtained on the platinum surface. The tip fluorescence is enhanced by the surface plasmon resonance of the TERS tip. The sample affects the surface plasmon resonance, thus leading to a variation of the tip fluorescence depending on the position on the sample. By dividing the spectra of the islands by the background spectrum of the tip fluorescence (see blue “BG” graph in Fig. 5.6.1), we obtain the spectral distribution of the tip enhancement. Since the enhancement of the fluorescence is defined by the surface plasmon resonance frequency, the same curve represents the spectrum of the plasmon resonance at the tip. The resulting curves will be referred to as *SPR spectra* hereafter and are plotted for the areas 1 to 4B in Figure 5.6.2.

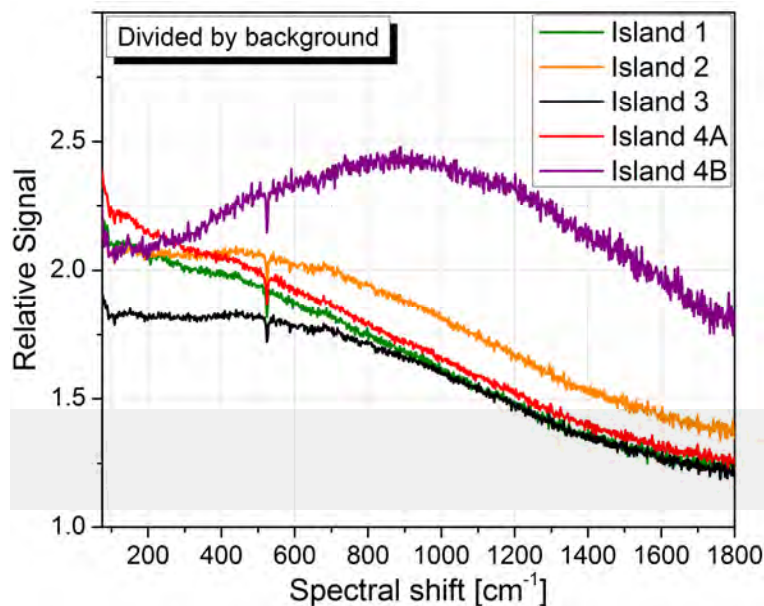


Figure 5.6.2: Spectra of the areas 1, 2, 3, 4A and 4B after division by the background signal (BG) as shown in Fig. 5.6.1. Most notable is the Lorentzian peak shape obtained on area 4B. The other areas (1-4A) lead to spectra that show a blue-shifted Lorentz peak with lower amplitude.

Position 4B shows a broad Lorentzian-curve³⁷ centered around 900 cm^{-1} (670 nm) with a width of about 2000 cm^{-1} (90 nm). Width and position of the SPR spectrum are in good agreement with the absorption spectrum of longitudinal plasmon resonances on ellipsoidal gold nanoparticles (see Fig. 2.5.5 on page 31). The areas 1-4A show a blue-shift of the SPR spectra with similar width but lower amplitude. The shift is caused by a variation of the plasmon resonance frequency of the tip depending on the tip position on the sample.

³⁷ Since only the upper part of the peak is visible, a decision between Lorentz and Gauss shape is difficult, but the analysis with a Voigt fit revealed a ratio of 65 %/35 % Lorentz/Gauss with an error margin of 10 %.

To conclude this interim result, we identified the spectrum of plasmon resonance on the gold tip. This spectrum corresponds to the enhancement of the tip and shows variations dependent on the position of the tip on the sample.

Lorentzian peak fit

We can now identify the plasmon resonance frequency of the tip by a fit of the SPR spectrum with the Lorentz peak function:

$$y(x) = y_0 + \frac{2A}{\pi} \frac{w}{4(x-x_c)^2 + w^2} \quad (5.6.1)$$

where y_0 is the offset of the baseline, A is the area under the curve, x_c is the center, and w is the full width at half maximum of the peak. All graphs from Figure 5.6.2 are fitted with the least means square method and the parameters y_0 , x_c , A and w as variables. The fit is applied to the spectrum between 400 cm^{-1} and 1800 cm^{-1} after the far-field silicon peak is removed. The fitted parameters are given in Table 3 and the graphs are shown in Figure 5.6.3.

Island	w [cm^{-1}]	w [nm]	x_c [cm^{-1}]	y_0 [a.u.]	A [a.u.]
1	1924 ± 34	87.7	287 ± 12	0.91 ± 0.01	3263 ± 098
2	1936 ± 26	88.3	457 ± 06	1.00 ± 0.01	3233 ± 072
3	1919 ± 26	87.5	458 ± 06	0.89 ± 0.01	2791 ± 062
4A	2081 ± 34	96.0	212 ± 13	0.90 ± 0.01	3865 ± 112
4B	2429 ± 62	114.9	862 ± 02	0.73 ± 0.06	6440 ± 378

Table 3: The table shows the fitted parameters of the Lorentz peaks in Figure 5.6.3. All values are fitted with the least mean square method and the given errors are the standard deviations based on the correlation between the parameters.

The widths of the fitted Lorentz-curves for the islands 1-4A are around 90 nm and 115 nm for 4B. The center of the resonance lies between 212 cm^{-1} and 458 cm^{-1} ($641 \text{ nm} - 652 \text{ nm}$) with an exception for island 4B which has its maximum at 862 cm^{-1} (669 nm). The increase of the width at longer wavelengths, as seen on island 4B, is expected in the case of a plasmon resonance red-shift (cf. Fig. 2.5.5). The baseline of the Lorentz curve is given by y_0 and is expected to be around 1³⁸. With the exception of island 2, all fits show a baseline 10 % to 30 % below 1. This can be explained by an increase in light absorption or stronger scattering in directions other than the detection angle of the objective caused by the PbTiO_3 islands.

³⁸ Due to the *division* of the Raman spectrum by the tip fluorescence, the value 1 is the expected value if *no* enhancement would occur.

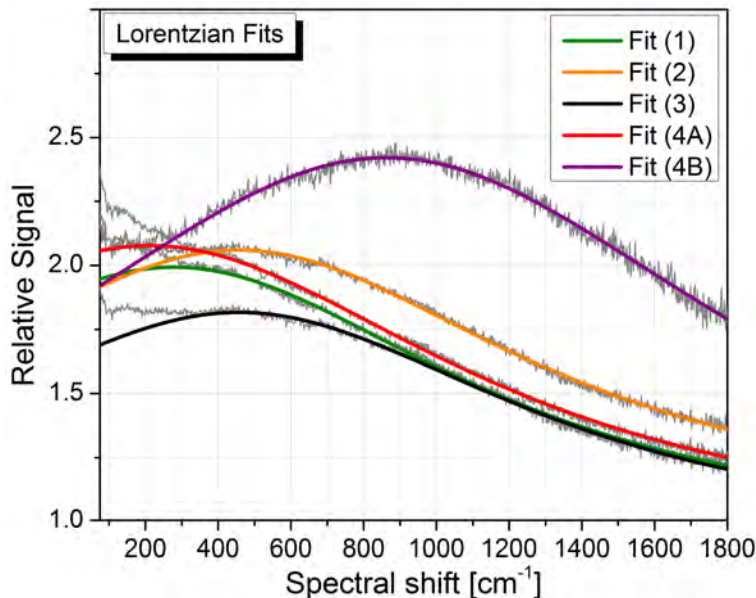


Figure 5.6.3: Plot of the Lorentz curve fits of the SPR spectra including the greyed out spectra for comparison. The Lorentz curves describe the SPR spectra accurately between 400 cm^{-1} and 1800 cm^{-1} . The deviations below 300 cm^{-1} are caused by the Raman signal from the PbTiO_3 islands.

We succeeded in extracting the resonance frequency and spectral width of the surface plasmon resonance of the tip from the fluorescence background in the TERS map. The variations of the enhancement show that the common assumption of a constant SPR frequency on the tip during scanning is not generally fulfilled. Furthermore, our results show that the tip enhancement is unequally distributed over the spectrum and leads to an increased enhancement at the center of SPR frequency. The approximation $g \approx g'$ that is used to derive the “4th-power rule” (see eq. 2.5.11 on p. 28) can thus lead to wrong results when measuring Raman spectra by TERS over a large spectral range.

5.6.2 TERS spectrum of the PbTiO_3 islands

Now that the SPR spectrum of the tip is known, the tip fluorescence can be filtered out in order to extract the Raman spectrum from the islands. In the first step, the background signal of the platinum is multiplied with the fitted Lorentzian-curve of each of the areas 1-4B to calculate the enhanced tip fluorescence signal. In the second step, the individually calculated tip fluorescence is subtracted from each TERS spectrum to yield the near-field Raman spectrum of the lead titanate islands:

$$\text{lead titanate Raman}_i = \text{TERS-Spectrum}_i - \underbrace{\text{Background} \cdot \text{Lorentzian-curve}_i}_{\text{Tip fluorescence}} \quad (5.6.2)$$

where i ranges from 1 to 4B for the areas on the sample.

The resulting Raman spectra are shown in Figure 5.6.4. The PbTiO_3 spectrum of the islands is almost identical within the noise level. This shows that the previous-

ly observed differences between the TERS spectra on the islands are only due to the variation of the plasmon resonance. All spectra show a signal increase towards low wavenumbers. The region between 300 cm^{-1} and 800 cm^{-1} contains small variations from 0 that are barely visible above the noise and can be attributed to Raman contributions from the far-field such as the silicon peak at 520 cm^{-1} . Above 800 cm^{-1} , no contribution from the sample can be seen.

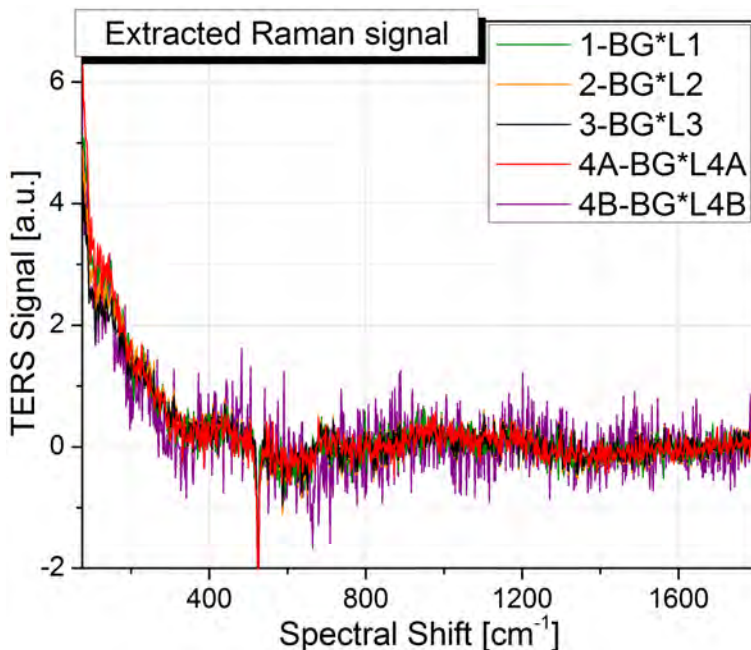


Figure 5.6.4: The TERS Raman of the islands 1-4B after removal of the tip fluorescence. The Raman signature appears to be identical within the noise level and shows an increase towards low wavenumbers.

The noise level can be reduced by adding the Raman signals of all four islands and by redistributing the spectral data points into bins with a width of 10 cm^{-1} . Figure 5.6.5 shows the resulting spectrum that finally presents the extracted and integrated TERS spectrum of the PbTiO_3 islands on the sample.

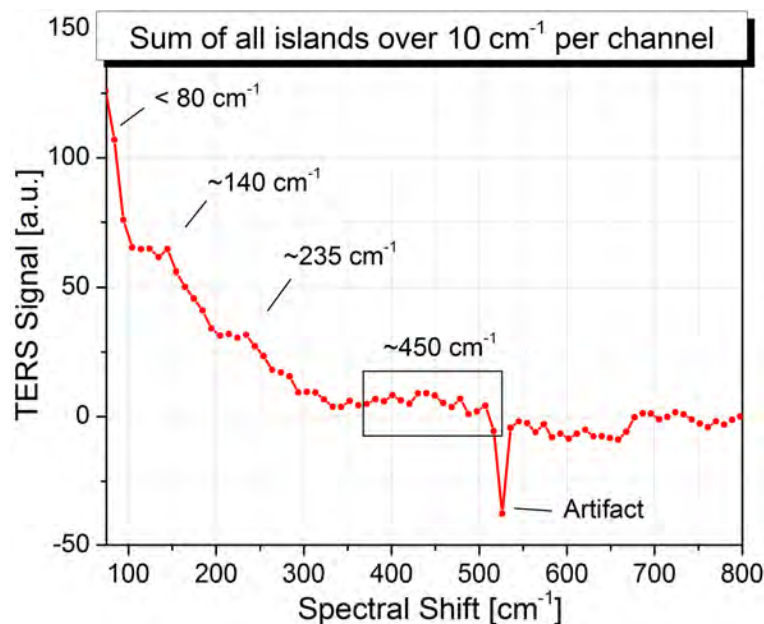


Figure 5.6.5: Sum of all PbTiO_3 -island Raman spectra (without fluorescence) after 5-channel-binning. We can carefully identify peaks at 80 cm^{-1} , 140 cm^{-1} , 235 cm^{-1} , and 450 cm^{-1} . The silicon peak from the far-field appears as negative peak in the Raman spectrum due to the background subtraction.

The sum of the PbTiO_3 Raman spectra in Figure 5.6.5 contains peaks that are visible above the noise level at $< 80 \text{ cm}^{-1}$, $\sim 140 \text{ cm}^{-1}$, $\sim 235 \text{ cm}^{-1}$ and $\sim 450 \text{ cm}^{-1}$. Comparing these peak positions with the Raman spectrum previously acquired on a PbTiO_3 thin film (cf. Fig. 5.3.4), reveals a strong blue-shift, broadening, and damping of the Raman peaks. These effects were previously observed by confocal Raman spectroscopy of nano-crystalline lead titanate powders [137, 141] and films [206]. As known from literature, the blue-shift and damping increases with smaller grains and higher temperatures close to the paraelectric phase transition at $490 \text{ }^\circ\text{C}$ [206].

Taguchi et al. published the Raman spectrum of PbTiO_3 in the temperature range from $20 \text{ }^\circ\text{C}$ to $476 \text{ }^\circ\text{C}$ [206] (see Fig. 5.6.6). The observed peaks in our TERS spectrum are identified as $E(1\text{TO})$ at $< 80 \text{ cm}^{-1}$, $E(2\text{TO})$ at $\sim 140 \text{ cm}^{-1}$, B_1+E at $\sim 235 \text{ cm}^{-1}$, and $E(3\text{TO})/A_1(3\text{TO})$ around $\sim 450 \text{ cm}^{-1}$, by direct comparison to Taguchi's spectrum at $476 \text{ }^\circ\text{C}$. The presence of Raman modes in the TERS spectrum indicates that the PbTiO_3 islands are still ferroelectric, although close to undergoing a phase transition.

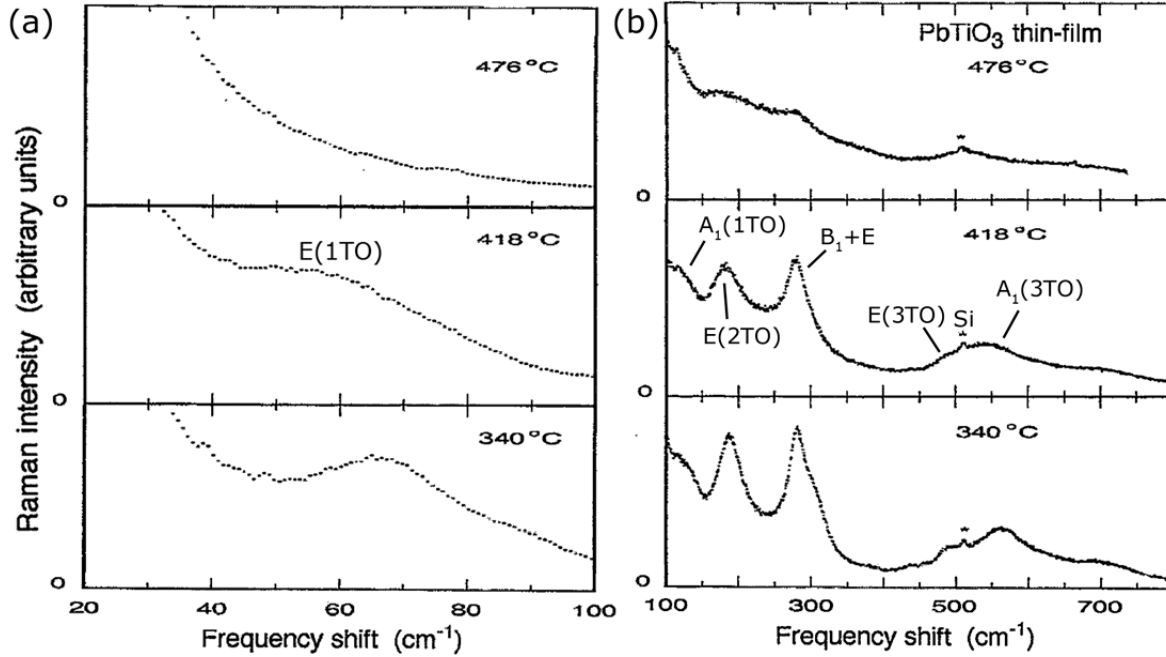


Figure 5.6.6: Confocal Raman spectra obtained on a PbTiO₃ thin film at elevated temperatures by Taguchi et al. All peaks show a blue-shift, peak-broadening, and increased damping with increasing temperature. At 476 °C, close to the transition temperature from the ferroelectric to the paraelectric phase, the peaks almost disappear completely and only a slope towards low wavenumbers (<60 cm⁻¹) remains. The little peak at 520 cm⁻¹ originates from the silicon substrate and is not temperature dependent. (Figures taken from ref. [206].)

As discussed previously in section 5.1, the phase transition can either be induced by a temperature increase or by a size dependent reduction of the phase-transition temperature. For the investigated island size of 100 nm in diameter and 30 nm thickness, we do not expect to see a substantial size effect (cf. Fig. 5.1.1 on p. 76). It is therefore likely that a heating effect due to the focused excitation laser and the near-field enhancement at the tip elevated the temperature of the islands, bringing them closer to undergoing a phase transition. Since the effect on the Raman spectrum by a *size-induced* as well as by a *temperature-induced* phase transition is similar, it is difficult to decide which effect is dominating.

At this point, we succeeded in obtaining a TERS spectrum of PbTiO₃ nano-islands located on the original substrate they were grown on. The spectrum showed highly damped phonon modes as expected for PbTiO₃ in the ferroelectric phase close to their phase transition. The results show that TERS can be used to identify the structural state of ferroelectric nano-islands. Since the enhancement factor of the tip was not very high, we expect that similar results can be achieved on smaller islands with a better tip. Caution, however, must be taken in terms of excitation power to limit the heating effect of the laser.

5.6.3 TERS map of PbTiO_3

We will now plot the PbTiO_3 TERS signal in a false color map to achieve a chemical image of the sample with nanometer resolution. We use the previously described algorithm in a program³⁹ to filter out the tip fluorescence for each of the 64x64 TERS spectra, following these steps:

1. Each of the 64x64 spectra is divided by the tip fluorescence that was obtained previously over the platinum area (blue “BG” graph in Fig. 5.6.1).
2. The divided data is fitted with the Lorentz function (Eq. 5.6.1)
3. The fitted function is multiplied with the tip fluorescence to calculate the tip-enhanced background.
4. The tip-enhanced background is subtracted from the spectrum to extract the TERS spectrum of PbTiO_3 at every position.

The extracted TERS signal is integrated from 66 cm^{-1} to 106 cm^{-1} and plotted as a 2-dimensional false-color image (see Fig. 5.6.7 (b)). The comparison with the original (unfiltered) TERS data in Figure 5.6.7 (a) shows two differences: First, the noise is significantly higher due to the low Raman signal from the islands; second, the PbTiO_3 signal appears strongest in the center of the islands where the tip can excite the largest volume. Island 3, however, shows a higher PbTiO_3 signal in the corners than in the center.

A similar result was obtained by PFM on different islands of the same sample (cf. Fig. 5.3.2 on p. 80). We assume that island 3 consists of several ferroelectric grains. During the growth process, the nucleation possibly started simultaneously at the corners and the columnar growth led to grain boundaries at which the lead titanate is closer to the paraelectric phase and therefore the Raman signal and the piezoresponse is reduced.

Before we analyze the island structure of island 3 in a scan with higher resolution in section 5.6.7, we will visualize the frequency shift of the tip’s plasmon resonance during this TERS mapping in the next section.

³⁹ The program was written by Julien Plathier in C++ based on my filter algorithm.

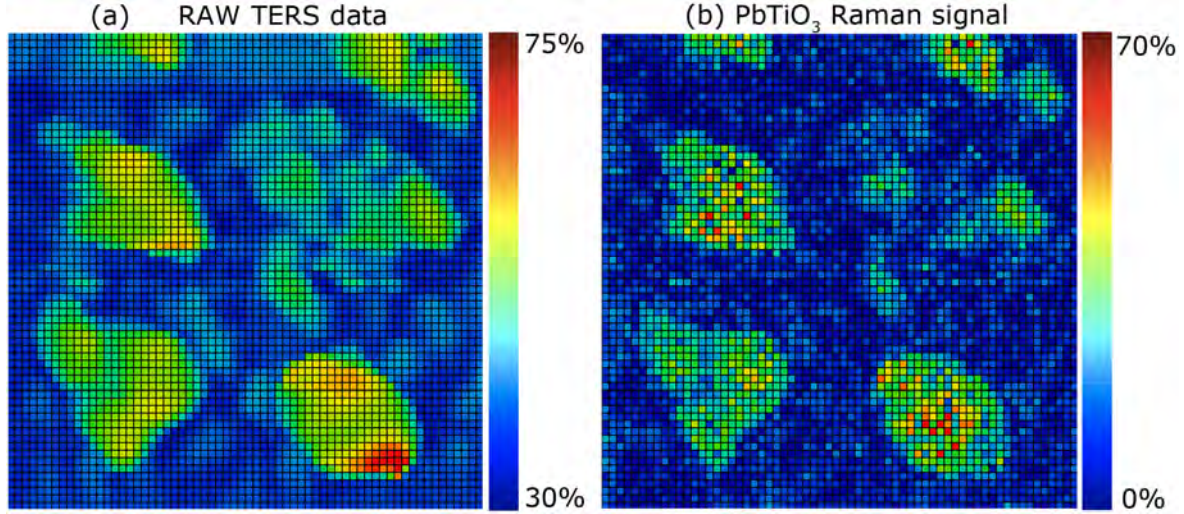


Figure 5.6.7: TERS maps of lead titanate islands (500 nm x 500 nm, 64 x 64 points). (a) Unfiltered TERS signal (integrated from 70 cm^{-1} to 1800 cm^{-1}). (b) TERS map of the lead titanate signal (after removal of the tip fluorescence, signal integrated from 66 cm^{-1} to 106 cm^{-1}). The percentage values of the color bars represent the dynamic range with respect to the highest and lowest Raman intensities.

5.6.4 Surface plasmon resonance mapping

The fitting algorithm, that describes the enhancement of the tip fluorescence by a Lorentz curve (equation 5.3.2), generates a set of parameters: the center of the peak x_c , the peak width w , the area under the peak A , and the baseline of the peak y_0 . These parameters can be plotted as 2-dimensional images in order to visualize the behavior of the surface plasmon resonance at the tip while the tip is scanned over the sample: x_c is the resonance frequency of the SPR with the spectral width w ; and $y_0 - 1$ can be interpreted as the optical absorption of the material around the tip. The area under the curve A can be used to calculate the amplitude y_{amp} according to:

$$y_{\text{amp}} = 2A/w\pi \quad (5.6.3)$$

$y_{\text{amp}} + 1$ can then be interpreted as the enhancement of the tip. Figure 5.6.8 shows the color plots of the four fitting parameters.

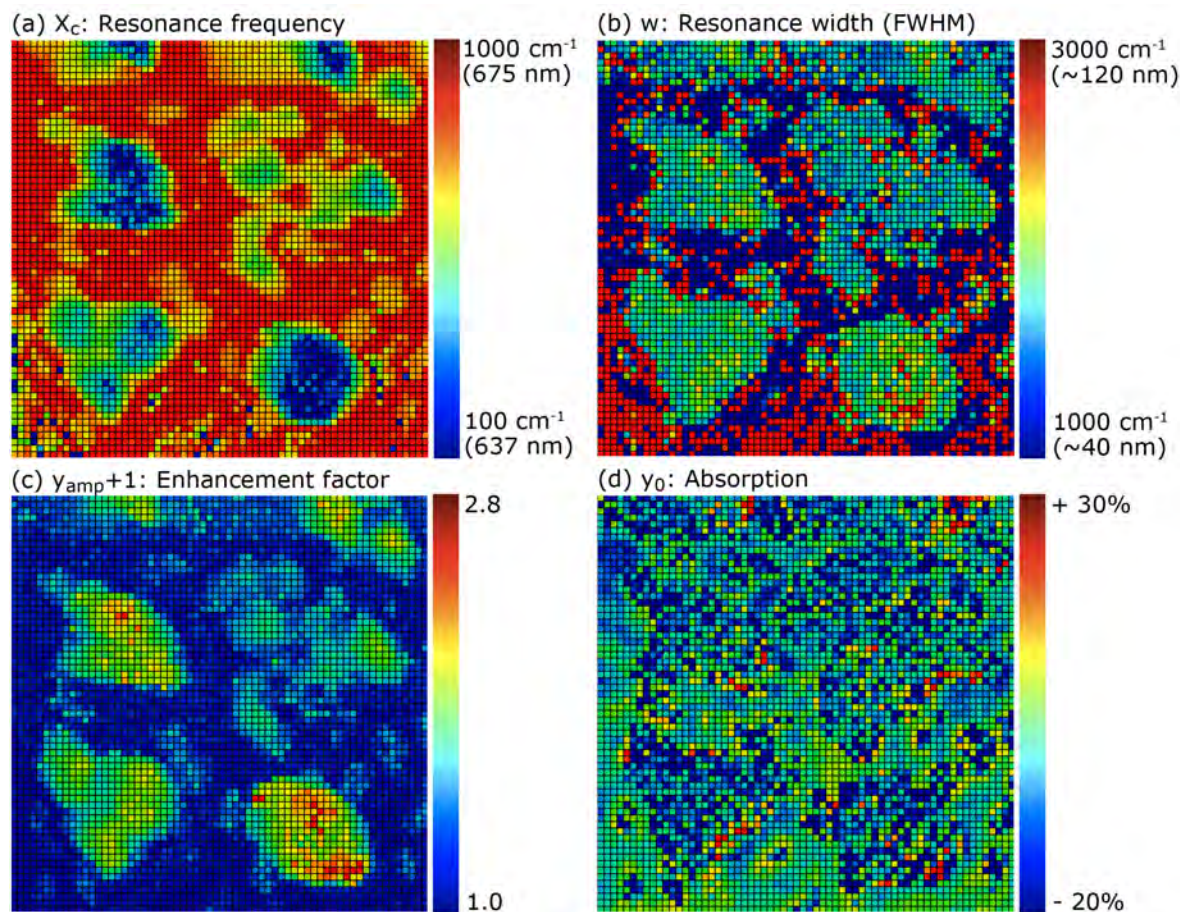


Figure 5.6.8: Fitting parameters of the plasmon resonance of the tip (cf. TERS map in Fig 5.6.7). (a) SPR frequency of the tip. The resonance shows a blue-shift when the tip is positioned over the islands. (b) Width of the resonance frequency. The spectral width is about 80 nm when the tip is above the islands. (c) Peak amplitude plotted as the enhancement factor of the tip ranging from 1 (over the platinum) to 2.8 (over the islands). (d) Deviation of the baseline y_0 of the Lorentz peak from 1. A decrease is seen over the islands and an increase at some positions at their perimeter. Negative values represent absorption and positive values may be caused by scattering towards the objective.

The surface plasmon resonance of the tip shows a blue-shift from 680 nm to 630 nm when the tip moves from the substrate to the islands. The highest blue-shift is found in the center of islands 1 and 4. The plasmon resonance has a spectral width of about 80 nm at the position of the islands. This width is in agreement with the expected values for surface plasmon resonances on a gold tip. Over the platinum substrate, the spectral width diverges because the amplitude y_{amp} approached 0, as we can see in Figure 5.6.8 (c).

y_{amp} reaches values of up to 1.8 over the islands corresponding to a signal enhancement by the tip of 280%. The baseline of the Lorentz-fit represents the absorption and reflection of the sample. Despite the high noise, increased absorption is visible over the center of islands while the edges appear to lead to an increased reflection.

To the best of our knowledge, this is the first experimental investigation of the SPR shift on a TERS tip during mapping. The results reveal a distinct sample dependence and thus the SPR shift is used to obtain additional information about the sample. In particular, we will employ the SPR frequency shift to image variations of the refractive index of island 3 in section 5.6.7.

5.6.5 Origin of the surface plasmon resonance shift

The resonance shift of the surface plasmon, shown in Figure 5.6.8 (a), has two possible origins: First, the permittivity of the islands affects the plasmon frequency of the tip; second, a distance variation between the tip and the metallic substrate affects the SPR frequency [53, 93].

Effect of the permittivity

The local, optical permittivity of the sample changes the plasmon resonance of the tip according to equation 2.5.6 ($\epsilon_{\text{tip}} = -2 \cdot \epsilon_{\text{surrounding}}$). The real part of the refractive index of lead titanate in the tetragonal phase is about $n = 2.7$ at 633 nm wavelength [218]. The optical permittivity $\epsilon \approx n^2$ is therefore larger than that of air ($n = 1$) or that of platinum, which has a negative optical permittivity.

When the tip approaches an island and the average permittivity of the tip environment increases, the resonance condition of the surface plasmon is only fulfilled when the permittivity of the gold tip decreases. As we know from Figure 3.1.1 on page 44, the permittivity of gold decreases for increasing wavelength. Consequently, the plasmon resonance of the tip is expected to undergo a red-shift when the tip approaches the lead titanate islands.

This red-shift, however, is overcompensated by the observed blue-shift caused by a variation of the tip-to-substrate distance.

Effect of the tip-to-substrate distance

The SPR frequency shift can be explained by a variation of the distance between the gold tip and the platinum substrate as the tip scans across the PbTiO_3 islands:

Pettinger et al. already observed a similar blue-shift of a fluorescence spectrum upon retraction of the TERS tip from the sample at a single position [53]. Jain et al. showed quantitatively, by a discrete dipole approximation (DDA) simulation, that the plasmon resonance between two ellipsoidal gold particles undergoes a blue-shift when the distance between the particles increases [93] (see Fig. 5.6.9 (a)). In order to compare our results to the DDA simulation, the SPR frequency was plotted as a function of the tip-to-substrate distance (see Fig. 5.6.9 (b)). The graph shows that the plasmon resonance frequency shifts to higher energies when the distance between tip and metal substrate increases. Although the geometry of our TERS experiment is slightly different, our observed frequency shifts are in good agreement with the DDA

simulation. The observed frequency shift can therefore be explained by a distance variation between the tip and the platinum substrate given by the height of the PbTiO_3 islands.

Other groups simulated the blue-shift of the plasmon resonance for increasing distances between a silver particle and a glass substrate [219], between a metallic sphere and a metal substrate [51], a metallic tip and a glass substrate [52], and between two gold particles [220].

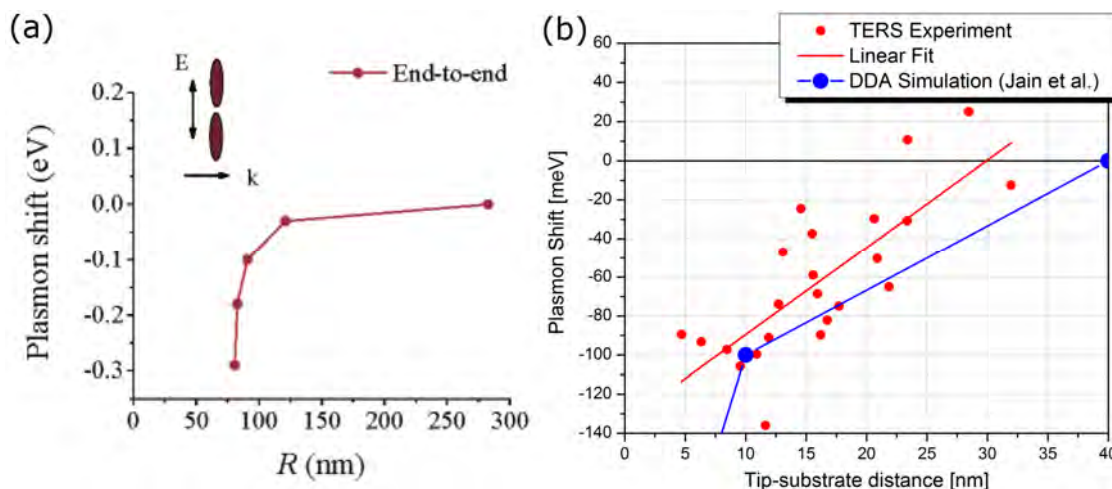


Figure 5.6.9: (a) Simulation by Jain et al.: Plasmon resonance shift of an ellipsoidal gold dimer, which is optically excited along its longitudinal axis, as a function of the particle distance R (center to center, the particles touch at a distance of 80 nm). The figure was taken from reference [93]. (b) Our experimental data: Shift of the plasmon resonance of the TERS tip plotted as a function of the distance between tip and platinum substrate (red points) taken from various positions of the TERS map. The simulation of Jain is shown in blue for comparison.

The plot in Figure 5.6.9 (b) shows that the blue-shift increases with a larger tip-to-substrate distance at the islands and therefore dominates over a possible red-shift that could be caused by the permittivity of the islands. The observed blue-shift per distance is 4.5 ± 0.8 meV/nm which corresponds to approximately 40 cm^{-1}/nm . A comparison with the data from Jain et al. [93] shows that our experiment is in excellent agreement with their simulation.

The shift of the SPR frequency has two consequences for TERS when scanning dielectric samples on metallic substrates:

1. The SPR shift will lead to a variation of the tip enhancement during mapping. The comparison of the absolute height of Raman peaks from different positions on the sample might thus lead to misinterpretation.
2. Due to the small spectral width of the plasmon resonance, the Raman modes undergo a different enhancement depending on their spectral position. The comparison between peak ratios, as often used in Raman maps to separate regions with different chemical compositions, can lead to wrong conclusions.

We would like to point out that the observation of the SPR shift was only possible in the present case due to tip fluorescence, presumably caused by a contaminant on the tip. In those cases where “clean” tips are used, the SPR shift cannot be measured and does thus not serve to deconvolute the TERS data. In such cases, the topography of the sample might help to theoretically estimate the magnitude of the surface plasmon resonance shift when interpreting the TERS spectra.

5.6.6 Finite-difference time-domain simulation

Sylvain Vedraïne and François Lagugn -Labarthet of the University of Western Ontario performed a finite-difference time-domain simulation based on our description of the TERS experiment. The goal was to simulate the surface plasmon resonance frequency and the tip enhancement at different tip positions on the sample, in order to evaluate the influence of the *permittivity of the islands* and the *tip-to-substrate distance* on the plasmon resonance during the TERS scan.

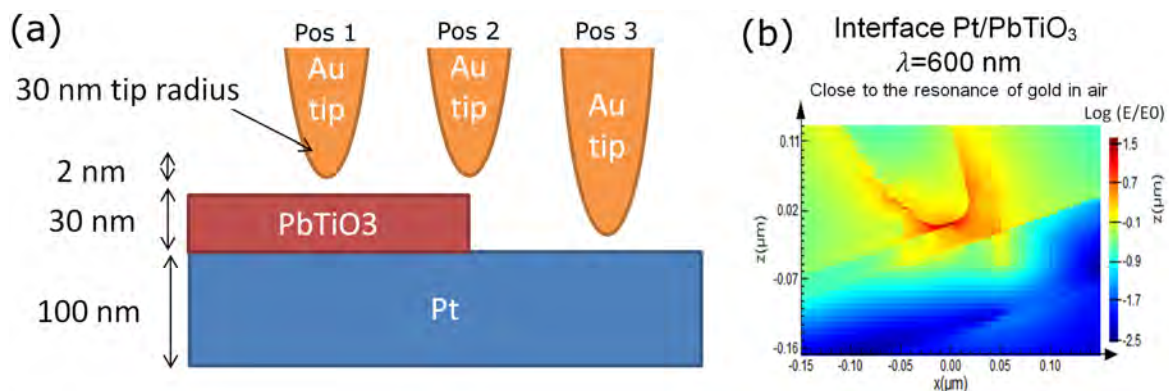


Figure 5.6.10: (a) Sketch of the simulated sample geometry and the three different tip positions used for the calculations. (b) Simulated field distribution around the gold tip in position 2 under an optical excitation at 600 nm wavelength. The simulated image is tilted in order to account for the 65°-inclination of the p-polarized excitation beam to the tip axis.

In the simulations, a gold tip with a radius of 30 nm is placed at three different positions 2 nm above the sample (see Fig. 5.6.10 (a)). The tip is excited by p-polarized laser pulses between 400 nm and 800 nm wavelength under a 65° angle, and the field distribution around the tip is calculated. By plotting the enhancement of the electric field as a function of the wavelength at each tip position, the spectral distribution of the plasmon resonance is obtained. Figure 5.6.11 (b) shows the electric field at the tip as a function of the wavelength for each of the three tip positions.

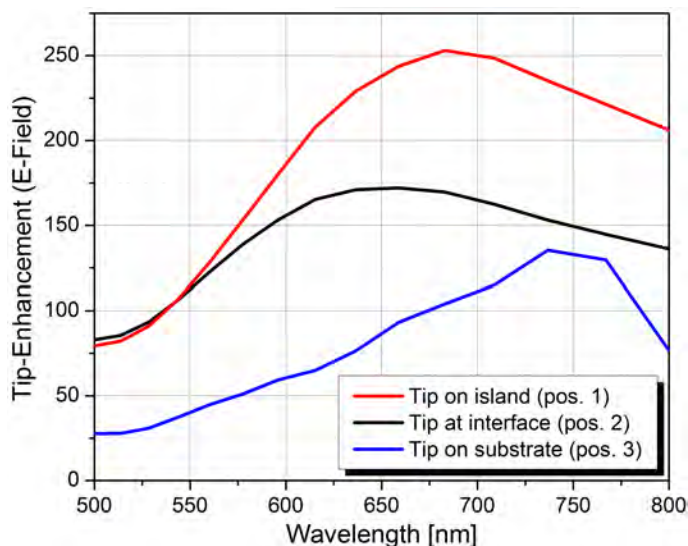


Figure 5.6.11: Simulated electric field enhancement at the tip as a function of the wavelength for three different tip positions.

All three tip positions lead to a different plasmon resonance frequency of the tip. The longest wavelength (750 nm) is observed when the tip is placed 2 nm above the platinum substrate (position 3). The shortest wavelength is 600 nm when the tip is placed at the edge of the island at a distance of 32 nm above the platinum substrate (position 2). When the tip is moved towards the center of the island and the tip-to-substrate distance is kept constant at 32 nm, the resonance wavelength increases again to 700 nm (position 1).

This simulation thus confirms our interpretation that an increase of the distance between the tip and the platinum substrate, due to the thickness of the PbTiO_3 island, leads to a blue-shift, and that the permittivity of the islands leads to a red-shift of the plasmon resonance.

The SPR frequencies of the simulation are red-shifted by about 70 nm compared to the experimental results. This might be caused by differences in the tip shape and tip radius, which is badly defined in our experiment. However, the relative shift of the plasmon frequency by 50 nm between position 1 and position 3, as well as the increase of the field enhancement as the tip approaches the island, are in good agreement with our experimental results.

Furthermore, we can use the simulated SPR frequency shift to explain the contrast at the perimeter of the islands in the Rayleigh scattering (PMT) image in Figure 5.5.2 (b): The blue-shift at the perimeter leads to an increased signal at the Rayleigh line and therefore a higher signal on the PMT.

5.6.7 High resolution mapping

In order to investigate the structure of an individual island, a second TERS map with an increased resolution is recorded on island 3. The mapping is carried out with a reduced scan range of 200 nm x 200 nm at 64x64 points, resulting in a scan

resolution of 3.1 nm per pixel. Figure 5.6.12 (a) shows the false color map of the tip-enhanced signal integrated over the full spectrum. Please note that the tip has now been used for two hours of constant scanning with a laser excitation of 8.5 mW but shows no indications of decreased enhancement.

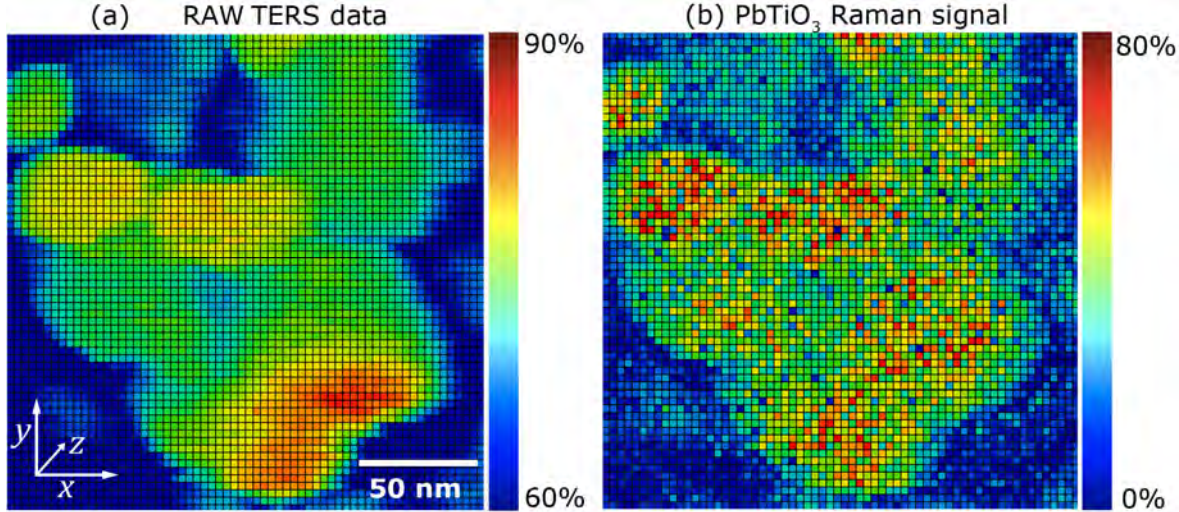


Figure 5.6.12: TERS map of island 3 with 64×64 points on $200 \text{ nm} \times 200 \text{ nm}$. (a) The Raman signal is integrated from 65 cm^{-1} to 1800 cm^{-1} . (b) Extracted Raman signal after removal of the fluorescent background. The plot shows the integrated signal between 65 cm^{-1} and 105 cm^{-1} .

The image shows island number 3 (visible by increased signal intensity) as it was grown on top of the platinum substrate (blue in the false color map). Two additional areas with a higher signal appear in the upper part of the map but cannot be assigned to the island because they are much flatter when compared in the topography scan (Figure 5.5.2 (a)). The island shows regions with different signal intensities. Increased intensity is observed along the perimeter while the center of the island features a signal decrease. In order to put the signal variation into context with the atomic structure of the island, the tip fluorescence is filtered out (with the algorithm described in section 5.6.3) and the Raman signal of the ferroelectric PbTiO_3 (between 65 cm^{-1} and 105 cm^{-1}) is plotted (Figure 5.6.12 (b)). The island appears to be composed of five individual ferroelectric grains that show reduced Raman scattering along their grain boundaries. We therefore assume that the nucleation of PbTiO_3 started simultaneously at several locations (here five) on the TiO_2 seed and led to less tetragonal grain boundaries due to different crystallographic orientations of the grains⁴⁰.

As an additional piece of evidence, we observe a red-shift of the SPR of 10 nm to 15 nm in wavelength along the grain boundaries, as the map of the surface plasmon resonance frequency in Figure 5.6.13 shows. Following our discussion in

⁴⁰ The epitaxial growth on a (111)-oriented platinum surface allows for two inequivalent nucleation sites that are not compatible and lead to grain boundaries. In conjunction with these two sites, the tetragonal structure of PbTiO_3 exhibits three possible orientations of the c-axis leading to 6 possible crystal orientations in total.

section 5.6.5, a red-shift can be caused by a local increase of the optical permittivity of the sample. Hosseini et al. calculated the optical permittivity for lead titanate at 650 nm wavelength for the tetragonal and cubic phase. Their results predict an increase in permittivity of approximately 15% when the phase of lead titanate changes from ferroelectric ($\epsilon \approx 7$) to paraelectric ($\epsilon \approx 8$) [218]. Based on the permittivity of gold (see Fig. 3.1.1) and the plasmon resonance condition from equation 2.5.6, such a permittivity change can lead to a red-shift of up to 50 nm in wavelength. It is therefore likely to observe an SPR red-shift at the grain boundaries during the TERS mapping of the island. The plasmon resonance shift of the TERS tip can therefore be used to locally investigate variations of the optical permittivity. This provides a new way to image local variations of the refractive index of a sample with nanometer resolution.

Due to a different refractive index of the grain boundaries compared to the ferroelectric grains [221, 222], our TERS map reveals the precise location of the grain boundaries in the PbTiO_3 island. The map also provides an explanation for the PFM images in Figure 5.3.2 (b). The PFM scans showed a decrease of piezoresponse in the center of the islands that is now confirmed to be caused by the grain boundaries due to nucleation of grains at different positions of the island.

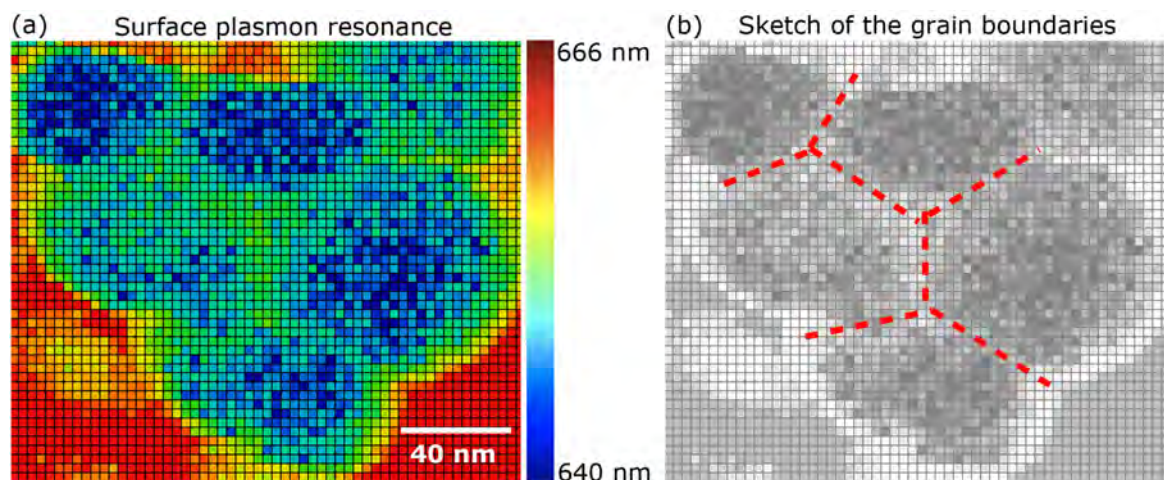


Figure 5.6.13: (a) Map of the surface plasmon resonance frequency of the TERS tip. The island contains five ferroelectric grains that lead to a blue-shift and are separated by grain boundaries with a higher permittivity that leads to relative red-shift of the SPR. (b) Sketch of the position of the grain boundaries (red) in the island (grey).

Last but not least, we would like to assess the lateral resolution. A closer look at the map of the raw TERS data in Figure 5.6.12 (a), shows that the contrast at the perimeter of the islands appear sharper in the Y-direction than in the X-direction. We assess the resolution specifically in the lead titanate Raman signal (Fig. 5.6.12 (b)) to verify that the direction dependence also occurs in the filtered Raman data. This ensures that we can quantify the TERS resolution without influence from the SPR shift. Figure 5.6.14 shows two cross sections of the extracted Raman signal across the perimeter of the island averaged over a width of 13 nm (4 pixels). The steepness of the transition between the platinum substrate and the

signal atop the islands can be used to estimate the lateral resolution. One cross section shows the transition across the island in the Y-direction and one cross section shows the transition in the direction of the fast scanning axis (X-direction). The highest resolution is found in the Y-direction with a contrast over approximately 3-4 nm. This resolution is over 200 times higher than the diffraction-limited resolution of the confocal setup.

The differences in resolution are likely to be related to different field gradients of the surface plasmon on the tip in the corresponding direction. Different field gradients might be caused by an asymmetry of the apex of the tip.

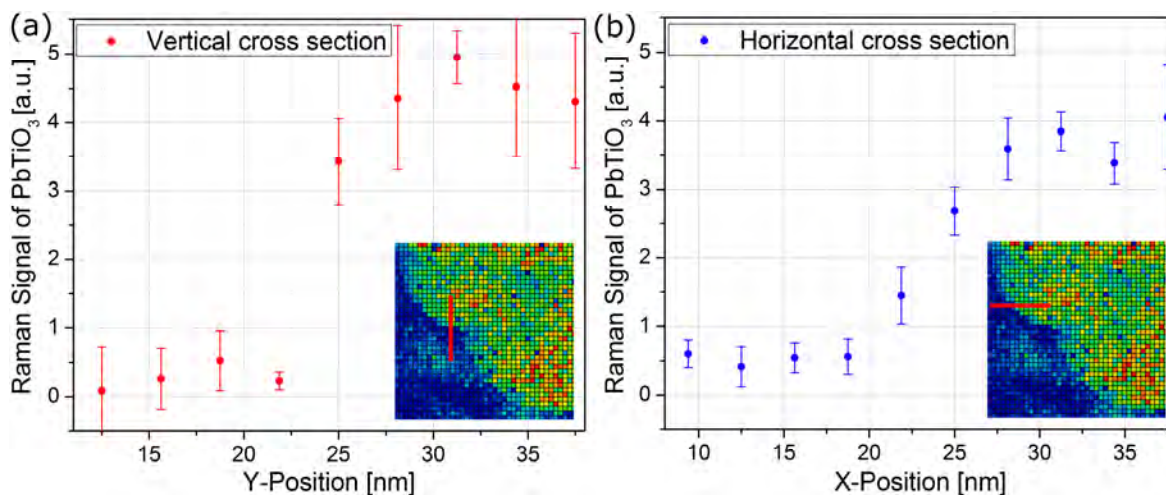


Figure 5.6.14: Cross sections of the extracted Raman signal from the PbTiO_3 of island 3 as indicated in the insets. The cross sections are averaged over a width of 4 pixels along the perimeter. (a) Y-direction: The transition from the platinum substrate to the island takes place over a distance of about 1 pixel. This corresponds to a resolution of 3-4 nm. (b) X-direction: The transition is visible over a distance of 3 pixels (10 nm).

5.7 Summary

The spatial resolution of TERS revealed a substructure of the nano-islands per seed. For a particular island, we observed five grains with a diameter of approximately 50 nm.

The tip that provided best TERS results on lead titanate showed a large fluorescence background that varied in intensity and peak position depending on the tip position. This fluorescence served to track the surface plasmon resonance of the tip based on a Lorentzian oscillator model. Numerical simulations predict a competition between blue and red-shift for increasing distance between tip and metal substrate, and for increasing refractive index, respectively. Following a deconvolution of the topography effect on the surface plasmon resonance shift, we extracted a refractive index profile of the nano-islands with a spatial resolution of less than 10 nm. Under the given experimental conditions, in particular laser heating, the grain boundaries appear to be in the paraelectric phase.

The Lorentzian model allows the successful removal of the tip fluorescence in order to extract the lead titanate Raman signal with a resolution of 4 nm. In addition to the chemical information, which identifies lead titanate as the only compound present on the surface, the Raman intensity decreases at the grain boundaries due to damping. Such a decrease is another indicator of the ferroelectric-to-paraelectric phase transition.

The refractive index distribution and the Raman intensity map thus independently indicate the occurrence of a phase transition along the grain boundaries with unprecedented resolution. The existence of these grain boundaries is a result of two inequivalent nucleation sites combined with the possible orientations of the tetragonal axis in columnar growth.

Due to these findings, earlier observations by PFM of inhomogeneous piezoresponse across individual nano-islands are thus a consequence of grain boundaries rather than chemical phase segregation into lead oxide and TiO_2 .

6 Conclusions

This work shows successful TERS operation under ambient conditions on non-transparent and partially non-conductive samples with pronounced topographic features and large contrasts in permittivity. This opens the door for TERS as a powerful analytical tool for nanoelectronic devices. We distinguished between metallic and semiconducting CNT, and identified the chemical composition, the phase, and the internal grain structure of lead titanate nano-islands with nanometer resolution by TERS. An important effect with relevance to future TERS experiments under comparable conditions was observed: The surface plasmon resonance on the tip drastically changes due to a competition of two separable effects: On one hand, the gap width between tip and metal surface, and on the other hand, variations of the dielectric permittivity across the sample. What initially appeared to be a challenge eventually transformed into a novel technique to determine refractive index changes on a nanoscale sample with unprecedented spatial resolution.

TERS thus holds the promise of providing chemical, structural, and functional information on nanoelectronic devices with unrivaled resolution two orders of magnitude below the diffraction limit of light.

TERS System

The TERS system was specifically designed to operate on 1-inch nanoelectronic samples under ambient conditions and has successfully demonstrated the following operations:

- Side-access TERS under 65 degrees with a 0.42 NA objective and strong p-polarization for the excitation of longitudinal surface plasmons on the TERS tip. This setup especially allows for the investigation of non-transparent samples.
- The objective-to-tip alignment is reproducibly achieved with sub-wavelength precision by a piezoelectric objective scanner while the tip is in feedback-contact with the sample. A misalignment of only 400 nm between the tip and the 0.42 NA objective was demonstrated to cause a 50 % decrease of the tip-enhanced Raman signal indicating that the alignment precision is truly determined by diffraction.
- STM-TERS mapping on single wall carbon nanotubes with a diameter of about 1.3 nm demonstrated a lateral resolution of 14 nm. The chemical sensitivity allowed differentiation between metallic and semi-conducting CNTs.
- AFM-TERS with quartz tuning forks in shear force mode on non-conductive nano-islands showed a lateral resolution of 4 nm.

TERS probe preparation

- TERS tips were successfully produced by electrochemical etching of gold wires with hydrochloric acid and rectangular voltage pulses.
- Reproducible production of tips with a smooth surface and a radius of 30 nm was achieved.
- The field enhancement was measured by TERS on CNTs and an amplification of the Raman signal intensity by a factor of up to 13,000 could be verified corresponding to an enhancement of the E-field by a factor of 10.
- For non-conductive samples, the tips were attached to quartz tuning forks while maintaining a high quality factor of over 5000. This allowed for stable scanning over a period of at least 12 hours.
- The tip-sample distance and the oscillation amplitude of the tuning forks were experimentally verified. Stable conditions were achieved at a distance of 1.5 nm and with an oscillation amplitude of 0.4 nm.

Tip-sample interaction on nanoelectronics

The surface plasmon resonance frequency of the TERS tip was investigated during the mapping of dielectric nanostructures on metallic electrodes and led to the following conclusions:

- A distance variation between the metallic substrate and the tip leads to a shift of the plasmon resonance frequency of 40 cm^{-1} per nanometer distance-change and consequently to a position dependence of the tip enhancement.
- An increase of the local optical permittivity of the sample from $\epsilon = 7$ to $\epsilon = 8$ was experimentally verified to cause a red-shift in the plasmon frequency of the tip of approximately 250 cm^{-1} .
- TERS on nanoelectronic samples thus encounters variations of the plasmon resonance frequency of the tip during scanning. With the finite spectral width of the SPR that leads to a pronounced enhancement of the Raman signal at the SPR frequency, the comparison of TERS spectra at different sample positions becomes misleading.
- Ideally, the functionality of the TERS tip should be verified on a reference sample with similar dielectric properties as the sample of interest.

Finite size effects of ferroelectric nanostructures

TERS was applied to individual lead titanate nano-islands on platinized silicon with the following results:

- TERS revealed the chemical identity of PbTiO_3 in its ferroelectric phase without the presence of secondary compounds.

-
- TERS revealed that the islands are close to the paraelectric phase. This is explained by elevated temperatures in the TERS volume due to laser heating and by a reduction of the transition temperature due to size effects.
 - A TERS map was recorded with 4 nm resolution and revealed the existence of several ferroelectric grains within a single lead titanate island. This confirms theories that the islands nucleate at several locations simultaneously during the growth process.
 - A map of the plasmon resonance shift on the TERS probe was numerically extracted and images local variations of the refractive index in the sample with nanometer resolution. Variations of the refractive index at grain boundaries are presumably associated to finite size effects.
 - Tracking the shift of the plasmon frequency during scanning can be used as an imaging tool for the refractive index on the nanoscale.

7 Outlook

TERS now claims a place among the characterization tools for complex nano-electronic samples. Through the investigation of the tip-sample interaction, we demonstrated the suitability of TERS for a wide range of applications and samples in nanotechnology. This paves the way for a wider use of TERS in the field.

The major challenge remains the inefficient provision of good TERS tips. All production methods defy precise control of the plasmon resonance of the tip, and therefore suffer from a relatively low yield of functioning tips in comparison with other scanning probe techniques such as AFM. The next step could be the industrialization of the tip production, including a screening process that measures the SPR frequency of each tip. The frequency characterization would allow for selecting tips specifically for the applied laser wavelength and in consideration of the permittivity of the sample.

The TERS system itself also leaves room for improvements. One option is to implement a wavelength-tunable laser to optimally excite the surface plasmons on the tip at their resonance frequency. This would, however, require a triple-stage spectrometer to adapt to a variable Rayleigh line suppression. Such a setup could theoretically even track the plasmon resonance frequency during the TERS mapping and thus compensate for sample-dependent frequency shifts such as observed on dielectric samples.

The application of TERS to the investigation of the superparaelectric limit at room temperature requires lower local temperatures and thus lower laser intensities than those used in this project. Lower intensities, in return, require tips with higher enhancement factors, but little is known about the heating effect within the near-field of the tip. The high field intensities at the tip are expected to lead to local temperatures that can be significantly above the melting point of the tip material, although melting was not observed experimentally in our case. Before drawing reliable conclusions about the superparaelectric limit from TERS measurements obtained on ferroelectrics, a better understanding of the temperature close to the tip is imperative. The ratio between Stokes and anti-Stokes shift is a precise indicator of the Boltzmann distribution of vibrational states, from which the local temperature can be extracted. Measuring the anti-Stokes shift requires the installation of a notch filter instead of an edge filter to allow the observations of higher energetic photons.

With the aforementioned technical improvements, TERS will be ready to be deployed to the following fields:

- Determination of the superparaelectric limit of ferroelectric nanostructures.
- Direct measurement of the growth of conductive filaments or conductive channels during the resistive switching of oxides [223].
- Imaging of the atomic structure and chirality of carbon nanotubes at intercalations [224, 225].
- Determination of the structural quality and/or doping levels of graphene layers implemented in electronic devices [226].

- Investigations of the lattice structure in phase-change materials [227].
- Quantification and imaging of the strain in thin films [228].
- Investigation of the strain-fields of individual dislocations in crystals [229].
- Surface analysis for chemical identification of nanometer-sized contaminants, e.g. for the cleaning of nano-lithography masks [230].
- TERS on electronic devices during operation.
- Imaging of local refractive index changes at the nanoscale, e.g. for investigations on optical waveguides.

8 Abbreviations

AFM	Atomic Force Microscopy (or Microscope)
CSD	Chemical Solution Deposition
DC	Direct Current
DRAM	Dynamic Random Access Memory
EM	Electromagnetic
FWHM	Full Width at Half Maximum
IR	Infrared
LA	Longitudinal Acoustic
LO	Longitudinal Optical
NSOM	Near-field Scanning Optical Microscopy (a.k.a. SNOM)
PFM	Piezoresponse Force Microscopy (or Microscope)
RMS	Root Mean Square
SEM	Scanning Electron Microscopy (or Microscope)
SERS	Surface-Enhanced Raman Spectroscopy (or Scattering)
SNOM	Scanning Near-field Optical Microscopy
SPM	Scanning Probe Microscopy (or Microscope)
SPR	Surface Plasmon Resonance
SPRS	Surface Plasmon Resonance Spectroscopy
STM	Scanning Tunneling Microscopy (or Microscope)
TA	Transversal Acoustic
TEM	Transmission Electron Microscopy (or Microscope)
TERS	Tip-Enhanced Raman Spectroscopy (or Scattering)
TO	Transversal Optical
UHV	Ultra High Vacuum
UV	Ultraviolet

9 Bibliography

- [1] G. Binnig, H. Rohrer, C. Gerber, and E. Weibel, 'Tunneling through a controllable vacuum gap', *Applied Physics Letters*, **40**, 178-180, (1982).
- [2] G. Binnig, and Gerber. C, 'Piezo drive with coarse and fine adjustment', *IBM Technical Disclosure Bulletin*, **22**, 2897-2898, (1979).
- [3] G. Binnig, and D. P. E. Smith, 'Single-tube 3-dimensional scanner for scanning tunneling microscopy', *Review of Scientific Instruments*, **57**, 1688-1689, (1986).
- [4] G. Binnig, H. Rohrer, C. Gerber, and E. Weibel, '7x7 reconstruction on Si(111) resolved in real space', *Physical Review Letters*, **50**, 120-123, (1983).
- [5] G. Binnig, C. F. Quate, and C. Gerber, 'Atomic Force Microscope', *Physical Review Letters*, **56**, 930-933, (1986).
- [6] Inc. Future Markets, 'The world market for advanced microscopes', 95, (2011).
- [7] Adolf Smekal, 'Zur Quantentheorie der Dispersion', *Die Naturwissenschaften*, **11**, 873, (1923).
- [8] Grigory Landsberg, and Leonid Mandelstam, 'Eine neue Erscheinung bei der Lichtzerstreuung in Krystallen', *Die Naturwissenschaften*, **16**, 557, (1928).
- [9] C. V. Raman, and K. S. Krishnan, 'A New type of Secondary Radiation', *Nature*, **121**, 502, (1928).
- [10] C. V. Raman, 'A change of Wave-length in Light Scattering', *Nature*, **121**, 619, (1928).
- [11] C. V. Raman, and K. S. Krishnan, 'The Optical Analogue of the Compton Effect', *Nature*, **121**, 711, (1928).
- [12] T. H. Maiman, 'Stimulated Optical Radiation in Ruby', *Nature*, **187**, 493-494, (1960).
- [13] R. Loudon, 'The raman effect in crystals', *Advances in Physics*, **13**, 423-482, (1964).
- [14] G. Gouadec, and P. Colomban, 'Raman Spectroscopy of nanomaterials: How spectra relate to disorder, particle size and mechanical properties', *Progress in Crystal Growth and Characterization of Materials*, **53**, 1-56, (2007).
- [15] Edward Hutchinson Synge, 'A suggested model for extending microscopic resolution into the ultra-microscopic region', *Philos. Mag.*, **6**, 356-362, (1928).
- [16] Edward Hutchinson Synge, 'An application of piezo-electricity to microscopy', *Philos. Mag.*, **13**, 297-300, (1932).
- [17] E. A. Ash, and G. Nicholls, 'Super-resolution aperture scanning microscope', *Nature*, **237**, 510, (1972).
- [18] Lukas Novotny, 'The History of Near-field Optics', in *Progress in Optics*, ed. by E. Wolf (Amsterdam, The Netherlands: Elsevier, 2007), pp. 137-184.
- [19] A. Lewis, M. Isaacson, A. Harootunian, and A. Muray, 'Development of a 500 Å spatial resolution light microscope', *Ultramicroscopy*, **13**, 227-231, (1984).
- [20] D. W. Pohl, W. Denk, and M. Lanz, 'Optical stethoscopy - Image recording with resolution $\lambda/20$ ', *Applied Physics Letters*, **44**, 651-653, (1984).
- [21] U. Durig, D. W. Pohl, and F. Rohner, 'Near-field optical-scanning microscopy', *Journal of Applied Physics*, **59**, 3318-3327, (1986).
- [22] E. Betzig, P. L. Finn, and J. S. Weiner, 'Combined shear force and near-field scanning optical microscopy', *Applied Physics Letters*, **60**, 2484-2486, (1992).
- [23] E. Betzig, and J. K. Trautman, 'Near-field optics - Microscopy, spectroscopy, and surface modification beyond the diffraction limit', *Science*, **257**, 189-195, (1992).
- [24] E. Betzig, J. K. Trautman, T. D. Harris, J. S. Weiner, and R. L. Kostelak, 'Breaking the diffraction barrier - Optical microscopy on a nanometric scale', *Science*, **251**, 1468-1470, (1991).

- [25] M. H. P. Moers, R. G. Tack, N. F. Vanhulst, and B. Bolger, 'A combined near-field optical and force microscope', *Scanning Microscopy*, **7**, 789-792, (1993).
- [26] R. Toledo-Crow, P. C. Yang, Y. Chen, and M. Vaeziravani, 'Near-field differential scanning optical microscope with atomic force regulation', *Applied Physics Letters*, **60**, 2957-2959, (1992).
- [27] R. Zenobi, and V. Deckert, 'Scanning near-field optical microscopy and spectroscopy as a tool for chemical analysis', *Angewandte Chemie-International Edition*, **39**, 1746-1756, (2000).
- [28] F. Zenhausern, M. P. Oboyle, and H. K. Wickramasinghe, 'Apertureless near-field optical microscope', *Applied Physics Letters*, **65**, 1623-1625, (1994).
- [29] E. Betzig, and R. J. Chichester, 'Single molecules observed by near-field scanning optical microscopy', *Science*, **262**, 1422-1425, (1993).
- [30] D. A. Smith, S. Webster, M. Ayad, S. D. Evans, D. Fogherty, and D. Batchelder, 'Development of a scanning near-field optical probe for localised Raman spectroscopy', *Ultramicroscopy*, **61**, 247-252, (1995).
- [31] N. Hayazawa, Y. Inouye, Z. Sekkat, and S. Kawata, 'Near-field Raman imaging of organic molecules by an apertureless metallic probe scanning optical microscope', *Journal of Chemical Physics*, **117**, 1296-1301, (2002).
- [32] M. Fleischmann, P. J. Hendra, and McQuilla. A. J., 'Raman-spectra of pyridine adsorbed at a silver electrode', *Chemical Physics Letters*, **26**, 163-166, (1974).
- [33] A. J. McQuillan, P. J. Hendra, and M. Fleischmann, 'Raman spectroscopic investigation of silver electrodes', *Journal of Electroanalytical Chemistry*, **65**, 933-944, (1975).
- [34] A. Wokaun, J. P. Gordon, and P. F. Liao, 'Radiation damping in surface-enhanced Raman-scattering', *Physical Review Letters*, **48**, 957-960, (1982).
- [35] D. L. Jeanmaire, and R. P. Vanduyne, 'Surface Raman Spectroelectrochemistry', *Journal of Electroanalytical Chemistry*, **84**, 1-20, (1977).
- [36] A. Campion, and P. Kambhampati, 'Surface-enhanced Raman scattering', *Chemical Society Reviews*, **27**, 241-250, (1998).
- [37] M. G. Albrecht, and J. A. Creighton, 'Anomalous Intense Raman-Spectra of Pyridine at a Silver Electrode', *Journal of the American Chemical Society*, **99**, 5215-5217, (1977).
- [38] J. Wessel, 'Surface-enhanced optical microscopy', *Journal of the Optical Society of America B-Optical Physics*, **2**, 1538-1541, (1985).
- [39] R. M. Stockle, Y. D. Suh, V. Deckert, and R. Zenobi, 'Nanoscale chemical analysis by tip-enhanced Raman spectroscopy', *Chemical Physics Letters*, **318**, 131-136, (2000).
- [40] M. S. Anderson, 'Locally enhanced Raman spectroscopy with an atomic force microscope', *Applied Physics Letters*, **76**, 3130-3132, (2000).
- [41] N. Hayazawa, Y. Inouye, Z. Sekkat, and S. Kawata, 'Metallized tip amplification of near-field Raman scattering', *Optics Communications*, **183**, 333-336, (2000).
- [42] Katrin Domke, 'Tip-enhanced Raman spectroscopy - Topographic and chemical information on the nanoscale' (Ph.D. Thesis, Freie Universität Berlin, 2006).
- [43] B. Pettinger, B. Ren, G. Picardi, R. Schuster, and G. Ertl, 'Tip-enhanced Raman spectroscopy (TERS) of malachite green isothiocyanate at Au(111): bleaching behavior under the influence of high electromagnetic fields', *Journal of Raman Spectroscopy*, **36**, 541-550, (2005).
- [44] R. Zhang, Y. Zhang, Z. C. Dong, S. Jiang, C. Zhang, L. G. Chen, L. Zhang, Y. Liao, J. Aizpurua, Y. Luo, J. L. Yang, and J. G. Hou, 'Chemical mapping of a single molecule by plasmon-enhanced Raman scattering', *Nature*, **498**, 82-86, (2013).
- [45] Rainer Waser, *Nanoelectronics and Information Technology*. 3 edn (Berlin: Wiley-VCH, 2012).
- [46] J. F. Scott, 'Applications of modern ferroelectrics', *Science*, **315**, 954-959, (2007).
- [47] Andreas Roelofs, 'Size Effects in Ferroelectric Thin Films' (Dissertation, RWTH Aachen University, 2004).

- [48] Johannes Stadler, Thomas Schmid, and Renato Zenobi, 'Developments in and practical guidelines for tip-enhanced Raman spectroscopy', *Nanoscale*, **4**, 1856-1870, (2012).
- [49] A. Cvitkovic, N. Ocelic, and R. Hillenbrand, 'Analytical model for quantitative prediction of material contrasts in scattering-type near-field optical microscopy', *Optics Express*, **15**, 8550-8565, (2007).
- [50] T. Haertling, P. Reichenbach, and L. M. Eng, 'Near-field coupling of a single fluorescent molecule and a spherical gold nanoparticle', *Optics Express*, **15**, 12806-12817, (2007).
- [51] J. A. Porto, P. Johansson, S. P. Apell, and T. Lopez-Rios, 'Resonance shift effects in apertureless scanning near-field optical microscopy', *Physical Review B*, **67**, 085409, (2003).
- [52] A. L. Demming, F. Festy, and D. Richards, 'Plasmon resonances on metal tips: Understanding tip-enhanced Raman scattering', *Journal of Chemical Physics*, **122**, 184716, (2005).
- [53] B. Pettinger, K. F. Domke, D. Zhang, R. Schuster, and G. Ertl, 'Direct monitoring of plasmon resonances in a tip-surface gap of varying width', *Physical Review B*, **76**, 113409, (2007).
- [54] S. Clemens, T. Schneller, A. van der Hart, F. Peter, and R. Waser, 'Registered deposition of nanoscale ferroelectric grains by template-controlled growth', *Advanced Materials*, **17**, 1357, (2005).
- [55] M. F. Crommie, C. P. Lutz, and D. M. Eigler, 'Confinement of electrons to quantum corrals on a metal surface', *Science*, **262**, 218-220, (1993).
- [56] S. Morita, R. Wiesendanger, E. Meyer, and Franz J. Giessibl, *Noncontact Atomic Force Microscopy* (Berlin ; New York: Springer, 2002).
- [57] Knut Urban, *Probing the Nanoworld, 38th Spring School, IFF Spring School, Forschungszentrum Jülich* (Jülich, Germany, 2007).
- [58] A. G. T. Ruiter, K. O. van der Werf, J. A. Veerman, M. F. Garcia-Parajo, W. H. J. Rensen, and N. F. van Hulst, 'Tuning fork shear-force feedback', *Ultramicroscopy*, **71**, 149-157, (1998).
- [59] D. I. Bradley, P. Crookston, M. J. Fear, S. N. Fisher, G. Foulds, D. Garg, A. M. Guenault, E. Guise, R. P. Haley, O. Kolosov, G. R. Pickett, R. Schanen, and V. Tsepelin, 'Measuring the Prong Velocity of Quartz Tuning Forks Used to Probe Quantum Fluids', *Journal of Low Temperature Physics*, **161**, 536-547, (2010).
- [60] K. Karrai, and R. D. Grober, 'Piezoelectric tip-sample distance control for near-field optical microscopes', *Applied Physics Letters*, **66**, 1842-1844, (1995).
- [61] F. J. Giessibl, 'Atomic resolution on Si(111)-(7x7) by noncontact atomic force microscopy with a force sensor based on a quartz tuning fork', *Applied Physics Letters*, **76**, 1470-1472, (2000).
- [62] M. Heyde, M. Sterrer, H. P. Rust, and H. J. Freund, 'Atomic resolution on MgO(001) by atomic force microscopy using a double quartz tuning fork sensor at low-temperature and ultrahigh vacuum', *Applied Physics Letters*, **87**, 083104, (2005).
- [63] Frank Peter, 'Piezoresponse Force Microscopy and Surface Effects of Perovskite Ferroelectric Nanostructures' (Ph.D. Thesis, Forschungszentrum Jülich, 2006).
- [64] M. Nicklaus, M. Moretti, and A. Ruediger, 'Application Note: High-resolution ferroelectric domain imaging and hysteresis measurement by piezoresponse force microscopy with the SmartSPM 1000', *AIST-NT Inc.*, (2011).
- [65] A. Roelofs, T. Schneller, K. Szot, and R. Waser, 'Towards the limit of ferroelectric nanosized grains', *Nanotechnology*, **14**, 250-253, (2003).
- [66] M. Nicklaus, A. Pignolet, C. Harnagea, and A. Ruediger, 'Noncontact atomic force microscopy imaging of ferroelectric domains with functionalized tips', *Applied Physics Letters*, **98**, 162901, (2011).
- [67] I.R. Lewis, and H.G. Edwards, *Handbook of Raman Spectroscopy - From the Research Laboratory to the Process Line* (New York: Taylor and Francis Group, 2001).

- [68] R.L. McCreery, *Raman Spectroscopy for Chemical Analysis* (New York: John Wiley and Sons, 2000).
- [69] W.H. Weber, and R. Merlin, *Raman Scattering in Materials Science* (Berlin: Springer-Verlag, 2000).
- [70] G. B. Wright, and Mooradian A., 'Raman scattering from donor and acceptor impurities in silicon', *Physical Review Letters*, **18**, 608-610, (1967).
- [71] Ludwig Bergmann, Clemens Schäfer, and Wilhelm Raith, *Lehrbuch der Experimentalphysik, Bd. 6 Festkörper* (Berlin, Germany: De Gruyter, 1992).
- [72] P. A. Temple, and C. E. Hathaway, 'Multiphonon Raman spectrum of silicon', *Physical Review B*, **7**, 3685-3697, (1973).
- [73] E. Abbe, 'Beiträge zur Microscopie und der Microscopischen Wahrnehmung', *Arch. Mikrosk. Anat.*, **9**, 413-468, (1873).
- [74] L. Rayleigh, 'Investigations in optics with special reference to the spectroscope', *Phil. Mag.*, **8**, 261, (1879).
- [75] Dai Zhang, Xiao Wang, Kai Braun, Hans-Joachim Egelhaaf, Monika Fleischer, Laura Hennemann, Holger Hintz, Catrinel Stanciu, Christoph J. Brabec, Dieter P. Kern, and Alfred J. Meixner, 'Parabolic mirror-assisted tip-enhanced spectroscopic imaging for non-transparent materials', *Journal of Raman Spectroscopy*, **40**, 1371-1376, (2009).
- [76] Rose Solé, Luisa Bausa, and Daniel Jaque, *An Introduction to the Optical Spectroscopy of Inorganic Solids* (New York: John Wiley & Sons, 2005), p. 114.
- [77] Lukas Novotny, and Bert Hecht, *Principles of Nano-Optics* (Cambridge, England: Cambridge University Press, 2011).
- [78] J. D. Jackson, *Classical Electrodynamics, 3rd Ed.* (New York: Wiley, 1998).
- [79] C. Girard, and A. Dereux, 'Near-field optics theories', *Reports on Progress in Physics*, **59**, 657-699, (1996).
- [80] T. Lecklider, 'The world of the near field', *Evaluation Engineering*, **44**, 52, (2005).
- [81] P. B. Johnson, and R. W. Christy, 'Optical constants of noble metals', *Physical Review B*, **6**, 4370-4379, (1972).
- [82] P. R. West, S. Ishii, G. V. Naik, N. K. Emani, V. M. Shalaev, and A. Boltasseva, 'Searching for better plasmonic materials', *Laser & Photonics Reviews*, **4**, 795-808, (2010).
- [83] E. D. Palik, *Handbook of Optical Constants of Solids* (San Diego: Academic Press, 1998).
- [84] Monas Shahzad, Gautam Medhi, Robert E. Peale, Walter R. Buchwald, Justin W. Cleary, Richard Soref, Glenn D. Boreman, and Oliver Edwards, 'Infrared surface plasmons on heavily doped silicon', *Journal of Applied Physics*, **110**, 123105, (2011).
- [85] H.J.; Mitchell Simon, D.E.; Watson, J.G., 'Surface plasmons in silver films - A novel undergraduate experiment', *American Journal of Physics*, **43**, 630, (1975).
- [86] J. M. Pitarke, V. M. Silkin, E. V. Chulkov, and P. M. Echenique, 'Theory of surface plasmons and surface-plasmon polaritons', *Reports on Progress in Physics*, **70**, 1-87, (2007).
- [87] A. Otto, 'Excitation of nonradiative surface plasma waves in silver by the method of frustrated total reflection', *Zeitschrift für Physik*, **216**, 398-410, (1968).
- [88] E. Kretschmann, 'Die Bestimmung optischer Konstanten von Metallen durch Anregung von Oberflächenplasmaschwingungen', *Zeitschrift für Physik*, **241**, 313-324, (1971).
- [89] Debdulal Roy, Jian Wang, and Craig Williams, 'Novel methodology for estimating the enhancement factor for tip-enhanced Raman spectroscopy', *Journal of Applied Physics*, **105**, 013530, (2009).
- [90] S. S. Kharintsev, G. G. Hoffmann, A. I. Fishman, and M. K. Salakhov, 'Plasmonic optical antenna design for performing tip-enhanced Raman spectroscopy and microscopy', *Journal of Physics D-Applied Physics*, **46**, 145501, (2013).
- [91] Stefanie Dengler, Christian Kuebel, Andreas Schwenke, Gunnar Ritt, and Bernd Eberle, 'Near- and off-resonant optical limiting properties of gold-silver alloy nanoparticles for intense nanosecond laser pulses', *Journal of Optics*, **14**, 075203, (2012).

- [92] S. Link, and M. A. El-Sayed, 'Size and temperature dependence of the plasmon absorption of colloidal gold nanoparticles', *Journal of Physical Chemistry B*, **103**, 4212-4217, (1999).
- [93] P. K. Jain, K. S. Lee, I. H. El-Sayed, and M. A. El-Sayed, 'Calculated absorption and scattering properties of gold nanoparticles of different size, shape, and composition: Applications in biological imaging and biomedicine', *Journal of Physical Chemistry B*, **110**, 7238-7248, (2006).
- [94] W. Lee, S. Y. Lee, R. M. Briber, and O. Rabin, 'Self-Assembled SERS Substrates with Tunable Surface Plasmon Resonances', *Advanced Functional Materials*, **21**, 3424-3429, (2011).
- [95] M. Moskovits, 'Surface-enhanced spectroscopy', *Reviews of Modern Physics*, **57**, 783-826, (1985).
- [96] K. Kneipp, H. Kneipp, I. Itzkan, R. R. Dasari, and M. S. Feld, 'Surface-enhanced Raman scattering and biophysics', *Journal of Physics-Condensed Matter*, **14**, R597-R624, (2002).
- [97] Evan J. Blackie, Eric C. Le Ru, and Pablo G. Etchegoin, 'Single-Molecule Surface-Enhanced Raman Spectroscopy of Nonresonant Molecules', *Journal of the American Chemical Society*, **131**, 14466-14472, (2009).
- [98] B. Pettinger, G. Picardi, R. Schuster, and G. Ertl, 'Surface enhanced Raman spectroscopy: Towards single molecular spectroscopy', *Electrochemistry*, **68**, 942-949, (2000).
- [99] V. Deckert, D. Zeisel, R. Zenobi, and T. Vo-Dinh, 'Near-field surface enhanced Raman imaging of dye-labeled DNA with 100-nm resolution', *Analytical Chemistry*, **70**, 2646-2650, (1998).
- [100] D. Zeisel, V. Deckert, R. Zenobi, and T. Vo-Dinh, 'Near-field surface-enhanced Raman spectroscopy of dye molecules adsorbed on silver island films', *Chemical Physics Letters*, **283**, 381-385, (1998).
- [101] M. Lee, S. Lee, J. H. Lee, H. W. Lim, G. H. Seong, E. K. Lee, S. I. Chang, C. H. Oh, and J. Choo, 'Highly reproducible immunoassay of cancer markers on a gold-patterned microarray chip using surface-enhanced Raman scattering imaging', *Biosensors & Bioelectronics*, **26**, 2135-2141, (2011).
- [102] M. J. Banholzer, J. E. Millstone, L. D. Qin, and C. A. Mirkin, 'Rationally designed nanostructures for surface-enhanced Raman spectroscopy', *Chemical Society Reviews*, **37**, 885-897, (2008).
- [103] Y. C. Liu, C. C. Wang, and C. E. Tsai, 'Effects of electrolytes used in roughening gold substrates by oxidation-reduction cycles on surface-enhanced Raman scattering', *Electrochemistry Communications*, **7**, 1345-1350, (2005).
- [104] C. L. Haynes, A. D. McFarland, and R. P. Van Duyne, 'Surface-enhanced Raman spectroscopy', *Analytical Chemistry*, **77**, 338A-346A, (2005).
- [105] E. Hao, and G. C. Schatz, 'Electromagnetic fields around silver nanoparticles and dimers', *Journal of Chemical Physics*, **120**, 357-366, (2004).
- [106] L. Gunnarsson, E. J. Bjerneld, H. Xu, S. Petronis, B. Kasemo, and M. Kall, 'Interparticle coupling effects in nanofabricated substrates for surface-enhanced Raman scattering', *Applied Physics Letters*, **78**, 802-804, (2001).
- [107] A. Sanchez-Iglesias, P. Aldeanueva-Potel, W. H. Ni, J. Perez-Juste, I. Pastoriza-Santos, R. A. Alvarez-Puebla, B. N. Mbenkum, and L. M. Liz-Marzan, 'Chemical seeded growth of Ag nanoparticle arrays and their application as reproducible SERS substrates', *Nano Today*, **5**, 21-27, (2010).
- [108] C. E. Talley, J. B. Jackson, C. Oubre, N. K. Grady, C. W. Hollars, S. M. Lane, T. R. Huser, P. Nordlander, and N. J. Halas, 'Surface-enhanced Raman scattering from individual Au nanoparticles and nanoparticle dimer substrates', *Nano Letters*, **5**, 1569-1574, (2005).
- [109] R. G. Freeman, K. C. Grabar, K. J. Allison, R. M. Bright, J. A. Davis, A. P. Guthrie, M. B. Hommer, M. A. Jackson, P. C. Smith, D. G. Walter, and M. J. Natan, 'Self-assembled metal colloid monolayers - An approach to SERS substrates', *Science*, **267**, 1629-1632, (1995).

- [110] K. A. Homan, J. Chen, A. Schiano, M. Mohamed, K. A. Willets, S. Murugesan, K. J. Stevenson, and S. Emelianov, 'Silver-Polymer Composite Stars: Synthesis and Applications', *Advanced Functional Materials*, **21**, 1673-1680, (2011).
- [111] Paolo Biagioni, Jer-Shing Huang, and Bert Hecht, 'Nanoantennas for visible and infrared radiation', *Reports on progress in physics. Physical Society (Great Britain)*, **75**, 024402, (2012).
- [112] J. J. Mock, S. M. Norton, S. Y. Chen, A. A. Lazarides, and D. R. Smith, 'Electromagnetic Enhancement Effect Caused by Aggregation on SERS-Active Gold Nanoparticles', *Plasmonics*, **6**, 113-124, (2011).
- [113] H. Im, K. C. Bantz, N. C. Lindquist, C. L. Haynes, and S. H. Oh, 'Vertically Oriented Sub-10-nm Plasmonic Nanogap Arrays', *Nano Letters*, **10**, 2231-2236, (2010).
- [114] Z. L. Yang, J. Aizpurua, and H. X. Xu, 'Electromagnetic field enhancement in TERS configurations', *Journal of Raman Spectroscopy*, **40**, 1343-1348, (2009).
- [115] M. Micic, N. Klymyshyn, Y. D. Suh, and H. P. Lu, 'Finite element method simulation of the field distribution for AFM tip-enhanced surface-enhanced Raman scanning microscopy', *Journal of Physical Chemistry B*, **107**, 1574-1584, (2003).
- [116] C. C. Neacsu, J. Dreyer, N. Behr, and M. B. Raschke, 'Scanning-probe Raman spectroscopy with single-molecule sensitivity', *Physical Review B*, **73**, 193406, (2006).
- [117] M. Nicklaus, C. Nauenheim, A. Krayev, V. Gavriluk, A. Belyaev, and A. Ruediger, 'Tip enhanced Raman spectroscopy with objective scanner on opaque samples', *Review of Scientific Instruments*, **83**, 066102, (2012).
- [118] K. F. Domke, D. Zhang, and B. Pettinger, 'Tip-enhanced Raman spectra of picomole quantities of DNA nucleobases at Au(111)', *Journal of the American Chemical Society*, **129**, 6708, (2007).
- [119] B. N. J. Persson, 'On the theory of surface-enhanced Raman-scattering', *Chemical Physics Letters*, **82**, 561-565, (1981).
- [120] P. Kambhampati, C. M. Child, M. C. Foster, and A. Champion, 'On the chemical mechanism of surface enhanced Raman scattering: Experiment and theory', *Journal of Chemical Physics*, **108**, 5013-5026, (1998).
- [121] E. V. Efremov, F. Ariese, and C. Gooijer, 'Achievements in resonance Raman spectroscopy review of a technique with a distinct analytical chemistry potential', *Analytica Chimica Acta*, **606**, 119-134, (2008).
- [122] J. R. Lombardi, R. L. Birke, L. A. Sanchez, I. Bernard, and S. C. Sun, 'The effect of molecular-structure on voltage induced shifts of charge-transfer excitation in surface enhanced Raman-scattering', *Chemical Physics Letters*, **104**, 240-247, (1984).
- [123] H. X. Xu, E. J. Bjerneld, M. Kall, and L. Borjesson, 'Spectroscopy of single hemoglobin molecules by surface enhanced Raman scattering', *Physical Review Letters*, **83**, 4357-4360, (1999).
- [124] A. Otto, I. Mrozek, H. Grabhorn, and W. Akemann, 'Surface-enhanced Raman-scattering', *Journal of Physics-Condensed Matter*, **4**, 1143-1212, (1992).
- [125] M. T. Sun, Y. R. Fang, Z. L. Yang, and H. X. Xu, 'Chemical and electromagnetic mechanisms of tip-enhanced Raman scattering', *Physical Chemistry Chemical Physics*, **11**, 9412-9419, (2009).
- [126] L. T. Nieman, G. M. Krampert, and R. E. Martinez, 'An apertureless near-field scanning optical microscope and its application to surface-enhanced Raman spectroscopy and multiphoton fluorescence imaging', *Review of Scientific Instruments*, **72**, 1691-1699, (2001).
- [127] B. Pettinger, B. Ren, G. Picardi, R. Schuster, and G. Ertl, 'Nanoscale probing of adsorbed species by tip-enhanced Raman spectroscopy', *Physical Review Letters*, **92**, 096101, (2004).
- [128] K. L. A. Chan, and S. G. Kazarian, 'Tip-enhanced Raman mapping with top-illumination AFM', *Nanotechnology*, **22**, 175701, (2011).

- [129] L. Novotny, E. J. Sanchez, and X. S. Xie, 'Near-field optical imaging using metal tips illuminated by higher-order Hermite-Gaussian beams', *Ultramicroscopy*, **71**, 21-29, (1998).
- [130] K. S. Youngworth, and T. G. Brown, 'Focusing of high numerical aperture cylindrical-vector beams', *Optics Express*, **7**, 77-87, (2000).
- [131] S. Quabis, R. Dorn, and G. Leuchs, 'Generation of a radially polarized doughnut mode of high quality', *Applied Physics B-Lasers and Optics*, **81**, 597-600, (2005).
- [132] N. Hayazawa, Y. Saito, and S. Kawata, 'Detection and characterization of longitudinal field for tip-enhanced Raman spectroscopy', *Applied Physics Letters*, **85**, 6239-6241, (2004).
- [133] O. Auciello, J. F. Scott, and R. Ramesh, 'The physics of ferroelectric memories', *Physics Today*, **51**, 22-27, (1998).
- [134] S. L. Miller, and P. J. McWhorter, 'Physics of the ferroelectric nonvolatile memory field-effect transistor', *Journal of Applied Physics*, **72**, 5999-6010, (1992).
- [135] Giovanni A. Salvatore, Livio Lattanzio, Didier Bouvet, Igor Stolichnov, Nava Setter, and Adrian M. Ionescu, 'Ferroelectric transistors with improved characteristics at high temperature', *Applied Physics Letters*, **97**, 053503, (2010).
- [136] D. S. Jeong, B. K. Cheong, and H. Kohlstedt, 'Pt/Ti/Al₂O₃/Al tunnel junctions exhibiting electroforming-free bipolar resistive switching behavior', *Solid-State Electronics*, **63**, 1-4, (2011).
- [137] G. Burns, and B. A. Scott, 'Raman studies of underdamped soft modes in PbTiO₃', *Physical Review Letters*, **25**, 167, (1970).
- [138] P. Ghosez, E. Cockayne, U. V. Waghmare, and K. M. Rabe, 'Lattice dynamics of BaTiO₃, PbTiO₃, and PbZrO₃: A comparative first-principles study', *Physical Review B*, **60**, 836-843, (1999).
- [139] Karin A. Rabe, Matthew Dawber, Celine Lichtensteiger, Charles H. Ahn, and Jean-Marc Triscone, 'Modern physics of ferroelectrics: Essential background', in *Physics of Ferroelectrics: A Modern Perspective*, ed. by K. M. Rabe, C. H. Ahn and J. M. Triscone, (2007), pp. 1-30.
- [140] Rainer Waser, *Nanoelectronics and Information Technology*. 1 edn (Berlin: Wiley-VCH, 2003).
- [141] K. Ishikawa, K. Yoshikawa, and N. Okada, 'Size effect on the ferroelectric phase-transition in PbTiO₃ ultrafine particles', *Physical Review B*, **37**, 5852-5855, (1988).
- [142] Manuel Lopes, Timothée Toury, M. L. De la Chapelle, Francesco Bonaccorso, and Pietro Guiseppe Gucciardi, 'Fast and reliable fabrication of gold tips with sub-50 nm radius of curvature for tip-enhanced Raman spectroscopy', *Review of Scientific Instruments*, **84**, 073702, (2013).
- [143] B. Ren, G. Picardi, and B. Pettinger, 'Preparation of gold tips suitable for tip-enhanced Raman spectroscopy and light emission by electrochemical etching', *Review of Scientific Instruments*, **75**, 837-841, (2004).
- [144] S. S. Kharintsev, A. I. Noskov, G. G. Hoffmann, and J. Loos, 'Near-field optical taper antennas fabricated with a highly replicable ac electrochemical etching method', *Nanotechnology*, **22**, 025202, (2011).
- [145] Y. Han, R. Lupitskiy, T. M. Chou, C. M. Stafford, H. Du, and S. Sukhishvili, 'Effect of Oxidation on Surface-Enhanced Raman Scattering Activity of Silver Nanoparticles: A Quantitative Correlation', *Analytical Chemistry*, **83**, 5873-5880, (2011).
- [146] Vladimir Poborchii, Tetsuya Tada, Toshihiko Kanayama, and Pavel Geshev, 'Optimization of tip material and shape for near-UV TERS in Si structures', *Journal of Raman Spectroscopy*, **40**, 1377-1385, (2009).
- [147] Melek Erol, Yun Han, Scott K. Stanley, Christopher M. Stafford, Henry Du, and Svetlana Sukhishvili, 'SERS Not To Be Taken for Granted in the Presence of Oxygen', *Journal of the American Chemical Society*, **131**, 7480, (2009).
- [148] Chun-Nam Lok, Chi-Ming Ho, Rong Chen, Qing-Yu He, Wing-Yiu Yu, Hongzhe Sun, Paul Kwong-Hang Tam, Jen-Fu Chiu, and Chi-Ming Che, 'Silver nanoparticles: partial

- oxidation and antibacterial activities', *Journal of Biological Inorganic Chemistry*, **12**, 527-534, (2007).
- [149] R. Boehme, M. Mkandawire, U. Krause-Buchholz, P. Rosch, G. Rodel, J. Popp, and V. Deckert, 'Characterizing cytochrome c states - TERS studies of whole mitochondria', *Chemical Communications*, **47**, 11453-11455, (2011).
- [150] L. J. Xue, W. Z. Li, G. G. Hoffmann, J. G. P. Goossens, J. Loos, and G. de With, 'High-Resolution Chemical Identification of Polymer Blend Thin Films Using Tip-Enhanced Raman Mapping', *Macromolecules*, **44**, 2852-2858, (2011).
- [151] O. L. Guise, J. W. Ahner, M. C. Jung, P. C. Goughnour, and J. T. Yates, 'Reproducible electrochemical etching of tungsten probe tips', *Nano Letters*, **2**, 191-193, (2002).
- [152] A. D. Muller, F. Muller, M. Hietschold, F. Demming, J. Jersch, and K. Dickmann, 'Characterization of electrochemically etched tungsten tips for scanning tunneling microscopy', *Review of Scientific Instruments*, **70**, 3970-3972, (1999).
- [153] J. P. Ibe, P. P. Bey, S. L. Brandow, R. A. Brizzolara, N. A. Burnham, D. P. Dilella, K. P. Lee, C. R. K. Marrian, and R. J. Colton, 'On the electrochemical etching of tips for scanning tunneling microscopy', *Journal of Vacuum Science & Technology a-Vacuum Surfaces and Films*, **8**, 3570-3575, (1990).
- [154] L. Zhu, J. Atesang, P. Dudek, M. Hecker, J. Rinderknecht, Y. Ritz, H. Geisler, U. Herr, R. Greer, and E. Zschech, 'Experimental challenges for approaching local strain determination in silicon by nano-Raman spectroscopy', *Materials Science-Poland*, **25**, 19-31, (2007).
- [155] K. Dickmann, F. Demming, and J. Jersch, 'New etching procedure for silver scanning tunneling microscopy tips', *Review of Scientific Instruments*, **67**, 845-846, (1996).
- [156] C. Zhang, B. Gao, L. G. Chen, Q. S. Meng, H. Yang, R. Zhang, X. Tao, H. Y. Gao, Y. Liao, and Z. C. Dong, 'Fabrication of silver tips for scanning tunneling microscope induced luminescence', *Review of Scientific Instruments*, **82**, 083101, (2011).
- [157] M. Iwami, Y. Uehara, and S. Ushioda, 'Preparation of silver tips for scanning tunneling microscopy imaging', *Review of Scientific Instruments*, **69**, 4010-4011, (1998).
- [158] C. Williams, and D. Roy, 'Fabrication of gold tips suitable for tip-enhanced Raman spectroscopy', *Journal of Vacuum Science & Technology B*, **26**, 1761-1764, (2008).
- [159] L. Billot, L. Berguiga, M. L. de la Chapelle, Y. Gilbert, and R. Bachelot, 'Production of gold tips for tip-enhanced near-field optical microscopy and spectroscopy: analysis of the etching parameters', *European Physical Journal-Applied Physics*, **31**, 139-145, (2005).
- [160] B. Pettinger, 'Tip-enhanced Raman spectroscopy (TERS)', *Surface-Enhanced Raman Scattering: Physics and Applications*, **103**, 217-240, (2006).
- [161] M. M. Jobbins, A. F. Raigoza, and S. A. Kandel, 'Note: Circuit design for direct current and alternating current electrochemical etching of scanning probe microscopy tips', *Review of Scientific Instruments*, **83**, 036105, (2012).
- [162] G. Tremiliosi-Filho, E.R. Gonzalez, A.J. Motheo, E.M. Belgsir, J.-M. Leger, and C. Lamy, 'Electro-oxidation of ethanol on gold: analysis of the reaction products and mechanism', *Journal of Electroanalytical Chemistry*, **444**, 31-39, (1998).
- [163] C.D. Breach, 'What is the future of bonding wire? Will copper entirely replace gold?', *Gold Bulletin*, **43**, 150, (2010).
- [164] C.W. Extrand, and S.I. Moon, 'Critical Meniscus height of liquids at the circular edge of cylindrical rods and disks', *Langmuir*, **25**, 992-996, (2009).
- [165] <http://www.solvaychemicals.com> Solvay Chemicals, 'Hydrochloric Acid - Surface Tension'
- [166] <http://www.handymath.com/cgi-bin/hcltbl3.cgi?submit=Entry> 'Density of hydrochloric acid',
- [167] Kenneth L. Osborne, 'Temperature-Dependence of the Contact Angle of Water on Graphite, Silicon, and Gold', Worcester Polytechnic Institute, (2009).
- [168] Thomas Schmid, Boon-Siang Yeo, Grace Leong, Johannes Stadler, and Renato Zenobi, 'Performing tip-enhanced Raman spectroscopy in liquids', *Journal of Raman Spectroscopy*, **40**, 1392-1399, (2009).

- [169] Elena Bailo, and Volker Deckert, 'Tip-enhanced Raman spectroscopy of single RNA strands: Towards a novel direct-sequencing method', *Angewandte Chemie-International Edition*, **47**, 1658-1661, (2008).
- [170] Boon-Siang Yeo, Thomas Schmid, Weihua Zhang, and Renato Zenobi, 'Towards rapid nanoscale chemical analysis using tip-enhanced Raman spectroscopy with Ag-coated dielectric tips', *Analytical and Bioanalytical Chemistry*, **387**, 2655-2662, (2007).
- [171] A. Rasmussen, and V. Deckert, 'Surface- and tip-enhanced Raman scattering of DNA components', *Journal of Raman Spectroscopy*, **37**, 311-317, (2006).
- [172] Y. Saito, T. Murakami, Y. Inouye, and S. Kawata, 'Fabrication of silver probes for localized plasmon excitation in near-field Raman spectroscopy', *Chemistry Letters*, **34**, 920-921, (2005).
- [173] T. Deckert-Gaudig, and V. Deckert, 'Tip-enhanced Raman scattering (TERS) and high-resolution bio nano-analysis-a comparison', *Physical Chemistry Chemical Physics*, **12**, 12040-12049, (2010).
- [174] Xiu-Mei Lin, Yan Cui, Yan-Hui Xu, Bin Ren, and Zhong-Qun Tian, 'Surface-enhanced Raman spectroscopy: substrate-related issues', *Analytical and Bioanalytical Chemistry*, **394**, 1729-1745, (2009).
- [175] Katharina Hering, Dana Cialla, Katrin Ackermann, Thomas Doerfer, Robert Moeller, Henrik Schneidewind, Roland Mattheis, Wolfgang Fritzsche, Petra Roesch, and Juergen Popp, 'SERS: a versatile tool in chemical and biochemical diagnostics', *Analytical and Bioanalytical Chemistry*, **390**, 113-124, (2008).
- [176] Xudong Cui, Weihua Zhang, Boon-Siang Yeo, Renato Zenobi, Christian Hafner, and Daniel Erni, 'Tuning the resonance frequency of Ag-coated dielectric tips', *Optics Express*, **15**, 8309-8316, (2007).
- [177] Yang Gan, 'A review of techniques for attaching micro- and nanoparticles to a probe's tip for surface force and near-field optical measurements', *Review of Scientific Instruments*, **78**, 081101, (2007).
- [178] J. J. Wang, Y. Saito, D. N. Batchelder, J. Kirkham, C. Robinson, and D. A. Smith, 'Controllable method for the preparation of metalized probes for efficient scanning near-field optical Raman microscopy', *Applied Physics Letters*, **86**, 263111, (2005).
- [179] Takayuki Umakoshi, Taka-aki Yano, Yuika Saito, and Prabhat Verma, 'Fabrication of Near-Field Plasmonic Tip by Photoreduction for Strong Enhancement in Tip-Enhanced Raman Spectroscopy', *Applied Physics Express*, **5**, 052001, (2012).
- [180] M. Fleischer, A. Weber-Bargioni, S. Cabrini, and D. P. Kern, 'Fabrication of metallic nanocones by induced deposition of etch masks and ion milling', *Microelectronic Engineering*, **88**, 2247-2250, (2011).
- [181] J. N. Farahani, H. J. Eisler, D. W. Pohl, M. Pavius, P. Fluckiger, P. Gasser, and B. Hecht, 'Bow-tie optical antenna probes for single-emitter scanning near-field optical microscopy', *Nanotechnology*, **18**, 125506, (2007).
- [182] A. Weber-Bargioni, A. Schwartzberg, M. Schmidt, B. Harteneck, D. F. Ogletree, P. J. Schuck, and S. Cabrini, 'Functional plasmonic antenna scanning probes fabricated by induced-deposition mask lithography', *Nanotechnology*, **21**, 065306, (2010).
- [183] M. Becker, V. Sivakov, G. Andrae, R. Geiger, J. Schreiber, S. Hoffmann, J. Michler, A. P. Milenin, P. Werner, and S. H. Christiansen, 'The SERS and TERS effects obtained by gold droplets on top of Si nanowires', *Nano Letters*, **7**, 75-80, (2007).
- [184] Michael Becker, Vladimir Sivakov, Ulrich Goesele, Thomas Stelzner, Gudrun Andrae, Hans J. Reich, Samuel Hoffmann, Johannes Michler, and Silke H. Christiansen, 'Nanowires enabling signal-enhanced nanoscale Raman spectroscopy', *Small*, **4**, 398-404, (2008).
- [185] Valentinas Snitka, Raul D. Rodrigues, and Vitas Lendraitis, 'Novel gold cantilever for nano-Raman spectroscopy of graphene', *Microelectronic Engineering*, **88**, 2759-2762, (2011).

- [186] E. Pensa, E. Cortes, G. Corthey, P. Carro, C. Vericat, M. H. Fonticelli, G. Benitez, A. A. Rubert, and R. C. Salvarezza, 'The Chemistry of the Sulfur-Gold Interface: In Search of a Unified Model', *Accounts of Chemical Research*, **45**, 1183-1192, (2012).
- [187] D. R. Lide, *Handbook of Chemistry and Physics*. Vol. 81st Edition CRC, 2000).
- [188] Robert L. Olmon, Brian Slovick, Timothy W. Johnson, David Shelton, Sang-Hyun Oh, Glenn D. Boreman, and Markus B. Raschke, 'Optical dielectric function of gold', *Physical Review B*, **86**, 235147, (2012).
- [189] Y. Golan, L. Margulis, and I. Rubinstein, 'Vacuum-deposited gold-films', *Surface Science*, **264**, 312-326, (1992).
- [190] A. Putnam, B. L. Blackford, M. H. Jericho, and M. O. Watanabe, 'Surface-topography study of gold deposited on mica using scanning tunneling microscopy - effect of mica temperature', *Surface Science*, **217**, 276-288, (1989).
- [191] J. A. Derose, T. Thundat, L. A. Nagahara, and S. M. Lindsay, 'Gold grown epitaxially on mica - Conditions for large area flat faces', *Surface Science*, **256**, 102-108, (1991).
- [192] S. Buchholz, H. Fuchs, and J. P. Rabe, 'Surface-structure of thin metallic-films on mica as seen by scanning tunneling microscopy, scanning electron microscopy, and low-energy electron-diffraction', *Journal of Vacuum Science & Technology B*, **9**, 857-861, (1991).
- [193] C. Nogues, and M. Wanunu, 'A rapid approach to reproducible, atomically flat gold films on mica', *Surface Science*, **573**, L383-L389, (2004).
- [194] T. Deckert-Gaudig, and V. Deckert, 'Ultraflat Transparent Gold Nanoplates - Ideal Substrates for Tip-enhanced Raman Scattering Experiments', *Small*, **5**, 432-436, (2009).
- [195] Xueshen Wang, Qunqing Li, Jing Xie, Zhong Jin, Jinyong Wang, Yan Li, Kaili Jiang, and Shoushan Fan, 'Fabrication of Ultralong and Electrically Uniform Single-Walled Carbon Nanotubes on Clean Substrates', *Nano Letters*, **9**, 3137-3141, (2009).
- [196] C. Fantini, A. Jorio, M. Souza, M. S. Strano, M. S. Dresselhaus, and M. A. Pimenta, 'Optical transition energies for carbon nanotubes from resonant Raman spectroscopy: Environment and temperature effects', *Physical Review Letters*, **93**, 147406, (2004).
- [197] A. G. Souza, S. G. Chou, G. G. Samsonidze, G. Dresselhaus, M. S. Dresselhaus, L. An, J. Liu, A. K. Swan, M. S. Unlu, B. B. Goldberg, A. Jorio, A. Gruneis, and R. Saito, 'Stokes and anti-Stokes Raman spectra of small-diameter isolated carbon nanotubes', *Physical Review B*, **69**, 115428, (2004).
- [198] H. Kataura, Y. Kumazawa, Y. Maniwa, I. Umez, S. Suzuki, Y. Ohtsuka, and Y. Achiba, 'Optical properties of single-wall carbon nanotubes', *Synthetic Metals*, **103**, 2555-2558, (1999).
- [199] <http://en.wikipedia.org/wiki/File:KatauraPlot.jpg> Wikipedia/user:NIMSooffice, 'Kataura Plot' [Accessed 2013/06/26].
- [200] A. Kukovecz, C. Kramberger, V. Georgakilas, M. Prato, and H. Kuzmany, 'A detailed Raman study on thin single-wall carbon nanotubes prepared by the HiPCO process', *European Physical Journal B*, **28**, 223-230, (2002).
- [201] H. Kataura, Y. Maniwa, S. Masubuchi, S. Kazama, X. Zhao, Y. Ando, Y. Ohtsuka, S. Suzuki, Y. Achiba, and R. Saito, 'Bundle effects of single-wall carbon nanotubes', in *Electronic Properties of Novel Materials-Molecular Nanostructures*, ed. by H. Kuzmany, J. Fink, M. Mehring and S. Roth, 2000), pp. 262-265.
- [202] Afshin Moradi, 'Theory of Carbon Nanotubes as Optical Nano Waveguides', *J. Electromagnetic Analysis & Applications*, **2**, 672-676, (2010).
- [203] Stefano Piscanec, Michele Lazzeri, J. Robertson, Andrea C. Ferrari, and Francesco Mauri, 'Optical phonons in carbon nanotubes: Kohn anomalies, Peierls distortions, and dynamic effects', *Physical Review B*, **75**, 035427, (2007).
- [204] A. Jorio, R. Saito, G. Dresselhaus, and M. S. Dresselhaus, 'Determination of nanotubes properties by Raman spectroscopy', *Philosophical Transactions of the Royal Society a-Mathematical Physical and Engineering Sciences*, **362**, 2311-2336, (2004).
- [205] G. Burns, and B. A. Scott, 'Lattice modes in ferroelectric perovskites - PbTiO₃', *Physical Review B*, **7**, 3088-3101, (1973).

- [206] I. Taguchi, A. Pignolet, L. Wang, M. Proctor, F. Levy, and P. E. Schmid, 'Raman-scattering from PbTiO₃ thin-films prepared on silicon substrates by radio-frequency sputtering and thermal-treatment', *Journal of Applied Physics*, **73**, 394-399, (1993).
- [207] A. Rudiger, T. Schneller, A. Roelofs, S. Tiedke, T. Schmitz, and R. Waser, 'Nanosize ferroelectric oxide - tracking down the superparaelectric limit', *Applied Physics a-Materials Science & Processing*, **80**, 1247-1255, (2005).
- [208] I. P. Batra, P. Wurfel, and Silverma.Bd, 'Phase-transition, stability, and depolarization field in ferroelectric thin-films', *Physical Review B*, **8**, 3257-3265, (1973).
- [209] I. P. Batra, P. Wurfel, and Silverma.Bd, 'New type of first-order phase-transition in ferroelectric thin-films', *Physical Review Letters*, **30**, 384-387, (1973).
- [210] S. Berweger, C.C. Neacsu, Y. Mao, H. Zhou, S.S. Wong, and M.B. Raschke, 'Optical nanocrystallography with tip-enhanced phonon Raman spectroscopy', *Nature Nanotechnology*, **4**, 496, (2009).
- [211] T. Schneller, and R. Waser, 'Chemical solution deposition of ferroelectric thin films - State of the art and recent trends', *Ferroelectrics*, **267**, 293-301, (2002).
- [212] R. W. Schwartz, T. Schneller, and R. Waser, 'Chemical solution deposition of electronic oxide films', *Comptes Rendus Chimie*, **7**, 433-461, (2004).
- [213] R. Waser, T. Schneller, P. Ehrhart, and S. Hoffmann-Eifert, 'Chemical deposition methods for ferroelectric thin films', *Ferroelectrics*, **259**, 205-214, (2001).
- [214] S. Clemens, S. Rohrig, A. Rudiger, T. Schneller, and R. Waser, 'Embedded ferroelectric nanostructure arrays', *Nanotechnology*, **20**, 075305, (2009).
- [215] S. Buhlmann, P. Muralt, and S. Von Allmen, 'Lithography-modulated self-assembly of small ferroelectric Pb(Zr,Ti)O₃ single crystals', *Applied Physics Letters*, **84**, 2614-2616, (2004).
- [216] J. A. Sanjurjo, E. Lopezcruz, and G. Burns, 'High-pressure Raman-study of zone-center phonons in PbTiO₃', *Physical Review B*, **28**, 7260-7268, (1983).
- [217] E. Chingprado, A. Reynesfigueroa, R. S. Katiyar, S. B. Majumder, and D. C. Agrawal, 'Raman-spectroscopy and X-ray-diffraction of PbTiO₃ thin-film', *Journal of Applied Physics*, **78**, 1920-1925, (1995).
- [218] A.M. Hosseini, T. Movlaroooy, and A. Kompany, 'First-principles study of the optical properties of PbTiO₃', *European Physical Journal B*, **46**, 463-469, (2005).
- [219] J. Renger, S. Grafstrom, L. M. Eng, and V. Deckert, 'Evanescent wave scattering and local electric field enhancement at ellipsoidal silver particles in the vicinity of a glass surface', *Journal of the Optical Society of America a-Optics Image Science and Vision*, **21**, 1362-1367, (2004).
- [220] Phillip Olk, Jan Renger, Marc Tobias Wenzel, and Lukas M. Eng, 'Distance dependent spectral tuning of two coupled metal nanoparticles', *Nano Letters*, **8**, 1174-1178, (2008).
- [221] Ning Liu, Yu Su, and George J. Weng, 'A phase-field study on the hysteresis behaviors and domain patterns of nanocrystalline ferroelectric polycrystals', *Journal of Applied Physics*, **113**, 204106, (2013).
- [222] G. Arlt, 'THE INFLUENCE OF MICROSTRUCTURE ON THE PROPERTIES OF FERROELECTRIC CERAMICS', *Ferroelectrics*, **104**, 217-227, (1990).
- [223] Rainer Waser, Regina Dittmann, Georgi Staikov, and Kristof Szot, 'Redox-Based Resistive Switching Memories - Nanoionic Mechanisms, Prospects, and Challenges', *Advanced Materials*, **21**, 2632-2663, (2009).
- [224] Zhen Yao, Henk W Ch Postma, Leon Balents, and Cees Dekker, 'Carbon nanotube intramolecular junctions', *Nature*, **402**, 273-276, (1999).
- [225] Thomas Rueckes, Kyoung-ha Kim, Ernesto Joselevich, Greg Y Tseng, Chin-Li Cheung, and Charles M Lieber, 'Carbon nanotube-based nonvolatile random access memory for molecular computing', *Science*, **289**, 94-97, (2000).
- [226] Anindya Das, S Pisana, B Chakraborty, S Piscanec, SK Saha, UV Waghmare, KS Novoselov, HR Krishnamurthy, AK Geim, and AC Ferrari, 'Monitoring dopants by Raman

- scattering in an electrochemically top-gated graphene transistor', *Nature Nanotechnology*, **3**, 210-215, (2008).
- [227] Matthias Wuttig, and Noboru Yamada, 'Phase-change materials for rewriteable data storage', *Nature materials*, **6**, 824-832, (2007).
- [228] D Buca, B Hollander, H Trinkaus, S Mantl, R Carius, R Loo, M Caymax, and H Schaefer, 'Tensely strained silicon on SiGe produced by strain transfer', *Applied Physics Letters*, **85**, 2499-2501, (2004).
- [229] Krzysztof Szot, Wolfgang Speier, Gustav Bihlmayer, and Rainer Waser, 'Switching the electrical resistance of individual dislocations in single-crystalline SrTiO₃', *Nature materials*, **5**, 312-320, (2006).
- [230] Tod Robinson, Andrew Dinsdale, Ron Bozak, and Bernie Arruza, 'Advanced mask particle cleaning solutions', in *27th Annual BACUS Symposium on Photomask Technology* International Society for Optics and Photonics, 2007), pp. 67301Y-67301Y-67311.

10 Publications and conference contributions

Publications

1. Polar properties of hydrothermally synthesized BiFeO₃ thin films, I. Velasco, M. Moretti, M. Nicklaus, C. Nauenheim, S. Li, R. Nechache, C. Gomez-Yanez, A. Ruediger, *Applied Physics A*, accepted (2013)
2. Ultrafast Microwave Hydrothermal Synthesis of BiFeO₃ Nanoplates, S. Li, R. Nechache, I. Velasco, G. Goupil, L. Nikolova, M. Nicklaus, J. Laverdiere, A. Ruediger, F. Rosei, *Journal of the American Ceramic Society*, accepted, doi: 10.1111/jace.12473 (2013)
3. Tip enhanced Raman Spectroscopy with objective scanner on opaque samples, M. Nicklaus, C. Nauenheim, A. Krayev, V. Gavriluk, A. Belyaev, A. Ruediger, *Review of Scientific Instruments* 83, 066102 (2012)
4. Effect of vertical mechanical compression on the resistive switching currents of titanium dioxide thin films, M. Moretti, M. Nicklaus, C. Nauenheim, A. Ruediger, *International Journal of Nanoscience* 11 1240025 (2012)
5. Epitaxial Patterning of Bi₂FeCrO₆ Double Perovskite Nanostructures: Multiferroic at Room Temperature, R. Nechache, C.V. Cojocar, C. Harnagea, C. Nauenheim, M. Nicklaus, A. Ruediger, F. Rosei, A. Pignolet, *Advanced Materials* 23, 1724 (2011)
6. Non-contact atomic force microscopy imaging of ferroelectric domains with functionalized tips, M. Nicklaus, A. Pignolet, C. Harnagea, A. Ruediger, *Applied Physics Letters* 98, 162901 (2011)

Conference contributions

- 10/2013 Talk: “Tip enhanced Raman spectroscopy for imaging dielectric nano-structures on non-transparent substrates” *MS&T Conference* Montréal, Canada.
- 05/2013 **Poster Award:** “Tip Enhanced Raman Spectroscopy for Chemical Characterization of Nano-Structures”, *Canadian Chemistry Society Conference*, Québec City, Canada.
- 10/2012 **Invited Speaker:** “Tip Enhanced Raman Spectroscopy for Chemical Characterization on the Nanoscale”. Session: Frontier of Nanosciences and Technologies, *2nd Annual World Congress of Nano Sciences & Technologies*, Qingdao, China.
- 07/2012 **Poster Award:** “Tip Enhanced Raman Spectroscopy for Chemical Characterization of Nano-Structures” *Inauguration de l’Unité Mixte Internationale*, Orford, Canada.
- 06/2012 Talk: “Tip Enhanced Raman Spectroscopy for chemical characterization of nano-structures” *Photonics North*, Montréal, Canada.
- 05/2012 Poster: *Colloque Plasma-Québec*, Montréal, Canada.
- 03/2012 **Poster Award:** “Tip Enhanced Raman Spectroscopy for Chemical Characterization of Nano-Structures”, *NanoQuébec Conference*, Montréal, Canada.
- 06/2009 Poster: “Domain contrast in tapping mode with dipole molecules on a tip” International Symposium – Piezoresponse Force Microscopy and Nanoscale Phenomena in Polar Materials, Aveiro, Portugal.

Résumé en français

Spectroscopie Raman Exaltée par effet de pointe pour la Nanoélectronique

1	Introduction	I
1.1	Motivation.....	II
1.2	Objectifs.....	II
2	Méthodes	II
2.1	Microscopie à sonde locale.....	III
2.2	Spectroscopie Raman.....	III
3	Exaltation de champ	IV
4	Conception du système TERS	V
5	Production de pointes TERS	VI
6	TERS sur les nanotubes de carbone	VII
7	TERS sur les nanocristaux de titanate de plomb	IX
7.1	Cartographie TERS.....	X
7.2	Décalage de la fréquence de résonance des plasmons de surface.....	XIII
8	Conclusions	XV
9	Bibliographie	XVI

1 Introduction

Au cours des dernières années, est apparue une demande accrue pour une meilleure compréhension des effets chimiques et structuraux ayant lieu dans les systèmes nanoélectroniques en opération. Elle soulève des questions dont les réponses ne peuvent pas être fournies par les modèles macroscopiques ou les caractérisations électroniques indirectes seuls. Une compréhension fondamentale de ces effets physiques est nécessaire pour les modèles afin de permettre le développement systématique de nouveaux matériaux et des systèmes conçus pour des applications.

La microscopie électronique et la microscopie à sonde locale ne permettent que de révéler les informations chimiques et structurales de manière très limitée. Ces informations sont, néanmoins, déjà accessibles par les méthodes de spectroscopies optiques comme les spectroscopies Raman et infrarouge. Cependant, ces dernières techniques sont physiquement limitées en résolution latérale à quelques centaines de nanomètres. Dans le but de réunir les forces des deux méthodes, la spectroscopie Raman exaltée par effet de pointe (dont le sigle anglais TERS, pour *Tip Enhanced Raman Spectroscopy* est communément utilisé) est la combinaison de la spectroscopie Raman et de la microscopie à sonde locale permettant une caractérisation chimique et structurale d'une surface avec une résolution nanométrique et une sensibilité moléculaire. Cela permet une compréhension approfondie des propriétés chimiques, structurales et électroniques des nanomatériaux. La figure 1 illustre la réunion d'une haute résolution spatiale avec les informations chimiques par un exemple photographique.



Figure 1: Analogie photographique : (a) Couleurs floues : la microscopie optique classique est limitée à l'échelle micrométrique. (b) Photographie en noir et blanc : Topographie haute résolution obtenue par microscopie électronique à balayage ou microscopie à force atomique mais (presque) sans information chimique. (c) Photographie en couleur: le TERS combine une haute résolution latérale avec des informations (photographie de la Basilique Notre Dame de Montréal par Harold Stiver).

Le TERS crée un champ proche optique par la focalisation d'un laser externe sur une pointe afin d'exciter un plasmon de surface à l'apex de la pointe. Sous certaines conditions de résonance déterminées par le rayon de la pointe, la longueur d'onde du laser, la permittivité et la géométrie de l'environnement immédiat de la pointe, le champ électrique oscillant du laser peut exciter la résonance des plasmons de surface (dont le sigle anglais SPR, pour *Surface Plasmon Resonance* est communément utilisé). Le champ proche électromagnétique résultant possède une intensité très élevée qui permet d'obtenir une quantité détectable de photons issus de la diffusion Raman quand un échantillon nanométrique est placé dans le champ proche. Par ailleurs, l'intensité du champ décroît rapidement lorsque la distance d entre la pointe et l'échantillon augmente. Cette décroissance suit approximativement une dépendance en $(r + d)^{-10}$ où r est le rayon de la pointe [1].

Quand la pointe effectue un balayage à une distance de 1-2 nm de la surface de l'échantillon, la dépendance du champ proche à la distance permet une résolution optique de quelques nanomètres. La détection d'une seule molécule a été réalisée sur des molécules résonantes à la diffusion Raman en 2005 [2] avec un système inversé et sous vide avec une résolution sub-moléculaire en 2013 [3]. Malgré ces succès, le TERS n'est pas encore devenu une technique de mesure usuelle. Cela est principalement dû à sa complexité en lien avec les contraintes d'échantillons transparents et fortement Raman actifs qui sont requis pour la plupart des systèmes TERS, enfin, dernier point mais non des moindres, l'absence d'un procédé de production de pointes TERS viables.

1.1 Motivation

Un exemple d'effet nanométrique qui nécessite une meilleure compréhension est la limite super-paraélectrique des cristaux ferroélectriques. Les ferroélectriques ont été un sérieux candidat pour l'industrie de la microélectronique, utilisé comme matériau dans les mémoires non volatiles, ce qui a soulevé des questions sur l'effet de la réduction d'échelle. Du fait que la polarisation intrinsèque des ferroélectriques est basée sur leur structure atomique, que cette structure subit une transition de phase dépendante de la taille, et que le rapport surface sur volume augmente dans les petit cristaux, les ferroélectriques peuvent devenir paraélectrique et perdre leur polarisation à l'échelle nanométrique. C'est ce qui est appelée la limite super-paraélectrique. Ishikawa et al. ont utilisé la spectroscopie Raman pour déterminer la température de transition du titanate de plomb pour des poudres dont les grains avec une la taille de 22 nm [4].

Le TERS confère la capacité de sonder des îlots individuels sans altérer leur état après la croissance sur le substrat. La grande intensité de la lumière du TERS génère assez de diffusion Raman dans le volume nanométrique de l'îlot cristallin pour mettre à jour l'état structurel du cristal. De plus, la haute résolution latérale du TERS peut être utilisée pour créer une cartographie chimique et structurelle de nanocristaux isolés.

1.2 Objectifs

Les objectifs de ce projet sont doubles : Premièrement, définir et réaliser un système TERS qui correspond aux contraintes des systèmes nanoélectroniques en élargissant le champ d'application et la polyvalence du TERS et de tester l'exaltation du signal sur un échantillon de référence fait de nanotubes de carbone ; deuxièmement, utiliser le système TERS sur des nanocristaux ferroélectriques de titanate de plomb (PbTiO_3) dans le but de vérifier leur état structurel et d'étudier l'interaction optique entre la pointe et l'échantillon.

2 Méthodes

Le TERS est basé sur deux méthodes d'analyse. La microscopie à sonde locale est utilisée pour analyser la topographie de l'échantillon et pour déplacer la sonde à champ exalté à une distance contrôlée de la surface de l'échantillon. La spectroscopie Raman est utilisée pour analyser la lumière rétrodiffusée provenant de la pointe dans le but d'obtenir les informations concernant la composition chimique et les propriétés structurelles de l'échantillon.

2.1 Microscopie à sonde locale

Les deux types de microscopie à sonde locale utilisés pour effectuer du TERS sont la microscopie à effet tunnel (dont le sigle anglais STM, pour *Scanning Tunneling Microscopy* est communément utilisé) et la microscopie à force atomique (dont le sigle anglais AFM, pour *Atomic Force Microscopy* est communément utilisé). Les deux méthodes sont basées sur une pointe aigüe qui balaye la surface de l'échantillon, à l'aide d'un système de positionnement piézoélectrique, pour générer une image topographique.

Le STM utilise l'effet tunnel qui se traduit par un faible courant électrique entre une pointe atomiquement aigüe et un échantillon métallique quand la pointe se trouve à environ 1 nm de l'échantillon. Ce courant est utilisé pour contrôler la distance entre la pointe et l'échantillon. Dans ce projet, le STM a été utilisé avec des pointes en or gravées, avec un procédé électrochimique, afin de balayer des nanotubes de carbone sur un substrat d'or pour les études TERS.

Puisque le STM peut seulement être utilisé sur des surfaces conductrices, les études des cristaux de titanate de plomb par TERS ont été menées en utilisant l'AFM. L'AFM utilise généralement une pointe située à l'extrémité d'un cantilevier flexible en silicium qui oscille verticalement au-dessus de la surface. L'amplitude des oscillations du cantilevier décroît quand la pointe se rapproche de l'échantillon, ce qui permet un contrôle de la distance. Dans le but d'utiliser l'AFM avec des pointes en or gravées avec un procédé électrochimique, qui sont nécessaires pour générer le plasmon de surface, les pointes sont collées sur des diapasons en quartz de manière à osciller parallèlement à l'échantillon en utilisant les forces de cisaillement pour contrôler la distance entre la pointe et l'échantillon.

2.2 Spectroscopie Raman

L'effet Raman décrit une interaction inélastique des photons avec la matière qui mène à l'excitation des modes vibrationnels et rotationnels des molécules, ou à l'excitation des phonons dans les cristaux. Le principe de la spectroscopie Raman est de mesurer le spectre d'énergie des phonons permettant de déduire les informations chimiques et structurales de l'échantillon.

Un photon peut interagir avec la matière pour permettre à un électron d'accéder à un état d'énergie virtuel plus élevé et égal à l'énergie E_i du photon incident. L'électron revient instantanément à un état d'énergie plus faible en effectuant une transition radiative. Cet état peut être l'état d'origine de l'élection dans le cas de la diffusion Rayleigh, ou un état correspondant à un mode de vibrationnel et rotationnel d'énergie E_k supérieur à l'état d'origine. Ce dernier cas décrit la diffusion Raman et le photon émis à une énergie $E_R = E_i - E_k$. En raison de la faible section efficace de l'effet Raman, seul un photon issu de la diffusion Raman est émis pour 10^6 photons issus de la diffusion Rayleigh. Le spectre optique de la lumière Raman représente les énergies des modes vibrationnels (phonons) de l'échantillon. Cet effet est illustré dans le diagramme de Jablonski en figure 2.

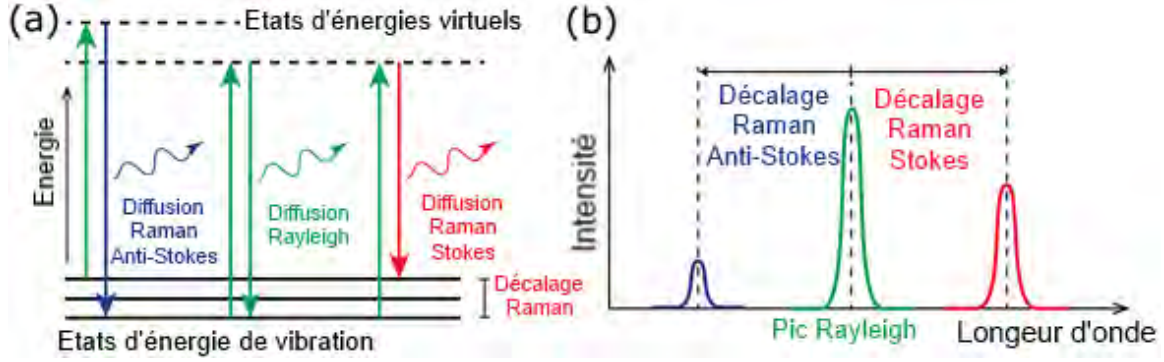


Figure 2: (a) Diagramme de Jablonski des transitions radiatives Rayleigh et Raman dans la matière. Le décalage Raman est donné par la différence d'énergie entre l'état initial et final and et peut être soit négative (décalage Stokes) si un phonon est généré, ou positive (décalage anti-Stokes) si un phonon est absorbé. (b) Spectre d'énergie incluant les régions Stokes et anti-Stokes.

3 Exaltation de champ

L'effet d'exaltation est généré par l'excitation optique d'une résonance de plasmon de surface (SPR) à l'apex de la pointe TERS. Le SPR mène à une amplification du champ électrique proche de l'apex de la pointe par un facteur de 10-100 [5]. L'apex de la pointe TERS peut être décrit, dans un modelé simplifié, par une sphère métallique avec un moment dipolaire $\vec{p} = \vec{E} \cdot \alpha(\lambda)$ soumis à un champ électrique externe E (voir Fig. 3). La polarisabilité α dépend de la longueur d'onde d'excitation et peut être déduite de la relation de Clausius-Mossotti, ce qui mène à :

$$\alpha = 4\pi\epsilon_0 r^3 \frac{\epsilon_{\text{met}}(\lambda, r) - \epsilon_{\text{env}}}{\underbrace{\epsilon_{\text{met}}(\lambda, r) + 2\epsilon_{\text{env}}}_{:=g}}$$

Où r est le rayon de la sphère, ϵ_{env} la permittivité de l'environnement (par exemple, 1 for air), et ϵ_{met} la permittivité de la sphère métallique à la fréquence d'excitation. Ce quotient représente le facteur d'exaltation du champ électrique et est souvent désigné comme le facteur g .

Dans le TERS, le facteur g exalte la lumière incidente ainsi que la lumière issue de la diffusion Raman, provenant de l'échantillon. De plus, l'intensité de la lumière étant de l'ordre de E^2 , le signal Raman détecté est de l'ordre de la 4^{ème} puissance de g : $I_{\text{TERS}} \propto g^4$. Cela mène à une exaltation du signal Raman au niveau de la pointe allant jusqu'à sept ordre de grandeur [2]. Des facteurs d'exaltation aussi élevés sont atteints uniquement directement au niveau de la pointe et le champ électrique décroît rapidement avec la distance :

$$E \propto (R_s + r)^{-10}$$

Où R_s est le rayon de la pointe et r la distance à l'échantillon [1, 2]. La perte rapide de l'intensité du champ sur quelques nanomètres permet des résolutions latérales de l'ordre du nanomètre obtenues en TERS quand la pointe balaye l'échantillon.

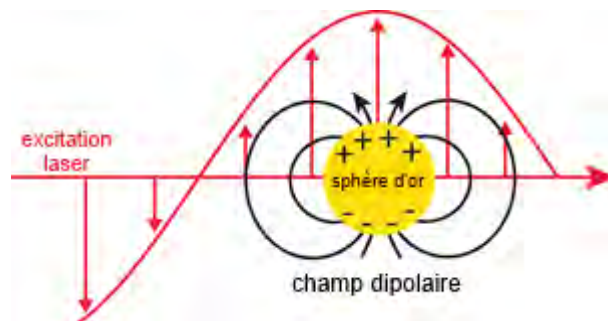


Figure 3: Schéma de l'excitation de la résonance d'un plasmon de surface sur une nanoparticule d'or. Les flèches rouges représentent le champ électrique du laser d'excitation et les lignes noires représentent le champ dipolaire dû aux déplacements des électrons et des trous dans la sphère d'or.

4 Conception du système TERS

Nous avons construits le système TERS pour des échantillons non-transparents et non-conducteurs dans le but de satisfaire aux exigences de la nanoélectronique et de fournir des capacités d'analyse pour un large éventail d'échantillons différents. Le microscope TERS est basé sur un système de balayage d'échantillon droit avec un accès optique latéral équipé d'un objectif d'ouverture numérique de 0.42 (voir Fig. 4). La pointe en or est excitée avec une longueur d'onde de 632.8 nm en polarisation p. Un objectif à balayage piézoélectrique permet d'ajuster focalisation afin de faciliter l'alignement optique entre la pointe et le laser (notre publication à propos de ce concept peut être trouvée en réf. [6]).

Le système optique permet de contrôler la puissance du laser, le diamètre du faisceau, et sa polarisation (voir Fig. 5). La lumière Raman rétrodiffusée est analysée par un spectromètre Czerny-Turner, tandis que la lumière Rayleigh rétrodiffusée est détectée par un tube photomultiplicateur (PM).

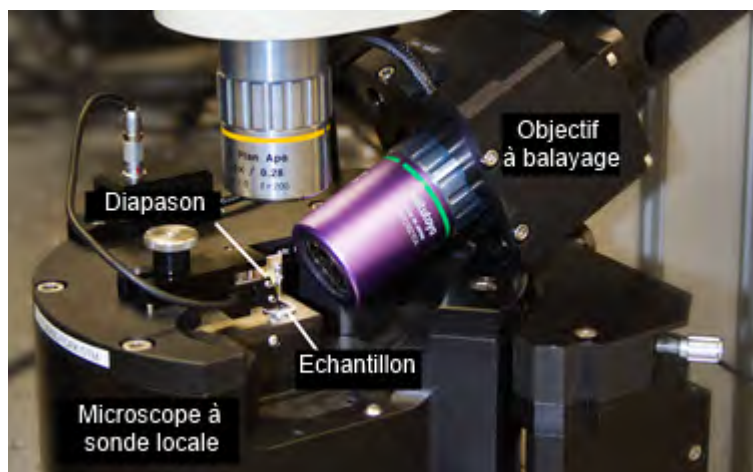


Figure 4: Photographie du microscope à sonde locale avec l'échantillon et le diapason mis en place. L'objectif confocal latéral (violet) et l'objectif de la caméra (argent).

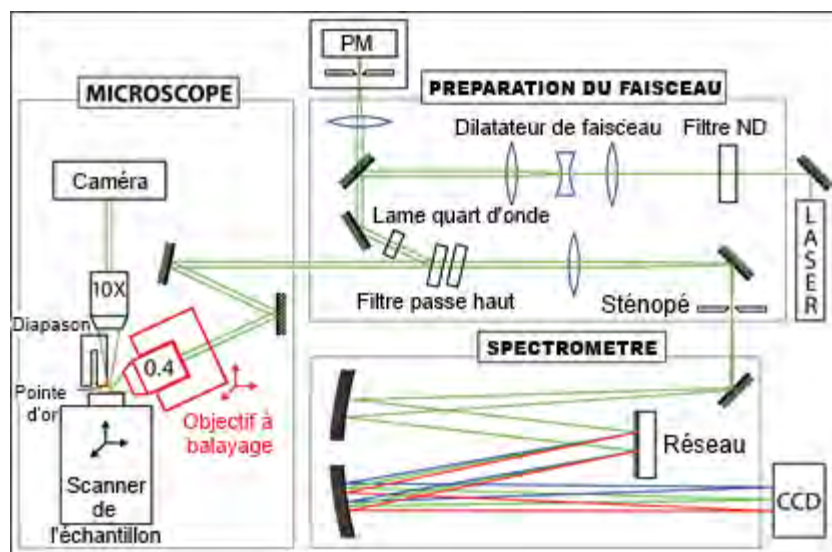


Figure 5: Schéma du montage optique du système TERS

5 Production de pointes TERS

La pointe est un élément crucial pour le TERS car elle définit l'ampleur de l'exaltation du processus Raman. Nous avons mis au point un système de gravure électrochimique pour la production de pointes en or coniques qui a permis d'étudier l'influence de différentes tensions de gravure sur la forme de la pointe et son rayon. Le but était de développer une recette donnant des pointes en or coniques avec un rayon de 30 nm et une faible rugosité de surface. La partie gravée de la pointe ne devrait pas être plus longue que 300 μm pour éviter les vibrations et les déformations de la pointe durant le balayage dont l'apex devrait avoir un faible angle d'ouverture (un rapport d'aspect élevé) pour permettre la création de plasmons de surface.

Après avoir essayé différentes méthodes, nous avons produit des pointes TERS avec une solution concentrée d'acide hydrochlorique et une tension pulsée haute fréquence. La tension de surface de l'acide permet la formation d'un ménisque, qui diminue lorsque le diamètre de la pointe décroît, ce qui donne un fil avec une forme conique à l'extrémité gravée. Le rayon de la pointe est de l'ordre de 30 nm. Le système de gravure est visible sur la figure 6 et les images de microscopie électronique à balayage (MEB) d'une pointe gravée sont montrées sur la figure 7.

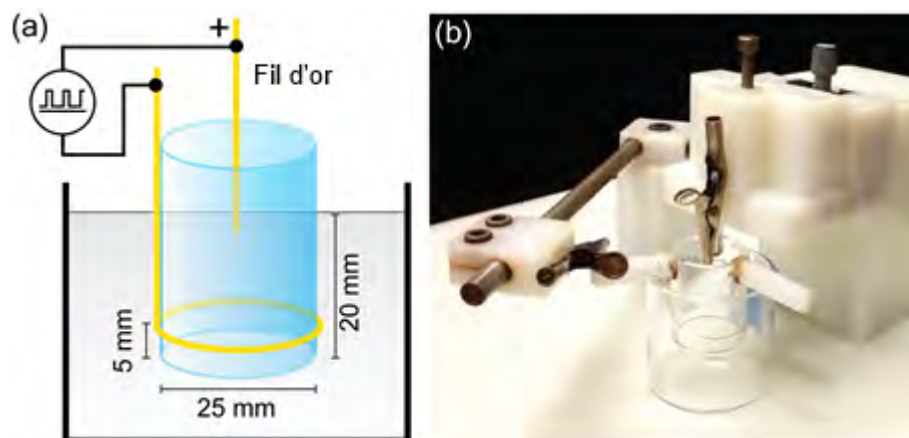


Figure 6: (a) Schéma du système de gravure. Un fil d'or est immergé à une profondeur d'un millimètre dans la solution. (b) Photographie du système de gravure. La pince crocodile au milieu tient le fil d'or.

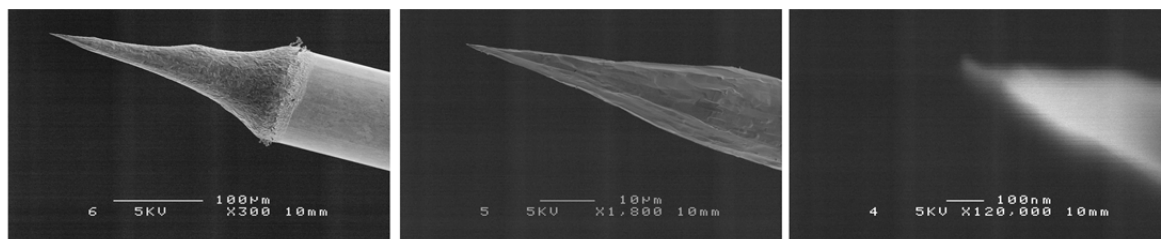


Figure 7: Images MEB d'une pointe gravée avec une tension pulsée à différentes échelles. La surface de la pointe est très lisse et l'apex a un rayon inférieur à 20 nm.

6 TERS sur les nanotubes de carbone

Les nanotubes de carbone représentent un échantillon de référence idéal pour le TERS. Tout d'abord, les nanotubes de carbone métalliques avec un diamètre proche de 1.3 nm sont des diffuseurs Raman résonants avec un fort signal lorsqu'ils sont excités avec de la lumière rouge (632.8 nm). Leur petit volume occupe seulement une petite fraction de la tache focale du laser ce qui réduit le bruit de fond et facilite la détermination du facteur d'exaltation. Deuxièmement, le petit diamètre permet de mesurer l'extension du champ proche optique et donc la résolution latérale de la pointe quand celle-ci balaye les nanotubes de carbone. Pour les expériences suivantes, nous avons déposé des nanotubes de carbone sur une couche mince d'or avec une densité d'environ 1 nanotube par μm^2 (voir Fig. 8).

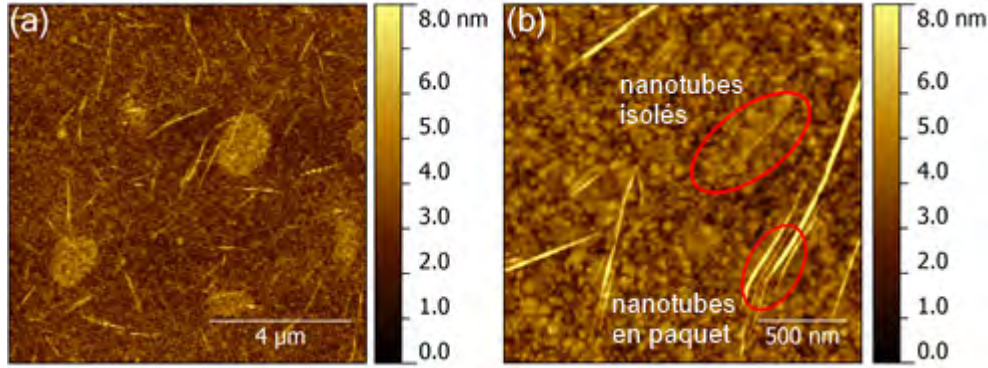


Figure 8: Images topographiques obtenue par AFM de nanotubes de carbone déposés sur une couche mince d'or à différentes résolutions. Les nanotubes avec un large diamètre sont en paquet.

L'exaltation des pointes de TERS gravées par le procédé électrochimique a été vérifiée en STM en focalisant la lumière sur l'apex de la pointe et en plaçant la pointe sur un nanotube de carbone. Une augmentation de la bande G du spectre du nanotube de carbone, qui n'est autrement pas visible en champ lointain, indique si la pointe permet une exaltation ou pas.

Nous avons utilisé une pointe TERS fonctionnelle pour balayer l'échantillon de nanotubes de carbone afin de faire une cartographie TERS. De plus, la pointe a été déplacée pas à pas au-dessus de l'échantillon et un spectre Raman a été enregistré à chaque position. Les données sont visualisées grâce à une image en fausses couleurs de la bande G des nanotubes de carbone en figure 9.

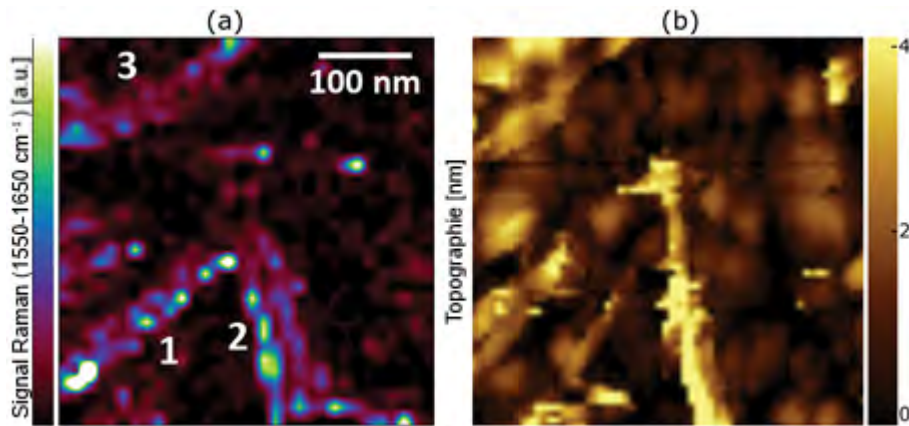


Figure 9: (a) Cartographie TERS de trois nanotubes de carbone sur un substrat d'or sur une surface de 400 nm x 400 nm avec 32x32 points (interpolés). L'image montre la somme du signal Raman entre 1550 cm^{-1} et 1650 cm^{-1} (région spectrale de la bande G). (b) Image topographique de la même zone enregistrée avant la cartographie.

Le facteur d'exaltation de la pointe peut être déterminé en se basant sur la cartographie TERS. En analysant le spectre TERS à différentes positions *sur* et quelques nanomètres à *côté* d'un nanotube, la variation du signal Raman montre l'exaltation aussi bien que la résolution latérale. La figure 10 montre le spectre TERS à trois positions différentes et montre une forte augmentation de la bande G quand la pointe est placée sur un nanotube de carbone.

Le signal de la bande G est au moins exalté 50 fois quand la pointe est placée sur un nanotube de carbone par rapport au niveau du bruit de fond (pas de bande G visible). Les petits

mouvements de la pointe de 20 nm qui mène à la variation du signal peuvent être interprétés comme le minimum de la résolution latérale.

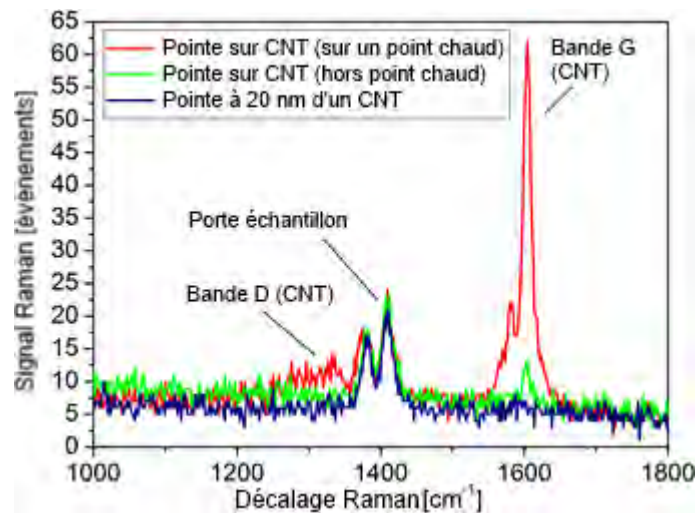


Figure 10: Le graphique montre le spectre Raman entre 1000 cm^{-1} et 1800 cm^{-1} comme comparaison de trois positions de la pointe issues de la cartographie TERS. Tandis que l'intensité de la bande G est fortement liée à la position de la pointe, le signal du champ lointain, clairement visible grâce aux pics aux alentours de 1400 cm^{-1} qui proviennent du porte échantillon en saphir, est constant.

7 TERS sur les nanocristaux de titanate de plomb

Les études TERS sur les nanocristaux ont été faites avec des substrats de platine couverts avec des nano-grains de PbTiO_3 . Les grains sont issus d'une croissance épitaxiale effectuée par Sven Clemens [7] et ont un diamètre de 100 nm, une épaisseur de 30 nm et une séparation de 250 nm. Cette géométrie d'échantillon est bien adaptée aux études TERS car les grains sont trop petits pour donner un signal Raman mesurable dans les conditions usuelles mais assez larges pour être ferroélectriques. La taille nanométrique permet de tester la sensibilité chimique et la résolution latérale du TERS sur les ferroélectriques, alors que la faible densité surfacique de seulement 10 ilots par μm^2 génère (environ) aucun champ lointain qui, sinon, interfère avec le signal exalté. La figure 11 montre des images topographiques, prises par AFM, des ilots de titanates de plomb qui ont une forme triangulaire indiquant leur cristallinité. De plus, la microscopie à force piézoélectrique a été utilisée pour vérifier l'état ferroélectrique et la polarisabilité des ilots comme une caractérisation préliminaire (non montrée dans ce résumé).

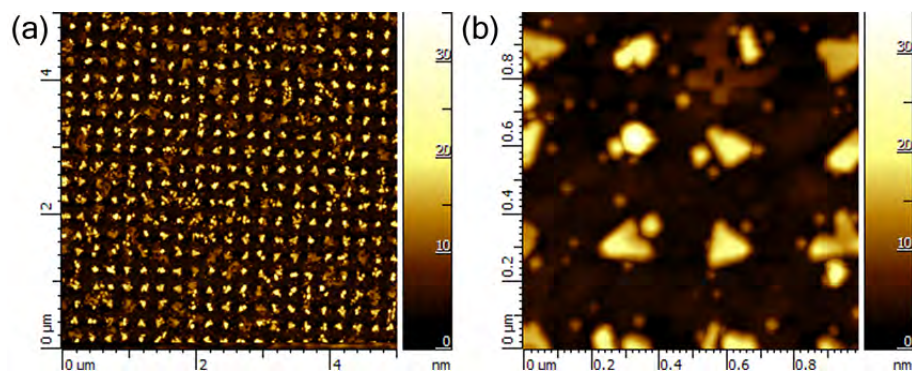


Figure 11: Image topographiques prise par AFM en mode contact intermittent de la dispersion des grains de PbTiO_3 . (a) Image $5 \mu\text{m} \times 5 \mu\text{m}$ qui montre l'arrangement géométrique des ilots. (b) Image $1 \mu\text{m} \times 1 \mu\text{m}$ qui montre les détails et l'orientation des grains.

7.1 Cartographie TERS

La figure 12 (a) montre la topographie, d'une surface de $500 \text{ nm} \times 500 \text{ nm}$, de quatre ilots de titanate de plomb balayée avec une pointe TERS, collée sur un diapason en quartz en mode de cisaillement. Les mêmes ilots ont ensuite été balayés en TERS avec une résolution de 64×64 points et un temps d'intégration d'une seconde par spectre ce qui donne un temps d'acquisition de 70 min pour l'image complète. Le rendu en fausses couleurs de l'intensité du signal intégré sur la gamme spectrale 70 cm^{-1} à 1800 cm^{-1} est montré en figure 12 (b). Les spectres TERS pris à différentes positions sont présentés à la figure 13 (a-c).

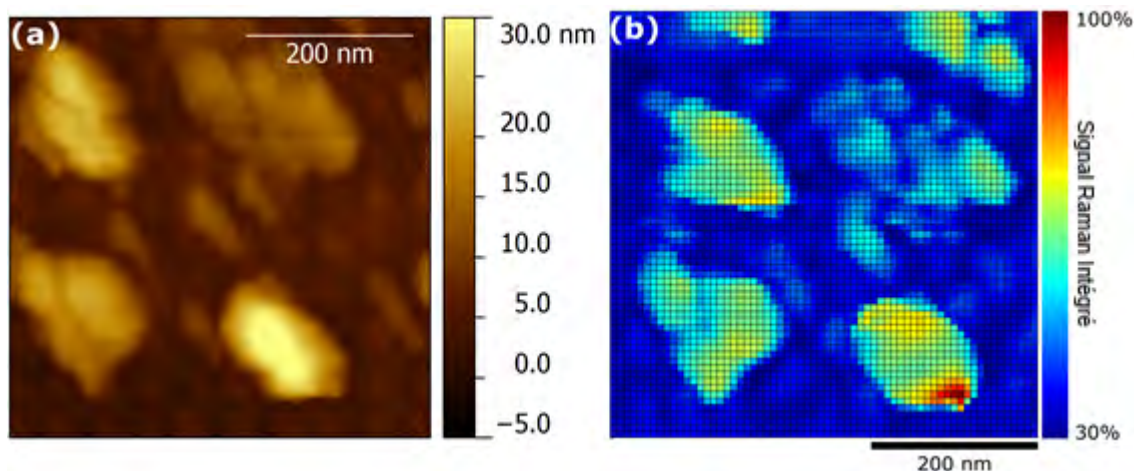


Figure 12: (a) Image topographique de quatre ilots de titanate de plomb prise avec une pointe en or, gravée par procédé électrochimique, montée sur un diapason. La même pointe a ensuite été utilisée pour le TERS sur la même zone. (b) Cartographie TERS des quatre ilots (légèrement décalée). La cartographie montre une surface de $500 \text{ nm} \times 500 \text{ nm}$, ce qui correspond à une résolution de $8 \text{ nm}/\text{pixel}$.

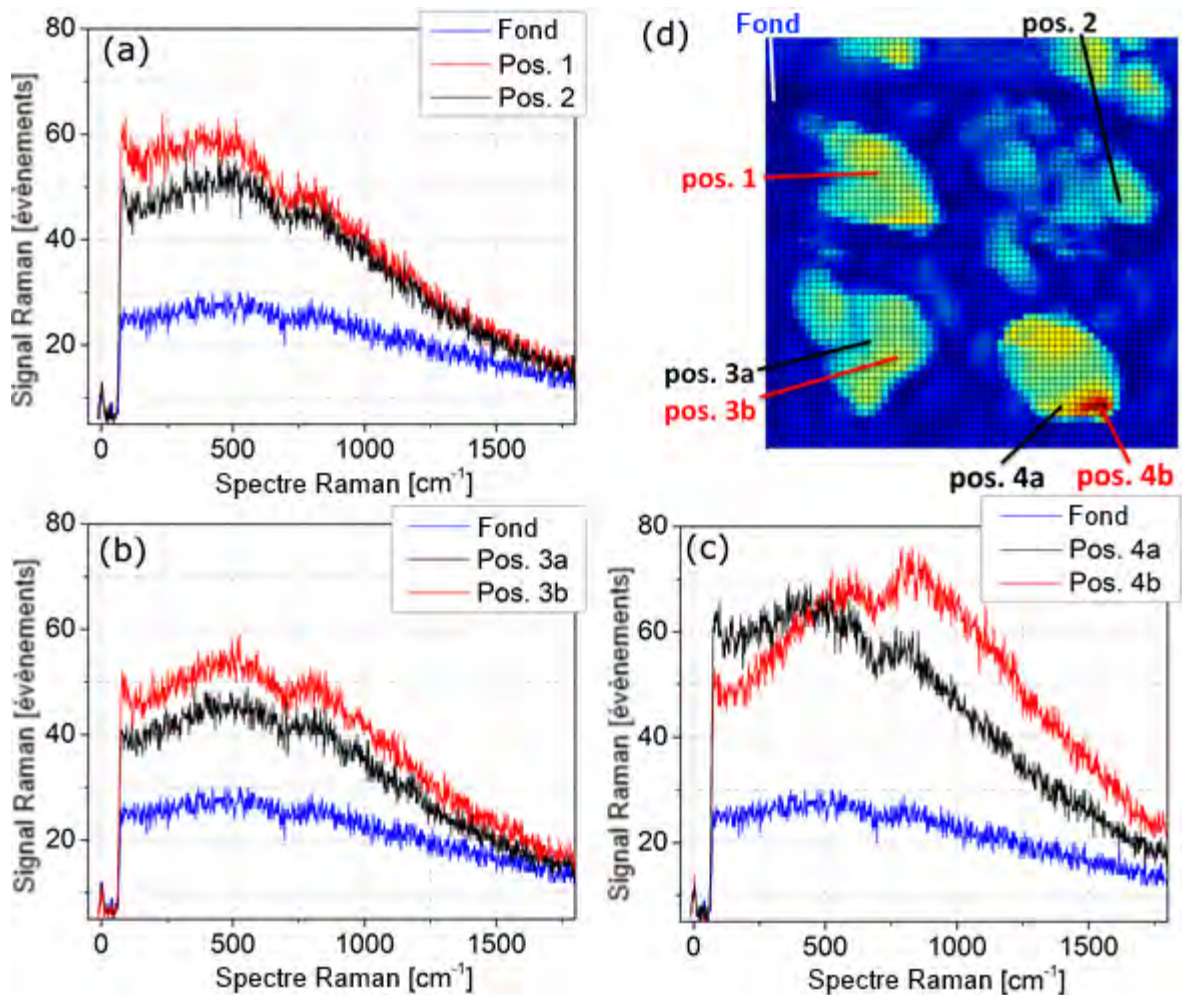


Figure 13: (a-c) Spectres de différentes positions de la cartographie TERS. Un spectre du signal de fond (Fond) pris sur le substrat de platine est montré sur chaque graphique (en bleu) pour la comparaison. (d) Position des spectres sélectionnés sur la cartographie TERS.

L'image en fausses couleurs de la cartographie TERS (Fig. 12 (b)) montre une augmentation de la diffusion Raman au niveau des ilots avec une résolution latérale d'un à deux pixels, ce qui correspond à environ 10-15 nm. Dans le but d'analyser l'information contenue dans les spectres TERS, ceux-ci ont été tracés pour différentes positions et comparés avec le signal provenant du substrat de platine (figures 13 (a-c)).

Sur les ilots, les spectres Raman apparaissent très larges et contiennent principalement un large pic sur tout le spectre avec une « dent » à environ 650 cm^{-1} . Un second petit pic peut être trouvé aux alentours de 100 cm^{-1} . En l'état, le rapport signal sur bruit des spectres est trop faible pour en tirer une conclusion sur le titanate de plomb et une analyse des données approfondie est nécessaire.

Nous avons supposé que le pic large provient d'une contamination fluorescente sur la pointe qui est exaltée au niveau des ilots à cause d'un décalage de la fréquence de la résonance du plasmon quand la pointe approche du titanate de plomb. Afin de démontrer cette hypothèse, nous avons calculé la somme des spectres Raman pour chacun des quatre ilots, puis divisé chaque spectre par le signal de fond mesuré sur le substrat de platine. Les spectres résultants ont une forme de pic de Lorentz avec une largeur correspondant à la largeur spectrale attendue de la résonance des

plasmons de surface (~90 nm). La figure 14 montre les courbes divisées et leur ajustement avec un pic de Lorentz.

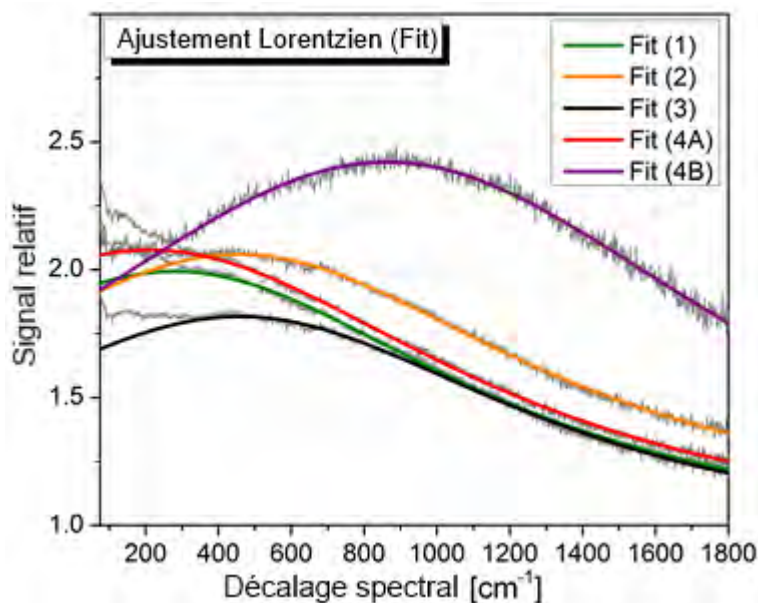


Figure 14: Ajustement par courbe de Lorentz incluant les spectres divisés par le signal de fond (en gris) pour comparaison. Le nom des courbes est basé sur la nomenclature utilisée en figure 13. Un spectre de la région ayant une intensité élevée sur l'îlot 4 a été tracé séparément. Les courbes de Lorentz s'ajustent particulièrement bien dans la gamme spectrale $400 \text{ cm}^{-1} - 1800 \text{ cm}^{-1}$. Les écarts dans la gamme spectrale en dessous de 300 cm^{-1} sont dus au signal Raman provenant des îlots de PbTiO_3 .

Maintenant que nous avons un modèle pour la fluorescence de fond, nous pouvons la soustraire aux données brutes dans le but d'extraire le signal Raman du titanate de plomb. Afin d'augmenter le rapport signal sur bruit, les spectres des quatre îlots ont été sommés et les données ont été rassemblées dans des canaux de 10 cm^{-1} de largeur. La figure 15 montre le spectre résultant qui représente le spectre TERS intégré provenant des îlots de PbTiO_3 sur l'échantillon.

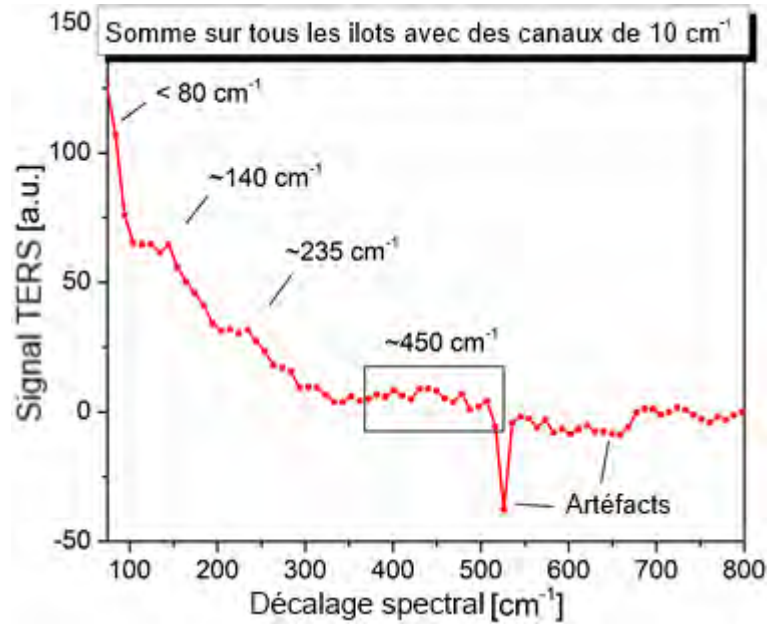


Figure 15: Somme des spectres Raman de tous les ilots de PbTiO_3 (sans la fluorescence) après fusion des canaux par groupe de 5. Nous pouvons, avec prudence, identifier trois pics à 80 cm^{-1} , 140 cm^{-1} et 235 cm^{-1} et une large augmentation autour de 450 cm^{-1} . Les deux artéfacts sont causés par le signal du substrat de silicium à 520 cm^{-1} et le pic d'absorption à 650 cm^{-1} provenant des composants optiques du spectromètre et apparaissent comme des pics négatifs à cause de la soustraction du signal de fond.

La somme des signaux Raman à des pics à $< 80 \text{ cm}^{-1}$, $\sim 140 \text{ cm}^{-1}$, $\sim 235 \text{ cm}^{-1}$ et $\sim 450 \text{ cm}^{-1}$ qui se distinguent du bruit de fond. Tous les pics sont placés sur la pente décroissante à côté du large pic à 450 cm^{-1} . Les valeurs négatives entre 550 cm^{-1} et 650 cm^{-1} sont dues à la contribution du champ lointain au signal de fond. Le spectre TERS est en accord avec les mesures Raman présentes dans la littérature pour le titanate de plomb ferroélectrique à 470°C , qui est proche de la température de transition de phase à laquelle le matériau devient paraélectrique [8].

La présence des modes Raman dans le spectre TERS indique que les ilots de PbTiO_3 sont toujours ferroélectriques, bien que proche de la température de transition de phase à cause de l'échauffement laser (8.5 mW, diamètre de la tache focale de $6 \mu\text{m}$).

7.2 Décalage de la fréquence de résonance des plasmons de surface

L'ajustement par courbe de Lorentz effectué précédemment qui a été utilisé pour soustraire le signal de fluorescence peut être utilisé pour étudier le comportement de la résonance de plasmon de surface durant le balayage TERS. Nous avons ajusté tous les spectres de la cartographie avec une courbe de Lorentz et tracé les paramètres des ajustements sous la forme d'images en fausses couleurs présentées en figure 16. Les paramètres sont le centre du pic x_c , la largeur de pic w , L'amplitude y_{amp} , et le décalage vertical du pic y_0 . x_c peuvent être interprétés comme la fréquence de résonance du SPR avec la largeur spectrale w , y_0 représente l'absorption optique du matériau autour de la pointe, et $y_{\text{amp}}+1$ peut être considéré comme le facteur d'exaltation.

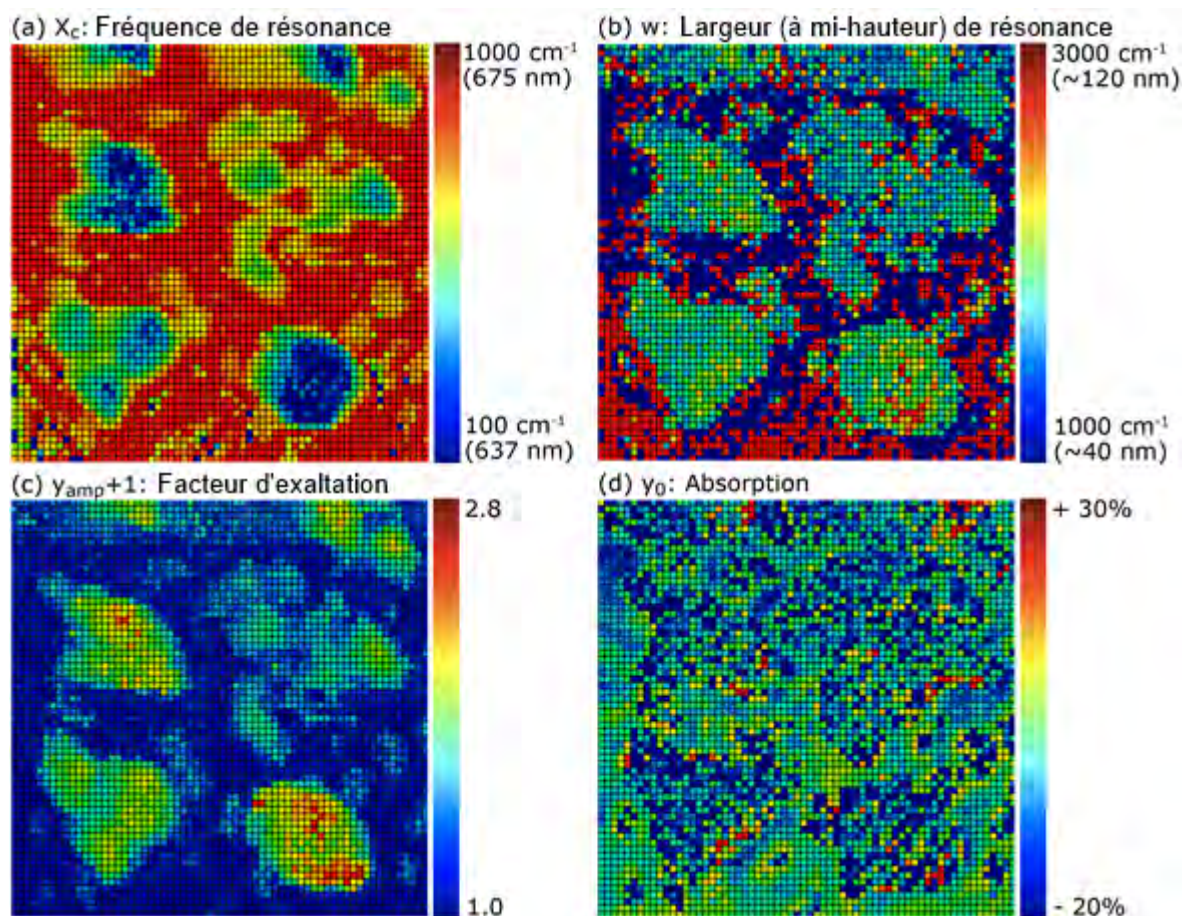


Figure 16: Images en fausses couleurs des paramètres d'ajustement de la résonance de plasmon. (a) La position du pic représente la fréquence du SPR qui est supérieure au niveau des ilots et montre un décalage vers le rouge quand la pointe se situe au-dessus du platine. (b) Largeur de la fréquence de résonance. La largeur spectrale est d'environ 80 nm quand la pointe se situe au-dessus des ilots. (c) Amplitude des pic tracé comme le facteur d'exaltation de la pointe qui varie de 1 (sur le platine) à 2.8 (sur les ilots). (d) Niveau de base interprété comme l'absorption. Les ilots ont environ 20% d'absorption, mais également un signal augmenté d'environ 30% à certaines positions aux alentours de leur contour. Les valeurs positives peuvent être reliées à une augmentation de la diffusion vis-à-vis de l'objectif.

Le décalage de la résonance du plasmon de surface peut avoir deux origines : la première, la permittivité des ilots peut affecter la fréquence du plasmon de la pointe ; la seconde, une variation de distance entre la pointe et la surface métallique peut également affecter la fréquence du SPR [9]. Nous avons été capable de relier le décalage de la fréquence à une augmentation de la distance entre la pointe et le substrat, ce qui provoque un décalage vers le bleu (la permittivité du titanate de plomb provoquerait un décalage vers le rouge). Une simulation des différences finies dans le domaine temporel a confirmé nos résultats et en plus a montré que le décalage vers le rouge dû à la permittivité des ilots est surcompensé par le décalage vers le bleu dû à l'augmentation de la distance entre la pointe et le substrat. La figure 17 montre le décalage énergétique du SPR sur la pointe en fonction de la distance pointe-substrat. Un ajustement linéaire montre un décalage de la résonance par environ 40 cm^{-1} par nanomètre de distance entre la pointe et le substrat. Nos résultats expérimentaux ont été comparés avec une simulation de l'approximation dipolaire discrète (dont le sigle anglais DDA, pour *discrete dipole approximation* est communément utilisé) sur des particules ellipsoïdales. Nos résultats et la simulation correspondent quantitativement [9].

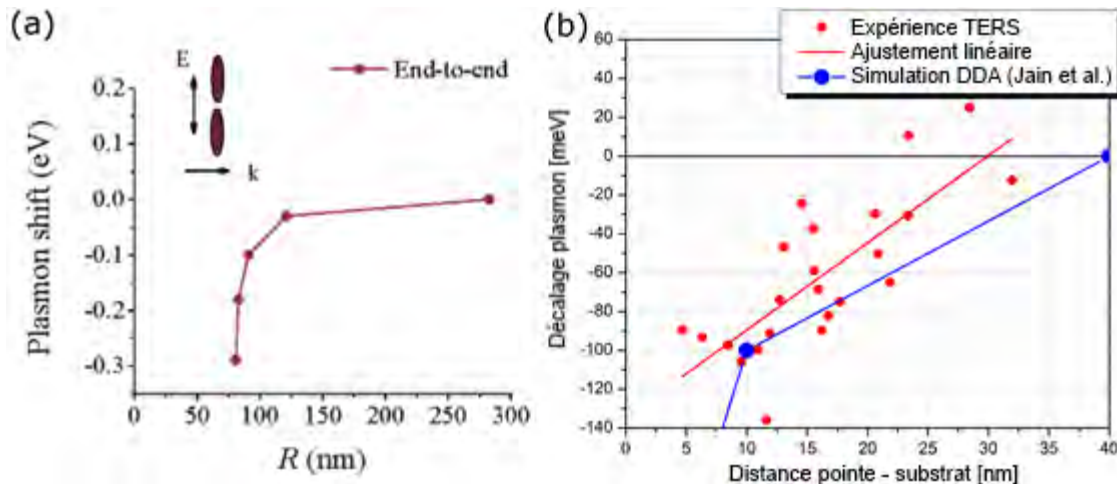


Figure 17: Décalage de la résonance du plasmon de la pointe TERS tracé en fonction de la distance entre la pointe et le substrat de platine (points rouges) pris à différentes positions de la cartographie. La simulation du DDA tirée de la réf. [9] est tracée en bleu pour comparaison.

8 Conclusions

Le confinement élevé du champ proche à la fin de la pointe TERS permet d'acquérir les spectres Raman de nanocristaux individuels avec une résolution latérale allant jusqu'à 5 nm dans des conditions ambiantes. Les cristaux ont été analysés dans leur état de croissance sur un substrat non transparent par AFM, ce qui prouve la faisabilité des études TERS des effets nanoélectronique sur une large gamme d'échantillons opaques et non conducteurs.

Dans l'optique d'obtenir un spectre TERS qui permet l'identification de pic individuel se démarquant du bruit de fond, un grand temps d'intégration et une haute intensité laser est nécessaire. Cependant, des temps d'intégration de l'ordre de la minute entravent la cartographie et l'augmentation de la puissance du laser produit une augmentation de la température de l'échantillon. L'effet de la température rend difficile l'utilisation du TERS pour l'étude de la limite super-paraélectrique et demande d'avantage de connaissance à propos de la dissipation thermique, dans la région d'interaction entre la pointe et l'échantillon, à l'échelle nanométrique. La puissance du laser et le temps d'intégration peuvent, néanmoins, être réduits en utilisant des pointes avec un facteur d'exaltation plus élevé. Les pointes avec un meilleur facteur d'exaltation sont statistiquement rares, ce qui souligne encore une fois l'importance d'un processus de production de pointe sophistiqué pour le TERS et est toujours considéré comme le principal obstacle.

Nos expériences ont, de plus, mis en avant les défis du TERS sur des échantillons composites fait de matériaux avec des permittivités différentes. A cause de la contamination de la pointe, qui a fournis un large fond de fluorescence, nous avons été en mesure d'analyser la fréquence de résonance du plasmon de surface pendant le balayage TERS. L'augmentation de la distance entre la pointe et le substrat métallique, quand la pointe balayait les îlots diélectriques, provoque un décalage vers le bleu de la fréquence de résonance de 2000 cm^{-1} ($\sim 90 \text{ nm}$ en longueur d'onde). Un tel décalage induit des variations du champ d'excitation au niveau de la pointe ainsi qu'une amplification dépendante du nombre d'onde du spectre Raman. Puisque cet effet dépend de la position, la comparaison entre les différentes régions d'un échantillon peut être trompeuse si le décalage de fréquence n'est pas pris en compte. La simulation des différences finies dans le domaine temporel a confirmé nos résultats expérimentaux.

9 Bibliographie

- [1] Katrin Domke, 'Tip-enhanced Raman spectroscopy - Topographic and chemical information on the nanoscale' (Ph.D. Thesis, Freie Universität Berlin, 2006).
- [2] B. Pettinger, B. Ren, G. Picardi, R. Schuster, and G. Ertl, 'Tip-enhanced Raman spectroscopy (TERS) of malachite green isothiocyanate at Au(111): bleaching behavior under the influence of high electromagnetic fields', *Journal of Raman Spectroscopy*, **36**, 541-550, (2005).
- [3] R. Zhang, Y. Zhang, Z. C. Dong, S. Jiang, C. Zhang, L. G. Chen, L. Zhang, Y. Liao, J. Aizpurua, Y. Luo, J. L. Yang, and J. G. Hou, 'Chemical mapping of a single molecule by plasmon-enhanced Raman scattering', *Nature*, **498**, 82-86, (2013).
- [4] K. Ishikawa, K. Yoshikawa, and N. Okada, 'Size effect on the ferroelectric phase-transition in PbTiO₃ ultrafine particles', *Physical Review B*, **37**, 5852-5855, (1988).
- [5] Debdulal Roy, Jian Wang, and Craig Williams, 'Novel methodology for estimating the enhancement factor for tip-enhanced Raman spectroscopy', *Journal of Applied Physics*, **105**, 013530, (2009).
- [6] M. Nicklaus, C. Nauenheim, A. Krayev, V. Gavriluk, A. Belyaev, and A. Ruediger, 'Tip enhanced Raman spectroscopy with objective scanner on opaque samples', *Review of Scientific Instruments*, **83**, 066102, (2012).
- [7] S. Clemens, T. Schneller, A. van der Hart, F. Peter, and R. Waser, 'Registered deposition of nanoscale ferroelectric grains by template-controlled growth', *Advanced Materials*, **17**, 1357, (2005).
- [8] I. Taguchi, A. Pignolet, L. Wang, M. Proctor, F. Levy, and P. E. Schmid, 'Raman-scattering from PbTiO₃ thin-films prepared on silicon substrates by radio-frequency sputtering and thermal-treatment', *Journal of Applied Physics*, **73**, 394-399, (1993).
- [9] P. K. Jain, K. S. Lee, I. H. El-Sayed, and M. A. El-Sayed, 'Calculated absorption and scattering properties of gold nanoparticles of different size, shape, and composition: Applications in biological imaging and biomedicine', *Journal of Physical Chemistry B*, **110**, 7238-7248, (2006).